

**TEMPORAL AND PETROGENETIC CONSTRAINTS ON VOLCANIC
ACCRETIONARY PROCESSES AT 9-10 DEGREES NORTH EAST PACIFIC
RISE**

By

Christopher L. Waters
B.S. Geology, University of New Hampshire, 2004

Submitted in partial fulfillment of the requirements for the degree of
Doctor of Philosophy

at the

MASSACHUSETTS INSTITUTE OF TECHNOLOGY

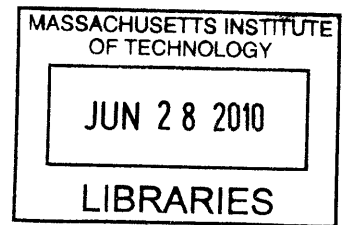
and the

WOODS HOLE OCEANOGRAPHIC INSTITUTION

June 2010

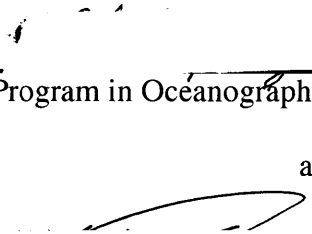
© 2010 Christopher Lee Waters
All rights reserved.

ARCHIVES

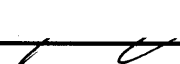


The author hereby grants MIT and WHOI permission to reproduce and to distribute publicly paper and electronic copies of this thesis document in whole or in part in any medium now known or hereafter created.

Signature of Author


Joint Program in Oceanography/Applied Ocean Science and Engineering
Massachusetts Institute of Technology
and Woods Hole Oceanographic Institution
April 22, 2010


Certified by


Kenneth W.W. Sims, Thesis Supervisor

Certified by


Maurice A. Tivey, Thesis Co-Supervisor

Accepted by


Dr. Bradford H. Hager
Chair, Joint Committee for Marine Geology and Geophysics
Massachusetts Institute of Technology/
Woods Hole Oceanographic Institution

TEMPORAL AND PETROGENETIC CONSTRAINTS ON VOLCANIC ACCRETIONARY PROCESSES AT 9-10 DEGREES NORTH EAST PACIFIC RISE

by

Christopher L. Waters

Submitted to the Joint Committee for Marine Geology and Geophysics on April 22nd, 2010 in partial fulfillment of the requirements for the degree of Doctor of Philosophy

ABSTRACT

Volcanic accretion at the fast-spreading East Pacific Rise (EPR) occurs over a ~2-4 km wide neo-volcanic zone on either side of the axial summit trough (AST). Eruption ages are critical for understanding the distribution and timing of volcanic and magmatic activity. Uranium series nuclides are susceptible to fractionation by magmatic processes that occur beneath mid-ocean ridges, and the half-lives of ^{226}Ra (1.6 kyrs) and ^{230}Th (75 kyrs) make them ideally suited for determining eruption ages and placing constraints on eruption frequency and temporal changes in magma chemistry. Accordingly, major and trace element, and long-lived radiogenic and ^{238}U - ^{230}Th - ^{226}Ra isotope compositions were measured in basalts from 9°-10°N EPR to determine eruption ages and to place temporal constraints on volcanic and magmatic processes.

At 9°30'N EPR, ^{238}U - ^{230}Th - ^{226}Ra compositions indicate that trace elementally and isotopically enriched mid-ocean ridge basalt (MORB) collected off-axis erupted >8 ka and that E-MORB magmatism is interspersed with normal, depleted MORB magmatism. Lava ages are consistent with eruption from the AST and flow down the ridge flanks, which is in contrast to previous studies that suggested E-MORB erupted from off-axis vents.

At 9°50'N EPR, discrete eruptive units are distinguished by high precision ^{238}U , ^{232}Th , and ^{226}Ra sample concentrations, but because the resolution of the ^{230}Th - ^{226}Ra model age dating technique is $\sim\pm 1$ kyrs, the surprisingly young ages of these lavas prohibit the construction of an explicit, time-constrained lava stratigraphy. Nonetheless, seven different flows identified within 0.8-2.0 km west of the AST imply greater frequency of flows to these distances than previously recognized.

Model age dating of ferrobasalts, basaltic andesites, andesites, and dacites sampled from the east limb of the overlapping spreading center at 9°03'N EPR is difficult due to uncertainties in magma residence times. However, ($^{226}\text{Ra}/^{230}\text{Th}$) disequilibria indicate recent basaltic volcanism ($\ll 8$ ka) up to ~ 4 km off-axis. The axial graben at the rise crest sources the most recent volcanic activity and is the dominant location for eruption of high-silica magmas. Major element, trace element, $^{87}\text{Sr}/^{86}\text{Sr}$, and ($^{234}\text{U}/^{238}\text{U}$) isotope compositions are consistent with the formation of dacite magmas by extensive crystallization, and ^{238}U - ^{230}Th - ^{226}Ra systematics imply crustal residence times of ~ 8 kyrs.

Thesis Supervisor: Dr. Kenneth W.W. Sims

Title: Associate Professor with Tenure, University of Wyoming

Thesis Co-Supervisor: Dr. Maurice A. Tivey

Title: Senior Scientist, Woods Hole Oceanographic Institution

ACKNOWLEDGMENTS

First and foremost, I would like to extend my deepest gratitude to my advisor, Ken Sims, who guided me through a world of uranium-series chemistry and mid-ocean ridge basalts—a world that has become a constant source of excitement, frustration, and confusion. It is strange to think that Ken has in no small way been responsible for a great many of the trials of the past six years of my life. Yet, after thrusting such challenges upon me, Ken provided me with the means and the reassurance needed to succeed. Ken has been a wonderful advisor and a constant advocate and friend, and for these things, I am truly grateful.

I would also like to thank my co-advisor Maurice Tivey, who stepped in when Ken decided to move to Wyoming. Maurice has been an attentive and responsible advisor, and discussions with him have helped to energize me throughout my final year. In addition, in the final hours of defense preparation, Maurice exposed me to the wide world of alternative career opportunities, such as lecturing in hairdressing, which naturally made me work harder to succeed.

Many thanks go to my committee members, including Tim Grove, who is a great teacher, an outstanding scientist, and an excellent mini-van driver. I am extremely grateful to Tim for bringing me along on a field trip to Mt. Shasta and Medicine Lake that has helped to keep my eyes open to sub-aerial volcanism while I've been immersed in studying volcanoes a mile and a half under water. Adam Soule's volcanological and geological expertise of the 9°-10°N EPR segment has been a tremendous asset; his map-making skills have served to make this a much more colorful and visually stimulating thesis; and, his exceptional softball skills have improved my experiences on the G&G softball team. Glenn Gaetani has been kind and generous to me from the start with a ready ear for a wide range of scientific questions and a staying hand for his enormous dog, Griffin. Jian Lin was a great thesis committee chair, and his excitement for science and attention to detail helped to make the defense process a smooth and constructive experience.

In addition, I am indebted to my collaborators on these research projects. In particular, I thank Jurek Blusztajn, who fortunately had enough optimism for both of us on the bad days in the lab, and enough decent gossip on the good days when the Neptune was running smoothly enough to bore. Rob Sohn provided exceptional support during the final days when I needed feedback on a manuscript in a crunch, or insight into data analysis and modeling. Janne Blichert-Toft (ENS-Lyon) provided essential data and the absolute fastest turn-around time on manuscripts, and she has always been a ready and willing supporter. Mike Perfit (U. of Florida) graciously provided many of the samples for this research, and he always had valuable comments and an intense excitement for all things EPR. I also thank Emily Klein, Scott White, Karen von Damm, and Dan Fornari who were PIs on the 2007 AT15-7 MEDUSA cruise to 9°03'N EPR.

I am grateful to the workers in the WHOI ICP facility who have made the U-series, Sr, and Nd analyses possible. In particular, I thank Jurek Blusztajn again (who I could never thank enough), Scot Birdwhistell, Lary Ball, and Dave Schneider, who have been essential to the data collection process. I would also like to thank Jeremy Inglis and Ethan Baxter for their assistance with Sr isotope analyses at the Boston University TIMS facility. Jurek Blusztajn, Lynne Elkins, Christian Miller, Jeff Standish, Bernhard Peucker-Ehrenbrink, Evy Mervine, Matt Jackson, Rama Chakrabarti, Zhengrong Wang, and Olivier Rouxel supplied an enormous amount of laboratory advice and assistance for wet chemical separations. Paul Henderson and Matt Charette are thanked for assistance with preparation of a ^{228}Ra spike at a critical research juncture. Many thanks go to Alison Shaw for access to a great place to pick sample glass.

The Academic Programs Office at WHOI made my educational experience a smooth one, and I am grateful for their support. In particular, Julia Westwater and Marsha Gomes have been invaluable assets who helped at every tough logistical step along the way, and they did it with smiles.

I've been lucky to meet such a wonderful group of people that have been a part of the Joint Program. Although the list could go on and on, I want to specifically thank Casey Saenger, who receives the outstanding office mate award, Emily Roland and Matt Jackson, who sparked such remarkably different, yet equally stimulating conversations while running with me, and Jeff Standish, who started it all off by teaching me how to clean lab dishes so he could work on *his* thesis. Trish Gregg was always a source for interesting conversation when I needed a break at work, and she and Cory were outstanding cooks for when I needed a meal and great company. Lynne Elkins and Joanna Gyory provided me with no end of roommate fun during my 'formative' years in the Joint Program. Mike Brosnahan reminds me that I will probably be the next 'durak,' but isn't afraid to ask inquisitive questions. Annette Hynes and Kate Buckman are great friends and brought great humor and honesty to my life. Louie Wurch taught me that it's okay to really go for it and miss, provided that a pitcher of PBR and video games are nearby. I also want to thank Katie Silverthorne, who most fortuitously shares an interest with me in the same genres of games and books. Lastly, but far from least, I want to thank Liz Orchard, who brings me joy through love, adventure, dance, and song.

I have everything to thank for my family's unconditional love and support. My parents and brother have a deeper sense of awe and wonder of the natural world than anyone I've ever met, and I'd like to believe I take some part of that wherever I go.

This research was made possible by funding from the Academic Programs Office, from the WHOI travel assistance funds, a Goldschmidt student travel grant, and National Science Foundation grants OCE-0623838, OCE-0527053, and OCE-0137325 to K.W.W.S.

TABLE OF CONTENTS

1	Introduction	11
2	Perspective on the genesis of E-MORB from chemical and isotopic heterogeneity at 9°-10°N East Pacific Rise	25
2.1	Introduction.....	26
2.2	Previous Studies of E-MORB.....	27
2.3	Sample locations and geological background.....	34
2.4	Analytical methods.....	38
2.5	Results.....	40
2.5.1	Major elements.....	40
2.5.2	Trace elements.....	41
2.5.3	Long-lived radiogenic isotopes: Sr, Nd, Hf, and Pb.....	42
2.5.4	U-Th-Ra disequilibria.....	44
2.6	Discussion.....	46
2.6.1	Correlations between chemical and isotopic variability.....	46
2.6.2	Are E-MORB erupted on- or off-axis?.....	48
2.6.3	Petrogenesis of E-MORB.....	60
2.7	Conclusions.....	65
	Tables.....	77
	Figures.....	86
	Appendix.....	106
3	Evaluating the resolution of U-series age constraints: an application to ridge flank construction at 9°-10°N East Pacific Rise	109
3.1	Introduction.....	110
3.2	Sample locations and descriptions.....	114
3.3	U-series model age dating.....	115
3.4	Comparison of U-series dating with other age constraints at 9°50'N EPR.....	118
3.5	Analytical methods.....	119

3.6	Results.....	121
3.6.1	Major elements.....	121
3.6.2	Trace elements.....	122
3.6.3	⁸⁷ Sr/ ⁸⁶ Sr isotopes.....	122
3.6.4	U-series isotopes.....	123
3.7	Discussion.....	129
3.7.1	Geochemical relationships among samples and flow units.....	130
3.7.2	Age constraints.....	132
3.7.3	Reconciling geochemical and model age observations with seafloor observations.....	134
3.7.4	Extrusive crustal construction at 9°-10°N EPR: the origin of shingled terrain.....	137
3.7.5	The youth of the neo-volcanic zone.....	139
3.7.6	Implications for lava stratigraphy.....	141
3.7.7	Rapid temporal variations in melt supply.....	143
3.8	Conclusions.....	144
	Tables.....	153
	Figures.....	163
	Appendix A. Dive summaries.....	179
	Appendix B. Cluster analysis.....	180
4	²³⁸U-²³⁰Th-²²⁶Ra constraints on the volcanic and magmatic evolution of an overlapping spreading center at 9°03'N East Pacific Rise	183
4.1	Introduction.....	184
4.2	Geologic setting and sample descriptions.....	186
4.3	U-series dating and MOR crustal construction.....	190
4.4	Analytical methods.....	194
4.5	Results.....	196
4.5.1	Major elements.....	196
4.5.2	Trace elements.....	198

4.5.3	$^{87}\text{Sr}/^{86}\text{Sr}$ and $^{143}\text{Nd}/^{144}\text{Nd}$ isotope compositions.....	199
4.5.4	^{238}U - ^{230}Th - ^{226}Ra	200
4.6	Discussion.....	203
4.6.1	Eruption Ages.....	203
4.6.2	The effect of residence times on model ages.....	206
4.6.3	Petrologic relationships among primitive basalts ($9^{\circ}17'\text{N}$ - $9^{\circ}54'\text{N}$) and ferrobasalt.....	208
4.6.4	Previous models for the genesis of MOR high-silica lavas.....	209
4.6.5	Apparent discrepancies with assimilation of partial melts of hydrothermally altered wall rock.....	209
4.6.6	Crystallization origin for the petrogenesis of dacites.....	212
4.6.7	^{238}U - ^{230}Th - ^{226}Ra systematics among basaltic andesites and dacites.....	216
4.6.8	Implications for volcanic accretion at the $9^{\circ}03'\text{N}$ OSC.....	218
4.7	Conclusions.....	221
	Tables.....	233
	Figures.....	244

CHAPTER 1: DETERMINING TIME SCALES OF MID-OCEAN RIDGE VOLCANISM AND IGNEOUS PETROGENESIS

Volcanic Construction at Mid-Ocean Ridges

The global mid-ocean ridge (MOR) system, a roughly 60,000 km long, nearly continuous volcanic lineament, marks the locus of the divergent plate boundaries throughout the ocean basins. The magnetic anomaly reversal patterns and broad scale age distribution of crust throughout the ocean basins indicates that MORs are the loci for the construction of new oceanic crust. The classical view of oceanic crustal formation assumes symmetric rifting occurs by continuous seafloor spreading and volcanic accretion and dike injection at the ridge axis (Kidd; 1977; Macdonald, 1982). Modern geophysical and geochemical studies have demonstrated that both volcanic accretion and magmatic processes are spatially and temporally complex and contribute to asymmetric crustal accretion over a region that is much wider than the immediate ridge axis.

Oceanic crustal construction at 9°-10°N along the fast-spreading East Pacific Rise (EPR) has typically been viewed as a geologically continuous process involving eruptions and dike emplacement within a narrow zone of magmatism defined by the axial summit trough (AST) (Haymon et al., 1991; Fornari et al., 1998; Perfit and Chadwick, 1998; Schouten et al., 2001; Sims et al., 2003; Soule et al., 2009). However, seismic studies suggest that layer 2A, inferred to be the extrusive volcanic crust, doubles in thickness within ~2-4 km from the AST (Christeson et al., 1994; 1996; Harding et al., 1993; Schouten et al., 1999; Sohn et al., 2004; Vera and Diebold, 1994). This geometry can only be generated if a large component of crustal accretion occurs outside of the AST

(Goldstein et al., 1994; Hooft et al., 1996; Perfit et al., 1994; Schouten et al., 1999; Sims et al., 2003; Soule et al., 2005; White et al., 2002). In light of the observed crustal thickening, recent efforts have focused on investigating the details of volcanic accretion. Several mechanisms have been proposed to explain this thickening of layer 2A: eruptions from vents outside the AST, often in the form of pillow ridges/mounds (Perfit et al., 1994), axial lobate or sheet lava flows that overflow the AST (Hooft et al., 1996; Schouten et al., 1999; Sims et al., 2003), and lava channels and tubes that transport axial lavas several km away from the AST (Hooft et al., 1996; Sims et al., 2003, Soule et al., 2005). High-resolution field mapping using autonomous benthic explorer (ABE) bathymetry and DSL-120A side-scan sonar provides evidence for contributions from all three mechanisms.

U-Series Nuclides: A Tool for Determining an Eruption Age Framework

Although seafloor and high-resolution remote sensing observations are critical for understanding volcanic accretion, eruption ages are also needed to provide a temporal framework in which to interpret these spatial observations. For example, how rapidly is the extrusive crust built? How rapidly does lava geochemistry change, and are these compositional changes related to time-dependent variations in the spatial distribution of lava emplacement? Eruption ages are critical for understanding the distribution and timing of volcanic and magmatic activity.

The half-lives of U-series nuclides, in particular, ^{226}Ra (1.6 kyrs) and ^{230}Th (75 kyrs), make them ideally suited for studying recent geological processes, especially

magmatism and volcanism. U-series nuclides may fractionate due to partial melting and/or crystallization, creating disequilibria, but radioactive decay during melt transport, crustal residence, and post-eruption aging will return them towards a steady-state condition called “secular equilibrium,” in which the activities of nuclides are equal. In addition, the magnitude of disequilibria produced by partial melting is affected by the initial abundance of the U-series nuclides in the melting rock. Thus, the extent of U-series disequilibrium measured in any lava reflects the integrated signal of a number of processes that modify an initial mantle rock composition—including partial melting, melt transport, crustal residence, and seafloor alteration—and the time scales over which these processes occur, namely subsurface residence in the mantle and crust and post-eruption aging.

In some instances, the relationships among U-series disequilibria and other geochemical metrics affected by source composition, partial melting, crystallization, and crustal residence (e.g., long-lived radiogenic isotope compositions, incompatible element ratios, and major and trace element abundances) can be used to help disentangle this convoluted geochemical signal and determine eruption ages. Because a number of physical volcanic processes contribute to the complicated distribution of lava flows about the ridge axis, eruption ages are essential for understanding the spatial and temporal extent of these processes. In particular, variations in eruption volumes, frequency, and distribution can have profound effects on upper crustal construction. In addition, eruption ages provide a necessary context for correctly interpreting observed geochemical

compositions of lavas in terms of variations in mantle geochemistry, partial melting processes, and subsurface melt distribution.

Indeed, studies of MOR basalts (MORB) using U-series nuclides have demonstrated their ability to place constraints on melting and melt transport rates in the mantle (e.g., Jull et al., 2002; Lundstrom et al., 1995; 1998; 1999; 2000; McKenzie et al., 1985; Rubin et al., 2005; Sims et al., 1995; 1999; 2002), crustal residence times (e.g., Cooper et al., 2003; Rubin et al., 2005; Sims et al., 2002), and eruption ages (e.g., Bergmanis et al., 2007; Goldstein et al., 1992; 1993; 1994; Rubin et al., 1990; 1994; Sims et al., 2003; Standish and Sims, 2010; Sturm et al., 2000; Volpe and Goldstein, 1993).

Applying U-Series Ages to Problems of Crustal Construction

Studies of long-lived radiogenic isotope systems in MORB and ocean island basalts (e.g., Rb-Sr, Sm-Nd, Lu-Hf, U-Pb) have demonstrated the existence of long-term chemical heterogeneities in the oceanic mantle at different length scales (e.g., Hart et al., 1973; Hedge and Peterman, 1970; Tatsumoto, 1966; White and Schilling, 1978; Zindler and Hart, 1986; Sims and Hart, 2006). Even far from the influence of any hot spot, such as at the East Pacific Rise (EPR), the adjacent and seemingly coeval occurrence of enriched (E-MORB), normal (N-MORB) and very depleted MORB (D-MORB) attests to the ubiquitous presence of heterogeneous mantle domains over short length scales (e.g., Allan et al., 1989; Castillo et al., 2000; Fornari et al., 1988; 1989; Hekinian et al., 1989; Langmuir et al., 1986; Lundstrom et al., 1999; Sims et al., 2002; Mahoney et al., 1994; Niu et al., 1997; Niu et al., 1999; Niu et al., 2002; Perfit et al., 1994; Prinzhofer et al.,

1989; Reynolds et al., 1992; Reynolds and Langmuir, 2000; Zindler et al., 1984). While the isotopic and chemical heterogeneity of the present-day mantle almost certainly represents the continuous processes of differentiation and remixing, the exact origin of these enriched mid-ocean ridge mantle domains and the genesis of E-MORB are still vigorously debated. Furthermore, because the ages of E-MORB are not well constrained, the petrogenetic, temporal, and geological relationships between the less abundant E-MORB and volumetrically predominant N-MORB are not known.

In Chapter 2, I report new major and trace element abundances, and Sr, Nd, Pb, Hf, and ^{238}U - ^{230}Th - ^{226}Ra isotope compositions for a suite of 16 off-axis MORB glasses from 9°30'N-9°54'N EPR, including eight off-axis E-MORB from 9°30'N. These new data, in concert with previously published isotopic data for N-MORB from this region (Sims et al., 2002; 2003), demonstrate the existence of an elementally and isotopically heterogeneous mantle source beneath the 9°-10°N region of the EPR. Based on U-series eruption ages obtained on off-axis E-MORB in the 9°30'N region, I argue that the reason E-MORB are primarily found off-axis in the 9°-10°N region is that after eruption from the AST and subsequent flow down the ridge flanks, these lavas remained exposed at the seafloor due to locally asymmetric volcanic construction. This is in contrast to previous studies that proposed that E-MORB erupt directly on crust several kilometers off-axis (Perfit et al., 1994). As a result, off-axis lavas provide a window into temporal changes in mantle composition through the melting region at 9°-10°N EPR. The range of eruption ages of E-MORB at 9°-10°N EPR and the geochemical mixing trends suggest that

enriched geochemical heterogeneities are periodically introduced into the mantle melting regime, producing short episodes of dominantly E-MORB magmatism.

In Chapter 3, I focus on determining eruption ages for a suite of comparatively homogeneous lavas collected within the neo-volcanic zone at 9°50'N EPR, an area ~2 km wide on either side of the AST that is argued to be the main location for emplacement of recently erupted lavas. In order to construct a time-constrained volcanic stratigraphy of the ridge crest, 22 MORB were collected from several flow units on the east and west flanks of the ridge axis at 9°50'N EPR in February-March of 2004 and were measured for major element, trace element, and $^{87}\text{Sr}/^{86}\text{Sr}$ and ^{238}U - ^{230}Th - ^{226}Ra isotopic compositions. Additional ^{238}U - ^{230}Th - ^{226}Ra data obtained from zero-aged samples from the 2005-2006 eruption sequence, when taken together with data for samples from the 1991-1992 eruption, suggest more diversity in initial ($^{226}\text{Ra}/^{230}\text{Th}$) than previously anticipated and limit the resolution of our dating technique to $\sim\pm 1$ kyrs. I find that ridge flank samples in this study are younger than ~ 2 kyrs, but that the range of geochemical compositions represented by these flank lavas as a group, particularly U, Th, and ^{226}Ra concentrations, is much greater than the range represented by samples from individual eruptions (e.g., 1991-92 and 2005-06). Some samples have identical geochemical compositions, and this allows us to identify seven distinct eruptive units despite indistinguishable model ages. These data suggest more frequent (<300 yrs) emplacement of flows up to 1-2 km from the AST than has been previously inferred from models of crustal accretion (Hooft et al., 1996; Bowles et al., 2006). In addition, the variability of geochemical compositions requires rapid, significant changes in parental melt composition on the order of a few

hundred years, though much smaller changes than required to produce the E-MORB discussed in Chapter 2.

Finally, in Chapter 4, I focus on the overlapping spreading center (OSC) centered at 9°03'N along the EPR, a large non-transform ridge discontinuity that has been the recent focus of extensive geophysical study (Bazin et al., 2001; 2003; Combier et al., 2008; Dunn et al., 2001; Kent et al., 2000; Toomey et al., 2007; Tong et al., 2002; 2003; White et al., 2009). This study has imaged significant melt bodies throughout the crust at this OSC and has revealed a highly complex and asymmetric crustal melt distribution compared to other nearby sections of the ridge. This complicated geometry is thought to have significant implications for the storage and evolution of melt in the crust, and indeed, a wide range of melt compositions have been sampled at the 9°03'N OSC, including highly differentiated lavas such as FeTi basalts and dacites (Langmuir et al., 1986; Wanless et al., 2007). Thus, the 9°03'N OSC is an ideal location to explore the relationships between melt composition, melt lens geometry, and crustal accretion.

Accordingly, in Chapter 4, I present major and trace element, and $^{87}\text{Sr}/^{86}\text{Sr}$, $^{143}\text{Nd}/^{144}\text{Nd}$, and U-series isotope compositions for a suite of 22 representative lavas, collected during a cruise in 2007 with the *Jason II* ROV, that come from along and across the east limb of the OSC and span a wide range of compositions. When compared with crystallization models and experiments, the major element compositions of ferrobasalts and dacites appear well explained by derivation by fractional crystallization of a primitive basaltic magma similar to that needed to explain compositional trends at 9°50'N EPR. Coherent mixing trends among major element, trace element, and U-series isotopic

compositions indicate that mixing of ferrobasaltic and dacitic end members produces intermediate basaltic andesite and andesite compositions. Constant $^{87}\text{Sr}/^{86}\text{Sr}$ ($\sim 0.70250 \pm 50$ ppm, 2σ) and near equilibrium ($^{234}\text{U}/^{238}\text{U}$) and ($^{226}\text{Ra}/^{230}\text{Th}$) isotopic compositions in the dacites argue against their formation by assimilation of partial melts of hydrothermally altered crust, a process previously proposed to explain the origin of high-silica MOR lavas (Wanless et al., 2009).

Significant ^{226}Ra excesses measured in all other lavas indicate recent ($\ll 8$ kyrs) volcanic activity has occurred along most of the east limb axial graben ($9^{\circ}03'$ - $9^{\circ}10'$) and out to 4 km off-axis in the region north of the overlap basin. Axial basalts have the highest ($^{226}\text{Ra}/^{230}\text{Th}$) (2.10- 2.41) and appear extremely young, whereas basalts collected off-axis have consistently lower ($^{226}\text{Ra}/^{230}\text{Th}$) (1.84-1.96) and appear much older, suggesting that the axial graben is the primary locus for recent volcanic activity. In addition, young-appearing axial dacites have much lower, near equilibrium ($^{226}\text{Ra}/^{230}\text{Th}$) values, yet ($^{230}\text{Th}/^{232}\text{Th}$) values that appear unchanged relative to that observed in zero-age basalts, suggesting residence times of ~ 8 kyrs.

References

- Allan, J.F., R. Batiza, M.R. Perfit, D.J. Fornari, and R.O. Sack (1989), Petrology of Lavas from the Lamont Seamount Chain and Adjacent East Pacific Rise, 10°N . *J. Petrol.* 30 (5), 1245-1298.
- Bazin, S., A. Harding, G. Kent, J. Orcutt, C. Tong, J. Pye, S. Singh, P. Barton, M. Sinha, R. White, R. Hobbs, H.V. Avendonk (2001) Three-dimensional shallow crustal emplacement at the $9^{\circ}03'\text{N}$ overlapping spreading center on the East Pacific Rise: correlations between magnetization and tomographic images, *J. Geophys. Res.* 106, 16,101-16,117.
- Bazin, S., A.J. Harding, G.M. Kent, J.A. Orcutt, S.C. Singh, C.H. Tong, J.W. Pye, P.J. Barton, M.C. Sinha, R.S. White, R.W. Hobbs, and H.J.A. Van Avendonk (2003)

- A three-dimensional study of a crustal low velocity region beneath the 9°03'N overlapping spreading center, *Geophys. Res. Lett.* 30.
- Bergmanis, E.C., J. Sinton, and K.H. Rubin (2007) Recent eruptive history and magma reservoir dynamics on the southern East Pacific Rise at 17°30'S, *Geochem., Geophys., Geosyst.*, 8(12), doi: 10.1029/2007GC001742.
- Bowles, J., J.G. Gee, D.V. Kent, M.R. Perfit, S.A. Soule, and D.J. Fornari (2006), Paleointensity applications to timing and extent of eruptive activity, 9°-10°N East Pacific Rise, *Geochem., Geophys., Geosyst.*, 7(6), doi:10.1029/2005GC001141.
- Castillo, P. R., E. Klein, J. Bender, C. Langmuir, S. Shirey, R. Batiza, and W. White (2000), Petrology and Sr, Nd, and Pb isotope geochemistry of mid-ocean ridge basalt glasses from the 11°45'N to 15°00'N segment of the East Pacific Rise. *Geochem., Geophys., Geosyst.*, 1 (1999GC000024).
- Christeson, G.L., G.M. Purdy, and G.J. Fryer (1994), Seismic constraints on shallow crustal emplacement processes at the fast-spreading East Pacific Rise, *J. Geophys. Res.*, 99, 17957-17973, 1994.
- Christeson, G.L., G.M. Kent, G.M. Purdy, and R.S. Detrick (1996), Extrusive thickness variability at the East Pacific Rise, 9°-10°N, constraints from seismic techniques, *J. Geophys. Res.*, 101, 2859-2873.
- Combiér, V., S.C. Singh, M. Cannat, J. Escartin (2008) Mechanical decoupling an thermal structure at the East Pacific Rise axis 9°N: Constraints from axial magma chamber geometry and seafloor structures, *Earth Planet. Sci. Lett.*, 272, 19-28.
- Dunn, R., D. Toomey, S. Solomon (2001) Three-dimensional seismic structure and physical properties of the crust and shallow mantle beneath the East Pacific Rise, *J. Geophys. Res.*, 105, 23,537-23,555.
- Fornari, D.J., M.R. Perfit, J.F. Allan, and R. Batiza (1988), Small-scale heterogeneities in depleted mantle sources--near-ridge seamount lava geochemistry and implications for mid-ocean ridge magmatic processes. *Nature* 331, 511-513.
- Fornari, D.J., M.R. Perfit, J.F. Allan, R. Batiza, R. Haymon, A. Barone, W.B.F. Ryan, T. Smith, T. Simkin, and M.A. Luckman (1989) Geochemical and structural studies of the Lamont Seamount--seamounts as indicators of mantle processes. *Earth Planet. Sci. Lett.*, 89(1), 63-83.
- Fornari, D.L., R. Haymon, M. Perfit, T.K.P. Gregg, and M.H. Edwards (1998), Axial summit trough of the East Pacific Rise, 9-10°N: Geological characteristics and evolution of the axial zone on fast spreading mid-ocean ridges, *J. Geophys. Res.*, 103, 9827-9855.
- Goldstein, S.J., M.T. Murrell, D.R. Janecky, J.R. Delaney, and D. Clague (1992), Geochronology and petrogenesis of MORB from the Juan de Fuca and Gorda Ridges by ²³⁸U-²³⁰Th disequilibrium, *Earth Planet. Sci. Lett.*, 109, 255-272.
- Goldstein, S.J., M.T. Murrell, and R.W. Williams (1993), ²³¹Pa and ²³⁰Th chronology of Mid-Ocean Ridge Basalts. *Earth Planet. Sci. Lett.*, 115, 151-160.
- Goldstein, S.J., M.R. Perfit, R. Batiza, D.J. Fornari, and M.T. Murrell (1994), Off-axis volcanism at the East Pacific Rise detected by uranium-series dating of basalts, *Nature*, 367, 157-159.

- Harding, A.J., G.M. Kent, and J.A. Orcutt (1993), A multichannel seismic investigation of upper crustal structure at 9°N on the East Pacific Rise: Implications for crustal accretion, *J. Geophys. Res.*, 98, 13925-13944.
- Hart, S. R., J.-G. Schilling, and J.L. Powell. (1973) Basalts from Iceland and along Reykjanes Ridge Sr isotope geochemistry. *Nature, Physical Science* 246 (155), 104-107.
- Haymon, R.M., D.J. Fornari, M.H. Edwards, S.C. Carbotte, D. Wright, and K.C. Macdonald (1991), Hydrothermal vent distribution along the East Pacific Rise Crest (9°09'-54'N) and its relationship to magmatic and tectonic processes on fast-spreading mid-ocean ridges, *Earth Planet. Sci. Lett.*, 104, 513-534.
- Hedge, C.E. and Z.E. Peterman (1970), The strontium isotopic composition of basalts from the Gordo and Juan de Fuca Rises, northeastern Pacific Ocean. *Contrib. Mineral. and Petrol.*, 27, 114-120.
- Hekinian R., G. Thompson, and D. Bideau. (1989) Axial and off-axial heterogeneity of basaltic rocks from the East Pacific Rise at 12°35'N-12°51'N and 11°26'N-11°30'N. *J. of Geophys. Res.* 94(B12), 17,437-17,463.
- Hooft, E.E.E., H. Schouten, and R.S. Detrick (1996), Constraining crustal emplacement processes from the variation in seismic layer 2A thickness at the East Pacific Rise, *Earth Planet. Sci. Lett.*, 142, 289-309.
- Jull, M., P.B. Kelemen, and K. Sims (2002), Consequences of diffuse and channelled porous melt migration on uranium series disequilibria. *Geochim. Cosmochim. Acta* 66(23), 4133-4148.
- Kent, G.M., S. Singh, A. Harding, M. Sinha, J. Orcutt, P. Barton, S. Bazin, R. Hobbs, C. Tong, J. Pye (2000) Evidence from three-dimensional seismic reflectivity images for enhanced melt supply beneath mid-ocean ridge discontinuities, *Nature* 406, 614-618.
- Kidd, R.G.W. (1977), A model for the process of formation of upper oceanic crust, *Geophys. J.R. Astron. Soc.* 50, 149-183.
- Langmuir, C. H., Bender, J.F. & Batiza, R. (1986) Petrological and tectonic segmentation of the East Pacific Rise, 5°30'-14°30'N. *Nature* 322, 422-429.
- Lundstrom, C.C. (2000) Models of U-series disequilibria generation in MORB: the effects of two scales of melt porosity. *Physics of the Earth and Planetary Interiors* 121, 189-204.
- Lundstrom, C.C., J. Gill, Q. Williams, and M.R. Perfit, (1995) Mantle melting and basalt extraction by equilibrium porous flow. *Science*, 270(5244), 1958-1961.
- Lundstrom, C.C., Q. Williams, and J.B. Gill (1998), Investigating solid mantle upwelling rates beneath mid-ocean ridges using U-series disequilibria, 1: a global approach. *Earth Planet. Sci. Lett.*, 157, 151-165.
- Lundstrom, C.C., D.E. Sampson, M.R. Perfit, J. Gill, and Q. Williams (1999), Insights into mid-ocean ridge basalt petrogenesis: U-series disequilibria from the Siqueiros Transform, Lamont Seamounts, and East Pacific Rise, *J. Geophys. Res.*, 104, 13,035-13,048.

- Macdonald, K.C. (1982), Mid-ocean ridges: fine scale tectonic, volcanic, and hydrothermal processes within the plate boundary zone, *Ann. Rev. Earth Planet. Sci.*, 50, 155-190.
- Mahoney, J. J., J.M. Sinton, M.D. Kurz, J.D. Macdougall, K.J. Spencer, and G.W. Lugmair (1994), Isotope and trace element characteristics of a super-fast spreading ridge: East Pacific rise, 13-23°S. *Earth Planet. Sci. Lett.* 121, 173-193.
- McKenzie, D. (1985), ²³⁰Th-²³⁸U disequilibrium and the melting processes beneath ridge axes, *Earth Planet. Sci. Lett.*, 72, 149-157.
- Niu, Y.L., and R. Batiza (1997), Trace element evidence from seamounts for recycled oceanic crust in the eastern Pacific mantle. *Earth Planet. Sci. Lett.*, 148, 471-483.
- Niu, Y., K.D. Collerson, R. Batiza, J.I. Wendt, and M. Regelous (1999), Origin of enriched-type mid-ocean ridge basalt at ridges far from mantle plumes: The East Pacific Rise at 11°20'N. *J. Geophys. Res.* 104(B4), 7067-7087.
- Niu, Y.L., M. Regelous, I.J. Wendt, R. Batiza, and M.J. O'Hara (2002) Geochemistry of near-EPR seamounts: importance of source vs. process and the origin of enriched mantle component. *Earth Planet. Sci. Lett.*, 199, 327-345.
- Perfit, M.R., and W.W. Chadwick Jr. (1998), Magmatism at mid-ocean ridges: Constraints from volcanological and geochemical investigations, in *Faulting and Magmatism at Mid-Ocean Ridges*, edited by W.R. Buck, P.T. Delaney, J.A. Karson, and Y. Lagabrielle, *Geophys. Monogr. Ser.* 106, pp. 59-115, AGU, Washington, D.C.
- Perfit, M., D. Fornari, M. Smith, J. Bender, C. Langmuir, and R. Haymon (1994), Small-scale spatial and temporal variations in MORB geochemistry and implications for ridge crest magmatic processes, *Geology*, 22, 375-379.
- Prinzhofer, A., E. Lewin, and C.J. Allegre (1989), Stochastic melting of the marble cake mantle--evidence from local study of the East Pacific Rise at 12°50'N. *Earth Planet. Sci. Lett.*, 92(2), 189-206.
- Reynolds, J. R., and C.H. Langmuir (2000), Identification and implications of off-axis lava flows around the East Pacific Rise. *Geochem., Geophys., Geosyst.* 1(1999GC000033).
- Reynolds, J. R., C.H. Langmuir, J.F. Bender, K.A. Kastens, and W.B.F. Ryan (1992), Spatial and temporal variability in the geochemistry of basalts from the East Pacific Rise. *Nature*, 359, 493-499.
- Rubin, K.H., and J.D. MacDougall, Dating of neovolcanic MORB using (²²⁶Ra/²³⁰Th) disequilibrium (1990), *Earth Planet. Sci. Lett.*, 101, 313-321.
- Rubin, K.H., J.D. MacDougall, and M.R. Perfit (1994), ²¹⁰Po-²¹⁰Pb dating of recent volcanic eruptions on the sea floor, *Nature*, 368, 841-844.
- Rubin, K.H., I. van der Zander, M.C. Smith, and E.C. Bergmanis (2005), Minimum speed limit for ocean ridge magmatism from ²¹⁰Pb-²²⁶Ra-²³⁰Th disequilibria, *Nature*, 437, 534-538.
- Schouten, H., M.A. Tivey, D.J. Fornari, and J.R. Cochran (1999), Central anomaly magnetization high: constraints on the volcanic construction and architecture of seismic layer 2A at a fast-spreading Mid-Ocean Ridge, the EPR at 9°30'-50'N, *Earth Planet. Sci. Lett.*, 169, 37-50.

- Schouten, H., M.A. Tivey, D.J. Fornari, D. Yoeger, A. Bradley, M. Edwards, P. Johnson, and Ship Board Science and Technical Teams (2001), Near-Bottom Investigations of the Central Anomaly Magnetic High (CAMH) at the East Pacific Rise 9°25'-57'N, Cruise Report R/V Atlantis Voyage 7 Leg 4, 11/05-12/04/2001. Report at <http://imina.soest.hawaii.edu/HMRG/EPR/index.htm> under AT7-4 Cruise Report.
- Sims, K.W.W., S.R. Hart (2006), Comparison of Th, Sr, Nd, and Pb isotopes in oceanic basalts: Implications for mantle heterogeneity and magma genesis. *Earth Planet. Sci. Lett.*, 245, 743-761.
- Sims, K. W. W., D.J. DePaolo, M.T. Murrell, W.S. Baldrige, S.J. Goldstein, and D. Clague (1995), Mechanisms of magma generation beneath Hawaii and mid-ocean ridges: Uranium/Thorium and Samarium/Neodymium isotopic evidence. *Science* 267(5197), 508-512.
- Sims, K.W.W., M. Jull, and P. Kelemen (1999), U-series disequilibria and melt transport in the mantle beneath mid-ocean ridges. Presented at American Geophysical Union Meeting, San Francisco CA. Abstract in E.O.S. (Trans. Amer. Geophys. Union), V22D.
- Sims, K.W.W., S.J. Goldstein, J. Blichert-Toft, M.R. Perfit, P. Kelemen, D.J. Fornari, P. Michael, M.T. Murrell, S.R. Hart, D.J. DePaolo, G. Layne, and M. Jull (2002), Chemical and isotopic constraints on the generation and transport of melt beneath the East Pacific Rise, *Geochim. Cosmochim. Acta*, 66, 3481-3504.
- Sims, K.W.W., J. Blichert-Toft, D.J. Fornari, M.R. Perfit, S.J. Goldstein, P. Johnson, D.J. DePaolo, S.R. Hart, M.T. Murrell, P.J. Michael, G.D. Layne, and L. Ball (2003), Aberrant youth: Chemical and isotopic constraints on the origin of off-axis lavas from the East Pacific Rise, 9°-10°N, *Geochem., Geophys., Geosyst.*, 4(10), Paper number 2002GC000443.
- Sohn, R. A., S. C. Webb, and J. A. Hildebrand (2004), Fine-scale seismic structure of the shallow volcanic crust on the East Pacific Rise at 9°50'N, *J. Geophys. Res.*, 109, B12104, doi:10.1029/2004JB003152.
- Soule, S.A., D.J. Fornari, M.R. Perfit, M.A. Tivey, W.I. Ridley, and H. Schouten (2005), Channelized lava flows at the East Pacific Rise crest 9°-10°N: the importance of off-axis lava transport in developing the architecture of young oceanic crust, *Geochem., Geophys., Geosyst.*, 6(8), doi: 10.1029/2005GC000912.
- Soule, S. A., J. Escartín, and D. J. Fornari (2009), A record of eruption and intrusion at a fast spreading ridge axis: Axial summit trough of the East Pacific Rise at 9–10°N, *Geochem. Geophys. Geosyst.*, 10, Q10T07, doi:10.1029/2008GC002354.
- Sturm, M.E., S.J. Goldstein, E.M. Klein, J.A. Karson, and M.T. Murrell (2000) Uranium-series age constraints on lavas from the axial valley of the Mid-Atlantic Ridge, MARK area, *Earth Planet. Sci. Lett.*, 181, 61-70.
- Tatsumoto, M. (1966), Genetic relations of oceanic basalts as indicated by lead isotopes. *Science*, 153, 1094-1101.
- Toomey, D.R., D. Jouselin, R.A. Dunn, W. Wilcock, R.S. Detrick (2007) Skew of mantle upwelling beneath the East Pacific Rise governs segmentation, *Nature* 446, doi:10.1038/nature05679.

- Tong, C.H., J. Pye, P. Barton, R. White, M. Sinha, S. Singh, R. Hobbs, S. Bazin, A. Harding, G. Kent, J. Orcutt (2002) Asymmetric melt sills and upper crustal construction beneath overlapping spreading ridge segments: Implications for the development of melt sills along ridge crests, *Geology* 30, 83-86.
- Tong, C.H., P. Barton, R.S. White, M.C. Sinha, S.C. Singh, J.W. Pye, R.W. Hobbs (2003) Influence of enhanced melt supply on upper crustal structure at a mid-ocean ridge discontinuity: a three-dimensional seismic tomographic study of 9°N East Pacific Rise, *J. Geophys. Res.* 108, doi:10.1029/2002JB002163.
- Vera, E.E., and J.B. Diebold (1994), Seismic imaging of oceanic layer 2A between 9°30 and 10°N on the East Pacific Rise from two ship wide-aperture profiles, *J. Geophys. Res.*, 99, 3031-3041.
- Volpe, A. M., S.J. Goldstein, S.J. (1993), ²²⁶Ra-²³⁰Th disequilibrium in axial and off-axis mid-ocean ridge basalts. *Geochim. Cosmochim. Acta*, 57, 1233-1242.
- Wanless, V.D., M.R. Perfit, W.I. Ridley, E. Klein, and A. Zaino (2007) From basalt to dacite: examining magmatic evolution at the 9°03'N overlapping spreading center, East Pacific Rise, *Eos. Trans. Am. Geophys. Union*, 88, Fall Meet. Suppl. Abstract T33B-1347.
- Wanless, V.D., M.R. Perfit, W.I. Ridley, P.J. Wallace, J.W. Valley, C.B. Grimes, E.M. Klein (2009), Geochemical evidence for crustal assimilation at mid-ocean ridges using major and trace elements, volatiles, and oxygen isotopes, *Eos. Trans. AGU*, 90(52), Fall Meet. Suppl. Abstract V51A-1665.
- White, S.M., R.M. Haymon, D.J. Fornari, M.R. Perfit, and K.C. Macdonald (2002), Correlation between volcanic and tectonic segmentation of fast-spreading ridges: evidence from volcanic structures and lava morphology on the East Pacific Rise, 9°-10°N, *J. Geophys. Res.*, 107(B8), 2173, doi:10.1029/2001JB000571.
- White, S.M., J.L. Mason, K.C. Macdonald, M.R. Perfit, V.D. Wanless, E.M. Klein (2009) Significance of widespread low effusion rate eruptions over the past two million years for delivery of magma to the overlapping spreading centers at 9°N East Pacific Rise, *Earth Planet. Sci. Lett.* 280, 175-184.
- White, W. M., and J.-G. Schilling (1978), The nature and origin of geochemical variation in Mid-Atlantic Ridge basalts from the Central North Atlantic. *Geochim. Cosmochim. Acta*, 42, 1501-1516.
- Zindler, A., and S.R. Hart (1986) Chemical Geodynamics. *Ann. Rev. Earth Planet. Sci.*, 14, 493-571.
- Zindler, A., H. Staudigel, and R. Batiza (1984) Isotope and trace element geochemistry of young Pacific seamounts: implications for the scale of upper mantle heterogeneity. *Earth Planet. Sci. Lett.*, 70(2), 175-195.

CHAPTER 2: PERSPECTIVE ON THE GENESIS OF E-MORB

FROM CHEMICAL AND ISOTOPIC HETEROGENEITY AT 9°-10°N

EAST PACIFIC RISE

ABSTRACT

The discovery of chemically and isotopically enriched mid-ocean ridge basalts (E-MORB) has lent substantial insight into the origin, length scales, and time scales of mantle heterogeneity. However, the exact process involved in producing this E-MORB enrichment is vigorously debated. Additionally, because the ages of E-MORB are not well constrained, the petrogenetic, temporal, and geological relationships between E-MORB and N-MORB are not known. To investigate these relationships and to explore how melting and melt transport processes contribute to or modify enriched mantle source compositions and generate E-MORB melts beneath mid-ocean ridges, we measured major and trace elements, and Sr, Nd, Hf, Pb, and U-Th-Ra isotopes for a suite of off-axis lavas, including several E-MORB, from 9°-10°N along the East Pacific Rise.

These data show coherent mixing trends among long-lived radiogenic isotopes, U-series nuclides, and incompatible trace elements, implicating mixing of melts from different sources and at different depths. Our results are consistent with previous studies that show that melting occurs in a two-porosity melting regime, with high-porosity channels forming deeply in the presence of garnet and transporting enriched melts with large Th excesses to the crust, while low-porosity channels transport melts more slowly, allowing them to equilibrate at shallow depths and develop large Ra excesses at the expense of diminished Th excesses. Forward modeling of the trace element data is also consistent with mixing of melts in a two-porosity melting regime.

U-series age constraints suggest that E-MORB erupt at different times from N-MORB, but not necessarily through different pathways. When viewed in light of both earlier paleointensity constraints and these new U-series age constraints, geological evidence suggests that the asymmetric, off-axis distribution of E-MORB at 9°-10°N EPR is better explained by eruption of E-MORB within the axial summit trough (AST), subsequent spreading away from the AST, and preservation of their surface expression through asymmetric construction of the extrusive layer. Taken together, the range of ages of E-MORB at 9°-10°N EPR and the geochemical mixing trends suggest that enriched geochemical heterogeneities (i.e. pyroxenite veins) are periodically introduced into the melting regime and preferentially melted, thus producing short episodes of dominantly E-MORB magmatism.

*This manuscript was submitted to *Journal of Petrology* in January 2010

2.1. INTRODUCTION

The formation of the continental crust from Earth's early mantle is thought to have left a complementary upper mantle reservoir largely depleted and broadly homogeneous with respect to its incompatible element abundances and long-lived radiogenic isotope compositions (e.g., Allègre *et al.*, 1983; DePaolo & Wasserburg, 1976; Hurley, 1968). This depleted reservoir, termed DMM (Zindler & Hart, 1986), or depleted MORB mantle, is considered to be the source for mid-ocean ridge basalts (MORB). However, long-term chemical heterogeneities in the oceanic mantle have long been known to exist at different length scales (e.g., Hart *et al.*, 1973; Hedge & Peterman, 1970; Tatsumoto, 1966; White & Schilling, 1978; Zindler & Hart, 1986; Sims & Hart, 2006). Even far from the influence of any hot spot, such as at the East Pacific Rise (EPR), the adjacent and seemingly coeval occurrence of enriched (E-MORB), normal (N-MORB) and very depleted MORB (D-MORB) attests to the ubiquitous presence of heterogeneous mantle domains over short length scales (e.g., Allan *et al.*, 1989; Castillo *et al.*, 2000; Fornari *et al.*, 1988; 1989; Hekinian *et al.*, 1989; Langmuir *et al.*, 1986; Lundstrom *et al.*, 1999; Sims *et al.*, 2002; Mahoney *et al.*, 1994; Niu *et al.*, 1997; Niu *et al.*, 1999; Niu *et al.*, 2002; Perfit *et al.*, 1994; Prinzhofer *et al.*, 1989; Reynolds *et al.*, 1992; Reynolds & Langmuir, 2000; Zindler *et al.*, 1984). While the isotopic and chemical heterogeneity of the present-day mantle almost certainly represents the continuous processes of differentiation and remixing, the exact origin of these enriched mid-ocean ridge mantle domains and the genesis of E-MORB are still vigorously debated. Furthermore, because the ages of E-MORB are not well constrained, the petrogenetic,

temporal, and geological relationships between the less abundant E-MORB and volumetrically predominant N-MORB are not known.

To investigate how melting and melt transport processes modify enriched mantle source compositions and generate E-MORB melts beneath mid-ocean ridges, and to understand the geological and temporal relationships between N-MORB and E-MORB, we have measured major and trace elements, and Sr, Nd, Hf, Pb, and U-Th-Ra isotopes for a suite of off-axis lavas, including several E-MORB, from 9°-10°N along the East Pacific Rise. These samples were collected using the deep submersible *Alvin* and their spatial and geological contexts are well known (Figure 1). U-series model ages of E-MORB and N-MORB provide an additional temporal context within which to interpret geochemical and isotopic variability, which reflect time-dependent variations in mantle melting processes and source compositions.

2.2. PREVIOUS STUDIES OF E-MORB

Although ocean floor basalts classified as E-MORB span a wide range and often a continuum of enrichment, there are several common compositional characteristics that are typically observed in E-MORB: (1) E-MORB tend to have slightly higher Al_2O_3 and lower FeO than N-MORB. (2) E-MORB are more enriched than N-MORB in highly incompatible trace elements such as Rb, Ba, Th, U, and Nb by more than roughly an order of magnitude. (3) E-MORB have more fractionated highly incompatible trace

elements than N-MORB (e.g. La/Sm is ~3 times that in N-MORB, and Ba/La up to ~5 times that in N-MORB). (4) In contrast to the light rare earth elements (LREE), heavy rare earth elements (HREE) are nearly chondritic (e.g. Dy/Yb_N~1). (5) The Sr isotope compositions of E-MORB tend to be more radiogenic than N-MORB, whereas Nd and Hf isotope compositions of E-MORB tend to be less radiogenic than N-MORB, reflecting enrichment of the more incompatible element (i.e. Rb, Nd, Hf) in the parent/daughter ratios Rb/Sr, Sm/Nd, and Lu/Hf and subsequent long-term ingrowth. Lastly, (6) young E-MORB also almost always have large ²³⁰Th excesses (i.e. (²³⁰Th/²³⁸U)>1) but small ²²⁶Ra excesses (i.e. (²²⁶Ra/²³⁰Th)>1) as compared to the relatively small ²³⁰Th excesses and large ²²⁶Ra excesses of N-MORB (and even smaller ²³⁰Th excesses and larger ²²⁶Ra excesses of D-MORB).

In the past, definitions of E-MORB have often relied on trace element enrichments, such as high K/Ti (defined as K₂O/TiO₂ x 100), Zr/Y, and La/Sm, without the supporting isotopic information on long-term source enrichment. Because incompatible elements may be enriched and fractionated by processes such as low extents of melting without the presence of a long-term enriched mantle source reservoir, a diagnostic property of E-MORB (as described above), definitions based on incompatible element abundances alone are incomplete. Prior to this study, studies of seamount lavas from near 9°-10°N EPR (Fornari *et al.*, 1988; 1989; Niu *et al.*, 1997; 1999; 2002; Prinzhofer *et al.*, 1989; Zindler *et al.*, 1984) and lavas from the nearby Siqueiros Fracture Zone at 8°25'N EPR (Sims *et al.*, 2002) have demonstrated the presence of isotopic source heterogeneity beneath this region of the EPR, but suggestions of heterogeneity in

the immediate area near the axis from 9°17'N-10°N have largely been defined by variations in incompatible element ratios such as K/Ti and Zr/Y (Batiza & Niu, 1992; Perfit *et al.*, 1994; Smith *et al.*, 2001). In fact, the samples selected for this study were defined as N-MORB and E-MORB according to the classification by Smith *et al.* (2001) that defines N-MORB as lavas with K/Ti <11 and E-MORB as lavas with K/Ti >11 (Figure 2). However, because incompatible element ratios may be variably fractionated due to differences in the degree of melting, comparison of long-lived radiogenic isotope compositions (i.e. Sr, Nd, Hf, Pb) with incompatible element ratios is required to decipher the relative effects of partial melting versus the presence of source heterogeneity over the length scale of melting (cf. Sims and Depaolo, 1997).

Enriched source compositions for E-MORB are generally argued to derive from either melt metasomatism of peridotite, either cryptically or in the form of fine dikes or veins (e.g., Donnelly *et al.*, 2004; Galer & O'Nions, 1986; Niu *et al.*, 2002) or from formation of garnet pyroxenite or eclogite veins through stretching and thinning of subducted oceanic crust (e.g., Allegre & Turcotte, 1986; Ben Othman & Allegre, 1990; Hirschmann & Stolper, 1996; Lundstrom *et al.*, 1999; Prinzhofer *et al.*, 1989). In all models positing a metasomatic origin, a common requirement is that an earlier episode of low-degree melting of some other enriched mantle source must occur to generate the elevated highly incompatible trace element abundances (Donnelly *et al.*, 2004; Niu *et al.*, 2002). Proposed low-degree melt mechanisms include metasomatism of overlying mantle by melting of eclogitized recycled crust in subduction zones (Donnelly *et al.*, 2004), metasomatism by melting of mantle within the low-velocity zone beneath oceanic

lithosphere (Niu *et al.*, 2002), and metasomatism of subcontinental lithosphere and subsequent delamination (Galer & O’Nions, 1986). These low-degree melt-metasomatized mantle packages subsequently undergo larger extents of melting (up to 10%) beneath oceanic ridges as spinel peridotite to produce E-MORB (Donnelly *et al.*, 2004). The absence of residual garnet is used to explain the observed chondritic Dy/Yb of most E-MORB (Donnelly *et al.*, 2004). However, this inference is contradictory to the observation that E-MORB typically have large Th excesses (Goldstein *et al.*, 1992; 1994; Sims *et al.*, 1995; Lundstrom *et al.*, 1995; 1998; 1999) which indicates residual garnet in the source (Beattie, 1993; Elkins *et al.*, 2008; Hauri *et al.*, 1994; LaTourrette *et al.*, 1993; Pertermann *et al.*, 2004; Salters & Longhi, 1999; Salters *et al.*, 2002).

Production of E-MORB by melting of mafic components in a two lithology mantle of pyroxenitic/eclogitic recycled crust and peridotite requires recent (<375 ka) low-degree melting in the presence of garnet to generate the large observed ^{230}Th excesses and efficient segregation and preservation of these low-degree melts. Melting of mafic veins has been proposed to explain U-Th disequilibria in E-MORB (e.g. Ben Othman & Allegre, 1990; Hirschmann & Stolper, 1996; Lundstrom *et al.*, 1995; 1998; 1999), but in the absence of isotopic heterogeneity, deep, low-degree melting of unmetasomatized garnet peridotite could also potentially explain the disequilibria (Sims *et al.*, 1995; 2002).

Although both the “metasomatic” and “recycling” models provide potential explanations for the ultimate origin of the long-term E-MORB mantle source reservoir, they do not account for how enriched melt compositions are preserved from the time the

enriched mantle source melts beneath the mid-ocean ridge to the time they are erupted on the seafloor. For example, E-MORB from the fast-spreading ridge at 9°17'-10°N EPR (Batiza & Niu, 1992; Perfit *et al.*, 1994; Perfit & Chadwick, 1998; Smith *et al.*, 2001) and similarly enriched “T-MORB” from 17°30'S EPR and 12°-13°N EPR (Bergmanis *et al.*, 2007; Reynolds *et al.*, 1992; Reynolds & Langmuir, 2000) have been sampled adjacent to N-MORB, suggesting that N-MORB and E-MORB melts are either generated and erupted at discrete time intervals (e.g. Batiza & Niu, 1992; Bergmanis *et al.*, 2007; Hekinian *et al.*, 1989; Reynolds *et al.*, 1992) or are extracted and transported to the seafloor along different mantle and crust pathways (e.g. Perfit *et al.*, 1994).

With regards to E-MORB melt preservation, it is important to note that pyroxenitic melts may react and freeze when they encounter a peridotitic matrix. Whether or not mafic lithologies freeze is a function of composition (i.e., more silica-rich melts produced by melting of MORB-like eclogite are more likely to freeze than silica-deficient garnet pyroxenite melts; Yaxley & Green, 1998; Hirschmann *et al.*, 2003; Kogiso *et al.*, 2004), the length scale of pyroxenite melt transport pathways, and the time scale over which pyroxenite melt interacts with peridotite matrix (Kogiso *et al.*, 2004). Thus, for melts of mafic lithologies to be preserved with U-series isotopic disequilibria requires that the enriched melts are extracted efficiently with little or no interaction with surrounding peridotite matrix. Evidence of enriched melt preservation requires the existence of distinct pathways where pyroxenite melts are effectively isolated from the ambient mantle peridotite matrix, whether by orthopyroxene reaction bands between pyroxenite melt and peridotite (e.g. Kogiso *et al.*, 2004), or by extraction through pre-

existing high porosity dunite conduits (e.g. Kelemen *et al.*, 1997). Alternative, ‘hybrid’ lithologies that melt only upon peridotite melting have been suggested as a consequence of freezing of silica-rich melts upon reaction with peridotite. However, as noted by Kogiso *et al.* (2004), such a reaction will create a permeability barrier that traps pyroxenite melt in reaction zones and prevent pervasive refertilization of peridotite. In addition, large reaction zones of pyroxenite melt will most likely not behave according to peridotite phase equilibria. Indeed, the correlations observed in this study among fast-diffusing major elements like FeO and MgO, slower diffusing trace elements, long-lived radiogenic isotopes (Sr, Nd, Hf, and Pb), and U-series isotopes imply efficient segregation of enriched, pyroxenite melts.

U-series and isotope studies examining the relationship between E-MORB and N-MORB have suggested that mixing of deep, small-degree melts with shallow, high-degree melts is required to produce correlations between U-Th disequilibria and Sm/Nd fractionation (Sims *et al.*, 1995). Studies of U-series disequilibria in demonstrably young (relative to the half-life of ^{226}Ra) 9°-10°N EPR N-MORB lavas have shown that for lavas to have both negatively correlated primary ^{226}Ra and ^{230}Th excesses and positively correlated ($^{230}\text{Th}/^{232}\text{Th}$) and ($^{238}\text{U}/^{232}\text{Th}$), the melting must occur in a two-porosity mantle, with high porosity channels forming deeply in the presence of garnet and transporting melts with large ^{230}Th excesses to the crust, while low porosity channels transport melts more slowly, allowing them to equilibrate at shallow depths and develop large ^{226}Ra excesses at the expense of diminished ^{230}Th excesses (Sims *et al.*, 1999; Jull *et al.*, 2002; Lundstrom, 2000; Sims *et al.*, 2002). Hence, given the observation of large ^{230}Th

excesses and small ^{226}Ra excesses in E-MORB, we hypothesize that E-MORB represent deep melts of an enriched source that have been effectively segregated into high porosity channels and largely removed from interaction with incompatible element-depleted, peridotitic, N-MORB melts.

To shed light on how melting and melt transport processes—in particular two-porosity melt transport—contribute to or modify enriched mantle source compositions and generate E-MORB melts beneath mid-ocean ridges, we analyzed major and trace element abundances, Sr, Nd, Hf, and Pb isotope compositions, and U-Th-Ra disequilibria for a suite of 16 off-axis N- and E-MORB glasses from $9^{\circ}31'\text{N} - 9^{\circ}54'\text{N}$ EPR. These glasses were collected off-axis during the AdVenture Series cruises (dive 2489; see Perfit & Chadwick, 1998, Fig 20)) from 1991-1997 and during the Abyssal Hill Cruise (dives 2697, 2700, 2701, 2702, 2703, 2706) in 1992 (Macdonald *et al.*, 1996) with the submersible *Alvin* from lava flows < 4 km west of the axis at $9^{\circ}50'\text{N}$ and < 5 km east of the axis at $9^{\circ}31'-9^{\circ}35'\text{N}$ (herein referred to as $9^{\circ}30'\text{N}$). Hence, the location and geological context of these samples are known precisely (Figure 1, Table 1). Given model eruption-age constraints from $^{238}\text{U}-^{230}\text{Th}$ and $^{230}\text{Th}-^{226}\text{Ra}$ disequilibria and accurate knowledge of the spatial distribution of E-MORB relative to N-MORB at $9^{\circ}-10^{\circ}\text{N}$, we can place additional constraints on the temporal variability of the isotopically and trace elementally heterogeneous EPR mantle.

2.3. SAMPLE LOCATIONS AND GEOLOGICAL BACKGROUND

The second-order ridge segment from 9°-10°N East Pacific Rise (EPR) is fast-spreading with a half-spreading rate of ~5.5 cm/yr. Magnetic data show that it has been spreading at this rate for the last 2 m.y. (Carbotte & Macdonald, 1992). This segment of the EPR is far from the influence of hot spot interaction and erupts predominantly N-MORB. It is bounded to the north by the Clipperton transform fault at 10°10'N and to the south by a large overlapping spreading center (OSC) at 9°03'N (Macdonald *et al.*, 1984; 1986). It is interrupted by a third order ridge discontinuity with a ~0.45 km offset and 3 km overlap at ~ 9°36- 9°38'N, which has been termed a 'small OSC' (Smith *et al.*, 2001). This discontinuity is thought to represent a volcanological divide: the eastern limb of the axial summit trough (AST) appears to be propagating southward, while magmatic activity on the western limb appears to be waning (Smith *et al.*, 2001). This interpretation is based largely on qualitative evidence, namely the presence of extinct hydrothermal vents and older-looking lava flows to the south of the discontinuity, as well as young-looking lava flows and hydrothermal activity indicative of a more recent eruption to the north (Smith *et al.*, 2001). North of 9°38'N, the ridge segment near 9°48'N – 9°52'N has a broad, inflated bathymetric cross-sectional profile with a shallow, narrow (~50 m) AST and is considered magmatically robust (Cochran *et al.*, 1999; Fornari *et al.*, 1998; Scheirer & Macdonald, 1993). Two eruptions have been documented north of 9°38'N near 9°50'N during 1991-1992 and 2005-2006 (Haymon *et al.*, 1993; Tolstoy *et al.*, 2006, Soule *et al.*, 2007) with no corresponding volcanism south of the small OSC. The profile

at 9°31'N is flatter, with a deeper, wider (~250 m) AST nested within the broad summit depression of a developing axial summit graben (ASG) (Fornari *et al.*, 1998; Scheirer & Macdonald, 1993). Hence, the ridge south of 9°36'N to ~9°30'N is thought to be comparatively magmatically “starved.”

Previous sampling of over 1200 basalts from between 9°17'N and 10°N EPR (major elements compositions for ~300 samples can be found at www.petdb.org; additional data is expected to be available 1/1/2010 at <http://marine-geo.org/portals/ridge2000>) has documented eight E-MORB (defined by K/Ti >11) near 9°30'N, with seven of the eight samples deriving from the east side of the AST (Perfit *et al.*, 1994; Perfit & Chadwick, 1998). Ten E-MORB were collected by wax-filled rock core at the small OSC at 9°36'-9°38'N (Smith *et al.*, 2001). Seven of these samples were collected from west of the western limb, two from east of the eastern limb, and one from in between the two limbs (Figure 1; see Figure 4 from Smith *et al.*, 2001). One E-MORB also was collected by dredging from just south and east of the western limb of the discontinuity at 9°35'N and has been measured for its Sr, Nd, Pb, ($^{238}\text{U}/^{232}\text{Th}$), ($^{230}\text{Th}/^{232}\text{Th}$), and ($^{226}\text{Ra}/^{230}\text{Th}$) isotopic compositions (sample R54-2; Batiza & Niu, 1992; Goldstein *et al.*, 1993; Harpp *et al.*, 1990; Volpe & Goldstein, 1993). Although there has been extensive sampling within and immediately adjacent to the AST, no E-MORB have been recovered from the axial region (< ~0.5 km) anywhere from 9°17'N-10°N EPR (Figure 1).

A more recent geochemical study of lavas recovered from the AST by the deep submersible Alvin from 9°17'N to 9°52'N EPR demonstrated that axial lavas (all

depleted, tholeiitic N-MORB) are homogeneous with respect to $^{87}\text{Sr}/^{86}\text{Sr}$, $^{143}\text{Nd}/^{144}\text{Nd}$, $^{176}\text{Hf}/^{177}\text{Hf}$, and $^{208}\text{Pb}/^{206}\text{Pb}$, suggesting that the mantle source region is isotopically (and by inference elementally) homogeneous over the length scale of melting (Sims *et al.*, 2002). Similarly, N-MORB collected up to 4 km off-axis in the 9°50' N region are isotopically indistinguishable from the axial lavas (Sims *et al.*, 2003). Sims *et al.* (2003) inferred that these off-axis lavas were produced from the same mantle source and underwent similar processes during melting and melt transport; however, they also noted that many of the off-axis flows were not sourced by off-axis eruptions, but erupted within the AST and subsequently flowed off-axis. (Indeed, at 9°51.2' N, lava from the recent eruption in 2005-2006 flowed up to ~2 km away from the axis (Soule *et al.*, 2007)). Given this assumption, it was possible to compare the ($^{230}\text{Th}/^{238}\text{U}$) and ($^{226}\text{Ra}/^{230}\text{Th}$) of the off-axis samples of unknown age to the ($^{230}\text{Th}/^{238}\text{U}$) and ($^{226}\text{Ra}/^{2230}\text{Th}$) of zero-age axial samples and date the off-axis samples. These ages are in agreement with ages estimated using paleointensity data (Bowles *et al.*, 2006), thus lending credence to the radiometric ages determined by Sims *et al.* (2003).

The existence of E-MORB in the study area suggests that MORB genesis is more complicated than what was inferred solely from N-MORB compositions (Sims *et al.*, 2002; 2003). Although incompatible element ratios (e.g., K/Ti, Nb/Th, Th/U, Zr/Y) cannot be used exclusively to infer source characteristics (e.g., Sims & DePaolo, 1997), the higher abundances of moderately and highly incompatible trace elements in E-MORB requires generation of enriched parent melts, whether by melting of a heterogeneous mantle source or by low degrees of melting of a homogeneous source, and subsequent

preservation of these melts. Notably, global studies of E-MORB have demonstrated that low degrees of melting of a homogeneous peridotitic mantle source alone cannot produce the trace element patterns of E-MORB (Donnelly *et al.*, 2004).

Previous studies of E-MORB at 9°-10°N EPR have arrived at two different models for the emplacement of E-MORB parent melts (Batiza & Niu, 1992; Perfit *et al.*, 1994). Based on $^{226}\text{Ra}/^{230}\text{Th}$ -Ba/Th model age dating of samples from 9°17'N – 9°54'N, including two N-MORB and one E-MORB (Volpe & Goldstein, 1990; 1993), and following the model of Hekinian *et al.* (1989), Batiza & Niu (1992) suggested that E-MORB ($T_{\text{model}} \sim 6.40$ kyrs) were generated from an older episode of magmatic activity different from that which produced N-MORB ($T_{\text{model}} \sim 2.40 - 2.65$ kyrs). This older episode potentially involved progressive melting and persistent depletion of a heterogeneous mantle source over time. In essence, Batiza & Niu (1992) suggested, as did Reynolds *et al.* (1992) for 12°N EPR and Bergmanis *et al.* (2007) for 17°S EPR, that periods of E-MORB eruption may alternate with periods dominated by N-MORB eruption, reflecting temporal changes in the composition of the mantle source and axial magma chamber (AMC) magma supply. In contrast, based on observations of young off-axis N-MORB (Goldstein *et al.*, 1994), Perfit *et al.* (1994) assumed that the adjacent E-MORB were also young and advocated for an off-axis pathway that allowed E-MORB melts to escape extensive mixing with the voluminous N-MORB melts that reside in the AMC. Here we use new major and trace element compositions, Sr, Nd, Hf, and Pb isotopic compositions, and U-Th-Ra disequilibria collected on a suite of off-axis lavas from 9°31'N-9°54'N EPR to explore these two hypotheses.

2.4. ANALYTICAL METHODS

The analytical details for major element analyses by electron microprobe are reported in the footnotes to Table 2. Details for trace element concentration data obtained by ICP-MS are reported in the footnotes to Table 3. Isotopic compositions were measured by MC-ICP-MS, and details of these measurements are reported in the footnotes to Table 4. ^{238}U and ^{232}Th concentrations were measured at WHOI by ID-ICP-MS using the ThermoFinnigan Element 2 and $^{234}\text{U}/^{238}\text{U}$, $^{230}\text{Th}/^{232}\text{Th}$ and ID ^{226}Ra were measured using the WHOI ThermoFinnigan Neptune MC-ICP-MS. Analytical details are reported in Table 5. For more information on the ^{238}U - ^{230}Th - ^{226}Ra chemical and analytical procedures at WHOI, see Appendix A1 of Sims *et al.* (2008a). More details of Th and U isotopic measurement methods and standards are summarized in Ball *et al.* (2008) and Sims *et al.* (2008b).

The data for 9°50'N off-axis lavas reported by Sims *et al.* (2003), compiled from ICP-MS data produced by the Geological Survey of Canada (GSC), plot at suspiciously high values for Lu/Hf, especially considering the exceptional compositional similarities of these off-axis samples as compared to axial samples reported in Sims *et al.* (2002). We reanalyzed 12 of the 14 off-axis samples reported by Sims *et al.* (2003) as well as seven of the 19 axial samples reported by Sims *et al.* (2002) (similarly compiled from data from the GSC) for a selection of REE and incompatible trace elements. These data are reported in the Appendix Table A1. Samples were measured at the University of Florida (UF) using a Thermo Finnigan Element2 inductively coupled plasma mass spectrometer (ICP-

MS), as were off-axis lavas reported in this study, and the analytical details are the same as described in Table 3. The new Lu and Hf UF ICP-MS data for off-axis samples plot at values more similar to the axial samples than the older GSC data. In fact, nine out of eleven off-axis samples reanalyzed at UF have Lu/Hf higher than the GSC measurements, with eight of these ~9-15% higher. Two off-axis samples have ~13% lower UF Lu/Hf than GSC. Notably, trace element abundances are not systematically offset between the GSC measurements and the UF measurements, but seven out of twelve of the UF Hf measurements of off-axis samples are ~11-16% lower than the GSC data, and only three GSC Hf measurements are higher than UF Hf measurements (6%, 6%, and 34%). Lu data from UF are more consistently offset to lower (~2-8%) values than the GSC measurements, with only two samples measured at UF with higher Lu. We also note that Sm, Nd, Th, and U concentrations as measured by ICP-MS at UF and GSC and by ID-TIMS at the University of California, Berkeley (Sims *et al.*, 2002; 2003) are all generally within $\pm 5-10\%$.

With regard to U-series analyses, we are suspicious of ($^{226}\text{Ra}/^{230}\text{Th}$) for three E-MORB samples that could not be replicated due to sample size limitations (2700-7, 2701-11a, and 2702-1). These samples have slight ^{226}Ra excesses of 1.06, 1.08, and 1.06, respectively, and video observations show sediment cover similar to that seen for samples 2489-3 and 2489-4a, which have replicated measurements of ($^{226}\text{Ra}/^{230}\text{Th}$) that are all in equilibrium within analytical uncertainties (2489-3: 0.97, 0.98; 2489-4a: 0.99, 1.02; Table 5). Thus, we interpret these three samples as being in secular equilibrium but with large measurement uncertainties ($\sim < 8\%$), though we cannot rule out the possibility that

they have small ^{226}Ra excesses. Regardless of whether these samples have small ^{226}Ra excesses or are in secular equilibrium, the main conclusions of this study do not change.

2.5. RESULTS

2.5.1. Major elements

Major element concentrations are reported in Table 2. These off-axis samples have a wide range of compositions, with K/Ti ranging from 5.5 to 25.1 and molar Mg# ($\text{Mg}/(\text{Mg} + \text{Fe})$) ranging from 0.51-0.62 (Figure 2A). The off-axis N-MORB from 9°30'N span the previously reported range in Mg# for 9°50'N off-axis samples and have relatively constant K/Ti. However, the off-axis samples, particularly those in the 9°30'N area, have more variable and lower Mg# (< 0.55) than the correlative axial samples. Compared to axial N-MORB samples, the off-axis E-MORB have lower and less variable Mg# and higher and more variable K/Ti. Off-axis E-MORB from 9°30'N EPR exhibit increasing K/Ti with decreasing Mg#. Additionally, K/Ti in E-MORB from 9°30'N EPR is negatively correlated with $\text{Fe}_{8,0}$ and $\text{CaO}/\text{Al}_2\text{O}_3$ (Figures 2B, 2C) and positively correlated with $\text{Na}_{8,0}$ (Figure 2D; $\text{Fe}_{8,0}$ and $\text{Na}_{8,0}$ were calculated by the method of Klein & Langmuir (1987) using a linear regression of MgO vs. FeO and Na_2O for 9°-10°N EPR samples from this study, axial samples from Sims *et al.*, 2002, and off-axis samples from Sims *et al.*, 2003). E-MORB trend towards lower $\text{Fe}_{8,0}$ (8.96-9.70) and $\text{CaO}/\text{Al}_2\text{O}_3$ (0.71-

0.82) yet have similar $\text{Na}_{8,0}$ (2.60-2.90) compared to N-MORB ($\text{Fe}_{8,0} = 9.49-10.50$; $\text{CaO}/\text{Al}_2\text{O}_3 = 0.78-0.85$, $\text{Na}_{8,0} = 2.57-2.86$).

2.5.2. Trace elements

Trace element abundances are reported in Table 3. Primitive mantle-normalized abundances of incompatible elements for off-axis N-MORB are similar to those in axial or previously reported off-axis samples (Figure 3; cf., Sims *et al.*, 2002; 2003). Compared to N-MORB, off-axis E-MORB have higher abundances of the most incompatible elements (Rb through Nd), but similar abundances of the less incompatible elements (Zr through Lu) (Figure 3) (see also Perfit *et al.*, 1994 and Smith *et al.*, 2001 for similar observations). This results in a continuum of spidergram patterns (Figure 3) from the most depleted N-MORB to the most enriched E-MORB, with the patterns essentially anchored by the heavy rare earth elements (HREE) and fanning out towards the more incompatible elements. N-MORB and E-MORB all have similar middle rare-earth element (MREE) and HREE abundances, but fanning light rare earth element (LREE) patterns. Both off-axis N-MORB and off-axis E-MORB patterns show consistent depletions of Pb and Sr relative to similarly incompatible elements (Figure 3). Aside from differences in the abundances of the more incompatible elements (Rb through Nd), the most striking difference between the E-MORB and N-MORB patterns is that E-MORB have Ba enrichments relative to Rb and Th, whereas both off-axis and axial N-MORB have Ba depletions relative to Rb and Th (Figure 3).

Correlations exist between incompatible element ratios for axial and off-axis lavas when including the off-axis E-MORB suite (e.g., Ce/Yb vs. Th/U, Sm/Yb vs. Sm/Nd; see Figures 4A, 4C). Although the axial and off-axis N-MORB appear to be compositionally similar, when also taking into consideration the off-axis E-MORB suite, the total range of trace element compositions and the correlations between incompatible element ratios are strongly suggestive of mixing. Thus, in terms of trace element compositions, the 9°30'N off-axis suite shows a continuum of compositions from depleted N-MORB (both off-axis and axial) to off-axis E-MORB.

2.5.3. Long-lived radiogenic isotopes: Sr, Nd, Hf, and Pb

Sr, Nd, Hf, and Pb isotopic compositions are reported in Table 4 and are shown in Figures 5 and 6. Note that we also report corrected Nd isotope values for Sims *et al.* (2002; 2003) using the time-dependent correction outlined in Bryce *et al.* (2005) (see Appendix Table A2 for details). The analytical details are reported in the footnotes to Table 4. The newly analyzed off-axis N-MORB data overlap with the range of existing data for axial and off-axis N-MORB samples (Sims *et al.*, 2002; 2003) with respect to Sr ($^{87}\text{Sr}/^{86}\text{Sr} = 0.70244\text{-}0.70257$), Nd ($\epsilon_{\text{Nd}} = +9.9$ to $+10.6$), and Hf ($\epsilon_{\text{Hf}} = +14.1$ to $+15.0$) isotopic compositions. However, the 9°30'N off-axis N-MORB exhibit overlapping, but slightly higher $^{87}\text{Sr}/^{86}\text{Sr}$ (0.70249-0.70262) and lower ϵ_{Hf} (+13.6 to +14.2) and ϵ_{Nd} (+9.7 to +10.1) values (Figure 5) than the 9°50'N N-MORB. In comparison, off-axis E-MORB from 9°30'N have more radiogenic Sr isotopes and exhibit a much wider range of $^{87}\text{Sr}/^{86}\text{Sr}$ (0.70248-0.70286) and a lower range of ϵ_{Nd} (+7.9 to +9.1) with a narrower,

lower range of ϵ_{Hf} (+10.7 to +12.7) compared to the N-MORB (Figure 5). The E-MORB from 9°50'N has Sr ($^{87}\text{Sr}/^{88}\text{Sr} = 0.70258$), Nd ($\epsilon_{\text{Nd}} = 10.0$), and Hf ($\epsilon_{\text{Hf}} = 14.6$) isotopic compositions that are strikingly similar to N-MORB despite having a primitive mantle-normalized incompatible element abundance pattern and incompatible element ratios more similar to E-MORB (Figures 2A, 3, 4, 7B).

Pb isotope data for newly analyzed off-axis N-MORB from 9°50'N coincide with existing Pb isotope data for axial and off-axis N-MORB (Figure 6; Sims *et al.*, 2002; 2003). The range in Pb isotopic compositions for the newly measured off-axis N-MORB is narrower than that of both off-axis and axial lavas reported by Sims *et al.* (2002; 2003). The off-axis E-MORB (sample 2697-1) from 9°50'N is compositionally indistinguishable from the N-MORB suites with respect to $^{208}\text{Pb}/^{204}\text{Pb}$ and $^{207}\text{Pb}/^{204}\text{Pb}$, but has slightly higher $^{206}\text{Pb}/^{204}\text{Pb}$ than the N-MORB suites for a given $^{208}\text{Pb}/^{204}\text{Pb}$ or $^{207}\text{Pb}/^{204}\text{Pb}$ (Figures 7B & 7C). As shown in Sims *et al.* (2002; 2003), $^{208}\text{Pb}/^{204}\text{Pb}$, $^{207}\text{Pb}/^{204}\text{Pb}$, and $^{206}\text{Pb}/^{204}\text{Pb}$ for 9°17'N-10°N lavas are positively correlated. The off-axis E-MORB from 9°30'N can be subdivided into two different groups in terms of Pb isotopic values: a “more radiogenic” group and a “less radiogenic” group (Figures 6 & 7). The “more radiogenic” group includes two samples that have higher $^{208}\text{Pb}/^{204}\text{Pb}$, $^{207}\text{Pb}/^{204}\text{Pb}$, and $^{206}\text{Pb}/^{204}\text{Pb}$ than all of the other lavas from 9°17'N-10°N EPR (Figure 6). The “less radiogenic” group has the lowest $^{208}\text{Pb}/^{204}\text{Pb}$ and $^{206}\text{Pb}/^{204}\text{Pb}$, and intermediate $^{207}\text{Pb}/^{204}\text{Pb}$ (Figures 6 & 7). Pb isotopes also correlate with incompatible element ratios and Sr, Nd, and Hf isotopes (Figure 7). Finally, correlations exist between incompatible element ratios and Sr, Nd, and Hf isotopes for off-axis lavas from 9°30'N. Many of these correlations appear to be

hyperbolic in geometry and are suggestive of two-component mixing (e.g., K/Ti vs. ϵ_{Nd} , Ce/Yb vs. ϵ_{Nd} ; Figures 4B, 4D).

2.5.4. U-Th-Ra Disequilibria

U, Th, and ^{226}Ra concentrations and ($^{234}\text{U}/^{238}\text{U}$), ($^{230}\text{Th}/^{232}\text{Th}$), ($^{230}\text{Th}/^{238}\text{U}$), and ($^{226}\text{Ra}/^{230}\text{Th}$) for 9°30'N and 9°50'N off-axis N-MORB and E-MORB are reported in Table 5 and are shown in Figure 8.

2.5.4.1. (^{238}U)-(^{234}U)

All samples measured have ($^{234}\text{U}/^{238}\text{U}$) in equilibrium within analytical uncertainties ($\pm 0.5\%$) indicating that these samples have not suffered secondary alteration due to seawater-rock interaction following eruption. Note that two samples have slightly higher ($^{234}\text{U}/^{238}\text{U}$) ~ 1.006 , but show no other signs of alteration (see Sims *et al.*, 2003 for discussion on alteration). ($^{234}\text{U}/^{238}\text{U}$) is a sensitive indicator of alteration for submarine basalts since seawater is significantly enriched in ^{234}U relative to ^{238}U (for seawater, ($^{234}\text{U}/^{238}\text{U}$) ~ 1.15) (Henderson *et al.*, 1993; Ku *et al.*, 1977; Robinson, 2004; Thurber, 1962).

2.5.4.2. (^{238}U)-(^{230}Th)-(^{226}Ra)

All of the samples measured from both 9°30'N and 9°50'N EPR have ($^{230}\text{Th}/^{238}\text{U}$) > 1 , or Th excesses. Based on experimental studies, this large ^{230}Th enrichment relative to ^{238}U indicates melting began in the presence of garnet (Beattie, 1993; Hauri *et*

al., 1994; Landwehr *et al.*, 2001; LaTourrette *et al.*, 1993; Salters & Longhi, 1999; Salters *et al.*, 2002). ^{230}Th excesses are highly variable (1.054-1.198), encompass much of the compositional range previously measured in MORB from this region, and are negatively correlated with $(^{238}\text{U}/^{232}\text{Th})$ (cf., Goldstein *et al.*, 1993; Goldstein *et al.*, 1994; Volpe & Goldstein, 1993; Lundstrom *et al.*, 1995; 1998; 1999; Sims *et al.*, 2002; Sims *et al.*, 2003) (Figure 8). In addition, $(^{230}\text{Th}/^{232}\text{Th})$ correlates with $(^{238}\text{U}/^{232}\text{Th})$, in which E-MORB have the lowest $(^{230}\text{Th}/^{232}\text{Th})$ (1.10-1.23) and $(^{238}\text{U}/^{232}\text{Th})$ (1.00-1.08), N-MORB have intermediate $(^{230}\text{Th}/^{232}\text{Th})$ (1.26-1.38) and $(^{238}\text{U}/^{232}\text{Th})$ (1.11-1.25) and D-MORB have high $(^{230}\text{Th}/^{232}\text{Th})$ (1.39-1.40) and $(^{238}\text{U}/^{232}\text{Th})$ (1.30-1.32) (Figure 8A). This correlation has previously been shown and discussed by Goldstein *et al.* (1993) for 9°-10°N EPR samples and extended by Lundstrom *et al.* (1999) to include E-MORB, N-MORB, and D-MORB from the Siqueiros Fracture Zone, N-MORB from 9°-10°N, and D-MORB from the Lamont Seamounts. The samples in this study augment this trend by including samples with compositions that are transitional to the E-MORB and D-MORB end members. Two samples have E-MORB-like $(^{230}\text{Th}/^{232}\text{Th})$ and $(^{238}\text{U}/^{232}\text{Th})$ but are only slightly enriched with respect to incompatible element compositions and have Sr, Nd, Hf, and Pb isotope compositions similar to N-MORB (e.g., 2697-1 and 2489-12 have Th/U = 2.94 and 2.73, respectively) (Figures 2-8). Additionally, samples 2697-9 and 2706-7 have $(^{230}\text{Th}/^{232}\text{Th})$, $(^{238}\text{U}/^{232}\text{Th})$, and incompatible element compositions that are transitional to Lamont and Siqueiros D-MORB compositions (Th/U = 2.33 and 2.30, respectively).

Three samples have measurable $(^{226}\text{Ra}/^{230}\text{Th})$ disequilibria. Sample 2697-1 ($(^{226}\text{Ra}/^{230}\text{Th}) = 1.65$) is an E-MORB collected from ~3.5 km off-axis at 9°50'N, and

samples 2697-9 ($(^{226}\text{Ra}/^{230}\text{Th}) = 1.37$) from $9^{\circ}50'\text{N}$ and 2706-7 ($(^{226}\text{Ra}/^{230}\text{Th}) = 1.52$) from $9^{\circ}30'\text{N}$ are both incompatible element-depleted N-MORB collected from <1.9 km off-axis (Figure 9B). All other samples analyzed for $(^{226}\text{Ra}/^{230}\text{Th})$ —including all E-MORB from $9^{\circ}30'\text{N}$ —are in equilibrium and were collected >1.9 km off-axis. For the three samples with ^{226}Ra excesses ($(^{226}\text{Ra}/^{230}\text{Th}) > 1$), ^{230}Th excesses can be assumed to be primary, as ^{230}Th undergoes insignificant decay over 8 kyrs (i.e., five half-lives of ^{226}Ra —the time it takes for $(^{226}\text{Ra}/^{230}\text{Th})$ to return to equilibrium). For the samples in equilibrium, this indicates an eruption age of at least 8 ka, and suggests that ^{230}Th excesses may need to be age-corrected to recover primary ^{230}Th disequilibria, assuming these samples were generated with significant ^{226}Ra excesses. Because most samples have $(^{226}\text{Ra}/^{230}\text{Th})$ in equilibrium, these samples do not conform to the apparent negative correlation between $(^{226}\text{Ra}/^{230}\text{Th})$ and $(^{230}\text{Th}/^{238}\text{U})$ observed for young axial samples. The samples with ^{226}Ra excesses have low $(^{226}\text{Ra}/^{230}\text{Th})$ compared to the axial, zero-age trend (Sims *et al.*, 2002), and this is likely an effect of aging.

2.6. DISCUSSION

2.6.1. Correlations between chemical and isotopic variability

Based on Sr, Nd, Hf, and $^{208}\text{Pb}/^{206}\text{Pb}$ isotopic evidence, Sims *et al.* (2002) considered the axial samples from $9^{\circ}17'\text{N}$ to 10°N EPR to be derived from a mantle source that was homogeneous over the length scale of melting. Our additional data show

that off-axis E-MORB have mantle source compositions that are isotopically distinct from all 9°-10°N EPR N-MORB. We posit that the majority of the trends observed when including the new data for off-axis N-MORB and E-MORB in addition to previously published data for N-MORB from 9°-10°N EPR (Sims *et al.*, 2002; 2003) result from mixing of melts derived from a heterogeneous mantle source with at least two major components that are chemically and isotopically distinct. As mentioned above, Pb isotopes appear to be more discriminating and demonstrate mixing between each of two distinct off-axis E-MORB end members and a more depleted end member. (In this regard, we note that Sims *et al.* (2002) also could not reconcile the Pb isotopes with their assumption of source homogeneity and decided that the $^{208}\text{Pb}/^{206}\text{Pb}$, which was uniform in their data set, was the most important variable for their interpretation of U-series data as it implied constant time-integrated source $^{232}\text{Th}/^{238}\text{U}$.) Despite this apparent tertiary mixing relationship with respect to Pb isotopes, we focus on two-component mixing because it appears sufficient to explain the entirety of the geochemical trends except Pb. This is consistent with other studies that have shown on a global scale that U-Th, Nd, and Sr isotope systematics support a model of binary mixing, whereas inclusion of Pb isotopes requires several additional components (Sims & Hart, 2006).

To test the plausibility of two-component mixing, we have calculated binary mixing curves between incompatible element and long-lived radiogenic isotope compositions using the most depleted off-axis sample (2706-7) and the most enriched off-axis E-MORB (sample 2703-1) from this study as end member compositions. The resulting mixtures appear to reproduce the 9°-10°N EPR trends quite well (Figures 4 &

5). We have also calculated mixing curves between Siqueiros E-MORB and D-MORB using the isotopic data from Sims *et al.* (2002) and the concentration data for the same samples published in Perfit *et al.* (1996) and Lundstrom *et al.* (1999). These represent some of the most incompatible element-enriched and -depleted samples from the first order EPR segment between the Siqueiros and Clipperton transform faults and may be plausible regional end member mantle source compositions. However, the mixing curves between these Siqueiros compositions do not appear to fit the 9°30'N off-axis data as well as mixing between depleted off-axis N-MORB and off-axis E-MORB. The isotopic variability present in the mantle source of Siqueiros transform fault lavas is similar to, but distinct from that at 9°30'N. Thus, it seems that 9°30'N and Siqueiros lavas may have slightly different mantle sources, which may reflect the length scale (or time scale) of mantle heterogeneities throughout the region. We have also calculated mixing between the Siqueiros D-MORB sample D20-2 (Lundstrom *et al.*, 1999) and the trend line age-corrected E-MORB sample 2701-1 (Figure 8; see Figure 8 caption for details). Again, binary mixing between end member melt compositions reproduces the entire data suite quite well.

2.6.2. Are E-MORB erupted on- or off-axis?

Two physical processes have been proposed to explain the emplacement of geochemically enriched signatures of E-MORB melts along the EPR. In the first process, as advocated by Perfit *et al.* (1994), E-MORB melts are transported away from the AMC to small, off-axis melt lenses, from which they subsequently erupt. Some unavoidable

mixing of enriched melts with depleted melts occurs, generating the observed mixing arrays. This model requires that E-MORB erupt off-axis. Although we cannot rule out this model, concurrent production of N-MORB with E-MORB melts while preserving the E-MORB signature requires minimal mixing in the crust between the enriched melts and the normal/depleted melts.

The alternative hypothesis, which in this case is better supported by the existing data, is that production of E-MORB and N-MORB occur at different times, and that mixing of enriched and depleted melts occurring during progressive depletion produced the observed geochemical variations (e.g., Batiza & Niu, 1992; Hekinian *et al.*, 1989). In other regions of the EPR, such as from 11°45'N-13°N, E-MORB are known to erupt within the ridge axis (e.g., Castillo *et al.*, 2000; Hekinian *et al.*, 1989; Reynolds *et al.*, 1992). They also display similar correlations between incompatible element enrichment and isotopic enrichment. At 17°30'S EPR, mantle melting processes and source characteristics have been argued to vary over the course of hundreds of years based on the distribution of five geochemically and magnetically distinct lava sequences (Bergmanis *et al.*, 2007). We expect similar variations here at 9°-10°N EPR, though perhaps over somewhat longer time scales, as the spreading rate is significantly slower (11 cm/yr at 9°-10°N vs. ~14.6 cm/yr at 17°S).

Because of the detailed studies conducted at 9°17'N-10°N EPR, we can readily identify relationships between spatial variations in lava chemistry and variations in lava age. In particular, we have excellent constraints on the extent of the neo-volcanic zone in this region from side-scan sonar imaging and magnetization profiles (e.g., Escartin *et al.*,

2007; Fornari *et al.*, 1998; Fornari *et al.*, 2004; Schouten *et al.*, 2004; Sims *et al.*, 2003; Schouten *et al.*, 1999; Soule *et al.*, 2005; Soule *et al.*, 2009), qualitative age constraints on lava flows outside of the axial summit trough from submersible observations (Haymon *et al.*, 1993; Sims *et al.*, 2003; Soule *et al.*, 2007), and quantitative age constraints obtained from paleointensity (Bowles *et al.*, 2006) and U-series analyses (e.g., Goldstein *et al.*, 1994; Rubin *et al.*, 1994; Sims *et al.*, 2003; Volpe & Goldstein, 1993).

2.6.2.1. Geological constraints

In the past, the coupled observations that E-MORB occur off-axis and young N-MORB occur in close relation (Goldstein *et al.*, 1994) have been used to infer that E-MORB are erupted off-axis (Perfit *et al.*, 1994). However, based on observations of E-MORB within the axis in other locations, particularly in the 12°-13°N region (e.g., Hekinian *et al.*, 1989; Langmuir *et al.*, 1986; Niu *et al.*, 1999; Reynolds & Langmuir, 2000; Reynolds *et al.*, 1992) and the 17°S EPR (Bergmanis *et al.*, 2007), there appears to be no justification for requiring off-axis eruption of these 9°-10°N EPR E-MORB melts. Instead, we suggest that the distribution of E-MORB is closely tied to the volcanic processes that locally contribute to crustal construction. The focus of many past studies at 9°-10°N EPR has been to understand why seismic layer 2A, interpreted as the extrusive crust, rapidly doubles in thickness within ~2 km of the AST and then maintains a constant thickness (Bowles *et al.*, 2006; Christeson *et al.*, 1994; 1996, Escartin *et al.*, 2007; Goldstein *et al.*, 1994; Harding *et al.*, 1993; Hooft *et al.*, 1996; Schouten *et al.*, 1999; Sims *et al.*, 2003; Vera & Diebold, 1994). Although many of these studies

preferentially advocate for different individual lava emplacement mechanisms, it is likely that lavas that breach the AST flow down the ridge flanks (particularly in channels and as larger flows) and interact with faults that dam these flows ~1-2 km off-axis to thicken the extrusive crust (Sims *et al.*, 2003; Soule *et al.*, 2005; Escartin *et al.*, 2007). Off-axis eruptions and pillow ridges probably play a less significant role in crustal construction (cf. Sims *et al.*, 2003). What has become increasingly clear from these studies is that lava emplacement is not confined to the AST and that young lava flows extend up to ~2 km on both sides of the AST (Figure 1). This area of young lavas has been termed the “neo-volcanic zone”, and the difference between young, “neo-volcanic” seafloor and flanking old seafloor has been interpreted to correspond to age differences ranging on the order of ~1-10 kyrs (Escartin *et al.*, 2007).

In general, E-MORB are located in areas of diminished volcanic activity, particularly near the dying western limb of the small OSC and east of the neo-volcanic zone in the 9°30'N region northwards to 9°36'N, with a smaller population west of the neo-volcanic region at 9°50'N (Figure 1). Evidence of decreased fault density (Escartin *et al.*, 2007), increased lava channel density (Soule *et al.*, 2005), thicker extrusive layer volumes (Harding *et al.*, 1993; Soule *et al.*, 2005; Escartin *et al.*, 2007), decreased apparent sedimentation in side-scan sonar (Fornari *et al.*, 1998, Fornari *et al.*, 2004, Soule *et al.*, 2009), higher magnetic anomalies (Schouten *et al.*, 1999), and a westward offset of the AMC relative to the AST (Crawford & Webb, 2002; Escartin *et al.*, 2007; Soule *et al.*, 2005) indicate that volcanic activity and crustal accretion are preferentially distributed to the west side of the axis at 9°30'N, opposite the highest concentration of E-

MORB. Similarly, at 9°50'N, these lines of evidence (note the AMC is offset to the east at 9°50'N) indicate that volcanism and crustal accretion are focused to the east side of the AST. Thus, given the sampling distribution of E-MORB, the geological evidence suggests that E-MORB (with the exception of R54-2, a dredged E-MORB sampled east of the small OSC at 9°37'N), are indeed older and not currently erupting within the AST, and that current exposure on the seafloor simply reflects the fact that they have not been covered by younger lava flows of axial N-MORB compositions.

2.6.2.2. Paleointensity Age Constraints

Bowles *et al.* (2006) reported paleointensities on ~175 samples from 9°-10°N EPR, including nine off-axis E-MORB. Of these nine off-axis E-MORB, three are from north of the small OSC at 9°37'N, and only two of these three samples have paleointensities >20 μ T, and one sample has a paleointensity ~7.7 μ T. The remaining six off-axis E-MORB come from east of the AST at 9°30'N, include three of our samples, and have paleointensities <15 μ T (samples 2489-3 (~13.8 μ T), 2489-4A (~12.4 μ T), and 2489-5 (14.7 μ T), see Table 6). Paleointensity measurements on off-axis N-MORB sample 2489-12 (~6.6 μ T) and other lavas from the same area east of the AST at 9°30'N have the lowest paleointensities of any samples from 9°-10°N EPR (~6-8 μ T) and are most likely associated with the globally-observed Laschamp excursion at ~40 ka (Bowles *et al.*, 2006). The Laschamp excursion lasted for at most a few kyrs, and it is the only period in the last ~100 kyrs when the paleointensity field reached such low magnitudes (see Bowles *et al.*, 2006; Laj *et al.*, 2000). Following the Laschamp excursion,

paleointensities increased until they peaked about ~500-2000 years ago ($< \sim 53 \mu\text{T}$) and since then have been declining to the present day value of $\sim 36 \mu\text{T}$. As noted above, the off-axis E-MORB also have relatively low paleointensities ($< 20 \mu\text{T}$), but because of incomplete knowledge of the paleointensity field variations, Bowles *et al.* (2006) restrict their interpretation to saying that these samples are most likely older than ~ 20 kyrs. Given the similarity in paleointensities and major element compositions of off-axis E-MORB samples 2489-3, 2489-4A, and 2489-5, Bowles *et al.* (2006) suggested that these samples were erupted within ~ 100 years of each other and may even have been part of the same flow unit (here we have shown that they are very similar with respect to trace element and isotopic compositions as well; see Tables 3 & 4). Because of the large number of samples east of $9^{\circ}30' \text{N}$ with low paleointensities, they suggest that no flows reached > 1.74 km from the axis for the last 20 kyrs.

2.6.2.3. U-series Age Constraints

^{238}U - ^{230}Th and ^{230}Th - ^{226}Ra disequilibria can be used to place constraints on lava eruption ages; these constraints are shown in Table 6. Both ($^{230}\text{Th}/^{238}\text{U}$) and ($^{226}\text{Ra}/^{230}\text{Th}$) return to secular equilibrium within analytical uncertainties after about five half-lives, or 375 and 8 kyrs, respectively. Thus, samples with ^{226}Ra excesses erupted less than ~ 8 ka, and samples with ($^{226}\text{Ra}/^{230}\text{Th}$) in equilibrium are older than 8 ka, assuming they were erupted with ^{226}Ra excesses. (Note that the inverse correlation between ($^{230}\text{Th}/^{238}\text{U}$) vs. ($^{226}\text{Ra}/^{230}\text{Th}$) would predict that E-MORB have high ^{230}Th excesses and low ^{226}Ra excesses.) Since all samples from this study have ^{230}Th excesses, they can be assumed to

be younger than ~375 ka. However, no E-MORB samples have ^{226}Ra excesses, indicating that all of these $9^{\circ}30'\text{N}$ E-MORB were erupted >8 ka (provided that they were even erupted with significant ^{226}Ra excesses). Only three samples from this study have significant ^{226}Ra excesses, indicating their eruption occurred within the last few thousand years: an N-MORB from $9^{\circ}30'\text{N}$, an N-MORB from $9^{\circ}50'\text{N}$, and an E-MORB from $9^{\circ}50'\text{N}$ (Figure 8B; see Results section).

A trend line model age technique has been applied to N-MORB from the $9^{\circ}50'\text{N}$ area to provide more rigorous lava age constraints (Sims *et al.*, 2003). We extend this trend line model age method to dating E-MORB at 9° - 10°N EPR. However, as explicitly outlined in Sims *et al.* (2003), calculating robust ^{238}U - ^{230}Th and ^{230}Th - ^{226}Ra model ages requires (1) that primary magmatic processes generated the initial ^{238}U - ^{230}Th and ^{230}Th - ^{226}Ra disequilibria and that these lavas have remained a closed system; (2) that magmas have not resided for significant periods of time in a magma chamber relative to the ^{238}U , ^{230}Th , and ^{226}Ra half-lives; (3) that the mantle source between the zero-age lava and a sample of unknown age is compositionally constant; and, (4) that the initial extent of disequilibria in the zero-age lava and sample of unknown age is the same. These criteria were met by off-axis N-MORB samples from $9^{\circ}50'\text{N}$ EPR (Sims *et al.*, 2003). However, because there is only one E-MORB sample from 9° - 10°N EPR with a ^{226}Ra excess (sample 2697-1), this is the only E-MORB from 9° - 10°N for which the initial ($^{230}\text{Th}/^{232}\text{Th}$) and ^{230}Th excess is also known. In turn, regressing initial ($^{230}\text{Th}/^{232}\text{Th}$) against ($^{238}\text{U}/^{232}\text{Th}$) data on an equiline diagram to generate a zero-age trend line for purposes of ^{238}U - ^{230}Th dating means that the enriched end of this trend line is weighted

only by this one sample, leaving the range of initial ^{230}Th disequilibria for E-MORB highly uncertain. Furthermore, there are no E-MORB with known zero-age ^{226}Ra excesses, and hence dating by the ^{230}Th - ^{226}Ra method is highly problematic.

Thus, more uncertainty lies in determining model ages for E-MORB. However, given the negative correlations among ^{226}Ra excesses, ^{230}Th excesses, and ($^{238}\text{U}/^{232}\text{Th}$) for E-MORB, N-MORB, and D-MORB samples from the Siqueiros Fracture Zone, the Lamont Seamounts, and 9°-10°N EPR, it seems likely that the primary processes (namely partial melting and mixing during melt transport) that generate U-series disequilibria in N-MORB are also responsible for generating disequilibria in E-MORB (Figure 8C). Furthermore, all samples in this study have been analyzed for ($^{234}\text{U}/^{238}\text{U}$) and are in equilibrium, indicating that these lavas have remained closed systems after eruption. Additionally, because long-lived radiogenic isotopic compositions, ($^{230}\text{Th}/^{232}\text{Th}$), and ($^{238}\text{U}/^{232}\text{Th}$) are all correlated because of mixing, as described above, the zero-age trend line also represents mixing of partial melts of isotopically distinct sources. Hence, by extrapolating the zero-age ^{238}U - ^{230}Th and ^{230}Th - ^{226}Ra trend lines for axial N-MORB to include D-MORB and E-MORB, we also account for source heterogeneity (note that Sims *et al.*, 2003 only regressed zero-age, axial N-MORB with uniform isotopic compositions to date off-axis N-MORB of unknown age). We note that this is not strictly true, since the Siqueiros E-MORB are not isotopically identical to the 9°-10°N E-MORB, have different U and Th abundances, and do not derive from the same mantle source as 9°-10°N E-MORB; yet, they heavily weigh the enriched end of the ^{238}U - ^{230}Th zero-age trend line.

Finally, a recent study of ^{210}Pb disequilibria by Rubin *et al.* (2005) limits crustal residence time at 9° - 10°N EPR to less than a few hundreds of years; thus—as with N-MORB—it is unlikely that magma storage has a significant impact on the extent of ^{230}Th and ^{226}Ra disequilibria in E-MORB. Although trend line model ages for E-MORB will not be as robust as those for N-MORB, they should still provide reasonable estimates. Better knowledge of primary ($^{230}\text{Th}/^{232}\text{Th}$) and ($^{238}\text{U}/^{232}\text{Th}$) in a larger number of E-MORB from 9° - 10°N EPR would undoubtedly allow for much more robust model age calculations. Details of the trend line model age calculations are reported in the caption to Table 6.

^{238}U - ^{230}Th trend line model ages for both N-MORB and E-MORB are generally significantly younger than the spreading ages, which is consistent with significant crustal accretion up to ~ 3 km off-axis (e.g., Goldstein *et al.*, 1993; Hooft *et al.*, 1996; Schouten *et al.*, 1999; Sims *et al.*, 2003) (Figure 9). All N-MORB (except for samples 2489-12) have ($^{230}\text{Th}/^{232}\text{Th}$) indistinguishable from axial N-MORB samples ($(^{230}\text{Th}/^{232}\text{Th}) > \sim 1.35$) and thus may have been more recently erupted. Four of these N-MORB samples have ($^{226}\text{Ra}/^{230}\text{Th}$) in equilibrium and must have erupted > 8 kyrs ago. Figure 9 illustrates the relationship between trend line age, spreading age (or distance from the AST) and the effect of off-axis emplacement on the spreading age. The relatively young trend line ages for the distance from the AST for these samples indicate lava emplacement generally occurred < 1 - 3 km off-axis, which is consistent with the extent of the neo-volcanic zone on the western side of the axis (Escartin *et al.*, 2007). Thus, lava distribution may have occurred via off-axis eruption or by eruption within the AST and subsequent transport to

the ridge flanks – a feature now well documented in the 9°50'N area (Schouten *et al.*, 2004; Sims *et al.*, 2003; Soule *et al.* 2005; 2009).

One of the most striking aspects of these data is that there is no systematic difference between E-MORB and N-MORB emplacement distances (and ages). Thus, there is also no reason to suspect that the mechanism of emplacement of E-MORB is different from N-MORB: both N-MORB and E-MORB likely erupt in the AST and flow off-axis up to several kilometers, though it is possible that a relatively small volume of N-MORB and E-MORB erupt off-axis from axis-parallel faults and fissures. It should be noted that many of the E-MORB in this study from 9°30'N were sampled from pillow lavas in association with fault scarps. However, these E-MORB were generally sampled at the tops of outward dipping faults, and several were sampled from intact pillows midway up fault scarps (e.g. 2701-1, 2702-1), suggesting that many of these E-MORB are pillow lavas draped over volcanic growth faults (Macdonald *et al.*, 1996). Thus, an axial origin for these lavas is consistent with dive observations, remote sensing imagery, and the paleointensity and ^{238}U - ^{230}Th - ^{226}Ra age constraints. From these lines of evidence, we can infer that these off-axis E-MORB were emplaced within <1-3 km of the axis within the present-day extent of the neo-volcanic zone (Fornari *et al.*, 1998; Schouten *et al.*, 1999; Sims *et al.*, 2003; Soule *et al.*, 2005), and that their distribution reflects that of preservation, and not eruption: abundant E-MORB are found in areas of diminished young volcanism and volcanic repaving of the ocean floor. Furthermore, though the resolution of the ^{238}U - ^{230}Th dating technique, particularly for E-MORB, is not precise enough to make a robust analysis, we speculate that variations in the mantle source

composition from N-MORB to E-MORB may occur over relatively short time scales, perhaps <1-10 kyrs (Figure 9).

E-MORB samples 2489-3 and 2489-4a plot above the line for axial emplacement because they have ^{238}U - ^{230}Th model ages of 81 ± 26 and 100 ± 27 kyrs, respectively, which are much greater than their spreading ages (41 kyrs and 48 kyrs, respectively). One possible explanation for why these lavas have model ages ~ 40 kyrs older than their spreading ages is that they have been exposed by faulting. However, although many of the E-MORB in this study—including samples 2489-3, 2489-4a, and 2489-5, which are nearly identical with respect to their chemical compositions and paleointensities—were sampled from a large volcanic growth fault (Macdonald *et al.*, 1996), the exposed graben on the east side of the axis at $9^{\circ}30'\text{N}$ is only ~ 75 m below what would be expected if the extrusive layer were constructed symmetrically. This only amounts to ~ 500 to several thousand years worth of volcanic construction (Escartin *et al.*, 2007). Thus, exposure of these E-MORB by uplift is not sufficient to explain this age disparity. Hence, this age disparity is physically implausible and must be explained otherwise.

Older eruption age estimates by ^{231}Pa model age dating on sample 2489-3 gave a similar result of 64 ± 3 kyrs (Goldstein *et al.*, 1994). Goldstein *et al.* (1994) attribute this discrepancy to either a longer magma residence time for this sample or asymmetric spreading with slower spreading on the Cocos side. Although longer magma residence times can explain this discrepancy, constraints from other U-series disequilibria, namely ^{226}Ra and ^{210}Pb disequilibria, indicate very short residence times (Sims *et al.*, 2002; Rubin *et al.*, 2005) of 100's of years, vs. the ~ 40 kyrs needed to explain this discrepancy.

Furthermore, such a melt body would likely undergo substantial cooling, crystallization, and compositional evolution over such a long span of time, and we note that these samples are not significantly differentiated. Despite substantial evidence for asymmetric construction of the extrusive layer to the east of the AST at 9°30'N, given the bilateral symmetry of small and large flow fronts on either side of the AST, spreading is most likely a symmetric process from 9°30'N to 9°50'N EPR (Fornari *et al.*, 2004). Instead, we suggest that the coherent isotopic variations seen between off-axis N-MORB and off-axis E-MORB from this area hint at complexity in the processes (namely, coupled variations in degree of melting and source composition) that generate U-series disequilibria, and as such, it is likely that both our model age calculations and those of Goldstein *et al.* (1994) may be flawed because of invalid assumptions about the initial ($^{230}\text{Th}/^{232}\text{Th}$) and ($^{231}\text{Pa}/^{235}\text{U}$) disequilibria (cf. Sims *et al.*, 2003).

We also note that Goldstein *et al.* (1994) calculated a model age of 74 ± 3 kyrs for sample 2489-12. This is consistent with the spreading age of 78 kyrs, but much greater than the age indicated by its paleointensity (~ 40 kyrs) and our U-Th model age of 31 ± 11 kyrs. The reason for this discrepancy is because we use a different initial ($^{230}\text{Th}/^{232}\text{Th}$) based on the zero-age trend line, whereas Goldstein *et al.* (1993; 1994) use a single and constant initial ($^{230}\text{Th}/^{232}\text{Th}$) and ($^{231}\text{Pa}/^{235}\text{U}$) value. For sample 2489-12, from its lower ($^{230}\text{Th}/^{232}\text{Th}$) and ($^{238}\text{U}/^{232}\text{Th}$) and more radiogenic isotope composition, we see that this assumption of constant initial disequilibria for all N-MORB is clearly erroneous.

Likewise, we speculate that near the E-MORB end member, our zero-age trend line is not necessarily an accurate representation of the initial ($^{230}\text{Th}/^{232}\text{Th}$) disequilibria for samples

2489-3 and 2489-4a. The initial ($^{230}\text{Th}/^{232}\text{Th}$) disequilibria for these samples were possibly much lower and more similar to the enriched Siqueiros lavas. The wide range of ($^{230}\text{Th}/^{232}\text{Th}$) and large scatter around the zero-age trend line exhibited by E-MORB from 9°-10°N EPR (Sims *et al.*, 2002; 2003; Goldstein *et al.*, 1993; 1994), Siqueiros (Lundstrom *et al.*, 1999), and Juan de Fuca and Gorda Ridge (Goldstein *et al.*, 1992; 1993) seem to suggest that it is somewhat difficult to predict initial ($^{230}\text{Th}/^{232}\text{Th}$) disequilibria for some samples for the purpose of model ages. In contrast, initial ($^{230}\text{Th}/^{232}\text{Th}$) disequilibria in N-MORB appear much more homogeneous and predictable, as suggested by the coherent ages determined by U-series (Sims *et al.*, 2003) and paleointensity (Bowles *et al.*, 2006) methods.

2.6.3. Petrogenesis of E-MORB

Recent studies of E-MORB far from hotspots have argued for a globally common process for MORB source enrichment through subduction of oceanic islands or through metasomatic enrichment of the mantle wedge or oceanic lithospheric mantle (Hemond *et al.*, 2006; Nauret *et al.*, 2006; Niu *et al.*, 2002; Donnelly *et al.*, 2004). For example, Donnelly *et al.* (2004) argue that E-MORB are produced by a process in which small-volume (0.5%), low-degree melts (1%) of eclogitized slab enrich the overlying mantle wedge peridotite (of depleted mantle composition) in the most incompatible trace elements. This metasomatized peridotite is subsequently entrained in the upper mantle, and undergoes high degrees of melting (9%) beneath ridges to produce E-MORB. By batch melting metasomatized spinel peridotite, this model accounts for the chondritic

Dy/Yb in E-MORB—as they argue that melting in the presence of garnet will produce too high Dy/Yb.

Although the Donnelly *et al.* (2004) model reproduces the trace element abundances of the EPR E-MORB fairly well (see Figure 12), they did not address the observations of ^{230}Th excesses in MORB (e.g. Goldstein *et al.*, 1992; 1993; 1994; Lundstrom *et al.*, 1995; 1999; 2000; Sims *et al.*, 1995; 2002; 2003; Volpe & Goldstein, 1993), which require very recent melting in the presence of garnet ($\ll 375$ kyrs). Previous experimental studies have demonstrated that large ^{230}Th excesses must be generated in the presence of garnet, and that even in the presence of garnet, significant fractionation of Th over U may only occur at very low degrees of melting (Beattie, 1993; Elkins *et al.*, 2008; Hauri *et al.*, 1994; Landwehr *et al.*, 2001; LaTourrette *et al.*, 1993; Pertermann *et al.*, 2004; Salters & Longhi, 1999; Salters *et al.*, 2002). Because of the small D values for Th and U in all relevant phases, batch melting of metasomatically enriched spinel peridotite to F~8-10% is inconsistent with observed large ^{230}Th excesses in both Pacific N-MORB and E-MORB (unless the metasomatism is recent—i.e. much less than ~375 ka). However, this recent metasomatism is not supported by the long-lived radiogenic isotope compositions of E-MORB, which imply an old (10^8 - 10^9 yrs) enrichment process and subsequent ingrowth.

Studies of U-series disequilibria at 9°-10°N EPR and the Juan de Fuca ridge demonstrate a positive correlation between ($^{230}\text{Th}/^{232}\text{Th}$) and ($^{238}\text{U}/^{232}\text{Th}$) (Figure 8a) (Goldstein *et al.*, 1993; Lundstrom *et al.*, 1995; Lundstrom *et al.*, 1999; Sims *et al.*, 1995; 2002) and negative correlations between Th excesses and ($^{238}\text{U}/^{232}\text{Th}$) and between

primary ^{230}Th and ^{226}Ra excesses (Figures 8b, 8c) (Lundstrom *et al.*, 1995; Lundstrom *et al.*, 1999; Sims *et al.*, 1995; 2002; Volpe & Goldstein, 1993). These N-MORB and E-MORB data also show a distinct correlation between ^{238}U - ^{230}Th disequilibria and Sm/Nd fractionation (Sims *et al.*, 1995). Data presented in this study augment these correlations (Figure 8). The most recent studies of U-series disequilibria in 9°-10°N EPR lavas have shown that for lavas to have both negatively correlated primary ^{226}Ra and ^{230}Th excesses and positively correlated ($^{230}\text{Th}/^{232}\text{Th}$) and ($^{238}\text{U}/^{232}\text{Th}$), the melting must occur in a two-porosity melting regime (Kelemen *et al.*, 1997; Sims *et al.*, 1999; Jull *et al.*, 2002; Lundstrom, 2000; Sims *et al.*, 2002). Based on these U-series constraints, which require recent fractionation in the presence of garnet and subsequent mixing of melts, we propose that the mixing trends among trace elements and long-lived radiogenic isotopes reflect mixing of melts during melt extraction and crustal residence and not ancient, low-degree melt metasomatism. Below, we posit an alternative model in which low-degree melting of an enriched, garnet-bearing source occurs deep in the MORB melting regime. We accept that metasomatism, recycling of ocean crust, and recycling of OIB are all still possible candidates for the origin of the mantle source enrichment, but not that the low-degree melting event responsible for the trace element enrichments in E-MORB occurs as a direct consequence of ancient metasomatism.

2.6.3.1. Melting Model

We model the melt extraction process as 1-D progressive depletion of a two lithology source composed of peridotite (52% olivine, 18% clinopyroxene, 30%

orthopyroxene) and pyroxenite (82% clinopyroxene, 18% garnet), similar to that of Stracke & Bourdon (2009). Melt fractions are calculated as a function of pressure using estimates of productivity for peridotite and pyroxenite (Petermann & Hirschmann, 2003). To simulate the effect of a two-porosity model on trace element abundances, we mix accumulated fractional melts generated at high pressure with accumulated fractional melts generated at low pressure. Model parameters are illustrated in Figures 10-12, and melting model details are given in the figure captions.

One of the strongest constraints on the genesis of EPR E-MORB is the presence of both shallow MREE/HREE slopes (Donnelly *et al.*, 2004) and large ^{230}Th excesses. Although the shallow, near chondritic MREE/HREE slope would suggest a lack of garnet in the mantle source residue, the ^{230}Th excesses indicate otherwise. This seeming discrepancy can be easily reconciled by recognizing that highly incompatible elements such as U and Th are strongly partitioned into the melt in the smallest melt fractions, whereas the concentrations of moderately incompatible elements like the MREEs and HREEs are much more sensitive to the degree of melting. For example, the melting trajectories in Figures 11A & B show there is a large change in Th/U (and Th and U abundances, not shown) for the first percent or so of melting of garnet pyroxenite and essentially no change in Sm/Yb (note that Mix1G (1405°C) pyroxenite starts mixing with peridotite at ~1.2% melting). At higher degrees of melting of pyroxenite (>1.2%), and by mixing increasing volumes of spinel peridotite melt into the relatively small volumes of pyroxenite melt (note that even small degrees of melting of peridotite will produce large volumes of depleted melt because of the large solid proportion of peridotite; Figure 10B),

the influence of deep garnet pyroxenite melts on the MREE and HREE composition of the mixed melts is rapidly diminished while there are no longer any significant changes in the concentrations of highly incompatible elements (Figure 11). Hence, in this progressive depletion model, the first increments of melting will determine the direction and initial extent of U-Th disequilibria but melting over a much larger interval will control the MREE/HREE slope.

Figures 11A and 11C show that the curvature of the 9°-10°N EPR mixing array can only be generated if the enriched component is substantial (i.e. generated in the first few degrees of melting of the enriched source). Mixing with peridotite at higher degrees of pyroxenite melting (>1-2%) results in a hyperbola with the wrong sense of curvature (Figure 11C-G2 mixed melts) or too high Sm/Yb at a given Sm/Nd (Figure 11C-Mix1G (1375°C) mixed melts). However, if the pyroxenite solidus is much closer to the peridotite solidus (i.e., a Mix1G solidus of 1405°C at 2.5 GPa), then only ~1% pyroxenite melting may occur prior to peridotite melting, and the curvature and magnitude of Sm/Nd and Sm/Yb fractionation is much closer to the observations. However, when considering more highly incompatible element ratios (i.e., Th/U), the melt mixing trend does a relatively poor job fitting the data (Figures 11A & B). Figure 12A shows how the overall trace element abundances that result from this type of progressive depletion model (rather than a two-porosity model) compare to E-MORB sample 2703-1. Although the trace element abundances produced by the progressive depletion model are not entirely unsatisfying, the two-porosity models provide much better matches to the data, particularly for Th and U (Figures 12B & C). The mismatch in the abundances,

particularly in the highly incompatible elements, may be due to differences in the model and actual source. In all cases, shallow melts produced by progressive depletion of a lithologically and chemically heterogeneous mantle source are reasonable matches to average 9°-10°N EPR N-MORB. Due to the higher peridotite productivity used for the case of Mix1G (1405°C), the N-MORB composition is more depleted in incompatible trace elements for the progressive depletion model than for the two-porosity models (Figure 12A).

2.7. CONCLUSIONS

Geological and geophysical evidence for diminished volcanic activity in the 9°30'N region, particularly to the east side, have been presented in numerous studies (e.g., Bowles *et al.*, 2006; Crawford & Webb, 2002; Escartin *et al.*, 2007; Fornari *et al.*, 1998; Harding *et al.*, 1993; Schouten *et al.*, 1999; Soule *et al.*, 2005). However, decreased volcanism and the preservation of E-MORB have so far only been tentatively linked (Reynolds *et al.*, 1992; Smith *et al.*, 2001). Our examination of geological, paleointensity, and U-Th-Ra age constraints indicates that 9°-10°N EPR E-MORB compositions are preserved on the surface because of locally diminished volcanic activity west of the AST at 9°50'N, east of the AST at 9°30'N, and near the dying western limb tip at 9°37'N. Paleointensities and U-Th-Ra disequilibria further suggest that emplacement of flows occurs up to ~3 km off-axis and is similar for E-MORB and N-

MORB throughout the 9°-10°N region. This further implies that E-MORB, like N-MORB, erupt from within or near to the AST.

Based on the nonsystematic model age distribution of E-MORB relative to N-MORB analyzed in this study, it seems likely that volumetrically small proportions of enriched pyroxenite veins periodically enter the mantle source region beneath 9°-10°N. In other words, the length scale among mantle heterogeneities is great enough that enriched mantle domains are not homogeneously distributed throughout the melting region beneath 9°-10°N EPR, and this is consistent with other studies that proposed alternating intervals of enriched and depleted melt supply to the ridge axis (Batiza & Niu, 1992; Bergmanis *et al.*, 2007; Hekinian *et al.*, 1989; Reynolds *et al.*, 1992). Prompted by U-series constraints on MORB petrogenesis in the 9°-10°N region, forward models of incompatible element data suggest an alternative model for E-MORB genesis in which small volumes of low-degree melts of pyroxenite veins mix with much greater volumes of large melt fractions of peridotite, either during melt extraction in a two-porosity melting regime or in the axial magma chamber. Due to the enhanced productivity of pyroxenite, intervals of E-MORB magmatism and volcanism are probably short-lived (<1-10 ka), with variations in the degree of enrichment reflecting the extent of depletion of the enriched source over time.

Acknowledgments

C.L.W. would like to thank Adam Soule, Maurice Tivey, Dan Fornari, Matt Jackson, and Adam Goss for thoughtful comments and discussions that have helped to improve this

paper. The manuscript benefited substantially from careful reviews of an earlier version by Craig Lundstrom, Charlie Langmuir, and Fred Frey. This research was supported by National Science Foundation (NSF) grants [OCE-0623838 and OCE-0137325] to KWWS. Field and laboratory research was supported by NSF grants OCE-9402360, 9403773, and 0138088 to MRP. Janne Blichert-Toft acknowledges financial support from the French Institut National des Sciences de l'Univers.

References

- Allan, J.F., Batiza, R., Perfit, M.R., Fornari, D.J., & Sack, R.O. (1989). Petrology of Lavas from the Lamont Seamount Chain and Adjacent East Pacific Rise, 10°N. *Journal of Petrology* **30** (5), 1245-1298.
- Allègre, C.J. & Turcotte, D.L. (1986). Implications of a two-component marble-cake mantle. *Nature* **323**, 123-127.
- Allègre, C.J., Hart, S.R., & Minster, J.-F. (1983). Chemical structure and evolution of the mantle and continents determined by inversion of Nd and Sr isotopic data, I. Theoretical methods. *Earth and Planetary Science Letters* **66**, 177-190.
- Ball, L., Sims, K.W.W. & Schweiters, J. (2008). Measurement of $^{234}\text{U}/^{238}\text{U}$ and $^{230}\text{Th}/^{232}\text{Th}$ in volcanic rocks using the Neptune MC-ICP-MS. *Journal of Analytical Atomic Spectrometry* **23**, 173-180.
- Batiza R. & Niu, Y. (1992). Petrology and magma chamber processes at the East Pacific Rise-9°30'N. *Journal of Geophysical Research* **97**, 6779-6797.
- Beattie P. (1993). Uranium-thorium disequilibria and partitioning on melting of garnet peridotite. *Earth and Planetary Science Letters* **363**, 63-65.
- Ben Othman D. & Allègre, C.J. (1990) U-Th isotopic systematics at 13°N east Pacific Ridge segment. *Earth and Planetary Science Letters*, **98**, 129-137.
- Bergmanis, E.C., Sinton, J. & Rubin, K.H. (2007). Recent eruptive history and magma reservoir dynamics on the East Pacific Rise at 17°30'S. *Geochemistry, Geophysics, Geosystems* **8**(12), doi:10.1029/2207GC001742.
- Blichert-Toft, J. & Albarède, F. (1997). The Lu-Hf isotope geochemistry of chondrites and the evolution of the mantle-crust system. *Earth and Planetary Science Letters* **148**, 243-258.
- Blichert-Toft J., Chauvel, C. & Albarede F. (1997). Separation of Hf and Lu for high-precision isotope analysis of rock samples by magnetic sector-multiple collector ICP-MS. *Contributions to Mineralogy and Petrology* **127**, 248-260.
- Bowles J., Gee, J.G., Kent, D.V., Perfit, M.R., Soule, S.A. & Fornari, D.J. (2006). Paleointensity applications to timing and extent of eruptive activity, 9°-10°N East Pacific Rise. *Geochemistry, Geophysics, Geosystems* **7**(6), (2005GC001141).
- Bryce, J.G., DePaolo, D.J. & Lassiter, J.C. (2005). Geochemical structure of the Hawaiian plume: Sr, Nd, and Os isotopes in the 2.8 km HSDP-2 section of Mauna Kea volcano. *Geochemistry, Geophysics, Geosystems* **6**(9), (2004GC000809).
- Carbotte, S. M. & Macdonald, K.C. (1992). East Pacific Rise 8°-10°30'N: Evolution of ridge segments and discontinuities from SeaMARC II and three-dimensional magnetic studies. *Journal of Geophysical Research* **97**, 6959-6982.
- Castillo, P. R., Klein, E., Bender, J., Langmuir, C., Shirey, S., Batiza, R. & White, W. (2000). Petrology and Sr, Nd, and Pb isotope geochemistry of mid-ocean ridge basalt glasses from the 11°45'N to 15°00'N segment of the East Pacific Rise. *Geochemistry, Geophysics, Geosystems* **1**(1999GC000024).
- Chauvel C. & Blichert-Toft, J. (2001). A hafnium isotope and trace element perspective on melting of the depleted mantle. *Earth and Planetary Science Letters* **190**, 137-151.

- Christeson, G. L., Kent, G.M., Purdy, G.M. & Detrick, R.S. (1996). Extrusive thickness variability at the East Pacific Rise, 9°-10°N, constraints from seismic techniques. *Journal of Geophysical Research* **101**, 2859-2873.
- Christeson, G. L., Purdy, G.M. & Fryer, G.J. (1994). Seismic constraints on shallow crustal emplacement processes at the fast-spreading East Pacific Rise. *Journal of Geophysical Research* **99**, 17957-17973.
- Cochran, J. R., Fornari, D.J., Coakley, B.J., Herr, R. & Tivey, M.A. (1999). Continuous near-bottom gravity measurements made with a BGM-3 gravimeter in DSV *Alvin* on the East Pacific Rise crest near 9°30'N and 9°50'N. *Journal of Geophysical Research* **104**, 10,841-10,861.
- Crawford W. C. & Webb, E. S. (2002). Variations in the distribution of magma in the lower crust and at the Moho beneath the East Pacific Rise at 9°-10°N. *Earth and Planetary Science Letters* **203**, 117-130.
- DePaolo, D.J. & Wasserburg, G.J. (1976) Nd isotopic variations and petrogenetic models. *Geophysical Research Letters* **3**(5), 249-252.
- Donnelly, K.E., Goldstein, S.L., Langmuir, C.H. & Spiegelman, M. (2004). Origin of enriched ocean ridge basalts and implications for mantle dynamics. *Earth and Planetary Science Letters* **226**, 347-366.
- Dupre, B., Lambret, B., Rousseau, D., & Allegre, C.J. (1981) Limitations on the scale of mantle heterogeneities under oceanic ridges. *Nature* **294**, 552-554.
- Elkins L. J., Gaetani, G.A., & Sims, K.W.W. (2008) Partitioning of U and Th during garnet pyroxenite partial melting: Constraints on the source of alkaline ocean island basalts. *Earth and Planetary Science Letters* **265**, 270-286.
- Escartin J., Soule, S.A., Fornari, D.J., Tivey, M.A., Schouten, H., & Perfit, M.R. (2007) Interplay between faults and lava flows in construction of the upper oceanic crust: The East Pacific Rise crest 9°25'-9°58'N. *Geochemistry, Geophysics, Geosystems* **8**(6).
- Fornari, D.J., Perfit, M.R., Allan, J.F., & Batiza, R. (1988) Small-scale heterogeneities in depleted mantle sources--near-ridge seamount lava geochemistry and implications for mid-ocean ridge magmatic processes. *Nature* **331**, 511-513.
- Fornari, D.J., Perfit, M.R., Allan, J.F., Batiza, R., Haymon, R., Barone, A., Ryan, W.B.F., Smith, T., Simkin, T., & Luckman, M.A. (1989) Geochemical and structural studies of the Lamont Seamount--seamounts as indicators of mantle processes. *Earth and Planetary Science Letters*, **89**(1), 63-83.
- Fornari D., R. Haymon, M. Perfit, T.K.P. Gregg, & M.H. Edwards. (1998) Axial summit trough of the East Pacific Rise, 9-10°N: Geological characteristics and evolution of the axial zone on fast spreading mid-ocean ridges. *Journal of Geophysical Research* **103**, 9827-9855.
- Fornari D., Tivey, M., Schouten, H., Perfit, M., Yoerger, D., Bradley, A., Edwards, M., Haymon, R., Scheirer, D., Von Damm, K., Shank, T., & Soule, A. (2004) Submarine Lava Flow Emplacement at the East Pacific Rise 9°50'N: Implications for Uppermost Ocean Crust Stratigraphy and Hydrothermal Fluid Circulation. In *Mid-Ocean Ridges: Hydrothermal Interactions between the Lithosphere and*

- Oceans*, Vol. 148 (ed. C. R. German, Lin, J., and Parson, L.M.), pp. 187-217. AGU.
- Galer, S.J.G. & O'Nions, R.K. (1986). Magmagenesis and the mapping of chemical and isotopic variations in the mantle, *Chemical Geology* **56**, 45-61.
- Goldstein, S.J., Murrell, M.T., Janecky, D.R., Delaney, J.R. & Clague, D.A. (1992). Erratum to Geochronology and petrogenesis of MORB from the Juan de Fuca and Gorda ridges by ^{238}U - ^{230}Th disequilibrium. *Earth and Planetary Science Letters* **109**, 255-272.
- Goldstein, S.J., Murrell, M.T., & Williams, R.W. (1993) ^{231}Pa and ^{230}Th chronology of mid-ocean ridge basalts. *Earth and Planetary Science Letters*, **115**, 151-159.
- Goldstein S. J., Perfit, M.R., Batiza, R., Fornari, D.J., & Murrell, M.T. (1994) Off-axis volcanism at the East Pacific Rise detected by uranium-series dating of basalts. *Nature* **367**, 157-159.
- Harding A. J., G.M. Kent, & J.A. Orcutt. (1993) A multichannel seismic investigation of upper crustal structure at 9°N on the East Pacific Rise: Implications for crustal accretion. *Journal of Geophysical Research* **98**, 13925-13944.
- Harpp K., W.M. White, & Batiza, R. (1990) Isotopic study of contrasting magmatic studies: The East Pacific Rise at 9°30'N and the MAR in the FAMOUS area. *Eos Transactions AGU* **71**, 658.
- Hart, S. R., Schilling, J.-G., & Powell, J.L. (1973) Basalts from Iceland and along Reykjanes Ridge Sr isotope geochemistry. *Nature, Physical Science* **246** (155), 104-107.
- Hart, S.R., Workman, R.K., Ball, L., & Blusztajn, J. (2004) High precision Pb isotope techniques from the WHOI NEPTUNE PIMMS. *WHOI Plasma Facility Open File Technical Report* **10** (http://www.whoi.edu/science/GG/people/shart/open_file.htm).
- Hart, S.R. & Blusztajn, J. (2006) Age and geochemistry of the mafic sills, ODP site 1276, Newfoundland margin. *Chemical Geology* doi:10.1016/j.chemgeo.2006.07.001.
- Hauri, E. H., Wagner, T.P. & Grove, T.L. (1994) Experimental and natural partitioning of Th, U, Pb, and other trace elements between garnet, clinopyroxene, and basaltic melts. *Chemical Geology* **117**, 149-166.
- Haymon, R. M., Fornari, D.J., Von Damm, K.L., Lilley, M.D., Perfit, M.R. & Edmond, J.M. (1993) Volcanic eruption of the mid-ocean ridge along the East Pacific Rise crest at 9° 45'-45'N: Direct submersible observations of seafloor phenomena associated with an eruption event in April, 1991. *Earth and Planetary Science Letters* **119**, 85-101.
- Hedge, C.E. & Peterman, Z.E. (1970) The strontium isotopic composition of basalts from the Gorda and Juan de Fuca Rises, northeastern Pacific Ocean. *Contributions to Mineralogy and Petrology*, **27**, 114-120.
- Hekinian R., G. Thompson, & D. Bideau. (1989) Axial and off-axial heterogeneity of basaltic rocks from the East Pacific Rise at 12°35'N-12°51'N and 11°26'N-11°30'N. *Journal of Geophysical Research* **94**(B12), 17,437-17,463.
- Hemond, C., Hofmann, A.W., Vlastélic, I. & Nauret, F. (2006). Origin of MORB enrichment and relative trace element compatibilities along the Mid-Atlantic

- Ridge between 10° and 24°N. *Geochemistry, Geophysics, Geosystems* **7**(12), (2006GC001317).
- Henderson, G.M., Cohen, A.S. & Onions, R.K. (1993) U-234/U-238 Ratios and Th-230 Ages for Hateruma Atoll Corals - Implications for Coral Diagenesis and Seawater U-234/U-238 Ratios, *Earth and Planetary Science Letters* **115**, 65-73.
- Hirschmann, M. M. (2000) Mantle solidus: Experimental constraints and the effects of peridotite composition. *Geochemistry, Geophysics, Geosystems* **1**, (2000GC000070).
- Hirschmann, M. M. & Stolper, E.M. (1996) A possible role for garnet pyroxenite in the origin of the 'garnet signature' in MORB. *Contributions to Mineralogy and Petrology* **124**, 185-208.
- Hirschmann, M.M., Kogiso, T., Baker, M.B. & Stolper, E.M. (2003). Alkalic magmas generated by partial melting of garnet pyroxenite. *Geology* **31**(6), 481-484.
- Hooft, E. E. E., Schouten, H. & Detrick, R.S. (1996) Constraining crustal emplacement processes from the variation in seismic layer 2A thickness at the East Pacific Rise. *Earth and Planetary Science Letters* **142**, 289-309.
- Hurley, P.M. (1968) Absolute abundance and distribution of Rb, K, and Sr in the Earth. *Geochimica et Cosmochimica Acta* **32**, 273-288.
- Ita, J. & Stixrude, L. (1992) Petrology, elasticity, and composition of the mantle transition zone. *Journal of Geophysical Research*, **97**, 6849-6866.
- Jull, M., Kelemen, P.B. & Sims, K. (2002). Consequences of diffuse and channelled porous melt migration on uranium series disequilibria. *Geochimica et Cosmochimica Acta* **66**(23), 4133-4148.
- Kelemen, P.B., Hirth, G., Shimizu, N., Spiegelman, M. & Dick, H.J.B. (1997). A review of melt migration processes in the adiabatically upwelling mantle beneath oceanic spreading ridges, *Philosophical Transactions of the Royal Society of London, Series A*, **355**(1723), 283-318.
- Klein, E. M. & Langmuir, C.H. (1987) Global correlations of ocean ridge basalt chemistry with axial depth and crustal thickness. *Journal of Geophysical Research* **92**, 853-874.
- Kogiso, T., Hirschmann, M.M. & Frost, D.J. (2003). High-pressure partial melting of garnet pyroxenite: possible mafic lithologies in the source of ocean island basalts. *Earth and Planetary Science Letters* **216**, 603-617.
- Kogiso, T., Hirschmann, M. M., & Reiners, P.W. (2004) Length scales of mantle heterogeneities and their relationship to ocean island basalt geochemistry. *Geochimica et Cosmochimica Acta* **68**(2), 345-360.
- Ku, T.-L., Knauss, K.G. & Mathieu, G.G. (1977) Uranium in open ocean: Concentration and isotopic composition. *Deep Sea Research* **24**, 1005-1017.
- La Tourette, T. Z., Kennedy, A.K. & Wasserburg, G.J. (1993) Thorium-uranium fractionation by garnet: Evidence for a deep source and rapid rise of oceanic basalts. *Science* **261**, 739-742.
- Laj, C., Kissel, C., Mazaud, A., Channel, J.E.T. & Beer, J. (2000) North Atlantic palaeointensity stack since 75 ka (NAPIS-75) and the duration of the Laschamp

- event. *Philosophical Transactions of the Royal Society of London, Series A*, **358**(1768), 1009-1025.
- Landwehr, D., Blundy, J., Chamorro-Perez, E.M., Hill, E. & Wood, B. (2001) U-series disequilibria generated by partial melting of spinel lherzolite. *Earth and Planetary Science Letters* **188**, 329-348.
- Langmuir, C. H., Bender, J.F. & Batiza, R. (1986) Petrological and tectonic segmentation of the East Pacific Rise, 5°30'-14°30'N. *Nature* **322**, 422-429.
- LaTourette, T.Z., Kennedy, A.K. & Wasserburg, G.J. (1993) Uranium-thorium fractionation of garnet -evidence for a deep source and rapid rise of oceanic basalts. *Science* **261**, 739-742.
- Lundstrom, C.C. (2000) Models of U-series disequilibria generation in MORB: the effects of two scales of melt porosity. *Physics of the Earth and Planetary Interiors* **121**, 189-204.
- Lundstrom, C.C., Gill, J., Williams, Q. & Perfit, M.R. (1995) Mantle melting and basalt extraction by equilibrium porous flow. *Science*, **270**(5244), 1958-1961.
- Lundstrom, C.C., Williams, Q. & Gill, J.B. (1998) Investigating solid mantle upwelling rates beneath mid-ocean ridges using U-series disequilibria, 1: a global approach. *Earth and Planetary Science Letters*, **157**, 151-165.
- Lundstrom, C.C., Sampson, D.E., Perfit, M.R., Gill, J. & Williams, Q. (1999) Insights into mid-ocean ridge basalt petrogenesis: U-series disequilibria from the Siqueiros Transform, Lamont Seamounts, and East Pacific Rise. *Journal of Geophysical Research* **104**(B6), 13,035-13,048.
- Macdonald K. C., Sempere, J.-C. & Fox, P.J. (1984) East Pacific Rise from Siqueros to Orozco fracture zones: Along-strike continuity of axial neovolcanic zone and structure and evolution of overlapping spreading centers. *Journal of Geophysical Research* **89**, 6049-6069.
- Macdonald, K. C., Fox, P.J., Alexander, R.T., *et al.* (1996) Volcanic growth faults and the origin of Pacific abyssal hills. *Nature* **380**, 125-129.
- Mahoney, J. J., Sinton, J.M., Kurz, M.D., Macdougall, J.D., Spencer, K.J. & Lugmair, G.W. (1994) Isotope and trace element characteristics of a super-fast spreading ridge: East Pacific rise, 13-23°S. *Earth and Planetary Science Letters* **121**, 173-193.
- McDonough, W.F. & Sun, S.S. (1995) The composition of the Earth. *Chemical Geology*, **120**, 223-253.
- Nauret, F., Abouchami, W., Galer, S.J.G., Hofmann, A.W., Hémond, C., Chauvel, C. & Dymont, J. (2006). Correlated trace element-Pb isotope enrichments in Indian MORB along 18-20°S, Central Indian Ridge. *Earth and Planetary Science Letters* **245**, 137-152.
- Niu, Y.L. & Batiza, R. (1997) Trace element evidence from seamounts for recycled oceanic crust in the eastern Pacific mantle. *Earth and Planetary Science Letters*, **148**, 471-483.
- Niu, Y., Collerson, K.D., Batiza, R., Wendt, J.I. & Regelous, M. (1999) Origin of enriched-type mid-ocean ridge basalt at ridges far from mantle plumes: The East Pacific Rise at 11°20'N. *Journal of Geophysical Research* **104**(B4), 7067-7087.

- Niu, Y.L., Regelous, M., Wendt, I.J., Batiza, R. & O'Hara, M.J. (2002) Geochemistry of near-EPR seamounts: importance of source vs. process and the origin of enriched mantle component. *Earth and Planetary Science Letters*, **199**, 327-345.
- Niu, Y. & O'Hara, M.J. (2008) Global correlations of ocean ridge basalt chemistry with axial depth: a new perspective. *Journal of Petrology* **49**(4), 633-664.
- Perfit, M., Fornari, D., Smith, M., Bender, J., Langmuir, C. & Haymon, R. (1994) Small-scale spatial and temporal variations in MORB geochemistry and implications for ridge crest magmatic processes. *Geology* **22**, 375-379.
- Perfit, M.R., Fornari, D.J., Ridley, W.I., Kirk, P.D., Casey, J., Kastens, K.A., Reynolds, J.R., Edwards, M., Desonie, D., Shuster, R. & Paradis, S. (1996) Recent volcanism in the Siqueiros transform fault: picritic basalts and implications for MORB magma genesis. *Earth and Planetary Science Letters* **141**, 91-108.
- Perfit M.R. & Chadwick, W.W. Jr. (1998) Magmatism at mid-ocean ridges: Constraints from volcanological and geochemical investigations. *Faulting and Magmatism at Mid-Ocean Ridges*. In: (eds. W.R. Buck, P. Delaney, J.A., Karson, and Y. Lababrille). American Geophysical Union, Washington, DC, pp. 41-70.
- Pertermann, M. & Hirschmann, M.M. (2003) Partial melting experiments on a MORB-like pyroxenite between 2 and 3 GPa: Constraints on the presence of pyroxenite in basalt source regions from solidus location and melting rate. *Journal of Geophysical Research* **108**(B2), 10.1029/2000JB000118.
- Pertermann, M., Hirschmann, M.M., Hametner, K., Gunther, K. & Schmidt, M.W. (2004) Experimental determination of trace element partitioning between garnet and silica-rich liquid during anhydrous partial melting of MORB-like eclogite. *Geochemistry, Geophysics, Geosystems*, **5**(5), (2003GC000638).
- Prinzhofer, A., Lewin, E. & Allegre, C.J. (1989) Stochastic melting of the marble cake mantle--evidence from local study of the East Pacific Rise at 12°50'N. *Earth and Planetary Science Letters*, **92**(2), 189-206.
- Reynolds, J.R., Segment-scale systematic of mid-ocean ridge magmatism and geochemistry, Ph.D. thesis, 483 pp., Columbia Univ., Palisades, N.Y., 1995.
- Reynolds, J. R. & Langmuir, C.H. (2000) Identification and implications of off-axis lava flows around the East Pacific Rise. *Geochemistry, Geophysics, Geosystems* **1**(1999GC000033).
- Reynolds, J. R., Langmuir, C.H., Bender, J.F., Kastens K.A. & Ryan, W.B.F. (1992) Spatial and temporal variability in the geochemistry of basalts from the East Pacific Rise. *Nature* **359**, 493-499.
- Richter, S. & Goldberg, S.A. (2003) Improved techniques for high accuracy isotope ratio measurements of nuclear materials using thermal ionization mass spectrometry. *International Journal of Mass Spectrometry* **229**, 181-197.
- Robinson, L.F., Belshaw, N.S. & Henderson, G.M. (2004) U and Th concentrations and isotope ratios in modern carbonates and waters from the Bahamas. *Geochimica et Cosmochimica Acta*, **68**(8), 1777-1789.
- Rubin K., MacDougall, J.D. & Perfit, M.R. (1994) ²¹⁰Po-²¹⁰Pb dating of recent volcanic eruptions on the sea floor. *Nature* **368**, 841-844.

- Rubin, K., van der Zander, I., Smith, M.C. & Bergmanis, E.C. (2005) Minimum speed limit for ocean ridge magmatism from ^{210}Pb - ^{226}Ra - ^{230}Th disequilibria. *Nature* **437**, 534-538.
- Salters, V. J. M. & Longhi, J.E. (1999) Trace element partitioning during the initial stages of melting beneath ocean ridges. *Earth and Planetary Science Letters* **166**, 15-30.
- Salters, V. J. M., Longhi, J.E. & Bizimis, M. (2002) Near mantle solidus trace element partitioning at pressures up to 3.4 GPa. *Geochemistry, Geophysics, Geosystems* **3**(7), (2001GC000148).
- Scheirer, D. S. & Macdonald, K.C. (1993) Variation in cross-sectional area of the axial ridge along the East Pacific Rise: Evidence for the magmatic budget of a fast spreading center. *Journal of Geophysical Research* **98**, 22321-22338.
- Schouten, H., Tivey, M., Fornari, D.J., Seyfried, W. & Shipboard Science and Technical Teams. (2004) Central Anomaly Magnetic High and Volcanic Processes on Fast-spreading Mid-Ocean Ridges. *Cruise Report R/V Atlantis Voyage 11 Leg 7, 1/26-2/24/2004*.
- Schouten, H., Tivey, M.A., Fornari, D.J. & Cochran, J.R. (1999) Central anomaly magnetization high: constraints on the volcanic construction and architecture of seismic layer 2A at a fast-spreading Mid-Ocean Ridge, the EPR at 9°30'-50'N. *Earth and Planetary Science Letters* **169**, 37-50.
- Sims, K.W.W., Jull, M. & Kelemen, P. (1999). U-series disequilibria and melt transport in the mantle beneath mid-ocean ridges. Presented at American Geophysical Union Meeting, San Francisco CA. Abstract in E.O.S. (Trans. Amer. Geophys. Union), V22D.
- Sims, K. W. W., DePaolo, D.J., Murrell, M.T., Baldrige, W.S., Goldstein, S.J. & Clague, D. (1995) Mechanisms of magma generation beneath Hawaii and mid-ocean ridges: Uranium/Thorium and Samarium/Neodymium isotopic evidence. *Science* **267**(5197), 508-512.
- Sims, K. W. W. & DePaolo, D. J. (1997) Inferences about mantle magma sources from incompatible element concentration ratios in oceanic basalts. *Geochimica et Cosmochimica Acta* **61**(4), 765-784.
- Sims, K. W. W., Goldstein, S.J., Blichert-Toft, J., Perfit, M.R., Kelemen, P., Fornari, D.J., Michael, P., Murrell, M.T., Hart, S.R., DePaolo, D.J., Layne, G. & Jull, M. (2002) Chemical and isotopic constraints on the generation and transport of melt beneath the East Pacific Rise. *Geochimica et Cosmochimica Acta* **66**, 3481-3504.
- Sims, K. W. W., Blichert-Toft, J., Fornari, D.J., Perfit, M.R., Goldstein, S.J., Johnson, P., DePaolo, D.J., Hart, S.R., Murrell, M.T., Michael, P.J., Layne, G.D. & Ball, L. (2003) Aberrant youth: Chemical and isotopic constraints on the origin of off-axis lavas from the East Pacific Rise, 9°-10°N. *Geochemistry, Geophysics, Geosystems* **4**(10), (2002GC000443).
- Sims, K.W.W. & Hart, S.R. (2006) Comparison of Th, Sr, Nd, and Pb isotopes in oceanic basalts: Implications for mantle heterogeneity and magma genesis. *Earth and Planetary Science Letters* **245**, 743-761.

- Sims, K.W.W., Hart, S.R., Reagan, M.K., Blusztajn, J., Staudigel, H., Sohn, R.A., Layne, G.D., Ball, L.A. & Andrews, J. (2008a). ^{238}U - ^{230}Th - ^{226}Ra - ^{210}Pb - ^{210}Po , ^{232}Th - ^{228}Ra , and ^{235}U - ^{231}Pa constraints on the ages and petrogenesis of Vailulu'u and Malumalu Lavas, Samoa. *Geochemistry, Geophysics, Geosystems* **9**(4), (2007GC001651).
- Sims, K.W.W., Gill, J.B., Dosseto, A., Hoffmann, D.L., Lundstrom, C.C., Williams, R.W., Ball, L., Tollstrup, D., Turner, S., Prytulak, J., Glessner, J.J.G., Standish, J.J. & Elliot, T. (2008b). An inter-laboratory assessment of the thorium isotopic composition of synthetic and rock reference materials. *Geostandards and Geoanalytical Research* **32**, 65-91.
- Smith, M. C., Perfit, M.R., Fornari, D.J., Ridley, W.I., Edwards, M.H., Jurras, G.J. & Von Damm, K.L. (2001) Magmatic processes and segmentation at a fast spreading mid-ocean ridge; detailed investigation of an axial discontinuity on the East Pacific Rise crest at 9°37'N. *Geochemistry, Geophysics, Geosystems* **2**(2000GC000134).
- Soule, S. A., Fornari, D.J., Perfit, M.R., Tivey, M.A., Ridley, W.I. & Schouten, H. (2005) Channelized lava flows at the East Pacific Rise crest 9°-10°N: The importance of off-axis lava transport in developing the architecture of young oceanic crust. *Geochemistry, Geophysics, Geosystems* **6**(8), (2005GC000912)
- Soule, S. A., Fornari, D.J., Perfit, M.R. & Rubin, K.H. (2007) New insights into mid-ocean ridge volcanic processes from the 2005-2006 eruption of the East Pacific Rise, 9°46'N-9°56'N. *Geology* **35**(12), 1079-1082.
- Soule, S.A., Escartin, J.E. & Fornari, D.J. (2009) A record of eruption and intrusion at a fast-spreading ridge axis: the axial summit trough of the East Pacific Rise, *Geochemistry, Geophysics, Geosystems* **10**, Q10T07, (2008GC002354).
- Stracke, A. & Bourdon, B. (2009) The importance of melt extraction for tracing mantle heterogeneity. *Geochimica et Cosmochimica Acta* **73**, 218-238.
- Tatsumoto, M. (1966) Genetic relations of oceanic basalts as indicated by lead isotopes. *Science* **153**, 1094-1101.
- Thurber, D. (1962) Anomalous $^{234}\text{U}/^{238}\text{U}$ in nature. *J. Geophys. Res.* **67**, 4518.
- Todt, W., Cliff, R.A., Hanser, A. & Hofmann, A.W. (1996) Evaluation of a 202Pb-205Pb double spike for high-precision lead isotope analysis. In *Earth Processes Reading the Isotopic Code*, Vol. 95 (ed. S.R. Hart & A. Basu), pp. 429-437. AGU.
- Tolstoy, M., Cohen, J.P., Baker, E.T., Fornari, D.J., Rubin, K.H., Shank, T.M., Waldhauser, F., Bohnenstiehl, D.R., Forsyth, D.W., Holmes, R.C., Love, B., Perfit, M.R., Weekly, R.T., Soule, S.A. & Glazer, B. (2006) A seafloor spreading event captured by seismometers. *Science Express* 10.1126/science.1133950.
- Vera, E. E. & Diebold, J.B. (1994) Seismic imaging of oceanic layer 2A between 9°30 and 10°N on the East Pacific Rise from two ship wide-aperture profiles. *Journal of Geophysical Research* **99**, 3031-3041.
- Volpe, A. M. & Goldstein, S.J. (1990) Dating young MORB: ^{226}Ra - ^{230}Th isotopic disequilibria measured by mass spectrometer. *Eos Trans. AGU* **71**, 1702.
- Volpe A. M. & Goldstein, S.J. (1993) ^{226}Ra - ^{230}Th disequilibrium in axial and off-axis mid-ocean ridge basalts. *Geochimica et Cosmochimica Acta* **57**, 1233-1242.

- White W. M. & Schilling, J.-G. (1978) The nature and origin of geochemical variation in Mid-Atlantic Ridge basalts from the Central North Atlantic. *Geochimica et Cosmochimica Acta* **42**, 1501-1516.
- Workman R. K. & Hart, S.R. (2005) Major and trace element composition of the depleted MORB mantle (DMM). *Earth and Planetary Science Letters* **231**, 53-72.
- Yaxley, G.M. & Green, D.H. (1998) Reactions between eclogite and peridotite: Mantle refertilisation by subduction of oceanic crust. *Schweizerische Mineralogische und Petrographische Mitteilungen* **78**(2), 243-255.
- Zindler, A. & Hart, S.R. (1986) Chemical Geodynamics. *Annual Reviews of Earth and Planetary Science* **14**, 493-571.
- Zindler, A., Staudigel, H. & Batiza, R. (1984) Isotope and trace element geochemistry of young Pacific seamounts: implications for the scale of upper mantle heterogeneity. *Earth and Planetary Science Letters* **70**(2), 175-195.

Table 1. Sample Descriptions and Locations of 9°30'N and 9°50'N EPR Off-Axis Samples. Enriched MORB (E-MORB) are designated by **bold** sample numbers. Locations are shown in Figure 1.

Sample	Long. West (Degree, Decimal Minutes)	Lat. North (Degree, Decimal Minutes)	Time of Collection	Depth (m)	Distance from the AST (km)	Description
<u>9°50'N</u>						
2697-1	104°19.779'	9°53.2'	10:28	2774	3.52	Pillow from middle of outward dipping fault west of AST. 30% plag/olivine phenocrysts in variolitic, glassy groundmass.
2697-9	104°18.826'	9°52.8'	13:09	2695	1.90	Truncated pillow from the top of an outward dipping fault from trough west of axis
<u>9°30'N</u>						
2489-3	104°13.548'	9°31.8'	11:23	2664	2.24	Well formed pillows from small pillow mound
2489-4a	104°13.320'	9°31.7'	11:47	2689	2.64	Pillow bud from west facing pillow ridge next to east-facing scarp. <5% plag + cpx + olivine microphenocrysts in glassy microlitic
2489-5	104°13.050'	9°31.7'	12:18	2722	3.12	Pillow fragment from heavily sedimented depression. Few plag + cpx microphenocrysts in glassy groundmass
2489-12	104°12.438'	9°31.6'	14:40	2692	4.20	Round pillow bud
2700-7	104°12.870'	9°30.7'	14:28	2711	3.15	Lobate flow from top of outward dipping fault bounding a graben
2701-1	104°12.260'	9°35.1'	10:15	2806	5.00	Elongate old pillow from middle of outward dipping fault to east of
2701-11a	104°13.080'	9°35.3'	13:16	2840	3.64	Pillow in off-axis graben
2702-1	104°13.296'	9°34.8'	10:20	2706	3.08	Pillow in graben or on outward dipping fault east of axis at 9°35' south of dive 2701
2703-1	104°12.811'	9°33.3'	10:13	2812	3.88	Pillow in graben to south and west
2703-2	104°13.115'	9°33.3'	10:54	2725	3.33	Bulbous pillow from middle of outward dipping fault
2703-3	104°13.277'	9°33.2'	11:12	2687	3.00	Bulbous decorated pillow on top of outward dipping fault
2706-1	104°13.141'	9°32.8'	2:09	2676	3.15	Pillow at base of outward dipping fault between trough and ridge at
2706-5	104°13.801'	9°32.5'	5:31	2592	1.90	Pillow from the base of an inward dipping fault covered with talus. Dark, aphyric groundmass with subaligned microlites and many
2706-7	104°13.871'	9°32.6'	12:28	2623	1.80	Hackly sheet flow in local graben at summit of outward dipping

Table 2. Major Element Compositions (weight percent oxide) of 9°30'N and 9°50'N EPR Off-Axis Samples.

Sample	SiO ₂	TiO ₂	Al ₂ O ₃	FeO	MnO	MgO	CaO	Na ₂ O	K ₂ O	P ₂ O ₅	Total	(K ₂ O/TiO ₂) x100	Mg#
<u>9°50'N EPR</u>													
2697-1	49.0	1.23	15.4	9.36	0.14	8.30	12.6	2.51	0.16	0.15	98.92	13.0	0.61
2697-9	50.1	1.34	14.7	9.85	0.15	8.06	12.5	2.61	0.08	0.11	99.39	6.0	0.59
<u>9°30'N EPR</u>													
2489-3	51.0	1.83	14.5	10.71	0.20	6.69	11.0	3.26	0.41	0.28	99.87	22.4	0.53
2489-4A	51.0	1.80	14.4	10.88	0.19	6.65	11.0	3.25	0.42	0.26	99.86	23.1	0.52
2489-5	51.0	1.79	14.4	10.76	0.21	6.65	11.1	3.19	0.44	0.31	99.85	24.4	0.52
2489-12	50.3	2.00	14.1	11.56	0.22	6.80	11.3	3.14	0.20	0.22	99.84	9.8	0.51
2700-7	49.8	1.65	14.8	10.25	0.23	7.29	11.6	2.94	0.31	0.19	98.97	18.8	0.56
2701-1	49.4	1.64	15.6	9.88	0.17	7.83	11.7	2.85	0.27	0.19	99.55	16.5	0.59
2701-11a	49.7	1.74	14.5	10.52	0.18	6.92	11.5	3.01	0.33	0.22	98.65	19.0	0.54
2702-1	49.7	1.65	14.7	10.25	0.16	7.33	11.7	2.94	0.28	0.19	98.85	17.0	0.56
2703-1	49.1	2.03	15.3	10.59	0.20	7.01	10.8	3.20	0.51	0.33	99.00	25.1	0.54
2703-2	50.2	1.87	13.9	11.52	0.25	6.99	11.4	2.88	0.15	0.17	99.29	8.0	0.52
2703-3	50.1	1.75	14.4	10.78	0.21	7.46	11.7	2.94	0.14	0.17	99.59	8.0	0.55
2706-1	50.7	1.77	14.1	10.90	0.22	7.19	11.5	2.87	0.13	0.15	99.52	7.3	0.54
2706-5	50.4	2.01	13.9	11.53	0.17	6.86	11.1	2.93	0.14	0.17	99.14	7.0	0.51
2706-7	50.5	1.27	15.2	9.20	0.19	8.46	12.1	2.58	0.07	0.11	99.74	5.5	0.62

Major elements were analyzed on polished glass chips at the USGS Microbeam Laboratory in Denver, Co. using a JEOL 8900 Electron Microprobe. Analysis of seven to ten separate points (including spots on separate chips of the same sample) were averaged for each sample and then normalized and corrected for instrument drift based on the established values for in-house standards JdF-D2 (Reynolds et al., 1995) and ALV2392-9 (see Smith et al., 2001). The 2σ errors calculated from variation in the analyses of ALV2392-9 during these analytical runs are as follows: SiO₂ (0.29 wt.% or 0.57 relative %), TiO₂ (0.07 wt.% or 5.4%), Al₂O₃ (0.17 wt.% or 1.1%), FeO (0.17 wt.% or 1.8%), MnO (0.05 wt.% or 26.8%), MgO (0.11 wt.% or 1.3%), CaO (0.14 wt.% or 1.2%), Na₂O (0.09 wt.% or 3.6%), K₂O (0.02 wt.% or 18.8%), and P₂O₅ (0.04 wt.% or 29.8%).

Table 3. Trace-Element Compositions of 9°30'N and 9°50'N EPR Off-Axis Samples

Sample	Rb	Ba	Th	U	Nb	Ta	Pb	Sr	Zr	Hf	Y	La	Ce	Pr	Nd	Sm	Eu	Dy	Ho	Yb	Lu
<u>9°50'N EPR</u>																					
2697-1	1.9	22.20	0.2	0.09	3.55	0.23	0.36	119.5	77.8	1.96	23.01	3.60	10.40	1.66	8.11	2.6	0.99	3.88	0.83	2.3	0.35
2697-9	0.7	6.46	0.1	0.05	1.57	0.12	0.35	106.7	85.8	2.20	29.40	2.88	9.52	1.66	8.68	3.0	1.12	4.79	1.05	2.9	0.44
<u>9°30'N EPR</u>																					
2489-3	5.8	68.47	0.7	0.24	9.52	0.59	0.96	155.5	150.3	3.79	39.50	8.19	21.23	3.17	15.98	4.7	1.57	6.44	1.42	4.0	0.59
2489-4A	6.1	70.99	0.7	0.24	9.99	0.61	0.90	162.9	159.8	3.91	42.29	8.51	22.01	3.30	16.41	4.9	1.64	6.71	1.47	4.1	0.61
2489-5	5.8	67.63	0.7	0.23	9.54	0.58	0.85	155.8	150.1	3.72	39.71	8.18	21.07	3.10	15.69	4.7	1.58	6.37	1.42	3.9	0.58
2489-12	2.2	22.94	0.3	0.12	4.78	0.32	0.60	134.9	142.7	3.60	43.64	5.99	17.69	2.82	15.05	4.7	1.61	6.95	1.57	4.3	0.63
2700-7	4.3	53.84	0.5	0.17	7.20	0.45	0.68	142.4	126.9	3.21	35.15	6.63	17.52	2.67	13.57	4.2	1.42	5.78	1.28	3.5	0.53
2701-1																					
2701-11a	4.3	53.72	0.5	0.17	7.31	0.45	0.70	146.4	128.0	3.16	35.92	6.59	17.38	2.64	13.51	4.1	1.42	5.71	1.27	3.5	0.52
2702-1	3.7	46.51	0.4	0.15	6.19	0.39	0.64	141.8	120.1	3.00	34.48	5.90	15.94	2.49	12.74	3.9	1.36	5.57	1.23	3.4	0.50
2703-1	7.8	103.02	1.0	0.32	14.84	0.88	1.05	260.2	154.0	3.70	35.74	11.23	26.64	3.71	17.88	4.9	1.64	5.89	1.28	3.5	0.51
2703-2	1.1	10.18	0.2	0.07	2.62	0.20	0.60	116.3	116.8	3.05	38.63	4.25	13.36	2.27	12.13	4.1	1.42	6.21	1.40	3.9	0.58
2703-3	1.2	11.57	0.2	0.07	2.56	0.19	0.62	116.1	112.9	2.91	36.46	4.05	12.77	2.17	11.58	3.9	1.34	5.88	1.31	3.7	0.54
2706-1	1.0	9.68	0.2	0.07	2.50	0.18	0.60	120.0	113.2	2.90	37.10	4.03	12.85	2.17	11.52	3.8	1.36	5.87	1.32	3.7	0.55
2706-5	1.3	11.63	0.2	0.09	3.25	0.23	0.71	110.4	140.8	3.67	46.85	4.91	15.41	2.60	14.20	4.8	1.58	7.28	1.66	4.7	0.68
2706-7	0.6	5.18	0.1	0.04	1.24	0.11	0.71	110.9	83.8	2.18	28.63	2.78	9.37	1.66	8.66	3.0	1.12	4.71	1.02	2.9	0.43

Samples were analyzed for trace elements at the University of Florida using an Element II Inductively Coupled Plasma Mass Spectrometer (ICP-MS). The analyses were performed in medium resolution with Re and Rh used as internal standards to correct for instrumental drift and matrix effects. Concentrations were calculated by external calibration using a combination of USGS (BHVO-1) and in-house (ENDV, an Endeavor Ridge MORB standard from the Geological Survey of Canada, Ottawa) rock standards. Repeated chemical analyses of a second in-house MORB standard (ALV2392-9) during each run were used to assess instrumental drift as well as evaluate accuracy and precision of the measurements. Precision (2σ) was found to be better than $\pm 5\%$ for the REE, Ba, Hf, Nb, Rb, Sr, Th, Y, Zr, and better than $\pm 9\%$ for Pb, Ta, and U.

Table 4. Sr, Nd, Hf, and Pb Isotopic Compositions of 9°30'N and 9°50'N Off-Axis Samples

Sample	$^{87}\text{Sr}/^{86}\text{Sr}$	$^{143}\text{Nd}/^{144}\text{Nd}$	ϵ_{Nd}	$^{176}\text{Hf}/^{177}\text{Hf}$	ϵ_{Hf}	$^{208}\text{Pb}/^{204}\text{Pb}$	$^{207}\text{Pb}/^{204}\text{Pb}$	$^{206}\text{Pb}/^{204}\text{Pb}$	$^{208}\text{Pb}/^{206}\text{Pb}$
<u>9°50'N EPR</u>									
2697-1	0.702575	0.513151	10.0	0.283185	14.6	37.6898	15.4722	18.3378	2.0553
2697-9	0.702478	0.513160	10.2	0.283190	14.8	37.6394	15.4685	18.2301	2.0647
<u>9°30'N EPR</u>									
2489-3	0.702625	0.513086	8.7	0.283129	12.6	37.5729	15.4892	18.1786	2.0669
2489-4A	0.702860	0.513074	8.5	0.283130	12.7	37.5722	15.4890	18.1782	2.0669
2489-5	0.702760	0.513083	8.7	0.283129	12.6	37.5879	15.4904	18.1789	2.0677
2489-12	0.702498	0.513137	9.7	0.283174	14.2	37.6466	15.4696	18.2442	2.0635
2700-7	0.702478	0.513089	8.8	0.283122	12.4	37.5877	15.4853	18.1897	2.0664
2701-1	0.702678	0.513092	8.9	0.283127	12.6	37.8961	15.5061	18.4589	2.0530
2701-11a	0.702812	0.513090	8.8	0.283127	12.6	37.5754	15.4816	18.1860	2.0662
2702-1	0.702615	0.513104	9.1	0.283129	12.6	37.6047	15.4849	18.2006	2.0661
2703-1	0.702769	0.513043	7.9	0.283074	10.7	37.9965	15.5236	18.5743	2.0456
2703-2	0.702504	0.513153	10.0	0.283156	13.6	37.6656	15.4674	18.2547	2.0633
2703-3	0.702487	0.513152	10.0	0.283156	13.6	37.6651	15.4698	18.2456	2.0643
2706-1	0.702617	0.513144	9.9	0.283160	13.7	37.6820	15.4715	18.2600	2.0636
2706-5	0.702609	0.513155	10.1	0.283158	13.7	37.6514	15.4688	18.2422	2.0640
2706-7	0.702503	0.513157	10.1	0.283164	13.9	37.6781	15.4699	18.2408	2.0656
2706-7 (Replicate)				0.283169	14.0				

Analytical Notes:

(1) All Sr, Nd, and Pb isotopic analyses were conducted at WHOI using a ThermoFinnigan Neptune MC-ICP-MS. Sr and Nd analyses have internal precision of 5-10 ppm. After adjusting to 0.71024 (NBS SRM 987) and 0.511847 (La Jolla Nd Standard), for Sr and Nd, respectively, external precision is estimated at 15-30 ppm (2σ). ϵ_{Nd} values were calculated using $(^{143}Nd/^{144}Nd)_{CHUR(0)} = 0.512638$. Measurements of $^{208}Pb/^{204}Pb$, $^{207}Pb/^{204}Pb$, and $^{206}Pb/^{204}Pb$ have estimated internal precisions of 15-30 ppm and external precisions of 150-200 ppm (2σ). SRM 997 Tl was used as an internal standard, and measurements were then normalized to NBS 981 using the values of Todt et al. (1996). Further details can be found in Hart et al. (2004) and Hart and Blusztajn (2006). All Hf isotopic analyses were conducted at ENS Lyon by MC-ICP-MS using the VG Plasma 54 (Blichert-Toft et al., 1997). Measured isotope ratios were normalized for mass fractionation to $^{179}Hf/^{177}Hf = 0.7325$ using an exponential law. External analytical uncertainties of $<\pm 30$ ppm for Hf isotopic measurements were estimated from repeated runs of the JMC-475 Hf standard, which gave 0.282160 ± 0.000010 during the course of this study. In-run analytical errors were half that (i.e., $<\pm 0.000005$). ϵ_{Hf} values were calculated using $(^{179}Hf/^{177}Hf)_{CHUR(0)} = 0.282772$ (Blichert-Toft and Albarède, 1997).

(2) Nd isotopic compositions for axial and 9°50'N off-axis lavas, as well as Siqueiros lavas reported in Sims et al. (2002; 2003) were measured at UC Berkeley. However, in 1994-1995, a drift in the Nd isotopic measurements by the VG Sector 54 multicollector mass spectrometer began occurring. This drift became apparent around 2003, and measurements made during that time span, including the Sims et al. (2002; 2003) data, were affected. We have applied the necessary corrections to these measurements, and the corrected values are reported in Appendix Table A2. Details of this shift are documented in Bryce et al. (2005). As previously noted, Nd isotopic measurements for this study were conducted solely at WHOI and are unaffected by this drift.

Table 5. ($^{230}\text{Th}/^{232}\text{Th}$), ($^{230}\text{Th}/^{238}\text{U}$), ($^{226}\text{Ra}/^{230}\text{Th}$), ($^{234}\text{U}/^{238}\text{U}$), and U, Th, and ^{226}Ra concentrations of 9°30'N and 9°50'N EPR Off-Axis Samples

Sample	[Th] (ppm) ^b	[U] (ppm) ^b	Th/U	($^{238}\text{U}/^{232}\text{Th}$) ^c	($^{230}\text{Th}/^{232}\text{Th}$) ^{d,e}	($^{230}\text{Th}/^{238}\text{U}$) ^d	[Ra] (fg/g) ^c	($^{226}\text{Ra}/^{230}\text{Th}$) ^e	($^{234}\text{U}/^{238}\text{U}$) ^f
<u>9°50'N EPR</u>									
2697-1 (1)	0.239	0.081	2.935	1.033			54.8	1.65	1.000
2697-1 (2)^a	0.235	0.082	2.855	1.062	1.200	1.129	50.5	1.62	1.003
<i>2697-1 (avg.)</i>	<i>0.237</i>	<i>0.082</i>	<i>2.895</i>	<i>1.048</i>	<i>1.200</i>	<i>1.129</i>	<i>52.6</i>	<i>1.63</i>	<i>1.001</i>
2697-9	0.100	0.043	2.329	1.303	1.386	1.064	21.1	1.37	1.003
<u>9°30'N EPR</u>									
2489-3 (1)	0.661	0.221	2.998	1.012			80.0	0.97	1.002
2489-3 (2)^a	0.656	0.222	2.958	1.025	1.130	1.102	81.2	0.98	1.003
<i>2489-3 (avg.)</i>	<i>0.659</i>	<i>0.222</i>	<i>2.978</i>	<i>1.019</i>	<i>1.130</i>	<i>1.102</i>	<i>80.6</i>	<i>0.98</i>	<i>1.002</i>
2489-4A (1)	0.662	0.224	2.960	1.025			81.0	0.99	1.002
2489-4A (2)^a	0.654	0.227	2.880	1.054	1.128	1.071	84.0	1.02	1.003
<i>2489-4A (avg.)</i>	<i>0.658</i>	<i>0.226</i>	<i>2.920</i>	<i>1.040</i>	<i>1.128</i>	<i>1.071</i>	<i>82.5</i>	<i>1.01</i>	<i>1.002</i>
2489-12	0.290	0.106	2.734	1.110	1.259	1.134			1.003
2700-7	0.487	0.161	3.027	1.002	1.184	1.182	68.2	1.06	1.002
2701-1	0.488	0.165	2.963	1.024	1.101	1.075			1.006
2701-11a	0.488	0.173	2.817	1.077	1.191	1.106	69.4	1.08	1.004
2702-1	0.412	0.139	2.959	1.025	1.229	1.198	59.8	1.06	1.002
2703-2	0.166	0.070	2.365	1.283	1.352	1.054	25.3	1.02	1.003
2703-3	0.171	0.068	2.511	1.208	1.369	1.133	26.8	1.03	1.000
2706-1	0.159	0.066	2.426	1.251	1.377	1.101	24.9	1.02	1.006
2706-5	0.197	0.081	2.442	1.242	1.367	1.100	28.7	0.96	1.003
2706-7	0.085	0.037	2.298	1.320	1.400	1.061	20.1	1.52	1.001

Analytical Notes:

^a Duplicate measurements represent dissolution of separate glass splits; glass samples were leached on the ship in either distilled water or 6N HCl for 15 min, depending on the cruise. In the laboratory the samples were hand-picked under a microscope, then ultrasonically leached in sequential treatments of 0.1N HCl plus 2% H₂O₂ (15 min), DI water (twice, each time for 15 min), 0.1N oxalic acid plus 2% H₂O₂, and DI water (twice, each time for 15 min). Samples were then hand-picked by microscope for a second time and then lightly leached in the clean lab in 0.1N HCl plus 2% H₂O₂ (15 min) using ultra pure reagents. Sample splits (<1-3 g) were then dissolved, aliquoted, spiked and then U, Th, and Ra were separated using chemical techniques outlined in Sims et al. (2008a, b).

^b[U] and [Th] were measured using a ID-ICP-MS using the Thermo Finnigan Element. Measurement errors (2σ) for [U] and [Th] are <2.2% and <1.6%, respectively.

^c() denotes activity $\lambda_{238} = 1.551 \times 10^{-10} \text{ yr}^{-1}$; $\lambda_{232} = 4.948 \times 10^{-11} \text{ yr}^{-1}$; (²³⁸U/²³²Th) errors (2σ) range from 1.9%-4.4% and do not include uncertainties in λ_{238} (0.07%) or λ_{232} (0.5%).

^dTh isotopic compositions measured by Thermo Finnigan Neptune MC-ICP-MS at WHOI (Ball et al., 2008; Sims et al., 2008b); activity ratios calculated using $\lambda_{230} = 9.195 \times 10^{-6} \text{ yr}^{-1}$ and $\lambda_{232} = 4.948 \times 10^{-11} \text{ yr}^{-1}$; errors (2SE) range from 0.16% - 0.54% and do not include uncertainties in λ_{230} (0.4%) or λ_{232} (0.5%).

^e(²²⁶Ra) measured by isotope dilution using the Thermo Finnigan Neptune MC-ICP-MS at WHOI after Sims et al. (2008a); $\lambda_{226} = 4.331 \times 10^{-4} \text{ yr}^{-1}$; measurement errors (2σ) range from 1.9%-3.5% and do not include uncertainties in λ_{226} (0.4%) or λ_{230} . For all samples accuracy is limited by uncertainties (2σ; 1.5%) on the NBS ²²⁶Ra standard used to calibrate the ²²⁸Ra spike.

^f(²³⁴U/²³⁸U) measured by Thermo Finnigan Neptune MC-ICP-MS at WHOI; $\lambda_{234} = 2.823 \times 10^{-6} \text{ yr}^{-1}$, errors (2σ) < 1.0%; for these samples (²³⁴U/²³⁸U) = 1 within error, using an equilibrium (²³⁴U/²³⁸U) of 54.48 ppm for U010 (Richter and Goldberg, 2003). NBS 960 was first bracketed by standard U010 to cross-calibrate U010. U010 was then used as a bracketing standard for all sample measurements to determine mass bias.

Table 6. Spreading Rate Age, U-Th and Th-Ra Age Limits and U-Th and Th-Ra Model Ages^a

Sample	Distance from AST, km	Age Based on Spreading Rate, kyrs	U-Th-Ra Age Constraints, kyrs	U-Th Trend Line Age, kyrs	Th-Ra Trend Line Age, yrs	Emplacement Distance, km	Paleointensity Constraints, kyrs
<u>9°50'N EPR</u>							
2697-1	3.52	64.0	<8	0	2.3 ± 0.6	3.40	
2697-9	1.90	34.5	<8	0	4.4 ± 0.3	1.66	
<u>9°30'N EPR</u>							
2489-3	2.24	40.7	8 to 375	81 ± 26	>8	^b	>20
2489-4A	2.64	48.0	8 to 375	100 ± 27	>8	^b	>20
2489-5	3.12	56.7					>20
2489-12	4.20	76.4	<375	31 ± 11	NM	2.52	~40
2700-7	3.15	57.3	8 to 375	29 ± 25	>8 ^c	1.54	
2701-1	5.00	90.9	<375	85 ± 25	NM	0.34	
2701-11a	3.64	66.2	8 to 375	64 ± 29	>8 ^c	0.10	
2702-1	3.08	56.0	8 to 375	12 ± 26	>8 ^c	2.41	
2703-1	3.88	70.5					
2703-2	3.33	60.5	8 to 375	43 ± 16	>8	0.94	
2703-3	3.00	54.5	8 to 375	1 ± 14	>8	2.56	
2706-1	3.15	57.3	8 to 375	17 ± 15	>8	2.22	
2706-5	1.90	34.5	8 to 375	20 ± 15	>8	0.79	
2706-7	1.80	32.7	<8	0	3.6 ± 0.3	1.60	

^a Samples from 9°50'N are from to the west of the AST. All sample from 9°30'N are from the east of the AST. AST locations were determined by Soule *et al.* (2009). Spreading determined assuming a constant half-spreading rate of 5.5 cm/yr. Age constraints are based upon the presence or absence of (²³⁰Th/²³⁸U) or (²²⁶Ra/²³⁰Th) disequilibria and the half-lives of ²²⁶Ra and ²³⁰Th. To account for variations in (²³⁸U/²³²Th) and (²³⁰Th/²³²Th) when calculating a linear regression to estimate a U-Th zero-age trend line, we include all data for enriched and depleted samples with ²²⁶Ra excesses >1.05 from the Siqueiros Fracture Zone (Lundstrom *et al.*, 1999), the Lamont Seamounts (Lundstrom *et al.*, 1999), and the 9-10°N area (Volpe & Goldstein, 1993; Goldstein *et al.*, 1994, Sims *et al.*, 2002; Sims *et al.*, 2003)—including samples from this study (2697-1, 2697-9, 2706-7) (see “zero-age trend line,” Figure 9A). Hence, samples from this study with ²²⁶Ra excesses are assigned U-Th model ages of zero. U-Th model ages are calculated for any samples with no ²²⁶Ra excesses, even if the sample has (²³⁸U/²³²Th) and (²³⁰Th/²³²Th) disequilibria indistinguishable from zero-age lavas. Because (²³⁰Th/²³²Th) disequilibria decay along vertical trajectories, U-Th trendline model ages are calculated by assuming an initial (²³⁰Th/²³²Th) disequilibrium along the zero-age trend line at the sample (²³⁸U/²³²Th) and by determining the time needed for that initial (²³⁰Th/²³²Th) disequilibrium to decay to the (²³⁰Th/²³²Th) of the sample. Errors are estimated by accounting for model age variations due to +/- 1SD of the zero-age (²³⁰Th/²³²Th) for either N-MORB or E-MORB samples. Thus, E-MORB sample ages will have greater errors due to the fewer number of samples and the wider range of (²³⁰Th/²³²Th) nearer the enriched end member. Th-Ra minimum and maximum ages were calculated using the range of (²²⁶Ra/²³⁰Th) in the zero-age axial samples from 9°17'-10°N (2.01 to 2.89) from Sims *et al.* (2002). For Th-Ra model ages, a zero-age trendline was extrapolated through the axial samples from Sims *et al.* (2002) (Figure 9A). Model ages for N-MORB were calculated assuming vertical decay of (²²⁶Ra/²³⁰Th) from the Th-Ra zero-age trend line at constant ²³⁰Th excess (Sims *et al.*, 2003). As with U-Th ages, errors were calculated from +/- 1SD from the zero-age trendline. Since all E-MORB samples are in equilibrium within analytical uncertainties with respect to (²²⁶Ra/²³⁰Th), no Th-Ra ages were calculated for E-MORB. Paleointensity age constraints are from Bowles *et al.* (2006).

^b Samples 2489-3 and 2489-4a have U-Th trend line ages greater than the spreading age. See text and Figure 10 for details.

^c Samples 2700-7, 2701-11a, and 2702-1 have small ²²⁶Ra excesses of 6-8%, and although these excesses may be significant, we believe that this is unlikely and that these measurements are at the edge of our measurement uncertainties. Thus, for the purposes of age constraints, we assume that these samples are in secular equilibrium (see Analytical Methods section in text for details), and model ages and emplacement distances are calculated based on this assumption.

Figure 1. Sample location maps for 9°-10°N East Pacific Rise (EPR). Upper left inset shows the study area with respect to Mexico and the EPR from 8°N to 19°N. Multibeam bathymetry (Cochran *et al.*, 1999) in the lower left map underlies sample locations for samples collected from 9°29'N to 9°55'N EPR by rock core and *Alvin* (Perfit *et al.*, 1994; Perfit & Chadwick, 1998; Smith *et al.*, 2001; Sims *et al.*, 2002; Sims *et al.*, 2003). The axial high is at ~2100 m depth, with the flanks deepening to ~3000 m depth. The extent of the neo-volcanic zone is delimited by a red line; the axial summit trough (AST) is outlined by a thin black line (Soule *et al.*, 2009). Variations in sample K/Ti ($K_2O/TiO_2 \times 100$) are shown by colored symbols. Blue crosses designate samples analyzed in this study. Focus areas of this study are outlined by black boxes and expanded to the right. The upper and lower right-hand side maps show side scan sonar imaging for the western side of the 9°50'N region and the eastern side of the AST at 9°30'N – 9°35'N, respectively (Fornari *et al.*, 2004). Samples are colored as in the lower left map. Also shown are the AST (white line), neo-volcanic zone (red line) (Soule *et al.*, 2009) and faults (green lines) (Escartin *et al.*, 2007). Notably, all samples from this study were collected from outside of the neo-volcanic zone, and enriched MORB from 9°30'N were recovered from more highly tectonized terrain.

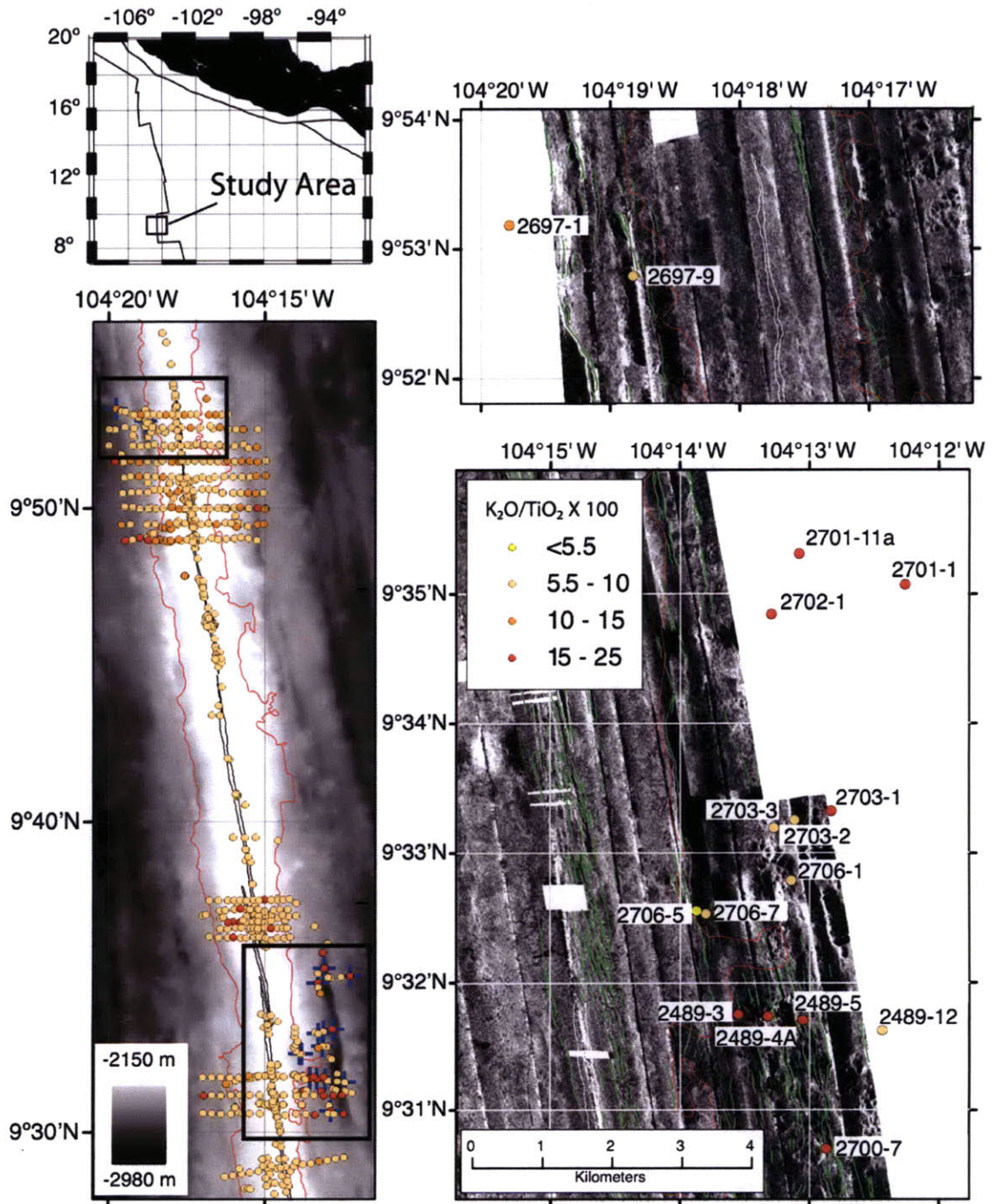
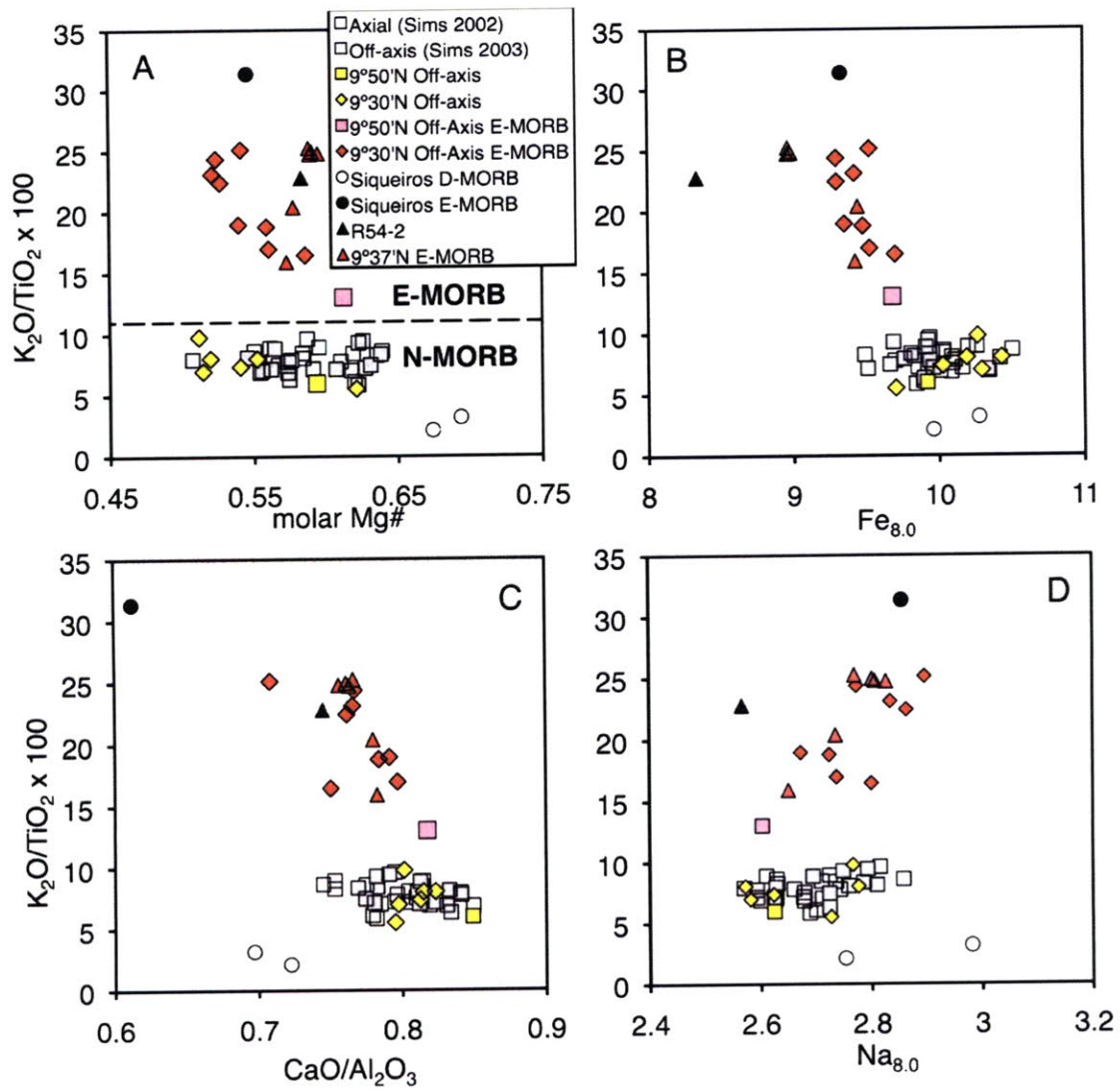


Figure 2. (A) Plot of molar Mg# vs. K/Ti (wt% K₂O/TiO₂ x 100). A horizontal dashed line at K/Ti = 11 separates the fields for N-MORB (<11) and E-MORB (>11) (Smith *et al.*, 2001). Off-axis lava samples from 9°30'N are labeled with black diamonds; off-axis samples for this study from 9°50'N are labeled with black squares. Axial samples from 9°17'N-9°54'N (Sims *et al.*, 2002) are labeled as white squares. Off-axis symbols from 9°50'N (Sims *et al.*, 2003) are labeled by gray squares. An E-MORB from Batiza & Niu (1992) at 9°35'N is marked by a black triangle, and E-MORB from the small OSC at 9°37'N (Smith *et al.*, 2001) are marked by red triangles. Siqueiros data (black and white circles) are from Perfit *et al.* (1996). (B) Plot of Fe_{8,0} vs. K/Ti. Fe_{8,0} is negatively correlated with K/Ti (as is Fe_{7,2}; Niu & O'Hara, 2008), where E-MORB trend to lower Fe_{8,0} and higher K/Ti than N-MORB. Similarly, (C) CaO/Al₂O₃ is negatively correlated with K/Ti. (D) Na_{8,0} is positively correlated with K/Ti. These correlations suggest that E-MORB melts derive from a greater contribution of garnet than N-MORB—more garnet results in higher Al₂O₃ concentration, lower CaO/Al₂O₃ and a more fertile mantle corresponds to more Na-rich clinopyroxene, a higher clinopyroxene/olivine abundance ratio, and lower Fe, Mg, and Mg# (Niu *et al.*, 2008).



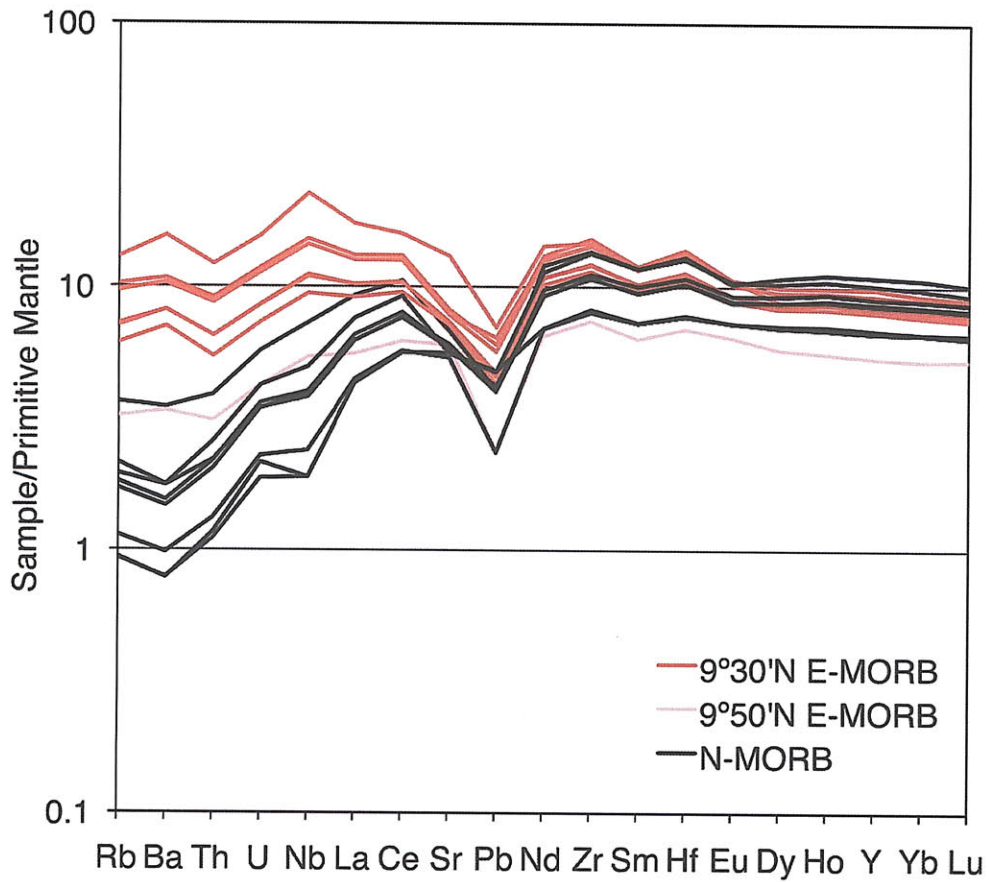


Figure 3. Spidergram of sample incompatible element concentrations normalized to primitive mantle concentrations (McDonough & Sun, 1995). E-MORB from 9°30'N are designated by red patterns, the E-MORB from 9°50'N by a pink pattern, and all N-MORB by black patterns. Note that E-MORB and N-MORB have similar, relatively flat, REE patterns. In contrast, E-MORB exhibit a wider range of highly incompatible elements and consistently have positive Ba anomalies.

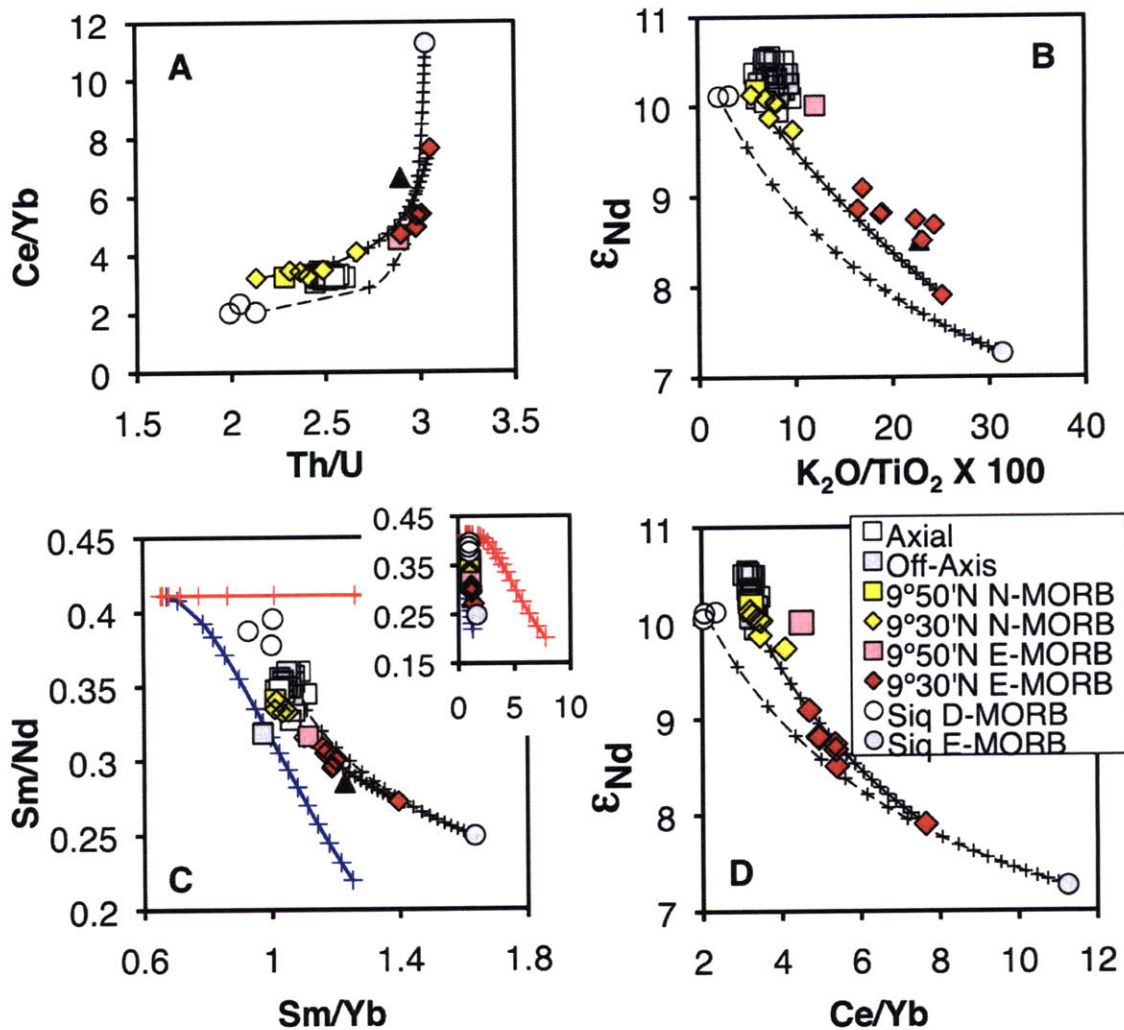


Figure 4. Plots of (A) Th/U vs. Ce/Yb, (B) $K_2O/TiO_2 \times 100$ vs. ϵ_{Nd} , (C) Sm/Nd vs. Sm/Yb, and (D) Ce/Yb vs. ϵ_{Nd} for 9°N EPR lavas. The dashed black line is a mixing trajectory between Siqueiros D-MORB (A2384-6) and E-MORB (A2390-5) end members (Perfit *et al.*, 1996; Lundstrom *et al.*, 1999; Sims *et al.*, 2002). The solid black line is a mixing trajectory between the most depleted (2706-7) and enriched (2301-1) samples from this study. Mixing increments of 5% are designated by black plusses. Also shown in (C) are modal accumulated fractional melting curves of garnet peridotite (red line) and spinel peridotite (blue line). Plusses on the melting trajectories indicate 0.1%, 1-10% in 1% increments, 12.5%, 15%, 17.5%, and 20-100% in 10% increments. See text for details. Inset is the same as (C) but at different Sm/Yb scale to show the large extent of Sm/Yb fractionation by garnet as compared to clinopyroxene. The symbols are the same as in Figure 2.

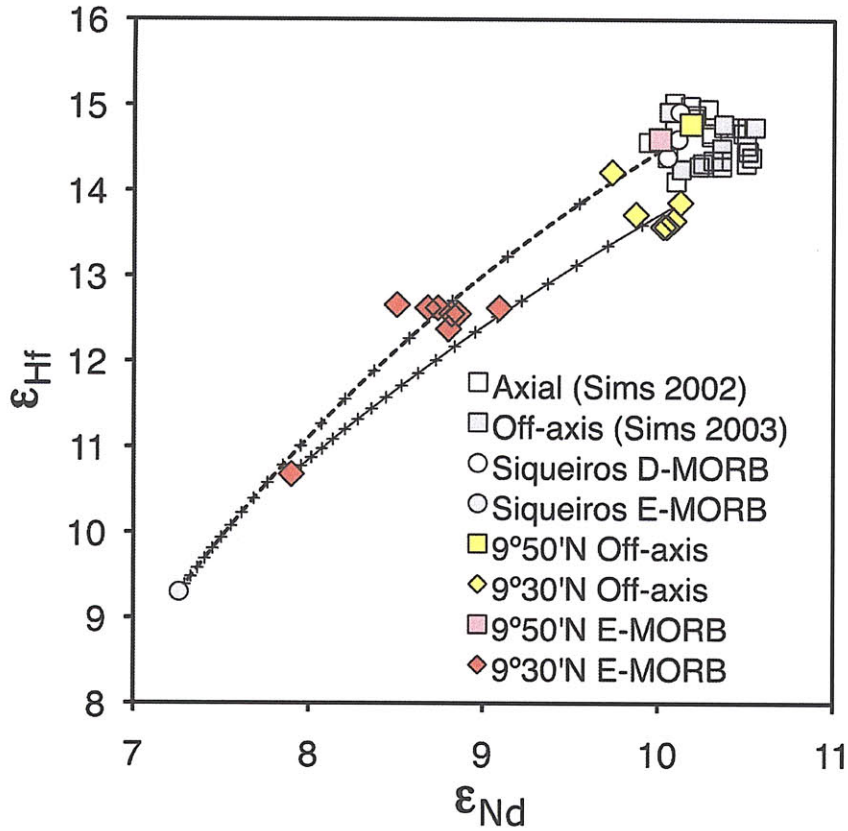


Figure 5. ϵ_{Nd} vs. ϵ_{Hf} for 9°-10°N EPR lavas. The dashed line is a binary mixing curve between Siqueiros E-MORB and D-MORB. The solid line is a binary mixing curve between 9°30'N off-axis N-MORB (sample 2706-7) and off-axis E-MORB (sample 2703-1). Data sources and symbols are the same as in Figure 2. Additional Siqueiros isotope data comes from Sims *et al.* (2002). Data for sample R54-2 comes from Harpp *et al.* (1990). See text for discussion.

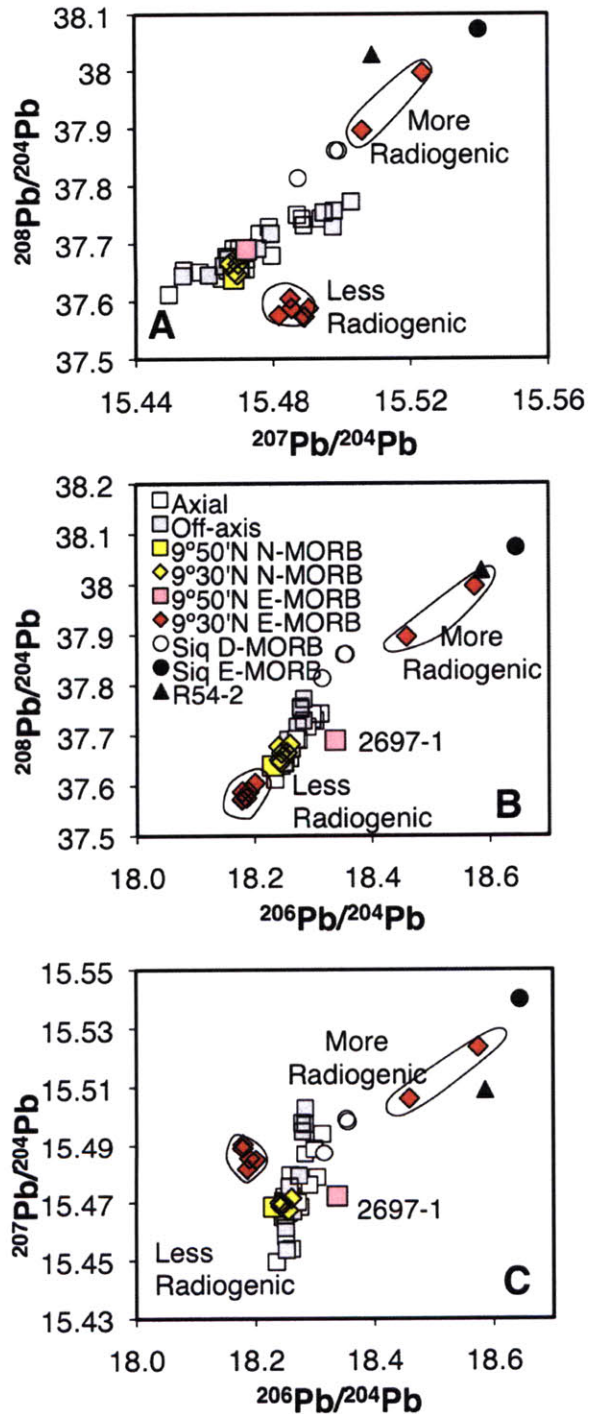


Figure 6. (A) $^{208}\text{Pb}/^{204}\text{Pb}$ vs. $^{207}\text{Pb}/^{204}\text{Pb}$, (B) $^{208}\text{Pb}/^{204}\text{Pb}$ vs. $^{206}\text{Pb}/^{204}\text{Pb}$, and (C) $^{207}\text{Pb}/^{204}\text{Pb}$ vs. $^{206}\text{Pb}/^{204}\text{Pb}$ for 9°-10°N EPR samples. Data sources and symbols are the same as in Figures 2 and 5. Also marked are “more radiogenic” and “less radiogenic” off-axis E-MORB groups as well as the off-axis E-MORB from 9°50'N—see text for discussion.

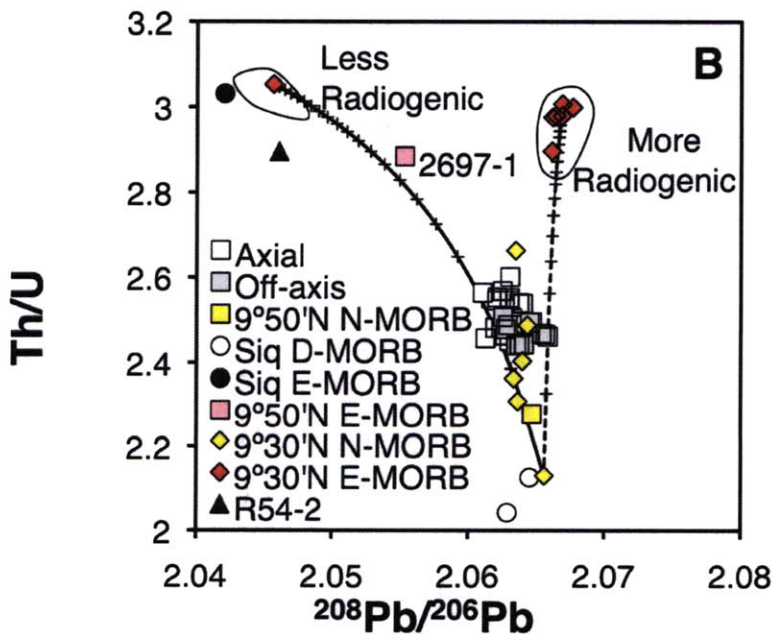
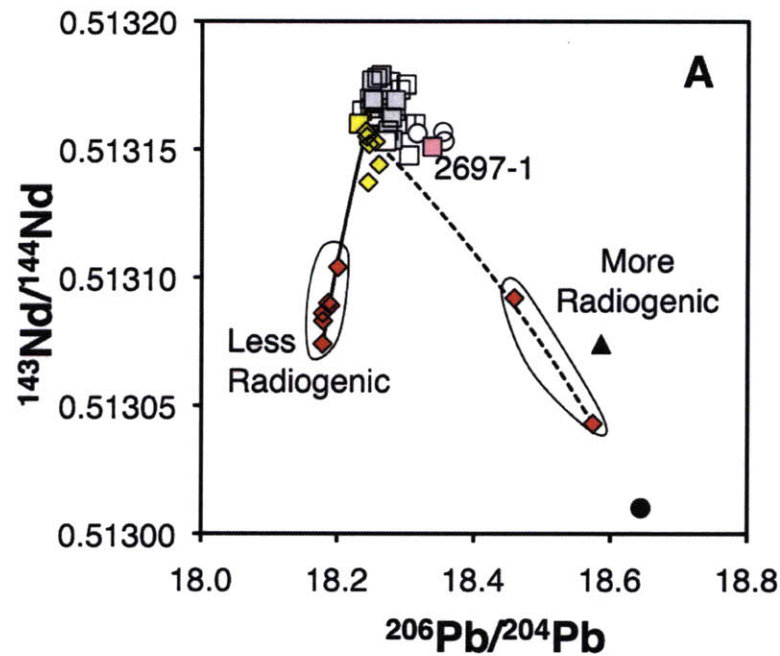
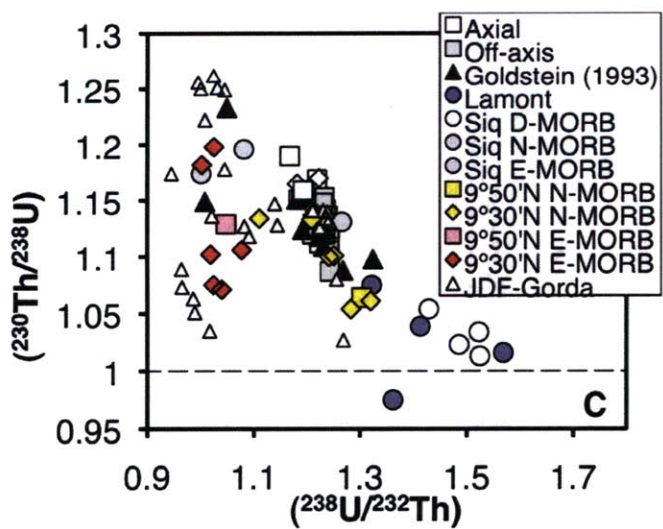
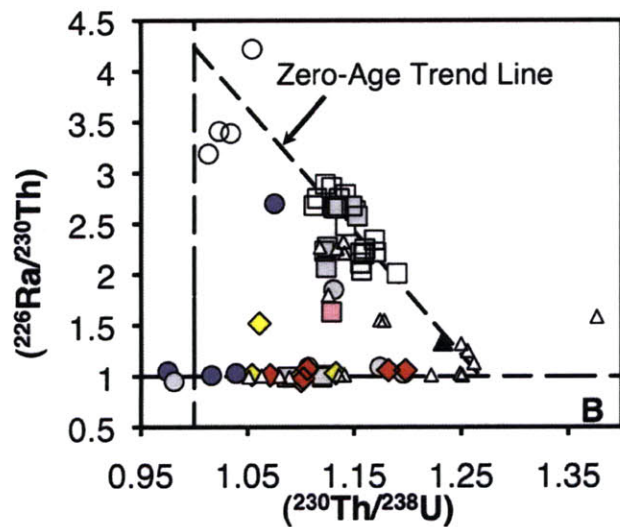
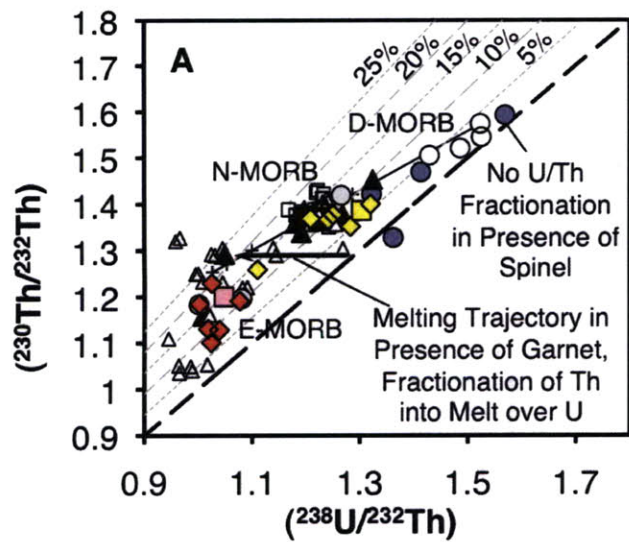


Figure 7. Plots of (A) $^{206}\text{Pb}/^{204}\text{Pb}$ vs. $^{143}\text{Nd}/^{144}\text{Nd}$, and (B) $^{208}\text{Pb}/^{206}\text{Pb}$ vs. Th/U. Mixing lines are designated by a dashed line between samples 2706-7 (depleted end member) and 2703-1 (more radiogenic E-MORB Pb end member) and a solid line between 2706-7 and 2489-3 (less radiogenic E-MORB Pb end member). Data sources and symbols are the same as in Figures 2 and 5.

Figure 8. (A) Plot of positively correlated ($^{238}\text{U}/^{232}\text{Th}$) vs. ($^{230}\text{Th}/^{232}\text{Th}$) for Pacific MORB showing the mixing relationship between D-MORB to E-MORB. D-MORB have essentially negligible ^{230}Th excesses, suggesting depleted melts were last equilibrated with spinel peridotite. In contrast, the large ^{230}Th excesses of E-MORB indicate melting in the presence of garnet. N-MORB represent mixtures of these enriched and depleted melts. Note the greater variability in ($^{230}\text{Th}/^{232}\text{Th}$) for E-MORB than for N- or D-MORB. Mixing between the Siqueiros D-MORB sample D20-2 (Lundstrom *et al.*, 1999) and the trend line age corrected E-MORB 2701-1 (the sample with the lowest ($^{238}\text{U}/^{232}\text{Th}$)) is represented by the black line, which is nearly identical to a regression line through samples with ^{226}Ra excesses from 9°-10°N EPR, the Siqueiros Fracture Zone, and the Lamont Seamounts, or those samples with primary ^{230}Th excesses. This regression line is the zero-age trendline used to calculate U-Th model ages in Table 6 and is described by the equation ($^{230}\text{Th}/^{232}\text{Th}$) = 0.6381 x ($^{238}\text{U}/^{232}\text{Th}$) + 0.6. Pluses along the mixing line represent 0%, 5%, 10%, 25%, 50%, and 100% mixing increments. ^{230}Th excesses are indicated in 5% increments by dashed lines. Symbols for samples from this study are the same as in Figure 2. Also included are samples from Juan de Fuca and Gorda Ridge (open triangles) (Goldstein *et al.*, 1992; 1994), additional samples from 9°-10°N EPR (solid triangles) (Goldstein *et al.*, 1993; 1994), and the Lamont Seamounts (blue circles) (Lundstrom *et al.*, 1999). (B) Plot of negatively correlated ($^{230}\text{Th}/^{238}\text{U}$) vs. ($^{226}\text{Ra}/^{230}\text{Th}$) for Pacific MORB. The linear regression used to estimate the zero-age trendline used for calculating Th-Ra model ages, indicated by a dashed line, included only samples from Sims *et al.* (2002) (open squares). (C) Plot of negatively correlated ($^{238}\text{U}/^{232}\text{Th}$) vs. ($^{230}\text{Th}/^{238}\text{U}$). E-MORB samples from Juan de Fuca and Gorda Ridge that lie below the correlation have been interpreted as being older (>50-220 kyrs; see Goldstein *et al.*, 1992; 1993 for details).



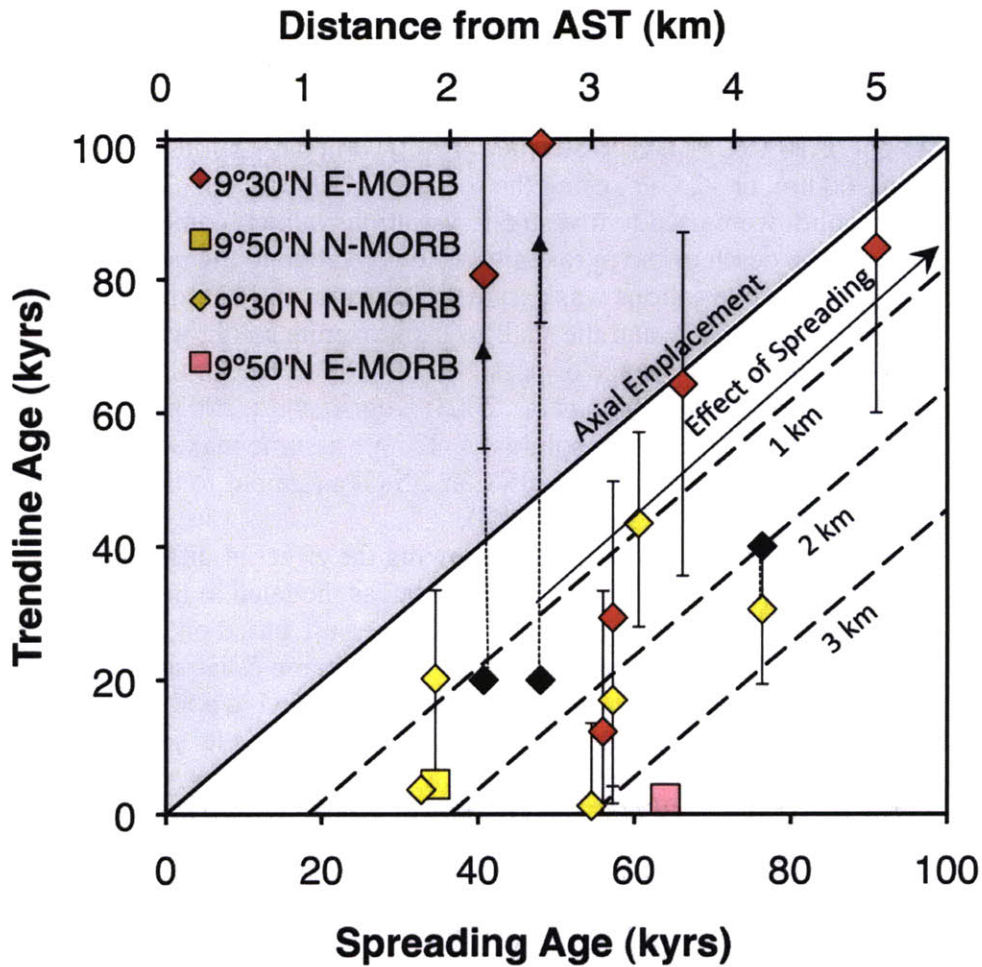
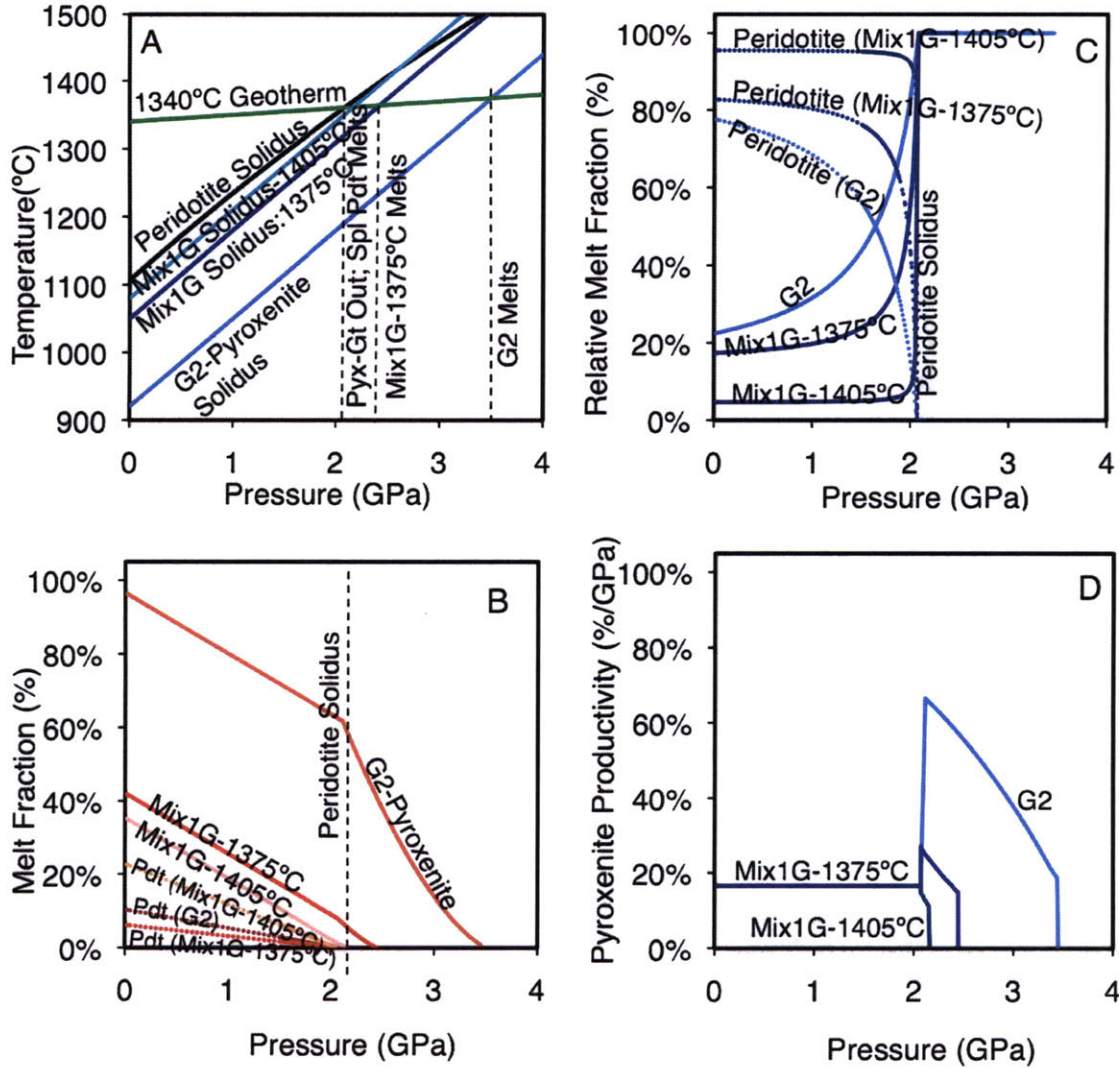


Figure 9. Plot of spreading age (kyrs) vs. model age trend line age (kyrs) and distance from the AST (km). Spreading ages were calculated as described in Table 6. Model U-Th and Th-Ra ages are plotted as colored symbols (as in Figure 2). Dashed lines between solid diamonds and colored symbols connect U-Th ages and paleointensity age constraints for samples (Bowles *et al.*, 2006). Black diamonds connected by dotted lines with arrows represent minimum ages from paleointensity constraints. Solid and dashed lines represent the effect of variable lava emplacement distances on spreading ages. Shown are lines for lava emplacement in the axial summit trough, 1 km off-axis, 2 km off-axis, and 3 km off-axis. We interpret the trend line age as the true sample age, whereas spreading ages may also reflect the distance the lava was emplaced off-axis. Trend line model ages significantly younger than the spreading ages are consistent with a significant component of off-axis volcanic accretion. Emplacement may occur via eruption within the AST and subsequent flow away from the AST or from direct emplacement due to off-axis eruption. The gray field represents lava ages older than the spreading age, a physical implausibility. Note that Th-Ra model ages often provide higher resolution, and significantly different age information than U-Th ages. Error bars for Th-Ra ages are smaller than the size of the symbol.

Figure 10. (A) Plot of pressure (GPa) vs. temperature (°C) showing the adiabatic gradient and the solidi for peridotite and three different pyroxenites used to calculate trace element compositions of melts produced by melting of a lithologically and compositionally heterogeneous mantle source. The mantle potential temperature was set at 1340°C with an adiabatic gradient of 10°C/GPa (Ita & Stixrude, 1992), which coincides with melting of dry peridotite at ~60 km, or ~2 GPa, using the solidus of Hirschmann (2000). Three different pyroxenite solidi were used to investigate variations in melt composition that result from changes in the depth of the pyroxenite solidus relative to the peridotite solidus. The deepest pyroxenite solidus was parameterized after the G2 solidus (Pertermann & Hirschmann, 2003), and the shallower pyroxenite solidi, which are intended to be representative of the range of possible solidi expected for the silica deficient pyroxenite Mix1G (Hirschmann *et al.*, 2003; Kogiso *et al.*, 2003; Elkins *et al.*, 2008), were assumed to be parallel to the solidus of G2. We assume maximum and minimum solidi for Mix1G of 1375°C and 1405°C at 2.5 GPa (similar to the range of 1375°C-1400°C found by Hirschmann *et al.*, 2003).

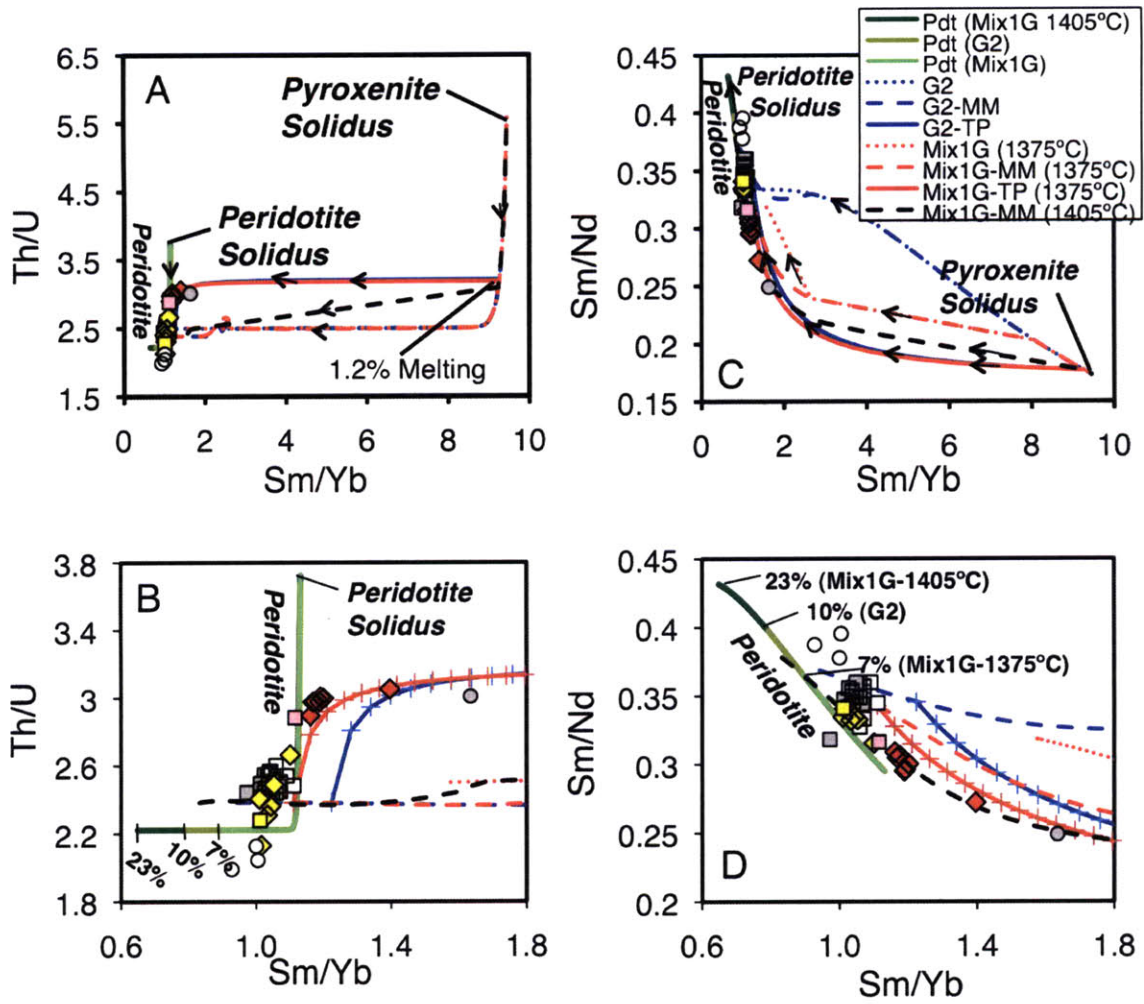
(B) Plot of pressure (GPa) vs. melt fraction (%), showing the effect of different productivities and solidi depths on the total melt fraction, as modeled in this study. Pyroxenite productivity was calculated as a function of pressure based on the parameterization of a silica-rich pyroxenite (G2) from Pertermann & Hirschmann (2003). Under these conditions, G2 pyroxenite crosses its solidus at ~3.5 GPa and melts >60% prior to peridotite melting. In contrast, the Mix1G pyroxenite crosses its solidus between 2.16 and 2.45 GPa and melts only ~1-8% before peridotite starts melting. Once peridotite melting begins, pyroxenite productivity decreases to a constant 16.5%/GPa (Hirschmann & Stolper, 1996). G2 pyroxenite melts almost 100% by the time peridotite melting ceases; total melting of Mix1G pyroxenite ranges from 35-42%. We assume peridotite melting begins in the spinel stability field and that peridotite productivity is constant, adjusting peridotite productivities in each of the three cases ($dF/dP_{G2} = 5\%/GPa$, $dF/dP_{Mix1G-1375^\circ C} = 3\%/GPa$, and $dF/dP_{Mix1G-1405^\circ C} = 1\%/GPa$) to best match the trace element abundances of E-MORB and N-MORB samples.

(C) Plot of pressure (GPa) vs. relative melt fraction (%), showing the relative contribution of melt from either peridotite or pyroxenite source for each different pyroxenite solidus, assuming pyroxenite constitutes 3% of the total solid mantle, which is consistent with constraints on G2 pyroxenite solid volumes based on crustal thickness (Pertermann & Hirschmann, 2003). Peridotite and pyroxenite melts are mixed in proportions based on their relative melt fractions (where relative melt fraction = $F_{pyx} \times X_{pyx} / (F_{pyx} \times X_{pyx} + F_{Peridotite} \times (1 - X_{pyx}))$, where X_{pyx} is the solid fraction of pyroxenite). Given the productivities shown in (D), for a large difference in pyroxenite and peridotite solidi, as is the case for G2 pyroxenite, pyroxenite melt compositions will have a more lasting influence on the bulk melt composition and ultimately contribute a much greater fraction of the total volume of melt than the unmelted pyroxenite did to the solid mantle (~22% vs. 3%). In contrast, more similar pyroxenite and peridotite solidi (e.g., Mix1G) result in much more rapid decreases in the proportion of pyroxenite melt and thus pyroxenite compositional influence. In all cases, however, peridotite melting overwhelms pyroxenite melting—pyroxenite melt constitutes only 5-22% of the total melt.



(Figure 10, cont'd) (D) Plot of pressure (GPa) vs. pyroxenite productivity (%/GPa) showing model parameterization, after Pertermann & Hirschmann (2003) and Hirschmann & Stolper (1996). G2 pyroxenite initiates melting at ~3.5 GPa and productivity increases rapidly to ~67%/GPa before peridotite begins melting. Mix1G pyroxenite (with the minimum solidus estimate of 1375°C) initiates melting ~2.45 GPa and productivity peaks at ~27%/GPa. The hotter Mix1G pyroxenite solidus (1405°C) crosses the adiabat at ~2.16 GPa and increases productivity to a rate of ~15%/GPa. Once peridotite begins melting, all pyroxenite productivities are ~16.5%/GPa. Pyx-Gt= garnet in pyroxenite; Spl=spinel; Pdt=peridotite.

Figure 11. (A) Sm/Yb vs. Sm/Nd; (B) blow up of (A); (C) Sm/Yb vs. Th/U; and (D) blow up of (C). Arrows along melting trajectories indicate decreasing pressure and increasing extent of melting. Each lithology undergoes modal fractional melting independently and the accumulated melts from both lithologies are mixed at all depths. These trajectories are marked as “mixed melts”. “Two-porosity” trajectories are generated by mixing of deep and shallow melts—see Figure 12 caption for details. Pluses along two-porosity mixing trajectories in (B) and (D) represent 1% mixing increments. Data symbols are the same as for Figure 2. For the peridotite source, we use the depleted DMM composition of Workman & Hart (2005), and for the pyroxenite source, we use the composition of Donnelly *et al.* (2004) for average EPR oceanic crust, noting that the true sources—particularly the enriched source—are not well-constrained. Peridotite partition coefficients are taken from a compilation by Donnelly *et al.* (2004), and bulk pyroxenite partition coefficients are calculated from Pertermann & Hirschmann (2004), using the cpx/melt Ds from run A343 and garnet/melt Ds from the “preferred average” (see Table 9 of Pertermann & Hirschmann, 2004). Spinel peridotite mineral proportions are 52% olivine, 18% clinopyroxene, and 30% orthopyroxene (from Donnelly *et al.*, 2004). Trace elements are assumed to partition between spinel and melt similarly to olivine/melt. Pyroxenite mineral proportions are 82% clinopyroxene and 18% garnet, as described by Pertermann & Hirschmann (2003). We also assume that garnet is no longer stable in pyroxenite at the peridotite solidus (Pertermann & Hirschmann, 2003). Pdt= peridotite; MM= mixed melts; TP= two-porosity.



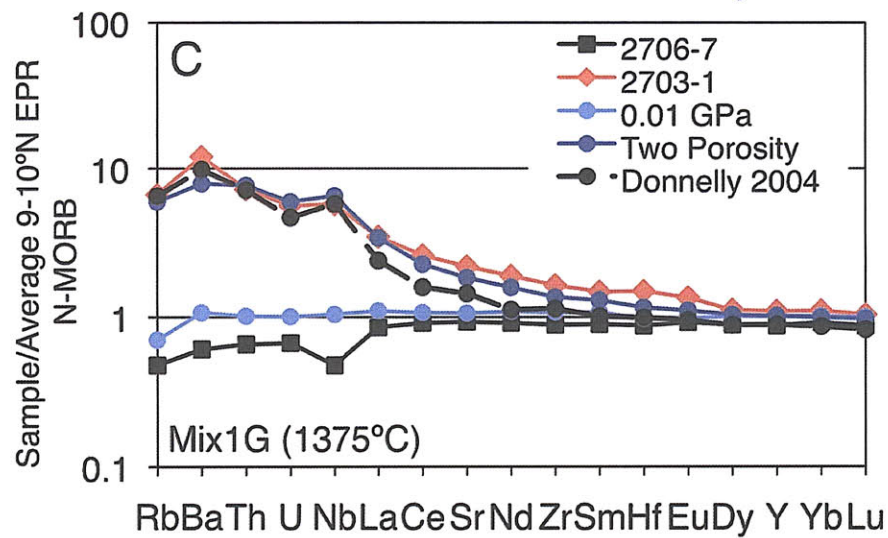
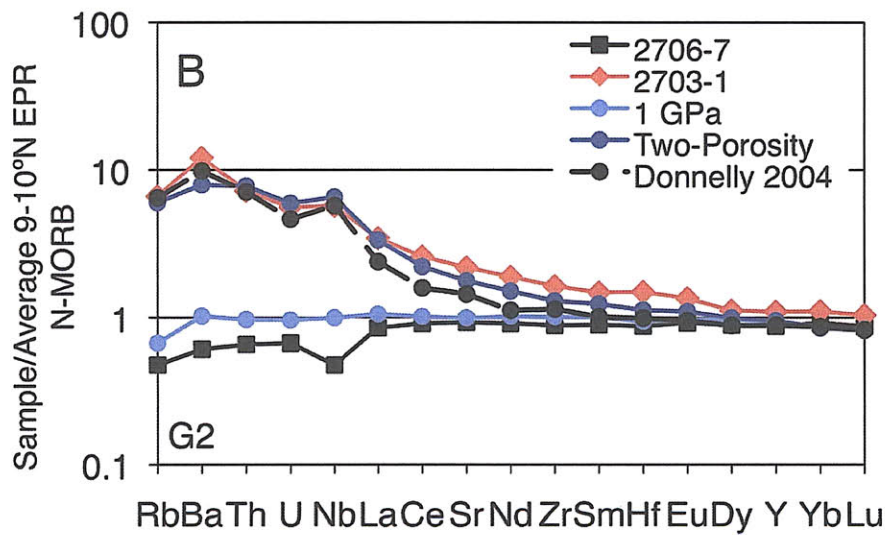
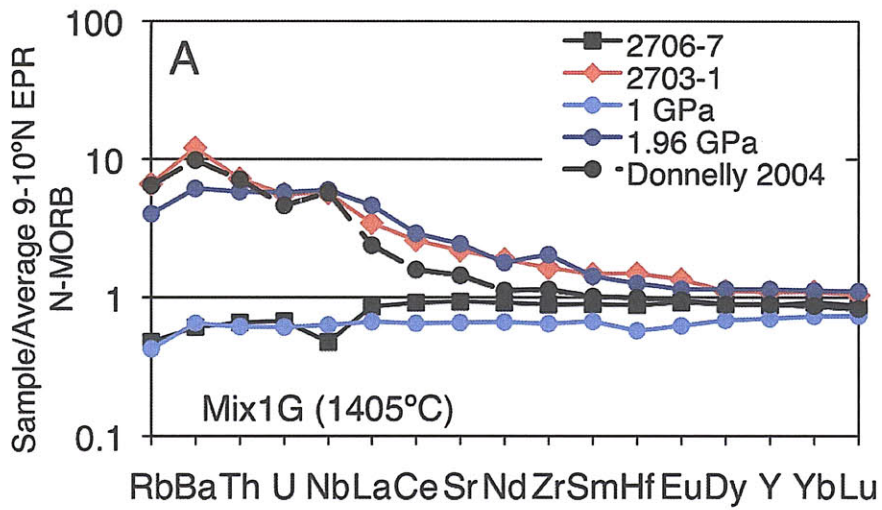


Figure 12. Trace element abundances of modeled E-MORB and N-MORB melts normalized to average axial 9°-10°N EPR N-MORB (Sims *et al.*, 2002) for 1-D melting of peridotite and (A) Mix1G (1405°C), (B) G2, and (C) Mix1G (1375°C) pyroxenites. The most enriched (2703-1) and depleted (2706-7) 9°30'N EPR samples from this study are shown for comparison. Using the parameters described in the captions to Figures 10 and 11, we have tried to match the most enriched E-MORB composition and still adequately match the average N-MORB composition by progressive depletion of a heterogeneous source. For extraction of N-MORB melt, we cease melting of Mix1G (1405°C) + peridotite at 1 GPa, G2 + peridotite at 1 GPa, and Mix1G (1375°C) + peridotite at 0.1 GPa. Both G2 and Mix1G (1375°C) model N-MORB are very similar to average 9°-10°N EPR N-MORB, but the Mix1G (1405°C) model N-MORB is more depleted than average 9°-10°N EPR N-MORB due to higher peridotite productivity (11%/GPa). Mix1G (1405°C) pyroxenite-peridotite mixed melts were extracted at ~1.96 GPa to best reproduce the incompatible element abundances of E-MORB 2703-1. In contrast, G2 and Mix1G (1375°C) pyroxenite-peridotite melt mixes resemble pure enriched pyroxenite melts when their abundances in the most incompatible elements are similar to E-MORB 2703-1 because these melts are largely composed of pyroxenite melt and peridotite melting has not substantially diluted the abundances of the MREE and HREE (Figure 11), so we can rule out progressive depletion as a source for E-MORB under conditions with deeper solidi. To simulate the effect of a two-porosity model on trace element abundances, we mix accumulated fractional melts generated at high pressure with accumulated fractional melts generated at low pressure (B&C). Binary mixing of ~1% melts of G2 and Mix1G (1375°C) pyroxenites (with deep melt proportions of 5%) with peridotite-pyroxenite melt mixes at 1 GPa and 0.1 GPa (the pressures for N-MORB extraction) result in excellent matches to the pattern for E-MORB 2703-1, suggesting a two-porosity melting regime is plausible, but indicating that melting of the enriched component must be limited to about 1% (for accumulated fractional melting).

Sample	Axial Lavas Originally Reported in Sims et al. (2002)							Originally Reported in Sims et al. (2003)					
	2359-4	2368-4	2752-6	2352-2	2358-3	2358-4	2365-3	2737-8	2746-7	2746-9	2746-14	2759-12	2759-14
Sc	40.3	38.5	37.3	40.4	41.5	40.9	42.0	36.1	38.4	38.1	42.0	43.6	40.8
Ti	13591	12361	11714	14327	15325	15190	15911	11294	12029	11952	15444	18892	15180
V	285	258	249	290	309	289	316	234	257	246	294	359	298
Cr	282	339	348	248	228	218	165	335	360	343	228	134	247
Co	39.0	41.4	40.3	38.6	40.8	38.4	39.5	40.3	41.2	40.5	38.8	42.2	40.2
Ni	82.3	116.4	121.1	71.4	69.8	66.7	60.5	120.8	113.6	110.2	66.7	52.0	79.9
Cu	67.0	74.2	72.3	64.4	63.9	62.7	64.4	73.1	72.6	73.2	65.8	63.4	64.4
Zn	76.2	72.0	70.3	78.1	81.5	79.7	82.6	69.0	71.0	71.5	80.0	93.0	80.2
Ga	15.9	16.1	15.3	16.3	16.9	16.7	17.3	14.9	15.4	15.4	16.7	18.8	16.6
Rb	0.91	0.80	0.93	0.96	1.08	1.04	1.06	0.73	0.84	0.83	1.00	1.09	0.92
Sr	111.6	122.9	116.4	113.3	118.1	115.1	116.2	115.3	114.5	115.2	118.5	122.9	120.5
Y	31.9	28.6	27.6	33.2	35.9	34.0	36.8	26.0	27.7	27.1	33.8	42.1	34.6
Zr	92.8	79.2	74.5	95.1	103.4	101.7	105.7	70.8	77.1	77.9	101.1	124.9	100.0
Nb	2.35	2.01	2.22	2.49	2.81	2.65	2.82	1.78	2.12	1.99	2.36	3.00	2.50
Ba	8.55	7.50	9.19	8.91	9.90	9.93	9.69	6.85	7.83	8.06	8.77	10.00	8.56
La	3.18	2.79	2.82	3.47	3.73	3.73	3.80	2.56	2.72	2.78	3.53	4.34	3.51
Ce	9.99	8.85	8.69	10.82	11.65	11.56	11.90	8.02	8.48	8.61	11.29	13.77	11.13
Pr	1.70	1.52	1.46	1.83	1.95	1.94	2.00	1.38	1.44	1.48	1.92	2.34	1.89
Nd	9.13	8.18	7.86	9.79	10.39	10.37	10.74	7.52	7.81	7.95	10.47	12.48	10.17
Sm	3.24	2.87	2.74	3.40	3.64	3.63	3.74	2.63	2.77	2.86	3.66	4.36	3.52
Eu	1.16	1.08	1.03	1.22	1.29	1.29	1.33	0.99	1.02	1.04	1.29	1.51	1.26
Gd	4.30	3.88	3.68	4.58	4.89	4.89	5.01	3.50	3.69	3.74	4.84	5.77	4.70
Tb	0.81	0.72	0.69	0.86	0.91	0.90	0.94	0.65	0.69	0.70	0.90	1.09	0.88
Dy	5.24	4.67	4.48	5.52	5.85	5.86	6.10	4.26	4.46	4.58	5.80	7.03	5.68
Ho	1.12	1.00	0.95	1.18	1.24	1.24	1.30	0.91	0.96	0.96	1.23	1.51	1.21
Er	3.19	2.83	2.73	3.39	3.60	3.57	3.72	2.62	2.74	2.80	3.58	4.35	3.47
Tm	0.49	0.43	0.41	0.51	0.54	0.55	0.57	0.39	0.42	0.43	0.54	0.66	0.53
Yb	3.12	2.77	2.62	3.30	3.50	3.46	3.65	2.54	2.67	2.73	3.45	4.21	3.38
Lu	0.47	0.41	0.40	0.50	0.53	0.53	0.56	0.38	0.41	0.41	0.53	0.64	0.52
Hf	2.55	2.18	2.04	2.62	2.81	2.83	2.92	1.94	2.09	2.14	2.76	3.37	2.69
Ta	0.160	0.143	0.136	0.167	0.183	0.188	0.186	0.122	0.140	0.134	0.159	0.200	0.165
Pb	0.431	0.385	0.367	0.438	0.487	0.481	0.510	0.347	0.365	0.361	0.490	0.585	0.459
Th	0.131	0.112	0.129	0.140	0.159	0.157	0.159	0.096	0.114	0.115	0.134	0.167	0.137
U	0.058	0.049	0.056	0.062	0.069	0.068	0.071	0.046	0.050	0.051	0.061	0.076	0.062

Sample	Originally Reported in Sims et al. (2003) (cont'd)					
	2768-3	2768-6	2768-8	2772-1	2772-2	2772-3
Sc		43.0	36.3	43.5	48.0	40.4
Ti		15241	11262	14684	16354	15716
V		316	231	311	328	295
Cr		244	329	248	275	206
Co		40.4	39.8	40.2	43.8	38.1
Ni		69.8	115.6	63.9	69.7	63.0
Cu		71.5	72.3	71.8	78.5	60.0
Zn		79.6	67.6	79.9	85.3	82.3
Ga		16.8	15.1	16.6	18.8	16.7
Rb	0.77	0.95	0.73	1.02	1.12	0.96
Sr	107.8	112.4	122.2	117.7	131.0	109.8
Y	34.3	34.1	25.5	34.0	35.7	36.3
Zr	101.2	96.8	73.1	96.0	103.2	104.6
Nb	1.80	2.57	1.90	2.62	2.78	2.62
Ba	7.27	7.3	6.99	9.21	10.07	8.81
La	3.42	3.41	2.66	3.44	3.80	3.77
Ce	11.28	10.82	8.29	10.74	11.83	11.89
Pr	1.96	1.84	1.39	1.81	1.99	2.03
Nd	10.44	9.90	7.54	9.71	10.63	10.88
Sm	3.57	3.44	2.64	3.37	3.78	3.84
Eu	1.28	1.23	1.00	1.21	1.36	1.34
Gd		4.66	3.52	4.55	4.97	5.11
Tb		0.87	0.66	0.86	0.94	0.95
Dy	5.56	5.67	4.26	5.59	6.10	6.19
Ho	1.24	1.21	0.90	1.19	1.31	1.33
Er		3.52	2.59	3.40	3.74	3.79
Tm		0.53	0.39	0.52	0.57	0.58
Yb	3.48	3.39	2.52	3.33	3.69	3.70
Lu	0.52	0.52	0.38	0.51	0.56	0.56
Hf	2.69	2.65	2.02	2.59	2.84	2.91
Ta	0.145	0.168	0.126	0.169	0.195	0.180
Pb		0.454	0.364	0.452	0.507	0.443
Th	0.130	0.138	0.108	0.144	0.160	0.148
U	0.055	0.063	0.050	0.065	0.070	0.064

APPENDIX.

Table A1. Replicate trace element analyses for sample analyses previously published in Sims et al. (2002) and Sims et al. (2003). Trace element analyses reported in this study were conducted at the University of Florida using the methods described in Table 3. See text for details (section 2.4).

Table A2. Corrected values for $^{143}\text{Nd}/^{144}\text{Nd}$ isotopic measurements reported in Sims et al. (2002) and Sims et al. (2003)^a. See Table 4 for details.

Originally Reported in Sims et al. (2002):		Originally Reported in Sims et al. (2003):	
Sample	Corrected $^{143}\text{Nd}/^{144}\text{Nd}$	Sample	Corrected $^{143}\text{Nd}/^{144}\text{Nd}$
2359-4	0.512358	2737-8	0.512376
2497-1 (1)	0.512353	2746-4	0.512362
2359-5	0.512363	2746-7 (1)	0.512361
2368-4	0.512367	2746-9	0.512366
2372-1	0.512363	2746-14	0.512364
2392-9	0.512362	2759-12 (1)	0.512373
2752-6	0.512357	2759-14 (1)	0.512366
2504-1	0.512352	2768-3	0.512361
2351-2	0.512368	2768-4	0.512364
2746-4	0.512367	2768-6	0.512375
2746-3b	0.512345	2768-8	0.512354
2370-6	0.512357	2771-1	0.512374
2370-1	0.512363	2772-1	0.512366
2355-8	0.512352	2772-2	0.512360
2356-7	0.512359	2772-3	0.512351
2361-6	0.512362		
2352-2	0.512370		
2358-3	0.512372		
2358-4	0.512373		
2365-3	0.512350		
<u>Siqueiros</u>			
2390-5	0.512208		
D20-2	0.512350		
A2384-3	0.512354		
A2384-6	0.512353		

^aFor data originally reported in Sims et al. (2002), a correction of 0.65 Epsilon units was applied. For data reported in Sims et al. (2003), the correction was 0.70 Epsilon units.

CHAPTER 3: EVALUATING THE RESOLUTION OF U-SERIES AGE CONSTRAINTS: AN APPLICATION TO RIDGE FLANK CONSTRUCTION AT 9°-10°N EAST PACIFIC RISE

ABSTRACT

Models of crustal accretion at fast-spreading ridge segments such as at 9°-10°N East Pacific Rise (EPR) assume that volcanic accretion is symmetrical and confined to a narrow, axial summit trough (AST). Recent studies have revealed that volcanic accretion occurs over an area up to at least ~2-4 km to either side of the ridge axis, and that lava may be emplaced in a variety of ways, including direct emplacement via off-axis eruptions on the ridge flanks as well as AST overflow and focused transport in off-axis lava channels or dispersed flow down the ridge flanks. Most of the ridge crest is dominated by overlapping flows that have breached the AST and flowed to variable distances off-axis, as observed in side-scan sonar and high resolution bathymetry that show the presence of 'shingled' terrains.

The primary objective of this study is to use ^{230}Th - ^{226}Ra model ages, in conjunction with precise knowledge of sampling locations, to identify the mechanisms and ordering of flow emplacement of individual 'shingles', and to discern the relationships between adjacent flow units. In order to construct a time-constrained volcanic stratigraphy of the ridge crest, 22 mid-ocean ridge basalts were collected from several flow units on the east and west flanks of the ridge axis at 9°50'N EPR in February-March of 2004 and were measured for major element, trace element, and $^{87}\text{Sr}/^{88}\text{Sr}$ and ^{238}U - ^{230}Th - ^{226}Ra isotopic compositions. Additional ^{238}U - ^{230}Th - ^{226}Ra data obtained from zero-aged samples from the 2005-2006 eruption sequence, when taken together with data for samples from the 1991-1992 eruption, suggest more diversity in initial ($^{226}\text{Ra}/^{230}\text{Th}$) than previously anticipated and limit the resolution of our dating technique to $\sim\pm 1$ kyrs. We find that ridge flank samples in this study are younger than ~2 kyrs, but that the range of geochemical compositions represented by these flank lavas as a group, particularly U, Th, and ^{226}Ra concentrations, is much greater than the range represented by samples from individual eruptions (e.g., 1991-92 and 2005-06). Some samples have identical geochemical compositions, and this allows us to identify seven distinct eruptive units despite indistinguishable model ages. These data suggest more frequent (<300 yrs) emplacement of flows up to 1-2 km from the AST than has been previously inferred from models of crustal accretion. In addition, the variability of geochemical compositions requires rapid, significant changes in parental melt composition on the order of a few hundred years.

3.1. INTRODUCTION

Mid-ocean ridge (MOR) spreading at the East Pacific Rise (EPR) from 9°-10°N has typically been viewed as a geologically continuous process involving eruptions and dike emplacement within a narrow zone of magmatism defined by the axial summit trough (AST) (Figure 1) [Gregg et al., 1996; Haymon et al., 1991; Fornari et al., 1998; Perfit and Chadwick, 1998; Schouten et al., 2001; Soule et al., 2009]. However, seismic studies suggest that seismic layer 2A, inferred to be the extrusive volcanic crust, doubles in thickness within ~2-4 km from the AST [Christeson et al., 1994; 1996; Harding et al., 1993; Schouten et al., 1999; Sohn et al., 2004; Vera and Diebold, 1994]. This geometry can only be generated if a large component of crustal accretion occurs outside of the AST [Goldstein et al., 1994; Hooft et al., 1996; Perfit et al., 1994; Sims et al., 2003; Soule et al., 2005; White et al., 2002]. In light of the observed crustal thickening, recent efforts have focused on investigating off-axis volcanic features and their spatial relationships.

Several mechanisms have been proposed to explain this thickening of layer 2A: eruptions from vents outside the AST, often in the form of pillow ridges/mounds [Perfit et al., 1994], lobate or sheet lava flows that overflow the AST [Hooft et al., 1996; Schouten et al., 1999; Sims et al., 2003], and lava channels and tubes that transport axial lavas several km away from the AST [Hooft et al., 1996; Sims et al., 2003, Soule et al., 2005]. High-resolution autonomous benthic explorer (ABE) bathymetry and DSL-120A side-scan sonar imagery in the 9°50'N region show that both the east and west ridge flanks up to ~2 km from the AST are dominated by shingle-patterned lava terrain with

high acoustic backscatter (Figure 2) [e.g., Fornari et al., 2004, Plate 2; Sims et al., 2003, Figure 1b]. Bounding this ~4 km wide, axially centered, but asymmetric, ‘neo-volcanic’ zone are regions of low acoustic backscatter, interpreted to be more heavily sedimented, older lavas [e.g., Escartin et al., 2007; Fornari et al., 2004; Soule et al., 2009]. The neo-volcanic zone is inferred to be produced by overflow of the AST and off-axis transport of relatively young lava by either dispersed flow or focused flow through channels or tubes down the ridge flanks [Fornari et al., 2004; Soule et al., 2005]. Off-axis pillow mounds are present but appear to comprise only a small component of off-axis accretion [cf., Sims et al., 2003, Figure 1b]. Thus, eruption from within the AST and lava flow down the ridge flanks appears to be the primary mechanism for volcanic accretion outside of the AST at 9°50’N EPR.

Although high-resolution spatial observations provide controls on the mechanisms of volcanic accretion, they are limited in their ability to quantitatively constrain temporal aspects of ridge evolution. In particular, identifying differences or similarities in the ages and compositions of adjacent ‘shingles’ (or flow lobes), as observed in side-scan and bathymetric imagery, is necessary for determining whether the shingled terrain observed along the ridge flanks outside of the AST at 9°50’N EPR [Fornari et al., 2004] is produced by the overlapping of flows from multiple eruptions, fed by lava tubes from the AST, or reflects ridge crest repaving by single, large eruptions.

Dating methods have the potential to address this important issue, but placing age constraints on young mid-ocean ridge basalts (MORB) has proven to be difficult. Age estimates based on sedimentation or alteration rates are qualitative, as they depend on

lava morphology and sedimentation rates [e.g., Haymon et al., 1993; Perfit and Chadwick, 1998; Rubin and MacDougall, 1990; Sturm et al., 2000]. Traditional radiometric dating techniques are either limited by their temporal sensitivity (e.g., Rb-Sr, Sm-Nd, U-Pb) or by a lack of requisite closed system behavior (e.g., K-Ar, Ar-Ar) [Duncan and Hogan, 1994]. Recent studies using magnetic paleointensities to constrain lava ages have proven valuable for young lava flows [Bergmanis et al., 2007; Bowles et al., 2006], but paleointensity field variations become non-unique after a few kyrs, which increases estimated uncertainties for older flows, and paleointensity estimates in MORB glasses may be biased slightly low due to local field effects and cooling rate bias [Bowles et al., 2006].

Uranium decay series (U-series) dating techniques provide an effective means for accurately dating MORB on timescales of ~0.1-375 ka, and they are not subject to the same limitations as paleomagnetic and traditional radiometric methods [Cooper et al., 2003; Goldstein et al., 1992; 1993; 1994; Lundstrom et al., 2003; Rubin and MacDougall, 1990; Rubin et al., 1994; Sims et al., 2003; Standish and Sims, 2009; Sturm et al., 2000; Waters et al., in review]. The presence or absence of disequilibria among the daughter products (e.g., ^{230}Th , ^{226}Ra , ^{210}Pb , and ^{231}Pa) can place absolute age limits on lava samples, and under certain conditions disequilibria can be used for model age dating, which can provide a much finer temporal resolution [Sims et al., 2003].

Sims et al. [2003] established the use of U-series model ages at 9°50'N EPR as a valid dating technique and provided temporal evidence confirming both geological and geophysical observations that MOR volcanic construction is not limited to the AST and

occurs over the full width of the neo-volcanic zone [e.g., Christeson et al., 1994; 1996; Fornari et al., 2004; Harding et al., 1993; Hoofstede et al., 1996; Perfit and Chadwick, 1998; Perfit et al., 1994; Schouten et al., 1999; Sohn et al., 2004]. Indeed, the ^{230}Th - ^{226}Ra model ages calculated by Sims et al. [2003] for the majority of samples collected within the neo-volcanic zone are much younger than ages expected based on the spreading rate and the sample distance from the axis, which is consistent with flow of lava off-axis. However, the samples dated by Sims et al. [2003] were collected using the submersible *Alvin* from a variety of locations on the 9°50'N EPR ridge flanks, with no more than a few samples selected in any one location, and thus Sims et al. [2003] lacked the sampling continuity needed to identify age relationships between adjacent lava flows.

During a recent cruise to 9°50'N EPR, new sample suites were collected by *Alvin* along two dive transects that traversed across the east and west ridge flanks from the edge of the neo-volcanic zone (~2 km) to ~0.7 km from the AST (Figures 1, 2) [Schouten et al., 2004]. These samples were collected directly from pillow lavas and adjacent lobate and sheet flows that correspond to the fronts and bodies of flow shingles, respectively, in side-scan sonar and ABE bathymetry. Thus, these suites provide the necessary sample resolution and continuity for determining the geochemical and age relationships among a stratigraphically related series of flow shingles. We study these sample suites to investigate the origin of shingled terrain and to place temporal constraints on the formation of the neo-volcanic zone at 9°50'N EPR.

3.2. SAMPLE LOCATIONS AND DESCRIPTIONS

Dives 3963 and 3974:

Dive 3963 and 3974 samples were collected using the submersible *Alvin* during cruise AT11-7 to 9°-10°N EPR [Schouten et al., 2004]. Lava samples were collected at and between inferred lava flow fronts up to ~2 km to the east and west side of the ridge crest, respectively (Fig. 1). Observations of lava morphology and qualitative age indicators were made along the dive tracks. ABE bathymetry, shipboard multibeam bathymetry, and high-resolution side-scan sonar imaging are also available for this area [Cochran et al., 1999; Fornari et al., 1998; 2004]. Dive track and sample locations are shown in Figures 1 and 2(A-D). *In situ* dive observations, hand sample descriptions, and the locations of samples with respect to morphological characteristics, such as pillow flow fronts and lobate/sheet flow units, are summarized in Table 1. Dive summaries can be found in Appendix A.

2005-2006 Flow: Five samples acquired from flows associated with the 2005-2006 eruption at 9°50'N EPR [Soule et al., 2007; Goss et al., in review] have also been analyzed for ^{238}U - ^{230}Th - ^{226}Ra disequilibria. Because these samples are recently erupted, they provide additional constraints on the initial disequilibria present upon eruption and augment the zero-age trend previously documented for samples erupted during 1991-1992 [Sims et al., 2002]. Four samples were collected with the submersible *Alvin*. Two of these (4202-4, 4202-6) were collected at 9°50'-9°51'N and the other two *Alvin* samples

(4205-5, 4205-6) were collected further south at 9°46'-9°47'N. The fifth sample (NH-D1A) was collected by dredge slightly off-axis at 9°54'N. Sample locations are shown in Figure 1.

3.3. U-SERIES MODEL AGE DATING

The assumed starting condition of U-series nuclides in the mantle source prior to partial melting is one of secular equilibrium, in which the activities of the constituent U-series nuclides are equal, and their activity ratios (herein denoted by parentheses) are equal to unity. Because the U-series decay chain is composed of different elements, in particular U, Th, and Ra, magmatic processes such as mantle melting, melt segregation, melt transport, and fractional crystallization may fractionate these elements and perturb the steady-state condition. In addition, the magnitude of disequilibria can be affected by the original mantle source composition. Secular equilibrium is again reached in roughly five half-lives, or ~8 kyrs and ~375 kyrs for ^{226}Ra ($t_{1/2}=1.6$ kyrs) and ^{230}Th ($t_{1/2}=75$ kyrs), respectively. Thus, the presence of disequilibrium in a lava, for example $(^{226}\text{Ra}/^{230}\text{Th})\neq 1$, or $(^{230}\text{Th}/^{238}\text{U})\neq 1$, immediately limits the lava eruption age to <8 ka or <375 ka.

Furthermore, if the initial extent of disequilibrium in a basalt sample upon eruption can be established, the difference between that initial activity and the current measured activity can be used to explicitly determine the lava eruption age. U-series model ages for off-axis MORB have been calculated by estimating the initial activities

from data for the youngest axial basalts and comparing these with the activities measured in a sample of unknown age [Goldstein et al., 1993; 1994; Sims et al., 2003]. For example, when calculating model ages of samples from 9°-10°N EPR, initial activity ratios can be estimated based upon measurements from lava collected exclusively within the AST and known to have erupted in 1991-92 (Figure 3; [Sims et al., 2002; 2003]).

It is important to note that these U-series ages are “model” ages in that they assume a constant source (spatially and temporally) and are the sum of magma chamber residence time and eruption age. When determining U-series model ages, several criteria must be met to assure that the initial extent of disequilibria in the lava of known age and the sample of interest is the same:

- (1) Primary magmatic processes initially created U-series disequilibria and the lavas being dated have not undergone significant secondary alteration. These lavas have remained a closed system with respect to Th/U after eruption.
- (2) After melt generation and transport, the magma has not resided for significant periods of time in a magma chamber relative to the half-lives of ^{230}Th (~75 kyrs) and ^{226}Ra (~1.6 kyrs).
- (3) The source of the axial and off-axis lavas is constant, both spatially and temporally, with respect to Th/U.
- (4) Both the axial lavas and the off-axis lavas were derived by similar degrees of melting and that the depths of melting and melt transport rates were also similar [e.g., McKenzie, 1985; Rubin et al., 2005; Spiegelman and Elliot, 1993; Williams and Gill, 1989].

These criteria were met by a suite of off-axis samples from a previous dating study at 9°50'N EPR [Sims et al., 2003]. Prior work has confirmed that U-series disequilibria in both axial and off-axis lavas have been generated by primary magmatic processes (i.e., melting, melt segregation, and melt transport in the mantle) [Sims et al., 2002; 2003]. These primary disequilibria are best represented by the negative correlation between ($^{226}\text{Ra}/^{230}\text{Th}$) and ($^{230}\text{Th}/^{238}\text{U}$) (Figure 3), the positive correlation between ($^{230}\text{Th}/^{232}\text{Th}$) and ($^{238}\text{U}/^{232}\text{Th}$), and the essentially constant ($^{231}\text{Pa}/^{235}\text{U}$) for variable ($^{230}\text{Th}/^{238}\text{U}$) in samples known to have erupted during 1991-1992. Samples are always screened for alteration/closed system behavior by measuring ($^{234}\text{U}/^{238}\text{U}$) and/or Cl/K ratios [Sims et al., 2002; 2003]. A recent study of ^{210}Pb disequilibria by Rubin et al. [2005] limits crustal residence time at 9°-10°N EPR to less than a few hundreds of years; thus, it is unlikely that magma storage has a significant impact on the extent of ^{230}Th and ^{226}Ra disequilibria. Furthermore, previous studies have characterized the 9°-10°N EPR axial lavas in terms of major and trace element compositions, and Sr, Nd, Hf, and Pb isotopic compositions [Sims et al., 2002; 2003]. The first of these studies [Sims et al., 2002] established that axial lavas are derived from a source that is constant with respect to the time-integrated values for Sm/Nd, Lu/Hf, Rb/Sr, and Th/U. The second study, focused at 9°50'N [Sims et al. 2003], demonstrated that the measured off-axis lavas in this region have isotopic compositions that are uniform and identical to the axial lavas, and hence are inferred to come from the same mantle source. In addition, recent Sr, Nd,

and Pb isotopic analyses on lavas from the 2005-2006 eruption also indicate constancy in the mantle-source composition [Goss et al., in review].

Having satisfied all of the above listed criteria, Sims et al. [2003] were able to calculate model ages using best fit trend lines on plots of ($^{238}\text{U}/^{232}\text{Th}$) vs. ($^{230}\text{Th}/^{232}\text{Th}$) and ($^{230}\text{Th}/^{238}\text{U}$) vs. ($^{226}\text{Ra}/^{230}\text{Th}$) to represent initial ($^{230}\text{Th}/^{232}\text{Th}$) and ($^{226}\text{Ra}/^{230}\text{Th}$) disequilibria in young (<200 yrs) lavas collected from within the AST from 9°17' -9°54'N EPR (Figure 3) [Sims et al., 2002; 2003]. Aging from these trend lines follows a vertical trajectory, and the difference in ($^{230}\text{Th}/^{232}\text{Th}$) and ($^{226}\text{Ra}/^{230}\text{Th}$) from the initial value estimated by the trend line can be used to calculate the lava eruption age, again assuming that the initial disequilibria in the sample of known age and the sample of interest are equal (Figure 3).

3.4. COMPARISON OF U-SERIES DATING WITH OTHER AGE CONSTRAINTS AT 9°50'N EPR

The Sims et al. [2003] study showed that model ages for spatially constrained and well-documented off-axis lavas are generally consistent with field observations of lava ages based on the extent of alteration and sediment cover. However, they also found that observations of sediment cover and alteration are qualitative and subject to local variations in hydrothermal and pelagic sedimentation rates. This is consistent with the findings of Sturm et al. [2000] on the Mid-Atlantic Ridge. Recent paleointensity measurements made on several of the same samples analyzed in Sims et al. [2003] and in

a recent study by Waters et al. [in review] are consistent with U-series ages, but are limited by an imperfect knowledge of field variations at 9°-10°N EPR and the inherent non-uniqueness of paleointensities [Bowles et al., 2006]. In addition, paleointensity measurements provide no constraints on petrogenetic processes. It is for these reasons that we use U-series measurements to provide the necessary information for deciphering individual flow units. We compare our quantitative age results with qualitative submersible and hand sample observations of sediment cover and glass alteration to further evaluate the value of each method.

3.5. ANALYTICAL METHODS

Major elements were analyzed on polished glass chips at the USGS Microbeam Laboratory in Denver, Co. using a JEOL 8900 Electron Microprobe. Analysis of seven to ten separate points (including spots on separate chips of the same sample) were averaged for each sample and then normalized and corrected for instrument drift based on the established values for in-house standards JdF-D2 [Reynolds et al., 1995] and ALV2392-9 [Smith et al., 2001]. The 2s errors calculated from variation in the analyses of ALV2392-9 during these analytical runs are listed in Table 2.

Samples were analyzed for trace elements at the University of Florida using a Thermo Finnigan Element II Inductively Coupled Plasma Mass Spectrometer (ICP-MS). The analyses were performed in medium resolution with Re and Rh used as internal

standards to correct for instrumental drift and matrix effects. Concentrations were calculated by external calibration using a combination of USGS (BHVO-1) and in-house (ENDV, and Endeavor Ridge MORB standard from the Geological Survey of Canada, Ottawa) rock standards. Repeated chemical analyses of a second in-house MORB standard (ALV2392-9) during each run were used to assess instrumental drift as well as evaluate accuracy and precision of the measurements. Precision (2s) was found to be better than $\pm 5\%$ for the rare earth elements, Ba, Hf, Nb, Rb, Sr, Th, Y, and Zr, and better than $\pm 9\%$ for Pb, Ta, and U.

Sr isotopic analyses were conducted both at Woods Hole Oceanographic Institution (WHOI) using a Thermo Finnigan Neptune multi-collector inductively coupled mass spectrometer (MC-ICP-MS) and at Boston University (BU) using the Thermo Finnigan Triton thermal ionization mass spectrometer (TIMS). Measurements of Sr isotopic compositions at WHOI have internal precision of 5-10 ppm. After adjusting to 0.710240 (NBS SRM 987), external precision is estimated at 15-30 ppm.

^{238}U , ^{232}Th , ^{226}Ra , ($^{230}\text{Th}/^{232}\text{Th}$), and ($^{234}\text{U}/^{238}\text{U}$) were measured at WHOI using the Thermo Finnigan Neptune MC-ICP-MS. Extensive details of the U-Th-Ra chemical and analytical procedures at WHOI are presented in Appendix A1 of Sims et al. [2008a]. More details of Th and U measurement methods and standards are summarized in Ball et al. [2008] and Sims et al. [2008b] and in the caption to Table 5.

3.6. RESULTS

3.6.1. Major Elements

Major element compositions are reported in Table 2 and have previously been reported by J. Hinds [M.S. Thesis, University of Florida, 2005]. All lava samples are low K, tholeiitic, normal MORB (N-MORB; $K/Ti < 0.11$). Samples from dive 3963—east of the axis—have wt% MgO ranging from 7.7-9.0 and molar Mg# (molar Mg# = $Mg/(Fe + Mg) \times 100$) from 60 to 67 (Fig. 4a, Table 2). Dive 3974 samples—west of the axis—have wt% MgO from 7.6 to 8.7 and Mg# from 60 to 64. In both flow sequences, the lavas closest to the AST are the most primitive, with lavas becoming progressively more evolved with increasing distance from the AST (Fig 4b, Fig. 6). Dive 3963 lavas have a bimodal distribution of Mg# and wt% MgO—samples 3963-1 through 3963-6 and 3963-8 have wt% MgO ~ 7.7 -8.0, whereas 3963-7 and 3963-9 through 3963-11 have wt% MgO ~ 8.7 -9.0 (Fig. 4a, Fig. 6). Samples 3963-1 through 3963-6 and 3963-8 either belong to flow fronts or flow units #1 or #2 (Table 1). Samples 3963-7, 9, 10, and 11 were sampled from flow front #3 or beyond. Sample 3963-9, which has the highest wt% MgO (~ 9.0) was sampled from a lava channel.

Dive 3974 lavas show a more continuous distribution of wt% MgO and Mg#. The first flow front (3974-2) and the sheet flow sampled before the first flow front (3974-1) have consistently lower wt% MgO (~ 7.6) as compared to the mixed lobate and sheet flow unit (3974-3, 4, 7) beyond them (wt% MgO ~ 8.0 -8.1). The second flow front (3974-5, 6, 8) has wt% MgO similar to the first flow front (~ 7.6 -7.9), which is also lower

than the flow unit beyond it (3974-9, wt% MgO ~8.4). In contrast to the first two flow fronts, the third flow front (3974-10) has relatively high wt% MgO (~8.3). The sample closest to the axis, 3974-11, has the most primitive wt% MgO (~8.7) and Mg# (~64).

3.6.2. Trace Elements

Trace element abundances are reported in Table 3 and have also previously been reported by J. Hinds [M.S. Thesis, 2005]. Dive 3963 and 3974 lavas are all depleted N-MORB with depletions in the most incompatible trace elements (Fig. 5). In general, compatible trace element abundances like Ni and Sc correlate with wt% MgO and Mg#, indicating most of these lavas are derived from a similar parent magma. However, samples 3974-5 through 3974-9 have higher incompatible element ratios (e.g., La/Sm = 1.25-1.34 for samples 3974-5 through 3974-9) than the other samples from both flows (La/Sm = 0.96-1.17).

3.6.3. $^{87}\text{Sr}/^{86}\text{Sr}$ Isotopes

$^{87}\text{Sr}/^{86}\text{Sr}$ isotope compositions are reported in Table 4. All Dive 3963 and 3974 samples are indistinguishable from each other within analytical uncertainty with respect to $^{87}\text{Sr}/^{86}\text{Sr}$ (BU Triton TIMS) isotope compositions ($^{87}\text{Sr}/^{86}\text{Sr} = 0.702465\text{-}0.702570$; Fig. 6). These samples are also isotopically indistinguishable from previously measured N-MORB lavas from 9°-10°N EPR with respect to $^{87}\text{Sr}/^{86}\text{Sr}$ [Goss et al., in review; Sims et al., 2002; 2003] (Fig. 6). Despite the fact that the precision of the $^{87}\text{Sr}/^{86}\text{Sr}$ isotopic measurements are better (~10-20 ppm 2SE) than the total range of the sample

compositions (± 50 ppm, 2σ), there are no discernable systematics between isotope compositions and major and trace element compositions, suggesting that indeed, variations in the melting and magma chamber processes are responsible for the major and trace element variability and not variations in mantle source composition. This is especially notable with regards to the incompatible element enrichment we see in the middle samples (5, 6, 7, 8, 9) from dive 3974.

3.6.4. U-series Isotopes

^{238}U - ^{230}Th - ^{226}Ra , ($^{230}\text{Th}/^{232}\text{Th}$), and ($^{234}\text{U}/^{238}\text{U}$) isotopic compositions and U, Th and Ra abundances, as measured by isotope dilution (ID), are reported in Table 5.

3.6.4.1. ($^{234}\text{U}/^{238}\text{U}$)

All samples measured have ($^{234}\text{U}/^{238}\text{U}$) in equilibrium within analytical uncertainties ($\pm 0.5\%$) indicating that these samples have not suffered secondary alteration due to seawater-rock interaction following eruption. For submarine basalts, ($^{234}\text{U}/^{238}\text{U}$) is a sensitive indicator of alteration, as seawater is significantly enriched in ^{234}U relative to ^{238}U (for seawater, ($^{234}\text{U}/^{238}\text{U}$) = 1.14 ± 0.03 ; [Thurber, 1962; Ku et al., 1977; Henderson et al., 1993; Robinson et al., 2005]).

3.6.4.2. U, Th, and ($^{238}\text{U}/^{232}\text{Th}$)

U and Th concentrations measured by isotope dilution (ID) are consistent with, but more precise than, trace element data measured by ICP-MS at the University of

Florida (Table 3; Table 5). Samples collected during dive 3974 have variable U and Th concentrations and ($^{238}\text{U}/^{232}\text{Th}$) (U = 0.056-0.096 ppm, Th = 0.131-0.247 ppm, ($^{238}\text{U}/^{232}\text{Th}$) = 1.173-1.304), but can be grouped based on their U and Th compositions, as several lavas have essentially identical compositions. Each group likely represents individual eruptions or lava flows. Samples 3974-3 and 3974-4 can be grouped (U = 0.072 ppm, Th = 0.175-0.176 ppm), as can samples 3974-5 and 3974-6 (U = 0.95-0.96 ppm, Th = 0.245-0.247 ppm), and samples 3974-7, 3974-8, and 3974-9 (U = 0.088 ppm, Th = 0.225 ppm). Samples 3974-1, 3974-2, 3974-10, and 3974-11 are distinct and cannot be grouped with other samples (though we note that 3974-1 and 3974-11 have strikingly similar U and Th compositions, though they are spatially removed from each other). Samples from the middle of the dive traverse (i.e., 3974-3 through 3974-9) have higher U (0.072-0.096 ppm) and Th (0.175-0.247 ppm) concentrations and lower ($^{238}\text{U}/^{232}\text{Th}$) (1.173-1.242), and 3974-5 and 3974-6 have the highest U and Th concentrations and lowest ($^{238}\text{U}/^{232}\text{Th}$). The samples most depleted in U and Th also have the highest ($^{238}\text{U}/^{232}\text{Th}$). The four samples analyzed for U and Th concentrations from dive 3963 are generally more depleted than dive 3974 samples (U = 0.039-0.065 ppm, Th = 0.093-0.153 ppm, ($^{238}\text{U}/^{232}\text{Th}$) = 1.282-1.293), with the exception of 3963-5 (U = 0.079 ppm, Th = 0.208 ppm, ($^{238}\text{U}/^{232}\text{Th}$) = 1.150). Because only four samples here have been measured, systematic variations are not as apparent as they are with dive 3974 samples, and there are no clear groupings, although samples 3963-9 and 3963-10 have similar U and Th concentrations, and 3963-6, 3963-9, 3963-10 have similar ($^{238}\text{U}/^{232}\text{Th}$). Sample 3963-5 is

distinctly enriched with respect to U and Th and has lower ($^{238}\text{U}/^{232}\text{Th}$) relative the other samples.

Our U-Th ID concentrations for samples from the 2005-2006 eruption are within ~1% and ~2% of the U and Th ID concentrations, respectively, for all samples measured at the University of Hawaii, SOEST [K. Rubin, pers. comm.] and the University of Bristol, Isotope Group [J. Prytulak and T. Elliot, pers. comm.], with the exception of sample 4205-6 which is ~4-5% low for both U and Th relative SOEST and Bristol. As a group, these U and Th ID measurements are consistently different from ICP-MS measurements reported in Goss et al. [in review], which are ~5-10% high for U and ~3-5% high for Th, values that are roughly within the analytical uncertainties reported by the University of Florida (see Section 5). These samples show subtle variations (e.g., samples 4202-4 and 4202-6 are indistinguishable from each other and slightly more depleted than similarly indistinguishable samples 4205-5 and 4205-6), but are in general very similar and quite depleted (U = 0.053-0.058 ppm, Th = 0.123-0.136 ppm, ($^{238}\text{U}/^{232}\text{Th}$) = 1.291-1.305). These samples have compositions within the range of previously measured, recently erupted samples from the AST from 9°17'N-9°54'N EPR, including samples from the eruption in 1991-1992 (U = 0.042-0.068 ppm, Th = 0.105-0.169 ppm, ($^{238}\text{U}/^{232}\text{Th}$) = 1.167-1.239) [Rubin et al., 2005; Sims et al., 2002].

3.6.4.3. ($^{230}\text{Th}/^{232}\text{Th}$) and ($^{230}\text{Th}/^{238}\text{U}$)

Dive 3974 samples have ($^{230}\text{Th}/^{232}\text{Th}$) ranging from 1.297-1.437 and are positively correlated with ($^{238}\text{U}/^{232}\text{Th}$), as shown on an equiline diagram (Figure 7). ($^{230}\text{Th}/^{232}\text{Th}$) is

negatively correlated with U and Th elemental abundances (not shown). As with Th and U abundances, ($^{230}\text{Th}/^{232}\text{Th}$) compositions are identical within analytical uncertainties for samples 3974-3 and 3974-4; samples 3974-5, 3974-6, and 3974-7; and, samples 3974-7, 3974-8, and 3974-9. Samples 3974-5 through 3974-9 have higher U and Th abundances and lower ($^{230}\text{Th}/^{232}\text{Th}$) than all previously measured normal, N-MORB samples from 9°50'N EPR. Samples 3974-1, 3974-2, 3974-10, and 3974-11 have distinct ($^{230}\text{Th}/^{232}\text{Th}$). These samples, as well as 3974-3 and 3974-4, are similar in U and Th concentrations and ($^{230}\text{Th}/^{232}\text{Th}$) to previously measured N-MORB from 9°50'N EPR [Goldstein et al., 1993; 1994; Lundstrom et al., 1999; Sims et al., 2002; 2003; Waters et al., in review]. All dive 3974 samples have ^{230}Th excesses (i.e. ($^{230}\text{Th}/^{238}\text{U}$) >1), which range from 1.130-1.171, well within the range of values previously measured (1.087-1.190) in young axial and off-axis samples with ^{226}Ra excesses from 9°50'N EPR [Sims et al., 2002; 2003]. ^{230}Th excesses are correlated with U and Th concentrations, and Th/U.

Dive 3963 samples have ($^{230}\text{Th}/^{232}\text{Th}$) similar to axial lavas, ranging from 1.342-1.410, with the most enriched sample (3963-5) having the lowest ($^{230}\text{Th}/^{232}\text{Th}$) and fitting into the trend defined by dive 3974 lavas that extends to lower ($^{230}\text{Th}/^{232}\text{Th}$) and ($^{238}\text{U}/^{232}\text{Th}$) than previously reported for young N-MORB from 9°50'N EPR [Sims et al., 2002; 2003]. Like dive 3974 samples, dive 3963 samples also all have ^{230}Th excesses (1.122-1.165) that are comparable to those of young N-MORB from 9°50'N EPR [Sims et al., 2002; 2003].

The five samples from the 2005-2006 eruption are indistinguishable from lavas collected from the 1991-1992 eruption with respect to ($^{230}\text{Th}/^{232}\text{Th}$). Four of these samples

define a very narrow range of ($^{230}\text{Th}/^{232}\text{Th}$) (1.383-1.398), though sample NH-D1A has somewhat higher ($^{230}\text{Th}/^{232}\text{Th}$) than the other samples ($(^{230}\text{Th}/^{232}\text{Th})=1.451$). This value is still within uncertainties of the ($^{230}\text{Th}/^{232}\text{Th}$) reported for axial samples by Sims et al. [2002]. We do note that NH-D1A was sampled by dredge slightly off-axis and has a major element composition that is different from all other samples from the 2005-2006 eruption (e.g. lower wt% MgO, Al₂O₃, CaO, and higher wt% TiO₂) [Goss et al., in review].

3.6.4.4. (^{226}Ra)-(^{230}Th)

All dive 3974 samples have large ^{226}Ra excesses ranging from 1.86-2.43 (Figure 8; Table 5) and trend to lower values than previously measured axial samples (2.01-2.89; [Rubin et al., 2005; Sims et al., 2002]). As with all other U-series concentration and isotope measurements, ^{226}Ra concentrations and ($^{226}\text{Ra}/^{230}\text{Th}$) can be used to group these samples (again, samples 3974-1, 2, 10, and 11 are all different from 3974-3 and 4, 3974-5 and 6, and 3974-7, 8, and 9). We note that ($^{230}\text{Th}/^{232}\text{Th}$) for sample 3974-7 is more similar to samples 3974-5 and 6 than to 3974-8 and 9, but given the similarity in the U, Th, and ^{226}Ra concentrations among samples 3974-7, 8, and 9, and the distinct and consistent U, Th, and ^{226}Ra concentrations of samples 3974-5 and 6, we assert that 3974-5 and 6 should be grouped, and samples 3974-7, 8, and 9 should be grouped. The samples with the highest ^{226}Ra excesses include both the lavas most proximal and distal to the axis: 3974-1, 3974-2, 3974-10, and 3974-11. Lavas from the middle of the dive transect have the lowest ^{226}Ra excesses (1.86-1.96) and highest [^{226}Ra] (60.75-69.76 fg/g). We also note the

gross similarity between samples 3974-1 (this study) and 2771-1 (reported in [Sims et al., 2003]) with respect to major element, trace element, and $^{87}\text{Sr}/^{86}\text{Sr}$ isotope compositions, and U-Th- ^{226}Ra concentrations and isotopic compositions. Sample 2771-1 was collected just to the south and west of sample 3974-1, and both are immediately adjacent to a prominent pillow ridge, as seen in the side scan sonar imagery (Figure 1).

All dive 3963 samples also have significant ^{226}Ra excesses (1.21-2.73). ^{226}Ra excesses are smallest for those samples farthest from the AST and increase with decreasing distance to the axis (east to AST: 3963-6, 3963-5, 3963-9, 3963-10). Although both 3963-9 and 3963-10 have indistinguishable ^{226}Ra excesses, all samples have distinct [^{226}Ra], implying that although these two lavas may be of a similar age, in contrast to dive 3974 samples, none of these samples was collected from the same flow unit.

Samples from the 2005-2006 eruption have ^{226}Ra excesses ranging from 2.41-2.56, with the exception of sample NH-D1a, which has an anomalously low ($^{226}\text{Ra}/^{230}\text{Th}$) of 1.11 (Table 5, Figure 8). Because we cannot satisfactorily explain this low ^{226}Ra excess with existing petrogenetic models, we suspect that this dredged sample is actually older and not part of the recent eruption. Major and trace element systematics are also not consistent with derivation from the 2005-06 eruption [Goss et al., in review]. Regardless, it is not critical to our current analysis, and we exclude this measurement from our age calculations and any further discussion. Samples 4202-4 and 4202-6 have indistinguishable [^{226}Ra] and ($^{226}\text{Ra}/^{230}\text{Th}$) compositions, as do samples 4205-5 and 4205-6, yet these two groups have compositions that are distinct from each other. These ^{226}Ra systematics match [U] and [Th] systematics, as discussed above. As compared to

previous ^{226}Ra data obtained on samples from the AST, these samples have slightly lower ($^{226}\text{Ra}/^{230}\text{Th}$) at a given ($^{230}\text{Th}/^{238}\text{U}$) (Figure 8).

Furthermore, because ^{230}Th does not decay appreciably over the time it takes for ^{226}Ra to return to secular equilibrium with ^{230}Th (about five half-lives of ^{226}Ra , or ~ 8 kyrs), both measured ($^{230}\text{Th}/^{232}\text{Th}$) and ($^{230}\text{Th}/^{238}\text{U}$) have not changed after eruption and can be interpreted as primary features of these lavas [Sims et al., 2002; 2003]. This is supported by the coherency of these data with data from the 1991-1992 eruption that show a negative correlation between ^{230}Th excesses and MgO (wt%) and Mg#. Finally, the presence of ^{226}Ra excesses indicates that all dive 3974 and 3963 lavas must have erupted within the last ~ 8 kyrs.

3.7. DISCUSSION

We seek to improve our understanding of ridge crest volcanic construction, and in particular, to place age constraints on the formation of the shingled terrain and the geochemical and temporal relationships between flow lobes. In the following section, we investigate whether measurements of U, Th, and ^{226}Ra concentrations and isotopic disequilibria can resolve geochemical differences among a suite of lavas that appear geochemically homogeneous by less sensitive metrics, and we assess whether ^{230}Th - ^{226}Ra model ages are sufficient for discerning age variations in lavas that appear to be of similar age based on limited variations in sediment cover and weathering. Finally, we

interpret our results in light of previous studies of neo-volcanic zone construction at 9°-10°N EPR and use these constraints to modify existing models.

3.7.1. Geochemical Relationships Among Samples and Flow Units

Because of the apparent geochemical similarities among dive 3974 samples, we conducted a cluster analysis on dive 3974 major element, trace element, and U-series data. Details of the cluster analysis and associated dendrograms (Figure A1) are reported in Appendix B. Given the geochemical similarities among many of these samples, we interpret samples that belong to the same cluster of the U-series dendrogram and were sampled adjacent to each other on the seafloor as belonging to the same flow unit. We use the U-series data for this purpose over the major and trace element data because the U-series data are most precise and least affected by fractional crystallization. Hence, based on our geochemical observations, and in keeping with geological observations as much as possible, we group 3974-3 and 3974-4 as ‘Flow 3,’ samples 3974-5 and 3974-6 as ‘Flow 4,’ and samples 3974-7, 3974-8, and 3974-9 as ‘Flow 5.’ We interpret samples 3974-1, 3974-2, 3974-10, and 3974-11 as belonging to distinct flow units, and we refer to them as ‘Flow 1,’ ‘Flow 2,’ ‘Flow 6,’ and ‘Flow 7’ (Table 6). Although significant similarities exist between other samples (e.g., between 3974-1 and 3974-11 and between Flow 3 samples and 3974-10), these samples were not collected from the same flow unit as defined by side-scan sonar imagery. Furthermore, although 3974-1 and 3974-11 have nearly identical U and Th concentrations, they have different ($^{230}\text{Th}/^{232}\text{Th}$); in contrast,

Flow 3 samples and 3974-10 have similar ($^{230}\text{Th}/^{232}\text{Th}$) but different U and Th concentrations.

Figure 9 shows Th concentration variations with longitude for dive 3974 and 3963 samples. The variability of Th concentrations among samples collected from within the AST from $9^{\circ}17'\text{N}$ - $9^{\circ}54'\text{N}$, including a few samples confirmed to be from the 1991-1992 eruption based on ^{210}Po - ^{210}Pb dating [Rubin et al., 2005; Sims et al., 2002] and samples from the 2005-2006 eruption, are also shown for comparison. Based on the extent of geochemical diversity within documented, discrete eruptions and the similarities in the geochemical compositions of lavas erupted during two eruptions thirteen years apart, it seems likely that at the least, Flows 4 and 5 originated from an eruption that was distinct from the eruptions that sourced Flows 1, 2, 3, 6, and 7. It also seems possible, if not probable, that each Flow unit originated from a different eruption. Because the four samples from dive 3963 for which we measured U-series concentrations and isotopic ratios all appear to have significantly different U, Th, and ^{226}Ra concentrations, we do not attempt to group these into flows. Instead, we also interpret each sample as belonging to a different flow unit. Lastly, there appear to be no geochemical relationships among dive 3963 and dive 3974 samples (e.g., Figures 4B, 8, 9). This suggests asymmetry either in the flow emplacement distribution of individual eruptions at this latitude [cf., Soule et al., 2009] or in the rate of seafloor resurfacing at this latitude. Alternatively, it cannot be ruled out that the sample coverage in this area is too sparse to recognize patterns in lava geochemistry about the axis.

3.7.2. Age Constraints

Table 6 shows the results of ^{230}Th - ^{226}Ra trend line model age dating and maximum and minimum ^{230}Th - ^{226}Ra ages for all samples (as described in section 3), as well as average lava flow unit ages. ^{230}Th - ^{226}Ra model ages were calculated using the model age equation from Sims et al., [2003]:

$$T = -\frac{1}{\lambda_{226}} \ln \frac{(^{226}\text{Ra}/^{230}\text{Th})_m - 1}{(^{226}\text{Ra}/^{230}\text{Th})_0 - 1} ,$$

where λ_{226} is the decay constant for ^{226}Ra ($4.332 \times 10^{-4} \text{ yr}^{-1}$), subscript (m) refers to the measured sample activity ratio, and subscript (0) refers to the initial disequilibria upon eruption. Table 6 reports model age uncertainties that include only analytical uncertainties on the $(^{226}\text{Ra}/^{230}\text{Th})$, which assumes that $(^{226}\text{Ra}/^{230}\text{Th})_0$ is known exactly. Because this is not the case, we have also calculated minimum and maximum model ages, as described above in section 3, though these ages most certainly overestimate the model age uncertainties. More robust age uncertainties require additional assessment of the error associated with uncertainty in initial $(^{226}\text{Ra}/^{230}\text{Th})$, which amounts to the uncertainty in fitting the zero-age data with a trend line.

We have calculated a double-error, maximum likelihood, non-linear least squares fit for a line [Sohn and Menke, 2002] to both data obtained on samples collected within the AST north of $9^{\circ}37'\text{N}$ EPR [Sims et al., 2002], and data obtained in this study for samples collected from flows associated with the 2005-2006 eruption (Figure 8). Many of the samples collected from the AST from north of $9^{\circ}37'\text{N}$ are presumed to have erupted during the 1991-1992 eruption including several samples whose eruption dates have been

constrained to the 1991-1992 eruption by ^{210}Po - ^{210}Pb dating [Rubin et al., 1994].

Estimates of standard error (90% confidence limits) on the slope (+5.3/-7.6) and intercept (+8.5/-6.1) were calculated by bootstrapping one thousand samples. We performed an outlier test by adding one sample from dive 3974 and 3963 to the zero-age data set (1991-92 and 2005-06 data), regressing these data with the slope and intercept set at -17.71283 \pm 8(s^2) and 22.66071 \pm 8(s^2), respectively, calculating the Studentized residuals for this data set, and comparing these samples to a critical value for outliers (based on the Bonferroni inequality) at the 95% confidence level [Sohn and Menke, 2002]. This procedure was repeated for all dive 3974 and 3963 samples. Using this method, only sample 3963-6 ($(^{226}\text{Ra}/^{230}\text{Th}) \sim 1.21$) was identified as an outlier at the 95% confidence interval. Thus, the scatter about the “zero-age” trend line results in poorly constrained initial $(^{226}\text{Ra}/^{230}\text{Th})$ at a given $(^{230}\text{Th}/^{238}\text{U})$, such that only one sample can be identified as belonging to a population that is distinct in both $(^{230}\text{Th}/^{238}\text{U})$ and $(^{226}\text{Ra}/^{230}\text{Th})$ from the zero-age population at the 95% confidence level. This result suggests that although flow units consisting of multiple samples can be distinguished based on geochemistry, the variability of $(^{226}\text{Ra}/^{230}\text{Th})$ and $(^{230}\text{Th}/^{238}\text{U})$ of zero-age samples prevents us from distinguishing these distinct flow units on the basis of U-series model ages. Instead, we can only say with certainty that with the exception of sample 3963-6 (3.6-5.1 ka), all samples are $< \sim 2$ ka.

3.7.3. Reconciling Geochemical and Model Age Observations with Seafloor

Observations

Figure 10 compares flow divisions based on geochemistry with those based on general *in situ* dive observations and the assumption that flow units consist of a terminal pillow flow front and an internal flow body of lobate and sheet flows. Sample 3974-2 is defined from *in situ* geological observations as being from the first flow front, but despite its close proximity to overlying lobate and sheet samples 3974-3 and 3974-4, it is geochemically distinct (Tables 1, 5; Figures 9, 11). However, samples 3974-3 (sheet) and 3974-4 (lobate) were interpreted as being collected from the same flow unit (Flow 3) consisting of mixed lobate and sheet flows, and this is confirmed by the geochemistry. Samples 3974-5 and 3974-6 are also confirmed by geochemistry as both belonging to a different pillow front, as was interpreted based on seafloor observations. Based on seafloor observations, sample 3974-8 was suggested as belonging to the same flow front as samples 3974-5 and 3974-6, and sample 3974-7 (sheet) was interpreted as being older than and underlying 3974-5, 3974-6, and 3974-8. However, although our model ages suggest that samples 3974-5 and 3974-6 may indeed be younger than 3974-7, from side-scan sonar imagery and ABE bathymetry (Figures 2A, 2C, and 11), it can be seen that 3974-7 lies at the western extent of a flow lobe that appears unrelated to flow 4. Additionally, from cluster analysis of the geochemistry (see Discussion above and Appendix B), we can confidently group 3974-7 with 3974-8 and 3974-9, which were all sampled from the same flow lobe as identified in side-scan sonar and bathymetric maps (Figures 2A, 2C, and 11). Interestingly, sample 3974-8 was taken from a pillow flow

front overlying sheet flow sample 3974-7; thus, it seems likely that flow fronts may not always represent the edges of flow units, and that breakouts can and do occur, complicating the identification of flow units from remote sensing techniques. Given the confusion surrounding *in situ* observations of the relationships among samples 3974-5, 3974-6, 3974-7, and 3974-8, we suggest that the inherently small field of view from the submersible and natural spatial variability that undoubtedly exists on an outcrop scale led to confusion about the relative locations of these different sampling sites. Note that samples 3974-5 and 3974-6 are north of 3974-7, -8, and -9 (Figures 2A, 2C, 10, 11).

Furthermore, photo observations of sediment cover suggest that samples 3974-5 and 3974-6 (i.e., Flow 4) are younger than adjacent Flows 3 and 5, and this observation is supported by the younger average model age of Flow 4 (~150 yrs) as compared to that of Flow 3 (~650 yrs) and Flow 5 (~750 yrs) (see Table 6, Figures 10, 11). Sample 3974-10 was interpreted as belonging to a pillow flow front that is distinct from Flow 5, and the morphological difference is also evidenced by a geochemical difference and an apparent age decrease (750 yrs to <150 years; Figure 10). Based on geochemical evidence, sample 3974-11 belongs to a different flow unit than 3974-10, but there is no evidence of a pillow front between the two samples, only a change in morphology. Thus, because pillow flow fronts were used to identify geologically distinct flow units, and there are no high relief pillow flow fronts between samples 3974-10 and 3974-11, *in situ* observations were unable to distinguish these two flow units (Figures 2A, 2C, 10, and 11). In general, there is a lack of pillow flow fronts within ~1 km of the AST, and this may be due to higher effusion rate near the AST, smoother substrate, or a propensity for EPR lavas to

travel >1 km. If pillow flow fronts do not necessarily occur at the termini of flows near the AST, for whatever reason, it will be more difficult to identify flow fronts in ABE bathymetric and side-scan sonar maps near the AST with the same ease as it is farther than ~1 km off-axis up to the edge of the neo-volcanic zone.

Geochemical constraints are consistent with seafloor observations made during dive 3963. Sample 3963-6 was interpreted as a sheet flow collected from below the pillow flow front of the “second” flow unit (sample 3963-5), and 3963-9 as a channel flow that is distinct from 3963-10, a pillow flow front (Table 1). In addition, based on relative sediment cover, sample 3963-6 was interpreted as being older than sample 3963-5 (Table 1, Figures 10, 11), and our model age calculations indicate this is true. At a qualitative level, it also appears that samples 3963-9 and 3963-10, which are closest to the axis, have much younger-looking ($^{226}\text{Ra}/^{230}\text{Th}$)-($^{230}\text{Th}/^{238}\text{U}$) systematics—they have maximum ^{230}Th - ^{226}Ra model ages that are less than the minimum model ages of samples 3963-5 and 3963-6. Thus, it appears that at least on the east side of the AST at 9°50'N, there is a general trend of increasing lava age with distance away from the AST.

In general, side-scan sonar and ABE bathymetric maps appear to correspond quite well with geochemical observations. In contrast, significant discrepancies between geochemical and seafloor observations exist, particularly with respect to the grouping of samples collected over distances significantly greater than a few hundred meters (Figure 10). Individual dive observations at sample locations (Table 1, Figure 11) are qualitatively consistent with model age constraints (Table 6). In general, the close correspondence of model ages with relative ages from photo observations suggests that

the statistical approach to our model age uncertainties is conservative. Based on this information, and given the inherent “near-sightedness” of submarine observations, we strongly recommend that high-resolution bathymetry and side-scan sonar imagery be used as maps for real-time seafloor navigation in complicated geological terrain. We also note that lower resolution maps than that of ABE bathymetry (~5m/pixel) do not show the detail necessary for resolving flow units at this scale.

3.7.4. Extrusive Crustal Construction at 9°-10°N EPR: The Origin of Shingled Terrain

Side-scan sonar, magnetic, and U-series and paleointensity dating studies at 9°50'N EPR have shown that the neo-volcanic zone extends up to ~2-4 km on each side of the AST [Bowles et al., 2006; Fornari et al., 1998; Goldstein et al., 1994; Schouten et al., 1999; Sims et al., 2003; Soule et al., 2009]. However, the surface construction of the neo-volcanic zone and the formation of the ubiquitous shingled flow lobes have not been satisfactorily explained. In a general sense, the thickening of seismic layer 2A (the extrusive layer) within the extent of the neo-volcanic zone can be well explained by a bimodal lava emplacement model in which ~50% of the extrusive volume is made up of small lava flows confined to the AST and 50% is made up of large flows that overflow the AST and spill out onto the ridge flanks [Hooft et al., 1996]. Presumably, shingled terrain is the surface expression of the large flows, but whether the shingle-like texture arises from stratigraphic superposition of flows, stagnation of individual flows forming

pillow fronts and subsequent breakouts of these same flows, or subsurface lava flow through existing lava tubes remains unclear.

Taken together, the geochemical concentration data (in particular the high-precision U-Th-²²⁶Ra ID data) and the ²³⁰Th-²²⁶Ra model ages are consistent with simple stratigraphic superposition of lavas emplaced by surface flow. As discussed above in section 7.1, the geochemical variations are large enough such that samples from adjacent flow units, as determined from ABE bathymetry and side-scan sonar, are not likely from the same eruption. Furthermore, there is sufficient evidence from side-scan sonar and seafloor observations to rule out an off-axis eruptive origin for all samples except 3974-1, which is geochemically similar to sample 2771-1 from Sims et al. [2003], and both may be related to a nearby off-axis pillow mound (see section 6.4.4. above, Figure 1). Although there is some limited evidence for breakouts from pillow lava fronts (see section 7.3), these breakouts do not appear to be a dominant, ubiquitous feature at flow fronts, and in general, do not produce areally extensive lava units. This is consistent with recent mapping of the 2005-2006 eruption that documented pillow lavas primarily at flow termini [Fundis et al., 2009].

Because dive 3974 and 3963 lava ages are sufficiently young such that we cannot statistically resolve sample ages within a ~2 kyr age population, we cannot rule out the possibility of subsurface transport of flows by lava tubes [e.g., Gregg and Fornari, 1998], which would cause younger flows to be emplaced farther from the axis than earlier flows. It should be noted that even if absolute lava ages could be determined for such young lavas, this type of plan-view, lava age distribution can also result from axis-parallel or

oblique flow of lava due to variable seafloor topography or fault/pillow ridge embankment, and does not necessarily preclude simple superposition of flows [cf. Escartin et al., 2007, Figure 3d].

Despite the lack of age constraints, not only do the surprisingly systematic geochemical variations distinguish individual flow units, but they also place constraints on the morphological makeup of flow units, the relationships between adjacent flow units, and the cross-axis extent of flow units (Figure 2). From these data, we know that samples from within an individual, chemically distinguishable flow unit may have different morphologies (e.g., Flow 3 is composed of both sheet and lobate morphologies whereas Flow 5 is composed of sheet, lobate, and pillow morphologies), and thus morphological contacts are not diagnostic of a geological contact between discrete lava flows. Instead, such morphological changes reflect variations in the local volume flux due to changes in the underlying substrate, slope, and/or effusion rate at the vent [e.g., Gregg and Fink, 1995; 2000].

3.7.5. The Youth of the Neo-volcanic Zone

One of our most striking results is the young model ages of lavas beyond the edge of the neo-volcanic zone as it has been interpreted from remote sensing data (Figure 2; Table 6; Escartin et al., 2007; Soule et al, 2005). These data suggest that the neo-volcanic zone is truly “young”: lavas within the neo-volcanic zone are much younger than their spreading rate ‘age’, and this can be explained by lavas that overflow the AST and flow down the ridge flanks. In fact, the age constraints from this study and other dating studies

at 9°50'N EPR [Bowles et al., 2006; Sims et al., 2003] are consistent with the region up to ~2 km (~36 kyrs spreading age) on either side of the AST at 9°50'N EPR being mostly covered by lavas less than ~2 ka. We dated only one lava sample, from the east side of the AST (sample 3963-6), that appears to be older than ~2 ka, but at ~5 kyrs (paleointensity of ~44.5 μ T is consistent with this age; [Bowles et al., 2006]), it is still considerably younger than its spreading age (~31 kyrs). Given similar age constraints obtained from ^{238}U - ^{230}Th and ^{230}Th - ^{226}Ra model age dating in other studies [Sims et al., 2003; Waters et al., in review], it appears that lavas outside the neo-volcanic zone are older (>5-10 kyrs), typically have equilibrium ($^{226}\text{Ra}/^{230}\text{Th}$) values, have paleointensities generally lower than the present-day field, and have ages that cannot be resolved from the spreading rate 'age' with lower resolution ^{238}U - ^{230}Th or ^{235}U - ^{231}Pa model ages. Overall, it appears that at 9°50'N, there is a bimodal distribution of lava ages (either >8 kyrs outside of the neovolcanic zone or <2 kyrs within the neovolcanic zone).

This bimodal age distribution may suggest that the region at 9°50'N EPR has experienced a period of increased volcanic activity for the past ~2 kyrs, with relatively frequent large volume flows reaching ~1-2 km on either side of the AST. This model is consistent with recent observations of the 2005-06 flow distribution and AST geometry at 9°-10°N EPR [Soule et al., 2009] and evidence from 17°-18°S EPR [Cormier et al., 2003] that support cyclic changes in magmatism over time. However, Bowles et al. [2006] find that age offsets of ~5-10 kyrs between neo-volcanic lavas and lavas on highly tectonized 'old' crust can be well explained by a unimodal lava emplacement model that links eruption volume linearly with time between eruptions [Bowles et al., 2006]. In this

model, the time between eruptions is not linked to the spreading rate but is instead determined by a standard gamma distribution with a median scaled to the median time between eruptions. Bowles et al. [2006] find ~70 year recurrence interval and a dike location with a standard deviation of ~100 m is a good match with their paleointensity observations. Their model shows that the time elapsed between flows preserved on the seafloor beyond ~1 km from the AST is >250 yrs [Bowles et al., 2006, Figure 13e]. At the sampling level represented by the Dive 3974 samples on the west flank, the average recurrence interval of eruptions that reach distances ~0.8-2 km from the AST is at most ~285 years (~330 yrs if we exclude 3974-1 on the basis that it erupted off-axis during construction of a pillow ridge). Although there are likely additional flow units to be identified in a cross-axis traverse of this section of the ridge flank, this recurrence interval is reasonably consistent with the model of Bowles et al. [2006]. Furthermore, we observe more frequent eruptions reaching ~1-2 km off-axis in this location (~6-7 per 2 kyrs) than the model of Bowles et al. [2006] predicts (2-3 per 2 kyrs).

3.7.6. Implications for Lava Stratigraphy

These observations have significant implications for volcanic stratigraphy, particularly for interpretations of and correlations among drill cores sampling the extrusive crust of a fast-spreading MOR. For example, the significance of subsurface lava flow and lava tubes is unclear from our seafloor mapping. If subsurface flow plays an important role in off-axis lava transport, it is likely that drill cores will sample a larger number of lava flows than we observe on the seafloor. Furthermore, if this is the case, it

cannot be assumed that the oldest flows are on the bottom of the core, and the youngest flows are at the top of the core. Although this may be the general trend when considering the entirety of the extrusive pile, in more detail, younger flows may be intercalated with older flows. We also observe that individual flow units may be composed of multiple lava morphologies (e.g., sheet vs. lobate. vs. pillow). This may result in variable thicknesses of individual flow units (e.g., pillow flow thicker than sheet flow); thus, correlating flow units based on flow thickness or morphology will likely often result in erroneous interpretations of stratigraphic relationships among spatially separated drill cores.

Additionally, plan-view lava flow relationships are complicated, as has been observed in this study and mapping studies of the 1991-92 and 2005-06 eruptions (Fornari et al., 1998; 2004; Soule et al., 2007; 2009). Lava flow geometry is not symmetrical about the ridge axis, and individual flow lobes of a single eruption extend to different distances off-axis at any given latitude. As a result, lava flow stratigraphy at any given location may be nearly unique, and therefore, a drill core section at one location may not be representative of any other location. In turn, we suggest, on the basis that the AST is the source of most volcanic activity at 9°-10°N EPR, that drilling and dating the extrusive section near the AST will produce the most complete record of eruptions and eruption ages, allowing for the best estimate of eruption frequency, with the caveat that not all eruptions/lava flows will be observed at any given latitude. Also, a lava flow present at the AST may or may not exist in the off-axis stratigraphy at a given location, depending on the distribution of that flow about the axis.

A second effect of complicated, plan-view, lava geometry is that the presence of an individual lava flow lobe at a given distance from the axis does not mean that the eruption that sourced that flow was large in volume—it simply indicates that a lava flow from an individual eruption reached a certain distance off-axis in one location. More extensive, detailed geochemical mapping, especially mapping done using trace element concentrations measured by isotope dilution, would be necessary in any attempt to correlate flow units along and across the axis and to determine flow volumes of individual eruptions. Thus, we are careful in this study to not interpret flow lengths as representative of flow volumes.

3.7.7. Rapid Temporal Variations in Melt Supply

A recent dating study of lavas at the very fast (14.6 cm/yr full spreading rate) spreading ridge at 17°30'S EPR used geochemical data, side scan sonar imaging, and submersible observations to map out several different flow fields. Based on the age constraints obtained from coupled paleointensity and ($^{210}\text{Pb}/^{226}\text{Ra}$) measurements of representative samples from each of these flows, they argued that at least five geochemically distinct eruptive episodes occurred over the last ~500 years [Bergmanis et al., 2007]. Indeed, Bergmanis et al. [2007] argued that significant major and trace element variations occurred over surprisingly short time scales, indicating variations in mantle melting processes at rates at least as frequent as eruption rates. Notably, even individual flow fields exhibit variable lava compositions.

The compositional variability among adjacent flow ‘units’ as we define them, which are markedly more divisive than the flow ‘fields’ described in Bergmanis et al. [2007], is often great enough such that each flow unit was probably sourced from a temporally distinct eruption. Given that all dive 3974 and 3963 samples (except one) were erupted within the last ~2 kyrs, the significant compositional variability among ridge flank lavas suggests relatively rapid variability in the parental magma compositions fed to the AMC, similar to that observed by Bergmanis et al. [2007]. As stated above, the average recurrence interval of eruptions that reach from 0.8-2 km is at most ~300 years. However, there are most certainly additional flow units to be identified in a cross-axis traverse of this section of the ridge flank, especially if pillow flow fronts do not mark the boundary between all flow units, as discussed above in section 7.3. Furthermore, as discussed by Bowles et al. [2006], eruption frequency may be linked with eruption volume; thus, an eruption size-frequency distribution is probably more meaningful than an average recurrence interval. Unfortunately, we do not have sufficient age constraints or clearly mapped flow contacts along and across the ridge flank to construct such a distribution. Nevertheless, our data suggest measurable mantle source variability on the order of less than a few hundred years.

3.8. CONCLUSIONS

In this study, we attempt to constrain the timing of emplacement and formation of different lobes of ‘shingled’ neo-volcanic terrain, the dominant feature observed in side-

scan sonar at 9°-10°N EPR. To this end, we have measured samples collected in a dive traverse across the western and eastern ridge flank for major element, trace element, $^{87}\text{Sr}/^{88}\text{Sr}$, and ^{238}U - ^{230}Th - ^{226}Ra isotope compositions. One of the most striking features of dive 3974 lavas is the similarity in major element, trace element, and U-series compositions of sets of two or three samples. Although the trace element concentrations strongly suggest that samples may be grouped (Figure 5), the U-Th- ^{226}Ra ID, ($^{230}\text{Th}/^{232}\text{Th}$), and ($^{226}\text{Ra}/^{230}\text{Th}$) compositions are identical within analytical error for several sets of samples (Figures 7, 8; Table 5). We believe that identical ^{238}U - ^{230}Th - ^{226}Ra systematics for a set of samples virtually necessitates that these samples are of the same age and therefore belong to the same lava flow. Hence, we interpret samples with identical U, Th, and ^{226}Ra concentrations as belonging to the same lava flow.

Seafloor dive observations and geochemical observations are sometimes discrepant, and this may be related to limited visibility in *Alvin* and lateral variability inherent in the emplacement of overlapping lava. In contrast, side-scan sonar and ABE bathymetry are relatively consistent with geochemical observations. The one exception to this may be that high relief pillow flow fronts, which can be observed in both bathymetric and side-scan sonar maps, do not always mark absolute boundaries delimiting the edges of flow units. Additionally, morphology is not a good indicator of flow boundaries, as a single flow unit may consist of pillow, sheet, and lobate morphologies. Rather, morphology is likely related to slope, substrate, or effusion rate properties.

Additional samples collected from the 2005-2006 eruption at 9°50'N EPR have been analyzed for U-Th- ^{226}Ra abundances and isotopic compositions to augment the

existing ^{230}Th - ^{226}Ra dataset and provide a more robust zero-age ($^{230}\text{Th}/^{238}\text{U}$)-($^{226}\text{Ra}/^{230}\text{Th}$) trend line from which to calculate unknown sample model ages. However, the large amount of scatter about the zero-age trend line indicates large uncertainties in initial ($^{226}\text{Ra}/^{230}\text{Th}$) disequilibria, and statistical analysis indicates that of all dive 3974 and 3963 samples, only sample 3963-6 has a sample age that is significantly different from the zero-age trend line (95% confidence limit). All other samples are surprisingly young (probably $\ll 2000$ yrs) and this suggests that the neo-volcanic zone marks a ~ 0 -2 km wide swath on either side of the axis that is similarly young.

We also note the rather large range in chemical variability documented by flows in this transect, and we reach a conclusion similar to that of Bergmanis et al. [2007], that variations in chemistry are rapid—perhaps even as rapid as the eruption frequency. In addition, with seven documented large volcanic events within the span of ~ 2000 years, the maximum eruption recurrence interval of eruptions reaching up to ~ 1 -2 km on the west flank at $9^{\circ}50'\text{N}$ EPR is ~ 300 years, which is more frequent than, but consistent with that predicted by Bowles et al. [2006].

Acknowledgments. This study was funded by NSF OCE-0623838 to K.W.W. Sims and S.A. Soule and NSF OCE-0527053 to K.W.W. Sims. CLW thanks Jeremy Inglis and Ethan Baxter for assistance with TIMS Sr isotopic analyses at Boston University, and Jurek Blusztajn for assistance with Sr isotopic analyses at WHOI. Paul Henderson, Matt Charette, and Christian Miller are especially thanked for their help preparing a new ^{228}Ra spike for isotope dilution measurements.

References

- Ball, L., K. Sims, S. Weyer, and J. Schweiters (2008), Measurement of $^{234}\text{U}/^{238}\text{U}$ and $^{230}\text{Th}/^{232}\text{Th}$ in volcanic rocks using the Neptune PIMMS, *J. Anal. At. Spectrom.*, 23, 173-180, doi: 10.1039/b703193a.
- Batiza, R. and Y. Niu (1992) Petrology and magma chamber processes at the East Pacific Rise-9°30'N, *J. Geophys. Res.*, 97, 6779-6797.
- Bergmanis, E.C., J. Sinton, and K.H. Rubin (2007) Recent eruptive history and magma reservoir dynamics on the southern East Pacific Rise at 17°30'S, *Geochem., Geophys., Geosyst.*, 8(12), doi: 10.1029/2007GC001742.
- Bowles, J., J.G. Gee, D.V. Kent, M.R. Perfit, S.A. Soule, and D.J. Fornari (2006), Paleointensity applications to timing and extent of eruptive activity, 9°-10°N East Pacific Rise, *Geochem., Geophys., Geosyst.*, 7(6), doi:10.1029/2005GC001141.
- Carbotte, S.M. and K.C. Macdonald (1992), East Pacific Rise 8°-10°30'N: Evolution of ridge segments and discontinuities from SeaMARC II and three-dimensional magnetic studies, *J. Geophys. Res.*, 97, 6959-6982.
- Christeson, G.L., G.M. Purdy, and G.J. Fryer (1994), Seismic constraints on shallow crustal emplacement processes at the fast-spreading East Pacific Rise, *J. Geophys. Res.*, 99, 17957-17973, 1994.
- Christeson, G.L., G.M. Kent, G.M. Purdy, and R.S. Detrick (1996), Extrusive thickness variability at the East Pacific Rise, 9°-10°N, constraints from seismic techniques, *J. Geophys. Res.*, 101, 2859-2873.
- Cochran, J.R., D.J. Fornari, B.J. Coakley, R. Herr, and M.A. Tivey (1999), Continuous near-bottom gravity measurements made with a BGM-3 gravimeter in DSV Alvin on the East Pacific Rise crest near 9°30'N and 9°50'N, *J. Geophys. Res.*, 104, 10,841-10,861.
- Cooper, K.M., S.J. Goldstein, K.W.W. Sims, and M.T. Murrell (2003), Uranium-series chronology of Gorda Ridge volcanism: new evidence from the 1996 eruption, *Earth Planet. Sci. Lett.*, 206, 459-475.
- Cormier, M.-H., W.B.F. Ryan, A.K. Shah, W. Jin, A.M. Bradley, and D.R. Yoerger (2003), Waxing and waning volcanism along the East Pacific Rise on a millennium time scale, *Geology*, 31(7), 633-636.
- Duncan, R.A. and L.G. Hogan (1994), Radiometric dating of young MORB using the ^{40}Ar - ^{39}Ar incremental heating method, *Geophys. Res. Lett.* 21, 1927-1930.
- Detrick, R.S., P. Buhl, E.E. Vera, J.C. Mutter, J.A. Orcutt, J.A. Madsen, and T.M. Brocher (1987), Multi-channel seismic imaging of a crustal magma chamber along the East Pacific Rise, *Nature (London)* 326(6108), 35-41.
- Elkins, L.E. (2009), Basalt Petrogenesis Beneath Slow- and Ultraslow-Spreading Arctic Mid-Ocean Ridges, Ph.D. Thesis, 139 pp., MIT/WHOI Joint Program in Oceanography, Woods Hole, MA.
- Escartin, J., S.A. Soule, D.J. Fornari, M.A. Tivey, and H. Schouten (2007), Interplay between faults and lava flows in construction of the upper oceanic crust: The East Pacific Rise crest 9°25'-9°58'N, *Geochem., Geophys., Geosyst.*, 8(6), doi: 10.1029/2006GC001399.

- Fornari, D.L., R. Haymon, M. Perfit, T.K.P. Gregg, and M.H. Edwards (1998), Axial summit trough of the East Pacific Rise, 9-10°N: Geological characteristics and evolution of the axial zone on fast spreading mid-ocean ridges, *J. Geophys. Res.*, *103*, 9827-9855.
- Fornari, D.L., M. Tivey, H. Schouten, M. Perfit, D. Yoerger, A. Bradley, M. Edwards, R. Haymon, D. Scheirer, K. Von Damm, T. Shank, and A. Soule (2004), Submarine Lava Flow Emplacement at the East Pacific Rise 9°50'N: Implications for Uppermost Ocean Crust Stratigraphy and Hydrothermal Fluid Circulation, in *Mid-Ocean Ridges: Hydrothermal Interactions between the Lithosphere and Oceans*, *Geophys. Monogr. Ser.*, vol. 148, edited by C.R. German, J. Lin, and L.M. Person, pp. 311, AGU, Washington, D.C.
- Fundis, A.T., S. Soule, D.J. Fornari, and M.R. Perfit (2009), Intra-flow morphology variations within a single submarine flow: the 2005-2006 East Pacific Rise eruption, *EOS Trans. AGU*, *90*(52), Fall Meet. Suppl., Abstract V51D-1725.
- Goldstein, S.J., M.T. Murrell, D.R. Janecky, J.R. Delaney, and D. Clague (1992), Geochronology and petrogenesis of MORB from the Juan de Fuca and Gorda Ridges by ^{238}U - ^{230}Th disequilibrium, *Earth Planet. Sci. Lett.*, *109*, 255-272.
- Goldstein, S.J., M.T. Murrell, and R.W. Williams (1993), ^{231}Pa and ^{230}Th chronology of Mid-Ocean Ridge Basalts. *Earth Planet. Sci. Lett.*, *115*, 151-160.
- Goldstein, S.J., M.R. Perfit, R. Batiza, D.J. Fornari, and M.T. Murrell (1994), Off-axis volcanism at the East Pacific Rise detected by uranium-series dating of basalts, *Nature*, *367*, 157-159.
- Gregg, T.K.P., and J.H. Fink (1995) Quantification of submarine lava-flow morphology through analog experiments, *Geology*, *23*(1), 73-76.
- Gregg, T.K.P., and J.H. Fink (2000) A laboratory investigation into the effects of slope on lava flow morphology, *J. Volcanol. Geotherm. Res.*, *96*, 145-159.
- Gregg, T.K.P., and D.J. Fornari (1998) Long submarine lava flows: Observations and results from numerical modeling, *J. Geophys. Res.*, *103*(B11), 27,517-27,531.
- Gregg, T.K.P., D.J. Fornari, M.R. Perfit, R.M. Haymon, and J.H. Fink (1996) Rapid emplacement of a mid-ocean ridge lava flow on the East Pacific Rise at 9°46'-51'N, *Earth Planet. Sci. Lett.*, *144*, E1-E7.
- Harding, A.J., G.M. Kent, and J.A. Orcutt (1993), A multichannel seismic investigation of upper crustal structure at 9°N on the East Pacific Rise: Implications for crustal accretion, *J. Geophys. Res.*, *98*, 13925-13944.
- Haymon, R.M., D.J. Fornari, M.H. Edwards, S.C. Carbotte, D. Wright, and K.C. Macdonald (1991), Hydrothermal vent distribution along the East Pacific Rise Crest (9°09'-54'N) and its relationship to magmatic and tectonic processes on fast-spreading mid-ocean ridges, *Earth Planet. Sci. Lett.*, *104*, 513-534.
- Haymon, R.M., D.J. Fornari, K.L. Von Damm, M.D. Lilley, M.R. Perfit, and J.M. Edmond (1993), Volcanic eruption of the mid-ocean ridge along the East Pacific Rise crest at 9° 45-45'N: Direct submersible observations of seafloor phenomena associated with an eruption event in April, 1991, *Earth Planet. Sci. Lett.* *119*, 85-101.

- Henderson, G.M., A.S. Cohen, and R.K. Onions (1993), U-234/U-238 Ratios and Th-230 Ages for Hateruma Atoll Corals - Implications for Coral Diagenesis and Seawater U-234/U-238 Ratios, *Earth Planet. Sci. Lett.*, 115, 65-73.
- Hinds, J. (2005), Construction of the Oceanic Crustal Layer 2A: A Detailed Petrographic and Geochemical Study of Lavas from 9°30'N and 9°50'N East Pacific Rise. M.S. Thesis, University of Florida.
- Hoof, E.E.E., H. Schouten, and R.S. Detrick (1996), Constraining crustal emplacement processes from the variation in seismic layer 2A thickness at the East Pacific Rise, *Earth Planet. Sci. Lett.*, 142, 289-309.
- Kent, G.M., A.J. Harding, and J.A. Orcutt (1990), Evidence for a smaller magma chamber beneath the East Pacific Rise at 9°30'N, *Nature*, 412, 145-149.
- Kent, G.M., A.J. Harding, and J.A. Orcutt (1993a), Distribution of magma beneath the East Pacific Rise between the Clipperton Transform and the 9°17'N Deval from forward modeling of common depth point data, *J. Geophys. Res.*, 98, 13,945-13,969.
- Kent, G.M., A.J. Harding, and J.A. Orcutt (1993b), Distribution of magma beneath the East Pacific Rise near the 9°03'N overlapping spreading center from forward modeling of common depth point data, *J. Geophys. Res.*, 98, 13,971-13,995.
- Ku, T.-L., K.G. Knauss, and G.G. Mathieu (1977) Uranium in open ocean: Concentration and isotopic composition, *Deep Sea Res.*, 1005-1017.
- Kurras, G.J., D.J. Fornari, M.H. Edwards, M.J. Perfit, and M.C. Smith (2000), Volcanic morphology of the East Pacific Rise Crest 9°49-52': Implications for volcanic emplacement processes at fast-spreading mid-ocean ridges, *Mar. Geophys. Res.* 21, 23-41.
- Lundstrom, C.C. (2003), Uranium-series Disequilibrium in Mid-ocean Ridge Basalts: Observations and Models of Basalt Genesis, in *Uranium-Series Geochemistry*, edited by B. Bourdon, G.M. Henderson, C.C. Lundstrom, S.P. Turner, 52, pp. 175-214, The Mineralogical Society of America, Washington, D.C., 2003.
- Lundstrom, C.C., D.E. Sampson, M.R. Perfit, J. Gill, and Q. Williams (1999), Insights into mid-ocean ridge basalt petrogenesis: U-series disequilibrium from the Siqueiros Transform, Lamont Seamounts, and East Pacific Rise, *J. Geophys. Res.*, 104, 13,035-13,048.
- Macdonald, K.C., P.J. Fox, S. Miller, S. Carbotte, M.H. Edwards, L. Perram, R. Pockalny, D. Scheirer, S. Tighe, C. Weiland, and D. Wilson (1992), The East Pacific Rise and its flanks 8-18°N: History of segmentation, propagation and spreading direction based on SeaMARC II and Sea Beam studies, *Mar. Geophys. Res.*, 14, 299-344, 1992.
- McKenzie, D. (1985), ²³⁰Th-²³⁸U disequilibrium and the melting processes beneath ridge axes, *Earth Planet. Sci. Lett.*, 72, 149-157.
- Perfit, M.R., and W.W. Chadwick Jr. (1998), Magmatism at mid-ocean ridges: Constraints from volcanological and geochemical investigations, in *Faulting and Magmatism at Mid-Ocean Ridges*, edited by W.R. Buck, P.T. Delaney, J.A. Karson, and Y. Lagabriele, *Geophys. Monogr. Ser.* 106, pp. 59-115, AGU, Washington, D.C.

- Perfit, M., D. Fornari, M. Smith, J. Bender, C. Langmuir, and R. Haymon (1994), Small-scale spatial and temporal variations in MORB geochemistry and implications for ridge crest magmatic processes, *Geology*, 22, 375-379.
- Reynolds, J.R. (1995), Segment-scale systematic of mid-ocean ridge magmatism and geochemistry, Ph.D. thesis, 483 pp., Columbia Univ., Palisades, N.Y.
- Richter, S. and S.A. Goldberg (2003), Improved techniques for high accuracy isotope ratio measurements of nuclear materials using thermal ionization mass spectrometry. *Int. J. Mass Spectrom.* 229, 181-197.
- Robinson, L.F., N.S. Belshaw, and G.M. Henderson (2004), U and Th concentrations and isotope ratios in modern carbonates and waters from the Bahamas. *Geochim. et Cosmochim. Acta*, 68(8), 1777-1789.
- Rubin, K.H., and J.D. MacDougall, Dating of neovolcanic MORB using ($^{226}\text{Ra}/^{230}\text{Th}$) disequilibrium (1990), *Earth Planet. Sci. Lett.*, 101, 313-321.
- Rubin, K.H., J.D. MacDougall, and M.R. Perfit (1994), ^{210}Po - ^{210}Pb dating of recent volcanic eruptions on the sea floor, *Nature*, 368, 841-844.
- Rubin, K.H., I. van der Zander, M.C. Smith, and E.C. Bergmanis (2005), Minimum speed limit for ocean ridge magmatism from ^{210}Pb - ^{226}Ra - ^{230}Th disequilibria, *Nature*, 437, 534-538.
- Schouten, H., M.A. Tivey, D.J. Fornari, and J.R. Cochran (1999), Central anomaly magnetization high: constraints on the volcanic construction and architecture of seismic layer 2A at a fast-spreading Mid-Ocean Ridge, the EPR at 9°30'-50'N, *Earth Planet. Sci. Lett.*, 169, 37-50.
- Schouten, H., M.A. Tivey, D.J. Fornari, D. Yoeger, A. Bradley, M. Edwards, P. Johnson, and Ship Board Science and Technical Teams (2001), Near-Bottom Investigations of the Central Anomaly Magnetic High (CAMH) at the East Pacific Rise 9°25'-57'N, Cruise Report R/V Atlantis Voyage 7 Leg 4, 11/05-12/04/2001. Report at <http://imina.soest.hawaii.edu/HMRG/EPR/index.htm> under AT7-4 Cruise Report.
- Schouten, H., M.A. Tivey, D.J. Fornari, D.R. Yoerger, A.M. Bradley, P. Johnson, M.H. Edwards, and T. Kurokawa (2002), Lava transport and accumulation processes on EPR 9°27'N to 10°N: interpretations based on recent near-bottom sonar imaging and seafloor observations using ABE, Alvin, and a new digital deep sea camera, *Eos Trans. AGU*, 83, T11C-1262.
- Schouten, H., M. Tivey, D.J. Fornari, W. Seyfried, and Ship Board Science and Technical Teams (2004), Central Anomaly Magnetic High and Volcanic Processes on Fast-spreading Mid-Ocean Ridges, Cruise Report R/V Atlantis Voyage 11 Leg 7, 1/26-2/24/2004.
- Sims, K.W.W., S.J. Goldstein, J. Blichert-Toft, M.R. Perfit, P. Kelemen, D.J. Fornari, P. Michael, M.T. Murrell, S.R. Hart, D.J. DePaolo, G. Layne, and M. Jull (2002), Chemical and isotopic constraints on the generation and transport of melt beneath the East Pacific Rise, *Geochim. Cosmochim. Acta*, 66, 3481-3504.
- Sims, K.W.W., J. Blichert-Toft, D.J. Fornari, M.R. Perfit, S.J. Goldstein, P. Johnson, D.J. DePaolo, S.R. Hart, M.T. Murrell, P.J. Michael, G.D. Layne, and L. Ball (2003), Aberrant youth: Chemical and isotopic constraints on the origin of off-axis lavas

- from the East Pacific Rise, 9°-10°N, *Geochem., Geophys., Geosyst.*, 4(10), Paper number 2002GC000443.
- Sims, K.W.W., S.R. Hart, M.K. Reagan, J. Blusztajn, H. Staudigel, R.A. Sohn, G.D., Layne, L.A. Ball, and J. Andrews (2008a), ^{238}U - ^{230}Th - ^{226}Ra - ^{210}Pb - ^{210}Po , ^{232}Th - ^{226}Ra , and ^{235}U - ^{231}Pa constraints on the ages and petrogenesis of Vailulu'u and Malumalu Lavas, Samoa, *Geochem., Geophys., Geosyst.*, 9(4), Q04003, doi:10.1029/2007GC001651.
- Sims, K.W.W., J.B. Gill, A. Dosseto, D.L. Hoffmann, C.C. Lundstrom, R.W. Williams, L. Ball, D. Tollstrup, S. Turner, J. Prytulak, J.J.G. Glessner, J.J. Standish, and T. Elliott (2008b), An Inter-Laboratory Assessment of the Thorium Isotopic Composition of Synthetic and Rock Reference Materials, *Geostandards and Geoanalytical Research*, 32, 65-91.
- Smith, M.C., M.R. Perfit, D.J. Fornari, W.I. Ridley, M.H. Edwards, G.J. Kurras, and K.L. Von Damm (2001), Magmatic processes and segmentation at a fast spreading mid-ocean ridge; detailed investigation of an axial discontinuity on the East Pacific Rise crest at 9°37'N, *Geochem., Geophys., Geosyst.*, 2 (Paper 2000GC000134).
- Sohn, R.A. (2005), A general inversion for end-member ratios in binary mixing systems, *Geochem., Geophys., Geosyst.*, 6(11), doi: 10.1029/2005GC000975.
- Sohn, R.A. and W. Menke (2002), Application of maximum likelihood and bootstrap methods to nonlinear curve-fit problems in geochemistry, *Geochem., Geophys., Geosyst.*, 3(7), doi:10.1029/2001GC000253.
- Sohn, R. A., S. C. Webb, and J. A. Hildebrand (2004), Fine-scale seismic structure of the shallow volcanic crust on the East Pacific Rise at 9°50'N, *J. Geophys. Res.*, 109, B12104, doi:10.1029/2004JB003152.
- Soule, S.A., D.J. Fornari, M.R. Perfit, M.A. Tivey, W.I. Ridley, and H. Schouten (2005), Channelized lava flows at the East Pacific Rise crest 9°-10°N: the importance of off-axis lava transport in developing the architecture of young oceanic crust, *Geochem., Geophys., Geosyst.*, 6(8), doi: 10.1029/2005GC000912.
- Soule, S.A., D.J. Fornari, M.R. Perfit, K.H. Rubin (2007), New insights into mid-ocean ridge volcanic processes from the 2005-2006 eruption of the East Pacific Rise, 9°46'N-9°56'N, *Geology*, 35(12), 1079-1082, doi: 10.1130/G23924A.1.
- Soule, S. A., J. Escartín, and D. J. Fornari (2009), A record of eruption and intrusion at a fast spreading ridge axis: Axial summit trough of the East Pacific Rise at 9-10°N, *Geochem. Geophys. Geosyst.*, 10, Q10T07, doi:10.1029/2008GC002354.
- Spiegelman, M., and T. Elliot (1993), Consequences of melt transport for uranium series disequilibrium in young lavas, *Earth Planet. Sci. Lett.*, 118, 1-20.
- Sturm, M.E., S.J. Goldstein, E.M. Klein, J.A. Karson, and M.T. Murrell (2000) Uranium-series age constraints on lavas from the axial valley of the Mid-Atlantic Ridge, MARK area, *Earth Planet. Sci. Lett.*, 181, 61-70.
- Thurber, D. (1962) Anomalous $^{234}\text{U}/^{238}\text{U}$ in nature, *J. Geophys. Res.*, 67, 4518.
- Toomey, D.R., S.C. Solomon, and G.M. Purdy (1994), Tomographic imaging of the shallow crustal structure of the East Pacific Rise at 9°30'N, *J. Geophys. Res.*, 99, 24,135-24,157.

- Vera, E.E., and J.B. Diebold (1994), Seismic imaging of oceanic layer 2A between 9°30 and 10°N on the East Pacific Rise from two ship wide-aperture profiles, *J. Geophys. Res.*, *99*, 3031-3041.
- White, S.M., R.M Haymon, D.J. Fornari, M.R. Perfit, and K.C. Macdonald (2002), Correlation between volcanic and tectonic segmentation of fast-spreading ridges: evidence from volcanic structures and lava morphology on the East Pacific Rise, 9°-10°N, *J. Geophys. Res.*, *107(B8)*, 2173, doi:10.1029/2001JB000571.
- White, S.M., R.M. Haymon, S. Carbotte (2006), A new view of ridge segmentation and near-axis volcanism at the East Pacific Rise, 8°-12°N, from EM300 multibeam bathymetry, *Geochem., Geophys., Geosyst.*, *7(12)*, doi: 10.1029/2006GC001407.
- Williams, C.M., M.A. Tivey, H. Schouten, and D.J. Fornari (2008), Central Anomaly Magnetization High documentation of crustal accretion along the East Pacific Rise (9°55'N-9°25'N), *Geochem., Geophys., Geosyst.*, *9(4)*, doi:10.1029/2007GC001611.
- Williams, R.W., and J.B. Gill (1989), Effects of partial melting on the uranium decay series, *Geochim. et Cosmochim. Acta*, *53*, 1607-1619.
- Wright, D.J., R.M. Haymon, and K.C. Macdonald (1995), Breaking new ground: Estimates of crack depth along the axial zone of the East Pacific Rise (9°12-54'N), *Earth Planet. Sci. Lett.*, *134*, 441-457, 1995.

Table 1. Sample Descriptions for *Alvin* Dives 3963 and 3974.

Sample	Time of Collection	Latitude	Longitude	Depth (m)	Flow Type	Geologic Context (Dive Observations)
3963-1	16:45	9°50.653'	104°16.360'	2562	Sheet	From <i>Alvin</i> touchdown area ~2.2 km east of AST, before first flow front.
3963-3	17:54	9°50.610'	104°16.458'	2557	Pillow	Flow front #1. To west and south of samples 1 and 2.
3963-4	18:15	9°50.502'	104°16.615'	2542	Pillow	Flow front #2. Same location as sample 5 –probably the same lava. Appears younger than 3963-6.
3963-5	18:16	9°50.502'	104°16.615'	2543	Pillow	Flow front #2. Same location as sample 4—probably same lava. Looks like a drained tube. Appears younger than 3963-6. Area is structurally disrupted with many slabs of crusts.
3963-6	18:32	9°50.501'	104°16.589'	2544	Sheet	Between flow front #1 and flow front #2. Part of lobate/sheet area to east of 3963-4 & -5. Underlies 3963-4 & -5. Complicated area of collapses and sheet flows.
3963-7	18:47	9°50.450'	104°16.746'	2532	Pillow	Flow front #3. Knobbly pillow flow front; appears younger than 3963-4 & -5. Overlies 3963-8. Less sediment here.
3963-8	19:25	9°50.452'	104°16.731'	2534	Lobate	To east and below 3963-7.
3963-9	19:45	9°50.288'	104°16.848'	2524	Sheet	Sheet flow from edge of 1m high channel. Not clear if it this sample is from the channel itself or from a collapsed channel above.
3963-10	20:36	9°50.294'	104°16.991'	2517	Pillow	Flow front #4. North and west of previous samples. Flow front is over lobate terrain that may be related to the channel sample 3963-9.
3963-11	20:43	9°50.305'	104°16.989'	2518	Pillow	Flow front #4. Same flow front as #10. Sampled very glassy toe of flow.

Table 1 (cont'd).

Sample	Time of Collection	Latitude	Longitude	Depth (m)	Flow Type	Geologic Context (Dive Observations)
3974-1	17:40	9°50.136'	104°18.571'	2603	Sheet	From <i>Alvin</i> touchdown area ~2 km west of the AST. Field of jumbled and hackly sheet flows in a low area west of the first flow front.
3974-2	18:00	9°50.164'	104°18.518'	2594	Pillow	Flow front #1. Lava from first flow front to the east of 3974-1. May be part of a pillow mound on the flow front.
3974-3	18:23	9°50.202'	104°18.461'	2595	Sheet	Hackly sheet flow taken from just after the pillows.
3974-4	18:47	9°50.254'	104°18.506'	2598	Lobate	Tubular flow in a terrain of mixed sheets and lobates.
3974-5	19:16	9°50.299'	104°18.505'	2599	Pillow	Flow front #2. From above 3974-4 on rise of flow front.
3974-6	19:47	9°50.349'	104°18.418'	2579	Pillow	Flow front #2. Taken from foot of flow.
3974-7	20:16	9°50.251'	104°18.326'	2569	Sheet	Flow on flat area to the west of flow front #2. Pillow 3974-6 may be younger/over this sample.
3974-8	20:26	9°50.252'	104°18.323'	2568	Pillow	Flow front #2(?). In contact with and directly overlying the sheet flow sampled by 3974-7. May be the same unit as 3974-6.
3974-9	20:50	9°50.386'	104°18.229'	2546	Lobate	Flow body #2. Taken from a field of lobate lava on plateau over flow front #2.
3974-10	21:14	9°50.284'	104°18.137'	2532	Pillow	Flow front #3. Sampled from a 10-15 m high flow front. Over sample 3974-9.
3974-11	21:55	9°50.348'	104°17.943'	2517	Lobate	Sampled from large flat area about 700 m east of the AST

Table 2. Major element compositions of lavas collected during Dives 3963 and 3974 at 9-10°N EPR.

Sample	SiO ₂	TiO ₂	Al ₂ O ₃	FeO	MnO	MgO	CaO	Na ₂ O	K ₂ O	P ₂ O ₅	Total	Mg#	K/Ti
3963-1	50.4	1.47	14.6	10.1	0.20	7.9	12.2	2.75	0.10	0.12	99.91	60.68	6.93
3963-3	50.3	1.59	14.8	10.4	0.20	7.7	12.0	2.78	0.14	0.16	100.03	59.57	8.93
3963-4i	50.4	1.52	14.9	10.0	0.20	7.7	12.1	2.78	0.15	0.15	99.97	60.37	9.81
3963-4o													
3963-5	50.5	1.57	14.8	10.0	0.20	7.7	12.1	2.78	0.15	0.14	99.93	60.14	9.62
3963-6	50.4	1.53	14.8	10.1	0.20	7.8	12.1	2.71	0.13	0.14	99.93	60.57	8.69
3963-6i													
3963-7	49.8	1.15	15.9	9.1	0.17	8.7	12.4	2.54	0.08	0.08	99.87	65.62	7.34
3963-8	50.2	1.58	14.8	10.2	0.20	8.0	11.9	2.76	0.13	0.15	99.91	60.84	8.27
3963-9	49.6	1.13	15.9	9.0	0.17	9.0	12.4	2.51	0.08	0.10	99.93	66.41	7.18
3963-10	49.5	1.18	16.3	8.8	0.17	8.9	12.3	2.51	0.10	0.10	99.90	66.68	8.11
3963-10-2													
3963-11	49.7	1.18	16.2	8.7	0.18	8.9	12.2	2.51	0.10	0.11	99.78	66.80	8.38
3974-1	50.7	1.57	14.8	10.3	0.21	7.6	11.6	2.76	0.12	0.13	99.89	59.43	7.31
3974-2	50.6	1.53	14.9	10.3	0.20	7.6	11.7	2.73	0.11	0.14	99.90	59.37	7.14
3974-3	50.5	1.41	15.3	9.7	0.18	8.1	11.9	2.57	0.12	0.14	99.93	62.11	8.75
3974-4	50.5	1.41	15.2	9.7	0.18	8.0	12.0	2.59	0.12	0.14	99.92	62.01	8.72
3974-5	50.7	1.58	15.0	10.1	0.20	7.6	11.7	2.75	0.16	0.15	99.90	60.01	9.91
3974-6	50.6	1.59	15.0	10.0	0.19	7.7	11.7	2.67	0.16	0.14	99.86	60.23	9.76
3974-7	50.4	1.43	15.5	9.5	0.20	8.1	11.9	2.59	0.13	0.13	99.87	62.76	9.43
3974-8	50.5	1.41	15.5	9.6	0.18	7.9	11.9	2.61	0.14	0.14	99.90	61.89	9.99
3974-8-2	50.5	1.43	15.5	9.6	0.19	7.9	11.9	2.62	0.14	0.15	99.87	61.97	9.96
3974-9	50.1	1.41	15.5	9.5	0.20	8.4	11.8	2.67	0.14	0.13	99.97	63.66	9.86
3974-10	50.1	1.36	15.6	9.5	0.20	8.3	12.1	2.66	0.12	0.14	100.07	63.51	8.50
3974-11	50.0	1.32	15.5	9.5	0.19	8.7	12.0	2.58	0.11	0.12	100.06	64.44	8.24

Major elements were analyzed on polished glass chips at the USGS Microbeam Laboratory in Denver, Co. using a JEOL 8900 Electron Microprobe. Analysis of seven to ten separate points (including spots on separate chips of the same sample) were averaged for each sample and then normalized and corrected for instrument drift based on the established values for in-house standards JdF-D2 [Reynolds et al., 1995] and ALV2392-9 [see Smith et al., 2001]. The 2 σ errors calculated from variation in the analyses of ALV2392-9 during these analytical runs are as follows: SiO₂ (0.29 wt.% or 0.57 relative %), TiO₂ (0.07 wt.% or 5.4%), Al₂O₃ (0.17 wt.% or 1.1%), FeO (0.17 wt.% or 1.8%), MnO (0.05 wt.% or 26.8%), MgO (0.11 wt.% or 1.3%), CaO (0.14 wt.% or 1.2%), Na₂O (0.09 wt.% or 3.6%), K₂O (0.02 wt.% or 18.8%), and P₂O₅ (0.04 wt.% or 29.8%).

Table 3. Trace element abundances of lavas collected during Dives 3963 and 3974 at 9-10°N EPR.

Sample	3963-1	3963-3	3963-4i	3963-4o	3963-5	3963-6	3963-6i	3963-7	3963-8	3963-9	3963-10	3963-10-2	3963-11
Sc	43	40	39	41	40	41	41	35	39	36	34	36	34
V	314	293	282	295	294	299	299	241	290	248	243	255	240
Cr	339	308	308	321	321	309	311	321	321	332	371	370	372
Co	38.7	36.0	34.8	36.4	36.3	36.7	36.6	37.4	36.7	38.5	38.5	38.5	37.8
Ni	74	75	73	76	76	79	79	121	86	125	146	141	145
Cu	84	69	69	73	73	74	74	77	70	79	78	79	77
Zn	82	76	72	77	75	76	76	65	77	67	66	75	65
Ga	17.4	16.2	15.7	16.2	16.3	16.4	16.4	14.8	16.4	15.3	15.1	16.1	15.2
Rb	1.0	1.5	1.7	1.8	1.8	1.2	1.2	1.0	1.4	1.0	1.0	0.9	1.0
Sr	114	117	116	119	120	120	120	107	120	111	117	123	119
Y	35	32	30	32	32	32	32	24	32	25	25	27	25
Zr	102	104	99	104	103	103	103	79	105	82	85	85	85
Nb	2.4	3.2	3.5	3.5	3.6	2.6	2.6	1.5	2.9	1.5	1.8	2.1	1.8
Hf	2.7	2.7	2.6	2.7	2.7	2.6	2.7	2.1	2.7	2.1	2.2	2.2	2.2
Th	0.13	0.19	0.21	0.21	0.22	0.16	0.16	0.10	0.17	0.10	0.11	0.12	0.11
U	0.07	0.08	0.08	0.08	0.09	0.07	0.07	0.04	0.07	0.04	0.05	0.06	0.05
La	3.43	3.80	3.80	3.90	3.93	3.54	3.54	2.39	3.71	2.48	2.67	2.97	2.68
Ce	11.02	11.90	11.55	11.99	12.05	11.37	11.34	8.19	11.82	8.41	8.94	9.43	8.93
Pr	1.9	2.0	2.0	2.1	2.0	2.0	2.0	1.5	2.0	1.5	1.6	1.6	1.6
Nd	10.15	10.31	9.81	10.20	10.18	9.91	9.88	7.20	10.34	7.48	7.88	8.28	7.82
Sm	3.43	3.43	3.25	3.37	3.37	3.33	3.34	2.49	3.45	2.54	2.62	2.73	2.58
Eu	1.26	1.22	1.16	1.21	1.20	1.18	1.19	0.93	1.22	0.96	0.98	1.07	0.97
Gd	4.8	4.8	4.6	4.8	4.7	4.7	4.7	3.8	4.8	4.0	4.0	3.9	4.0
Tb	0.88	0.84	0.79	0.83	0.83	0.82	0.83	0.64	0.84	0.67	0.67	0.69	0.67
Dy	5.56	5.41	5.08	5.29	5.28	5.27	5.27	4.05	5.37	4.15	4.16	4.38	4.15
Ho	1.19	1.17	1.10	1.14	1.14	1.13	1.14	0.85	1.15	0.88	0.87	0.93	0.87
Er	3.2	3.2	3.0	3.1	3.1	3.1	3.1	2.3	3.2	2.3	2.3	2.5	2.3
Tm	0.51	0.51	0.48	0.51	0.50	0.50	0.51	0.41	0.51	0.42	0.42	0.43	0.42
Yb	3.44	3.32	3.10	3.23	3.22	3.22	3.22	2.43	3.27	2.51	2.48	2.66	2.49
Lu	0.54	0.52	0.49	0.51	0.51	0.51	0.51	0.38	0.52	0.39	0.39	0.42	0.39

Table 3 (cont'd).

Sample	3974-1	3974-2	3974-3	3974-4	3974-5	3974-6	3974-7	3974-8	3974-9	3974-10	3974-11-2	3974-11-3
Sc	39	39	38	38	42	38	37	38	37	39	37	37.3
V	294	287	282	282	319	291	276	276	274	281	267	269
Cr	255	255	344	337	331	301	343	339	333	357	331	322
Co	35.9	36.5	36.7	35.7	41.2	36.6	37.5	36.4	36.4	37.7	36.7	38.7
Ni	82	96	96	94	97	99	119	113	113	109	115	119
Cu	66	68	71	70	81	68	74	71	71	76	72	74
Zn	81	80	73	76	84	76	72	76	76	77	78	78
Ga	16.3	16.0	16.0	15.5	18.2	16.6	16.2	16.0	15.3	16.5	16.2	16.5
Rb	0.9	0.8	1.5	1.2	3.6	2.1	1.9	1.7	1.6	1.2	1.1	1.0
Sr	115	114	123	119	163	141	132	130	126	128	116	120
Y	34	33	30	31	33	32	29	31	31	31	30	29
Zr	103	97	100	95	118	109	101	98	98	94	93	92
Nb	2.5	2.4	2.9	3.0	5.7	4.1	3.5	3.7	3.7	2.9	2.4	2.2
Hf	2.8	2.6	2.6	2.5	2.7	2.8	2.5	2.6	2.6	2.5	2.4	2.3
Th	0.13	0.12	0.18	0.17	0.30	0.26	0.23	0.22	0.22	0.16	0.14	0.1
U	0.05	0.05	0.07	0.06	0.13	0.10	0.09	0.08	0.08	0.06	0.07	0.1
La	3.53	3.25	3.64	3.57	5.00	4.48	4.01	4.10	4.01	3.52	3.38	3.40
Ce	11.34	10.57	11.44	11.04	14.26	13.35	12.09	12.08	11.92	10.90	10.58	10.76
Pr	2.0	1.9	1.9	1.9	2.4	2.2	2.0	2.0	2.0	1.9	1.8	1.8
Nd	10.29	9.59	9.69	9.26	11.81	11.00	9.93	9.90	9.60	9.23	9.06	9.42
Sm	3.48	3.26	3.20	3.10	3.74	3.52	3.20	3.20	3.12	3.12	2.92	3.13
Eu	1.23	1.17	1.15	1.10	1.31	1.25	1.14	1.13	1.10	1.12	1.12	1.16
Gd	4.8	4.5	4.5	4.3	5.1	4.8	4.5	4.3	4.3	4.3	4.2	4.3
Tb	0.87	0.82	0.79	0.79	0.83	0.84	0.77	0.79	0.79	0.79	0.74	0.78
Dy	5.54	5.26	5.00	4.99	5.22	5.33	4.88	5.01	4.97	5.00	4.80	4.83
Ho	1.20	1.13	1.08	1.07	1.11	1.13	1.04	1.08	1.05	1.07	1.01	1.06
Er	3.3	3.1	2.9	2.9	3.0	3.1	2.9	2.9	2.9	2.9	2.7	2.8
Tm	0.52	0.50	0.48	0.48	0.50	0.50	0.47	0.48	0.48	0.48	0.46	0.47
Yb	3.41	3.22	3.05	3.06	3.13	3.20	2.97	3.04	3.00	3.06	2.93	2.97
Lu	0.51	0.48	0.48	0.46	0.49	0.50	0.47	0.46	0.45	0.46	0.45	0.45

Table 3 (cont'd). Analytical Notes: Samples were analyzed for trace elements at the University of Florida using an Element II Inductively Coupled Plasma Mass Spectrometer (ICP-MS). The analyses were performed in medium resolution with Re and Rh used as internal standards. Concentrations were calculated by external calibration using a combination of USGS rock standards. Repeated chemical analyses of in-house MORB standard ALV2392-9 during each run were used to evaluate and correct for instrument drift as well as evaluate accuracy and precision of the measurements. Precision (2σ) was found to be better than $\pm 5\%$ for the REE, Ba, Hf, Nb, Rb, Sr, Th, Y, Zr, and better than $\pm 9\%$ for Pb, Ta, and U.

Table 4. $^{87}\text{Sr}/^{86}\text{Sr}$ isotopic compositions of lavas collected during Dives 3963 and 3974 at 9-10°N EPR.

Sample	$^{87}\text{Sr}/^{86}\text{Sr}$	± 2 SE (ppm)
3974-1	0.702653 ^a	
	0.702465 ^b	8
	0.702492 ^c	24
3974-2	0.702566 ^a	
	0.702504 ^b	10
	0.702491 ^c	33
3974-3	0.702580 ^a	
	0.702494 ^b	9
3974-4	0.702635 ^a	
	0.702492 ^b	7
	0.702501 ^c	11
3974-5	0.702610 ^a	
	0.702513 ^b	7
	0.702537 ^c	23
3974-6	0.702577 ^a	
	0.702524 ^b	11
	0.702590 ^c	36
3974-7	0.702581 ^a	
	0.702492 ^b	9
	0.702542 ^c	21
3974-8	0.702522 ^a	
	0.702570 ^b	8
	0.702558 ^c	17
3974-9	0.702592 ^a	
	0.702513 ^c	20
3974-10	0.702498 ^a	
	0.702569 ^b	9
	0.702588 ^c	29
3974-11	0.702536 ^a	
	0.702508 ^b	13
3963-3	0.702512 ^b	9
3963-5	0.702498 ^b	7
3963-6	0.702497 ^b	10
3963-9	0.702472 ^b	9
3963-10	0.702475 ^b	7

Analytical Notes: ^aSr isotopic composition measured at Woods Hole Oceanographic Institution by Neptune MC-ICP-MS; glass was not leached; internal precision is estimated at ± 5 -10 ppm. After adjusting to 0.71024 (NBS SRM 987), external precision is estimated at 15-30 ppm.

^bSr isotopic composition measured at Boston University by Thermofinnigan Triton TIMS on 2/23/09; glass was leached; ~100 ng of Sr was loaded onto a Re single filament.

^cSr isotopic composition measured at Boston University by Thermofinnigan Triton TIMS on 1/29/09; glass was leached; ~10 ng Sr was loaded onto the filament.

Table 5. ($^{230}\text{Th}/^{232}\text{Th}$), ($^{230}\text{Th}/^{238}\text{U}$), ($^{226}\text{Ra}/^{230}\text{Th}$), ($^{234}\text{U}/^{238}\text{U}$), and U, Th, and Ra concentrations measured by MC-ICP-MS and single-collector ICP-MS.

Sample	[Th] (ppm) ^{a,c}	[U] (ppm) ^{a,c}	Th/U ^a	($^{238}\text{U}/^{232}\text{Th}$) ^{a,d}	($^{230}\text{Th}/^{232}\text{Th}$) ^e	($^{234}\text{U}/^{238}\text{U}$) ^g	($^{230}\text{Th}/^{238}\text{U}$)	[^{226}Ra] (fg/g) ^f	($^{226}\text{Ra}/^{230}\text{Th}$)
3974-1	0.1418	0.0583	2.433	1.247	1.437	1.001	1.148	50.29	2.217
	0.1416	0.0585	2.423	1.252	1.431		1.140		
3974-2	0.1311	0.0536	2.445	1.241	1.401	0.999	1.130	45.91	2.238
	0.1314	0.0537	2.452	1.237					
3974-3	0.1760	0.0686	2.565	1.183	1.340	1.001	1.132	56.56	2.176
	0.1740	0.0679	2.568	1.181					
3974-4	0.1753	0.0686	2.555	1.187	1.343	0.999	1.136	57.14	2.197
	0.1738	0.0677	2.572	1.179					
3974-5	0.2472	0.0916	2.700	1.124	1.314	1.000	1.171	69.76	1.930
	0.2468	0.0913	2.709	1.120					
3974-6	0.2454	0.0907	2.704	1.122	1.309	1.001	1.164	68.22	1.913
	0.2444	0.0906	2.703	1.123					
3974-7	0.2250	0.0840	2.678	1.133	1.305	1.003	1.161	63.23	1.921
	0.2263	0.0839	2.704	1.122					
3974-8	0.2257	0.0842	2.681	1.132	1.300	1.002	1.147	60.75	1.859
	0.2255	0.0842	2.682	1.131					
3974-9	0.2253	0.0841	2.681	1.132	1.297	1.003	1.147	63.81	1.960
	0.2253	0.0839	2.689	1.128					
3974-10	0.1629	0.0638	2.553	1.188	1.352	1.004	1.150	55.27	2.240
	0.1638	0.0634	2.587	1.173					
3974-11	0.1420	0.0564	2.523	1.203	1.371	1.003	1.138	52.83	2.435
3963-5	0.2084	0.0790	2.638	1.150	1.342	1.004	1.165	52.69	1.693
3963-6	0.1535	0.0623	2.462	1.232	1.385	1.003	1.122	28.59	1.209
3963-9	0.0931	0.0377	2.474	1.226	1.394	1.003	1.134	39.36	2.726
3963-10	0.1075	0.0437	2.459	1.234	1.410	1.001	1.141	45.56	2.704

Table 5. (cont'd)

Sample	[Th] (ppm) ^{a,c}	[U] (ppm) ^{a,c}	Th/U ^a	(²³⁸ U/ ²³² Th) ^{a,d}	(²³⁰ Th/ ²³² Th) ^e	(²³⁴ U/ ²³⁸ U) ^g	(²³⁰ Th/ ²³⁸ U)	[²²⁶ Ra] (fg/g) ^f	(²²⁶ Ra/ ²³⁰ Th)
4202-4	0.1249	0.0515	2.430	1.249	1.398	1.000	1.118	46.72	2.405
4202-6	0.1233	0.0512	2.412	1.258	1.396	1.001	1.108	47.44	2.478
4205-5	0.1362	0.0553	2.467	1.230	1.383	1.002	1.122	53.57	2.555
4205-6	0.1335	0.0547	2.448	1.239	1.390	1.002	1.120	52.67	2.550
NHD1a	0.1255	0.0512	2.457	1.235	1.451	1.002	1.173	22.48	1.110
TML/3	30.3843	10.8194	2.814	1.078	1.082	1.002	1.002	3,669	1.011
	30.6250	10.7748	2.842	1.067	1.083		1.002	3,675	1.009
					1.081		1.000	3,709	1.018
					1.073		0.993	3,698	1.015
					1.074		0.994		
AThO/3	7.5223	2.2642	3.322	0.913	1.017	1.001	1.114	861.4	1.006
					1.028		1.124	834.6	0.975

Analytical Notes:

^a Duplicate measurements represent spiking and purification of U and Th for separate samples of the same glass dissolution. In the laboratory, the samples were hand-picked under a microscope, then ultrasonically leached in sequential treatments of 0.1N HCl plus 2% H₂O₂ (15 min), DI water (twice, each time for 15 min), 0.1N oxalic acid plus 2% H₂O₂, and DI water (twice, each time for 15 min). Samples were then hand-picked by microscope for a second time to assure clean glass devoid of visual alteration. Sample splits (~2-3 g) were then dissolved, aliquoted, spiked and then U, Th, and Ra were separated using chemical techniques outlined in Sims et al. [2008a, b].

^b ~400 mg of sample powder was dissolved for TML/3.

^c[U] and [Th] were measured using a ID-ICP-MS using the Thermo Finnigan Element. Measurement reproducibility (2s) for [U] and [Th] are estimated at <2.1% and <2.5%, respectively.

^d() denotes activity $\lambda_{238} = 1.551 \times 10^{-10} \text{ yr}^{-1}$; $\lambda_{232} = 4.948 \times 10^{-11} \text{ yr}^{-1}$; (²³⁸U/²³²Th) errors (2s) range from 1.9%-2.9% and do not include uncertainties in λ_{238} (0.07%) or λ_{232} (0.5%).

^eTh isotopic compositions measured by Thermo Finnigan Neptune MC-ICP-MS at WHOI [Ball et al., 2008; Sims et al., 2008b]; activity ratios calculated using $\lambda_{230} = 9.195 \times 10^{-6} \text{ yr}^{-1}$ and $\lambda_{232} = 4.948 \times 10^{-11} \text{ yr}^{-1}$; errors (2 σ) range from 0.7% - 1.6% and do not include uncertainties in λ_{230} (0.4%) or λ_{232} (0.5%).

^f(²²⁶Ra) measured by isotope dilution using the Thermo Finnigan Neptune MC-ICP-MS at WHOI after Sims et al. [2008a]; $\lambda_{226} = 4.331 \times 10^{-4} \text{ yr}^{-1}$; measurement errors (2 σ) range from 3.2% -6.5% and do not include uncertainties in λ_{226} (0.4%) or λ_{230} . For all samples accuracy is limited by uncertainties (2 σ ; 1.5%) on the NBS ²²⁶Ra standard used to calibrate the ²²⁸Ra spike.

^g(²³⁴U/²³⁸U) measured by Thermo Finnigan Neptune MC-ICP-MS at WHOI; $\lambda_{234} = 2.823 \times 10^{-6} \text{ yr}^{-1}$, errors (2 σ) <0.6%; for these samples (²³⁴U/²³⁸U) = 1 within error, using an equilibrium (²³⁴U/²³⁸U) of 54.48 ppm for U010 [Richter and Goldberg, 2003]. NBS 960 was first bracketed by standard U010 to cross-calibrate U010. U010 was then used as a bracketing standard for all sample measurements to determine mass bias.

Table 6. U-Th and Th-Ra model ages for dive 3974 and dive 3963 samples. Model ages include maximum, minimum, and trend line model ages.

Flow Unit	Sample #	Distance from AST (km) ^a	Age Based on Spreading Rate (kyrs) ^b	Th-Ra Minimum Age (yrs) ^c	Th-Ra Maximum Age (yrs) ^c	Th-Ra Trend Line Model Age (yrs) ^c	Average Flow Age (yrs)
<i>Flow 1</i>	3974-1	2.02	36.73	0	1316	269 ± 71	269
<i>Flow 2</i>	3974-2	1.92	34.93	0	1568	655 ± 75	655
<i>Flow 3</i>	3974-3	1.80	32.67	0	1658	725 ± 80	651
	3974-4	1.86	33.76	0	1533	576 ± 69	
<i>Flow 4</i>	3974-5	1.84	33.49	0	1391	0 - 83	151
	3974-6	1.67	30.27	0	1627	321 ± 100	
	3974-7	1.53	27.82	0	1671	420 ± 93	748
<i>Flow 5</i>	3974-8	1.53	27.75	0	2188	1030 ± 166	
	3974-9	1.35	24.45	0	1861	773 ± 96	
<i>Flow 6</i>	3974-10	1.17	21.20	0	1191	0 - 163	78
<i>Flow 7</i>	3974-11	0.80	14.53	0	1094	115 ± 78	115
	3963-5	1.65	30.00	0	2244	912 ± 107	912
	3963-6	1.69	30.73	3541	6002	4961 ± 262	4961
	3963-9	1.15	20.91	0	741	0 - 89	89
	3963-10	0.90	16.36	0	640	0 - 74	74

^a Distances determined using AST locations of Fornari et al. [1998].

^b Spreading ages were determined assuming a constant half-spreading rate of 5.5 cm/yr.

^c Trend line model ages were calculated using the equation from Sims et al. [2003] and assuming vertical decay from an initial zero-age trend line ($^{226}\text{Ra}/^{230}\text{Th}$) at the sample ($^{230}\text{Th}/^{238}\text{U}$) (see Figure 8 for details of the trend line calculation). Errors incorporate only analytical uncertainties in ($^{226}\text{Ra}/^{230}\text{Th}$) of the sample. Th-Ra minimum and maximum model ages were determined by calculating the mean offset from the zero-age trend line for the critical value of the Student's T-distribution at the 95% confidence level. We assume that trend lines representing maximum and minimum initial ($^{226}\text{Ra}/^{230}\text{Th}$) for this zero-age population (at the 95% confidence interval) can be represented by lines offset from the best-fit zero-age trend line by this critical value. Negative minimum ages are reported as zero years.

Figure 1. (Inset) Location map of the study area, 9°-10°N, along the East Pacific Rise (EPR). **(At Left)** EM300 bathymetric map of the region from 9°45'N-9°56'N EPR [White t al. 2006] showing sample locations for *Alvin* dives 3974 and 3963 as well as samples analyzed from the 2005-2006 eruption.

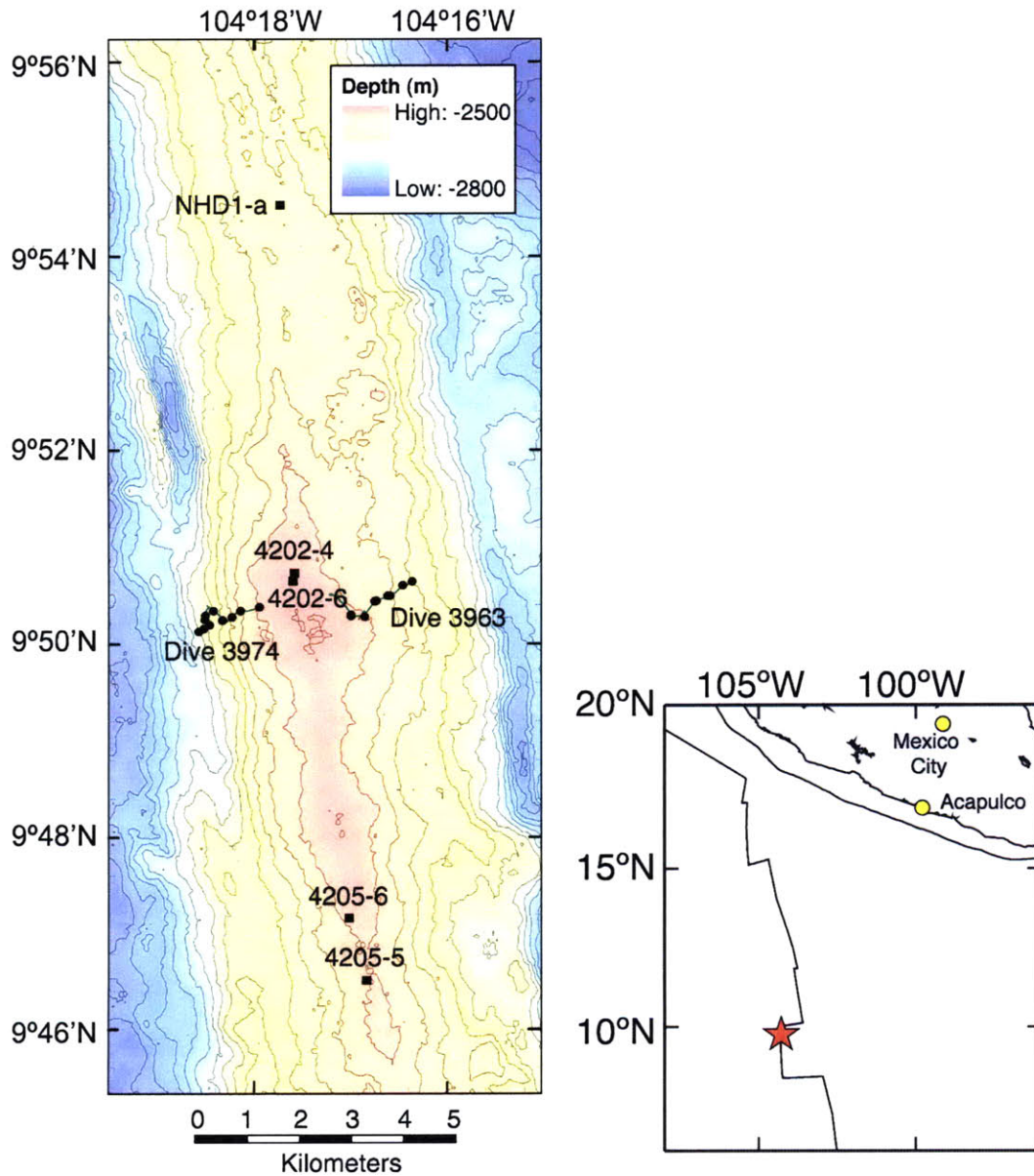


Figure 2. ABE bathymetric maps [Fornari et al., 2004] of (A) *Alvin* dive 3963 and (C) *Alvin* dive 3974 study areas, with 2 m contours showing flow fronts, sample locations, and dive track. DSL-120A side-scan sonar maps [Escartin et al., 2007; Fornari et al., 2004] of (B) *Alvin* dive 3963 and (D) *Alvin* dive 3974 study areas. The dive tracks are shown as white or yellow lines that connect red, numbered, sample locations.

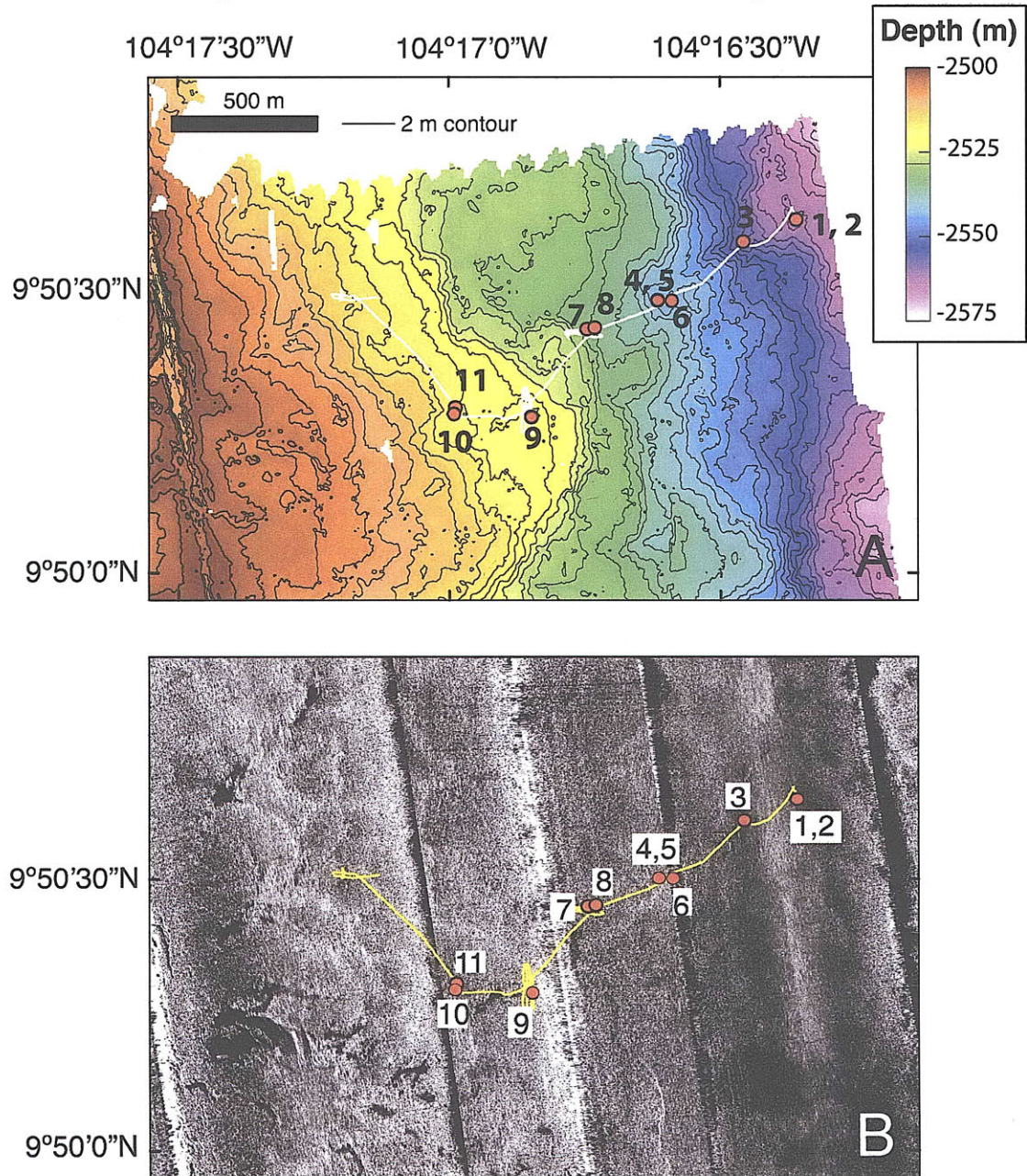
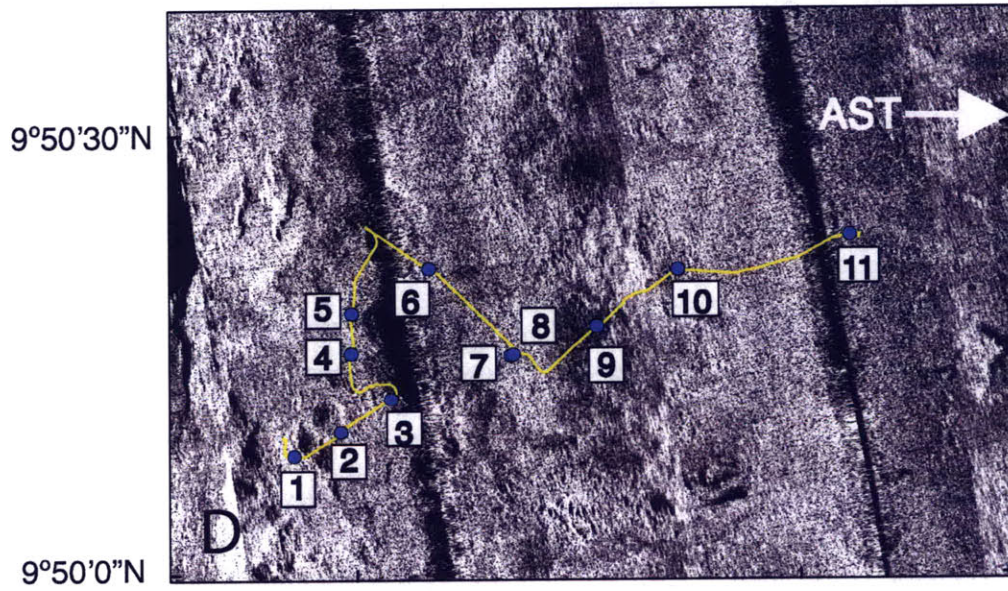
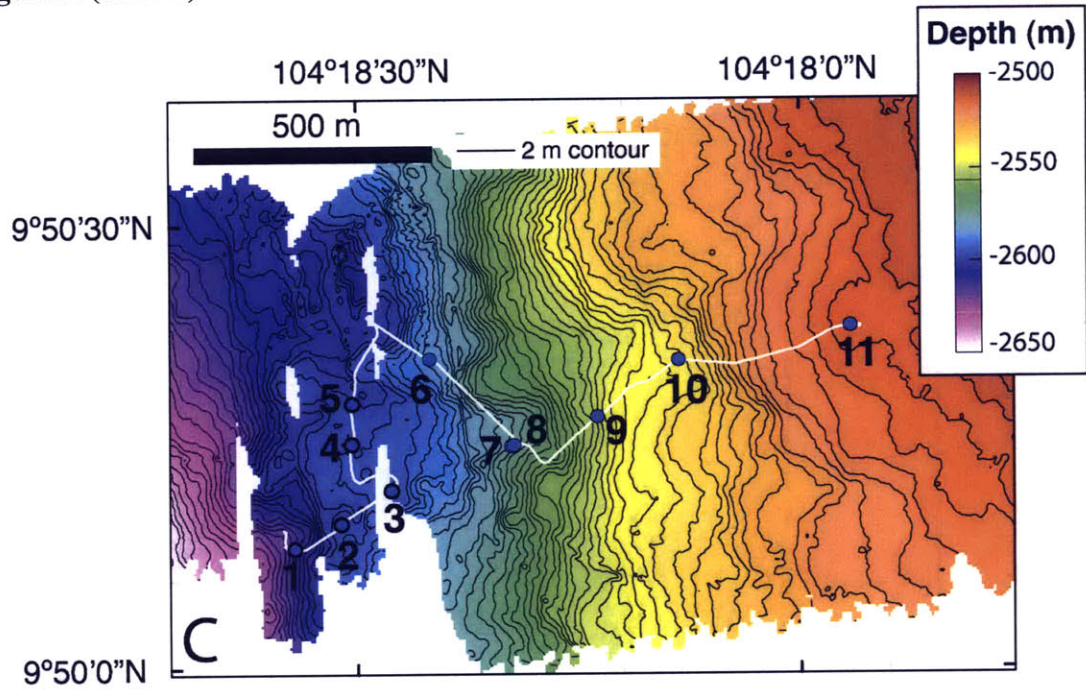


Figure 2 (cont'd).



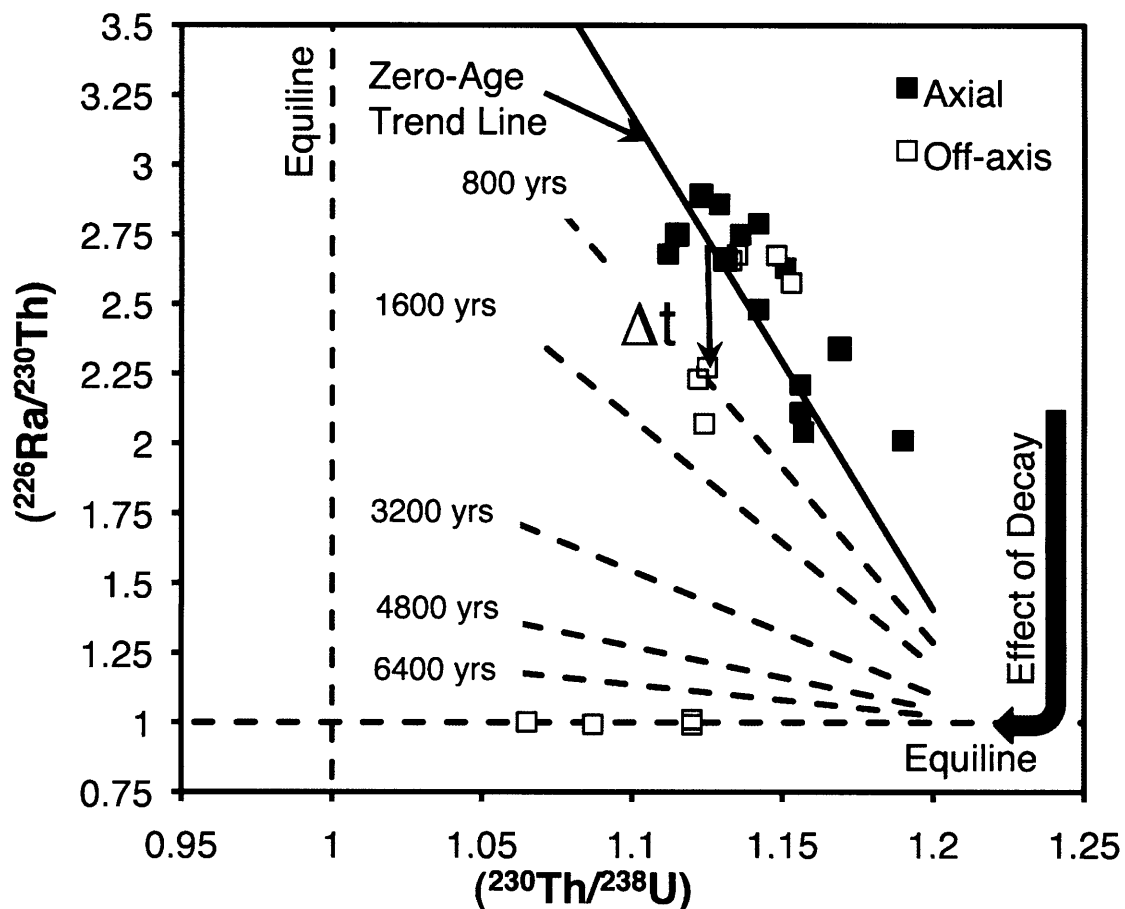


Figure 3. $(^{226}\text{Ra}/^{230}\text{Th})$ and $(^{230}\text{Th}/^{238}\text{U})$ disequilibria for 9° - 10°N EPR axial (solid black squares) and off-axis lavas (white squares) [Sims et al., 2002; 2003], showing the "zero-age" trend line (solid black line), an external isochron from which model ages can be calculated for other lavas at 9° - 10°N EPR. Dashed lines show isochrons after decay from the trend line from 0.5 – 4 half-lives of ^{226}Ra (800-6400 yrs). Model ages are determined by calculating the corresponding time interval (i.e., Δt) needed to produce the difference in the initial $(^{226}\text{Ra}/^{230}\text{Th})$ disequilibria and the current measured $(^{226}\text{Ra}/^{230}\text{Th})$ disequilibria by aging (cf., [Sims et al., 2003] for sample details). The initial extent of $(^{226}\text{Ra}/^{230}\text{Th})$ disequilibria in an unknown sample is assumed to correspond to the $(^{226}\text{Ra}/^{230}\text{Th})$ disequilibria on the zero-age trend line at the same $(^{230}\text{Th}/^{238}\text{U})$ as the sample. The solid black arrow shows the effect of decay due to aging. Decay follows a vertical trajectory until the $(^{226}\text{Ra}/^{230}\text{Th})$ disequilibria for a sample reaches the equiline after ~ 8 ka. Lavas that have no measurable ^{226}Ra excesses (i.e., $(^{226}\text{Ra}/^{230}\text{Th})=1 \pm 0.05$ (2SE)) are older than ~ 8 ka. After ~ 8 ka, decay of ^{230}Th becomes appreciable, and aging will shift samples along the $(^{226}\text{Ra}/^{230}\text{Th})$ to the left, towards $(^{230}\text{Th}/^{238}\text{U})=1$.

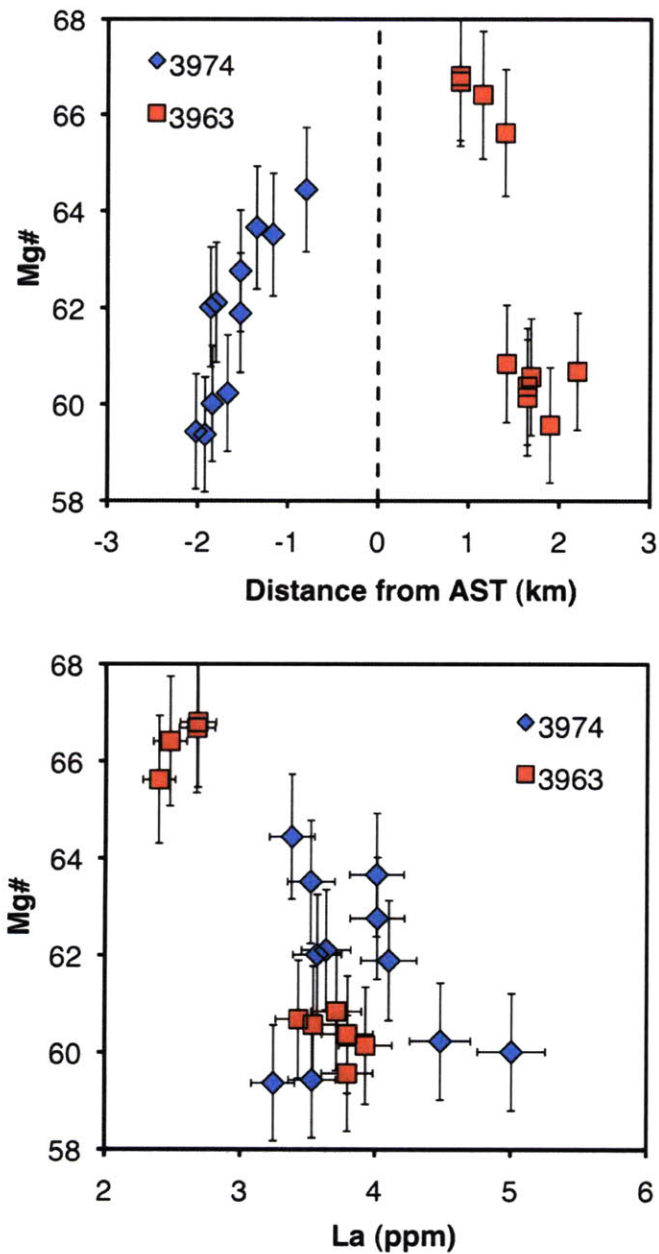


Figure 4. (A) Distance from the AST vs. molar Mg# ($\text{Mg}/(\text{Mg}+\text{Fe}) \times 100$) for dive 3974 (blue diamonds) and dive 3963 samples (red squares). Note the relative continuum of Mg# for dive 3974 samples contrasts with the bimodal distribution of Mg# for dive 3963 samples. Both suites of dive samples show an increase in Mg# with decreasing distance from the AST (dashed vertical line). (B) La (ppm) vs. Mg# for dive 3974 samples and dive 3963 samples. Mg# is independent of [La] for dive 3974 samples, whereas there is an apparent negative correlation between [La] and Mg#; i.e., the group of more evolved samples is also more enriched. This feature is also shown in Figure 5B.

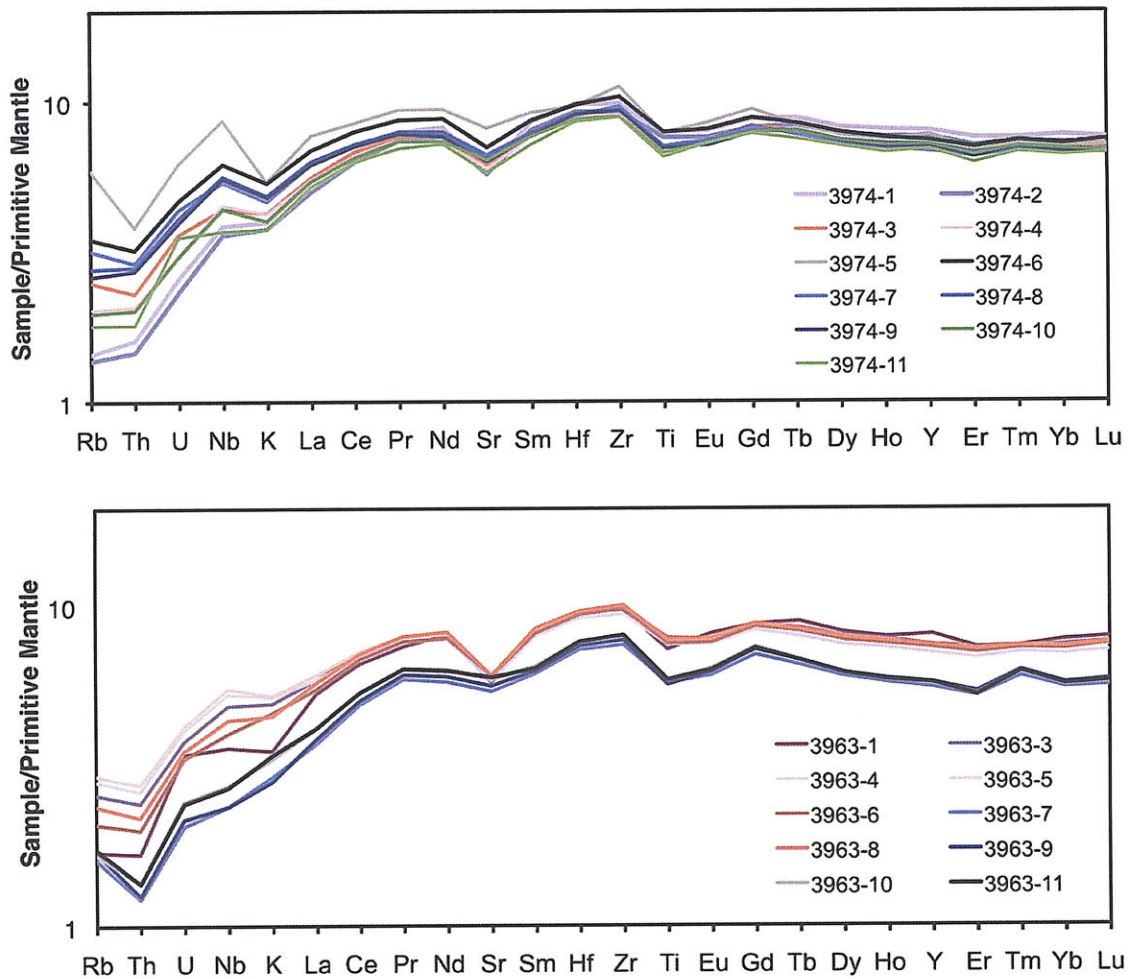


Figure 5. Spidergram showing trace element abundances of (A) dive 3974 lavas and (B) dive 3963 lavas. Dive 3974 lavas exhibit a continuum of trace element abundances; however, trace element abundances do not correlate with Mg#. In contrast, dive 3963 lavas can be divided into two groups: a group of more enriched samples that are relatively far from the AST and have low Mg#, and a more depleted group of samples closer to the AST that have higher Mg# (cf. Figure 4B).

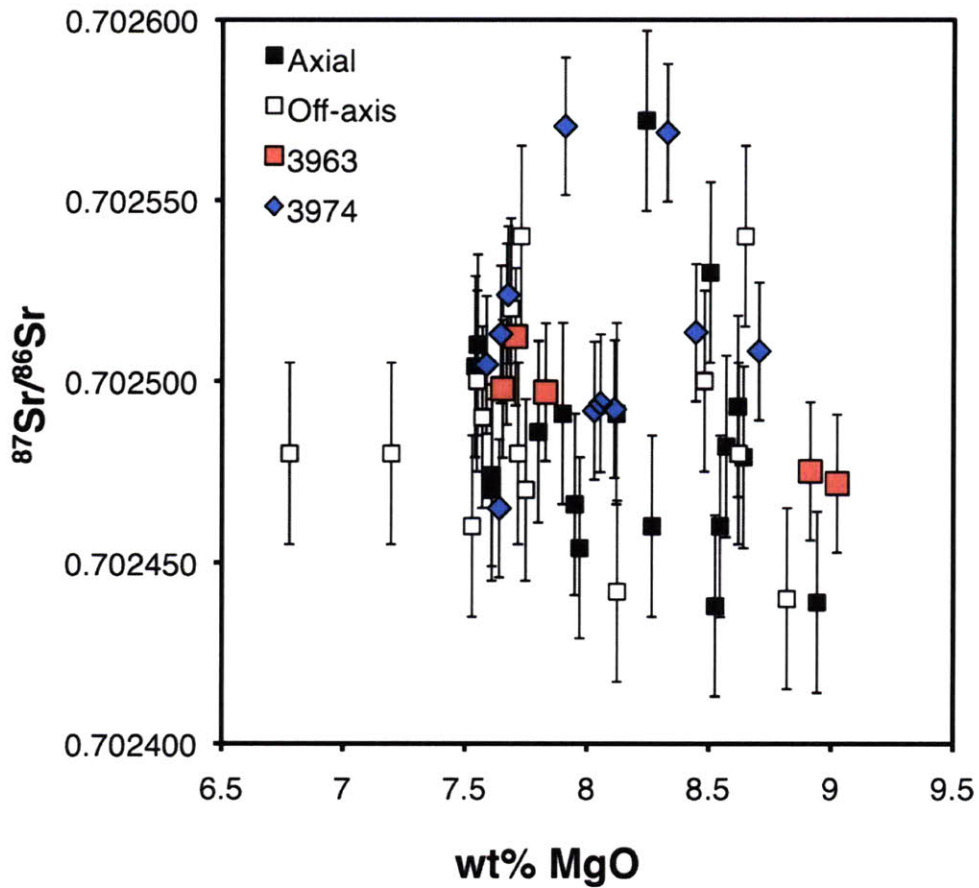


Figure 6. $^{87}\text{Sr}/^{86}\text{Sr}$ vs. wt% MgO shown in comparison to data from Sims et al. [2002; 2003] and Waters et al. [in review]. Axial samples are shown as black squares [Sims et al., 2002], off-axis samples as white squares [Sims et al., 2003; Waters et al., in review], dive 3974 samples as blue diamonds, and dive 3963 samples as red squares.

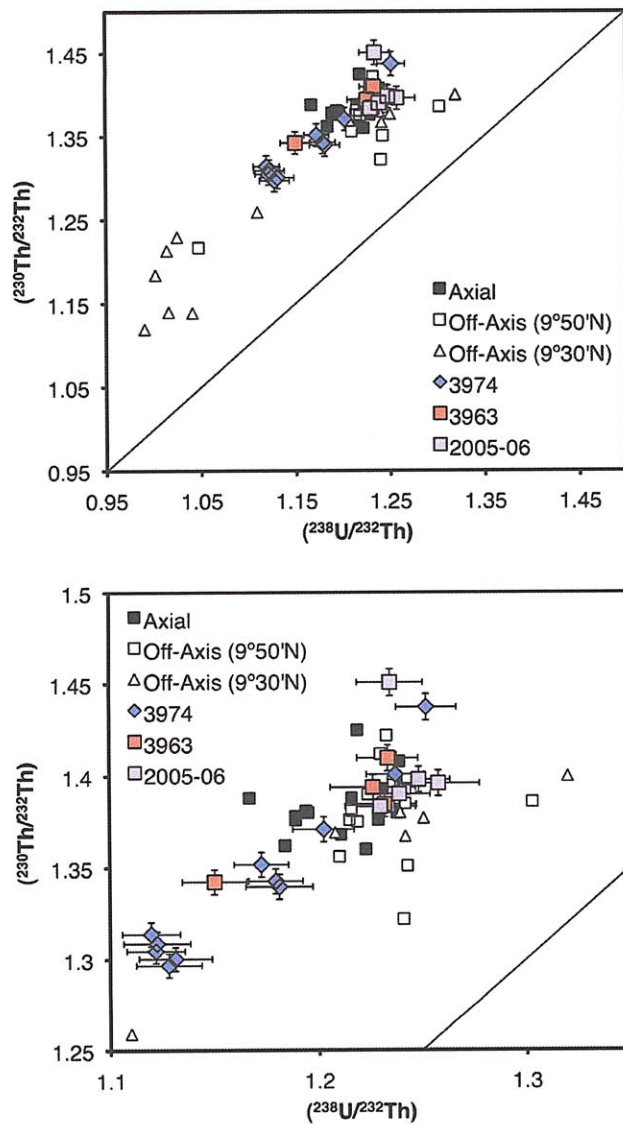


Figure 7. (A) Equiline diagram comparing $(^{238}\text{U}/^{232}\text{Th})$ with $(^{230}\text{Th}/^{232}\text{Th})$ among samples collected from within the AST from $9^{\circ}17'\text{N}$ - $9^{\circ}54'\text{N}$, including many presumed to be from the 1991-1992 eruption (black squares; [Sims et al., 2002]); samples collected from up to ~ 4 km off-axis at $9^{\circ}50'\text{N}$ (white squares; [Sims et al., 2003; Waters et al., in review]); E-MORB and N-MORB collected from up to ~ 5 km east of the AST at $9^{\circ}30'\text{N}$ (white triangles; [Waters et al., in review]); samples from dive 3974 on the west flank of the ridge crest at $9^{\circ}50'\text{N}$ (blue diamonds; this study); samples from dive 3963 on the east flank of the ridge crest at $9^{\circ}50'\text{N}$ (red squares; this study); and, samples collected from near the AST and presumed to represent the 2005-2006 eruption (purple squares; this study). (B) Expanded view of (A). Note the positive correlation between $(^{230}\text{Th}/^{232}\text{Th})$ and $(^{238}\text{U}/^{232}\text{Th})$ for *Alvin* Dive 3974 samples, which trend towards E-MORB compositions but do not have enriched long-lived radiogenic isotope compositions.

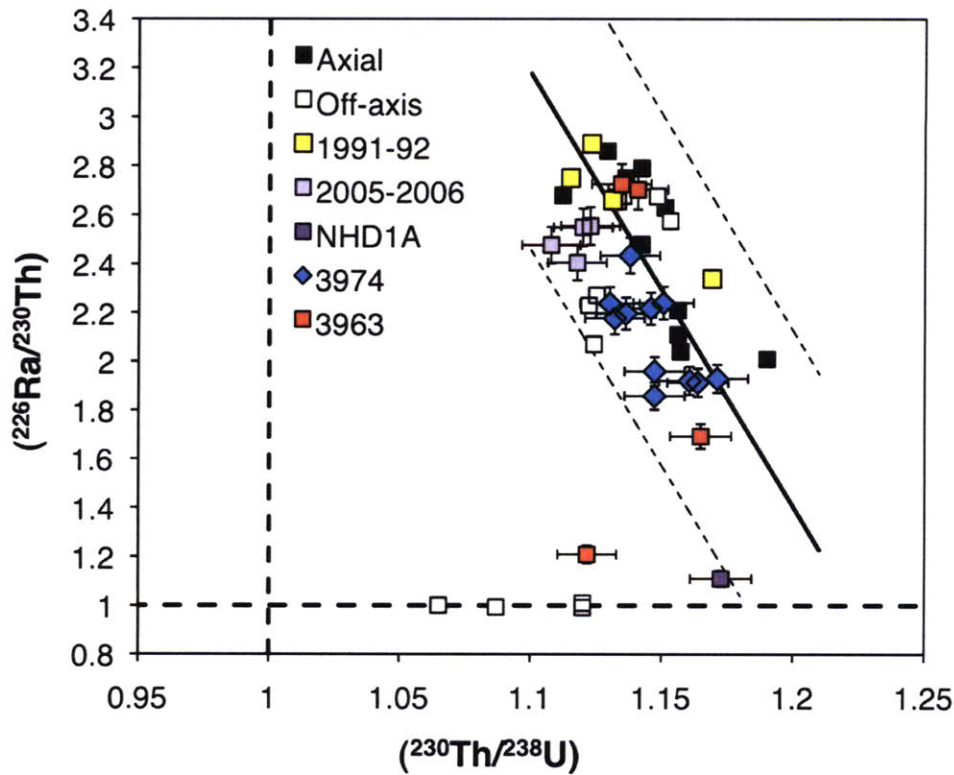


Figure 8. ($^{230}\text{Th}/^{238}\text{U}$) vs. ($^{226}\text{Ra}/^{230}\text{Th}$), showing the zero-age trend line calculated from a double-error, maximum likelihood, non-linear least squares fit for a line [Sohn and Menke, 2002] to both data obtained on samples collected within the AST north of $9^{\circ}37'\text{N}$ EPR (black squares; [Sims et al., 2002]), and data obtained in this study for samples collected from flows associated with the 2005-2006 eruption (purple squares). Many of the samples collected from the AST are presumed to have been erupted during the 1991-1992 eruption including several samples (yellow squares) whose eruption dates have been constrained to the 1991-1992 eruption by ^{210}Po - ^{210}Pb dating [Rubin et al., 1994]. (The equation for this line is $(^{226}\text{Ra}/^{230}\text{Th}) = -17.71283 \times (^{230}\text{Th}/^{238}\text{U}) + 22.66071$, $r = -0.665$, mean square of the weighted deviates (MSWD) = 10.051). The dashed lines that are parallel to the trend line are the 95% confidence limits for the ‘zero-age’ population. We note that this trend has previously been interpreted as a mixing trend [Sims et al., 2002; 2003] and since the denominators for the X- and Y-axes are not equivalent, we should expect mixing to be best approximated by a hyperbola. However, fitting a hyperbola to these data requires confidence in our knowledge of the end member mixing components [Sohn, 2005], but these end members are poorly constrained by few samples with known initial ($^{226}\text{Ra}/^{230}\text{Th}$) [cf., Elkins, 2009; Lundstrom et al., 1999; Sims et al., 2002; Waters et al., in review]. Thus, we approximate the mixing trend with a line, noting that fitting a binary mixing curve through these “zero-age” data [Sohn, 2005] using two (X,Y) coordinates calculated from the line fit for end member ratios results in a curvature of 0.967 ± 0.07 . This value is within error of 1, the case for a straight line, providing some evidence that our approximation of linearity is justified. Dive 3974 samples are plotted as blue diamonds, and dive 3963 samples are plotted as red squares. Also shown for comparison are samples collected off-axis at $9^{\circ}50'\text{N}$ and previously dated with the ^{230}Th - ^{226}Ra model age technique (white squares; [Sims et al., 2003; Waters et al., in review]).

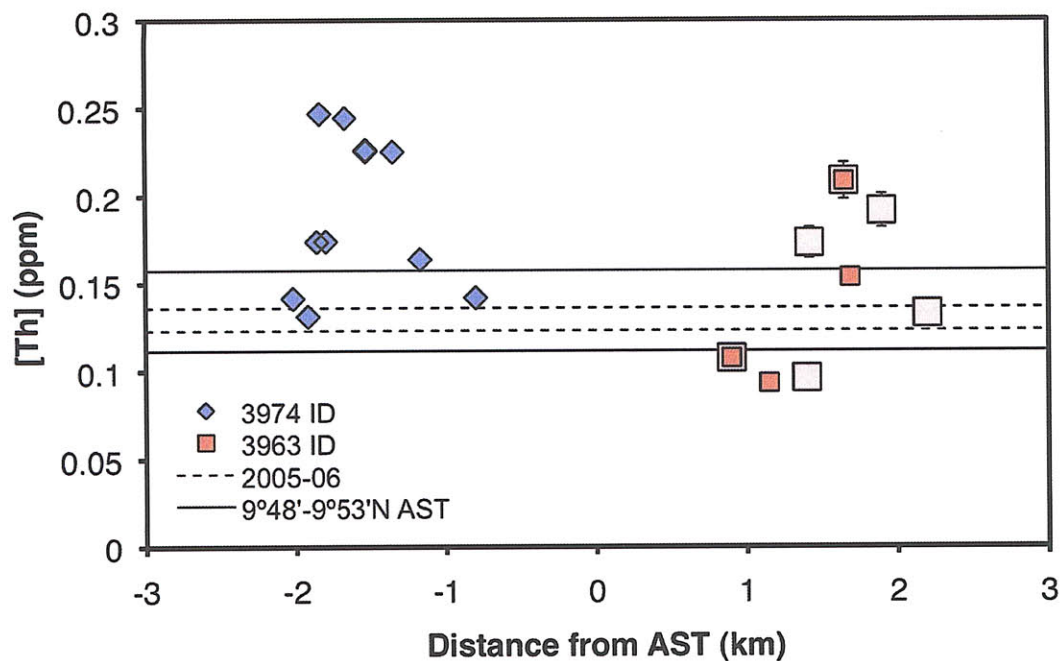
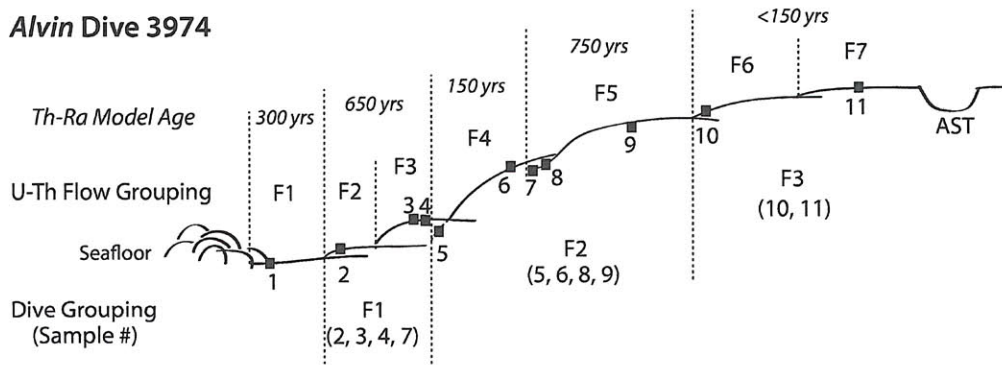
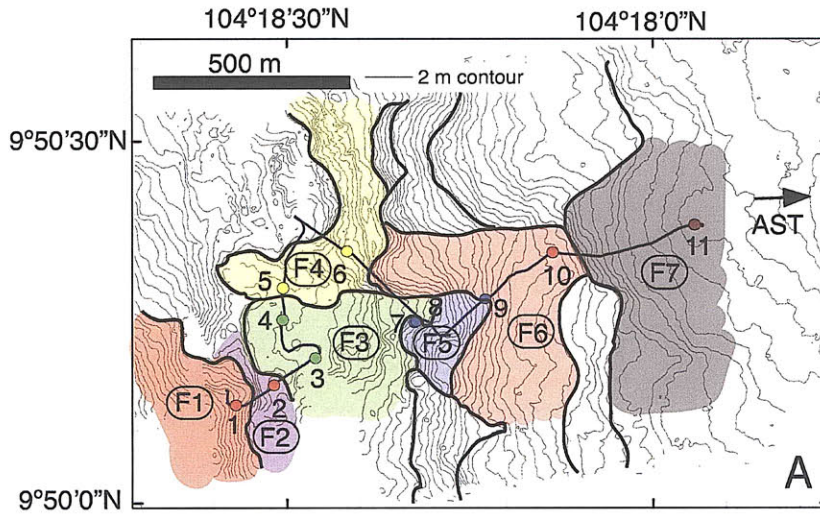


Figure 9. Plot of sample distance from the AST vs. Th concentration (ppm). Samples analyzed by isotope dilution (ID) from dive 3974 and dive 3963 are shown in blue diamonds and red squares, respectively. Dive 3963 ID data is supplemented by traditional ICP-MS concentration data where ID data is not available. Also shown are the ranges of concentrations for samples collected from the eruptions occurring from 1991-1992 (solid line, as measured by isotope dilution; [Sims et al., 2002]) and from 2005-2006 (dashed line, this study). Note that the samples defining the range in Th concentration for the 1991-1992 eruption may not all be from the 1991-1992 eruption but were collected from within the AST from 9°48'N-9°53'N and are likely less than ~ 200 yrs old [Sims et al., 2002].

Alvin Dive 3974



	Evolved ←				Primitive →		
Wt% MgO	7.6	7.6	8.0-8.1	7.6-7.7	7.9-8.4	8.3	8.7
La/Sm	1.02	1.00	1.14-1.15	1.27-1.34	1.25-1.28	1.13	1.16
Th/U	2.42	2.45	2.57	2.70	2.68	2.59	2.52
	Depleted ←		Enriched		Depleted →		



Alvin Dive 3963

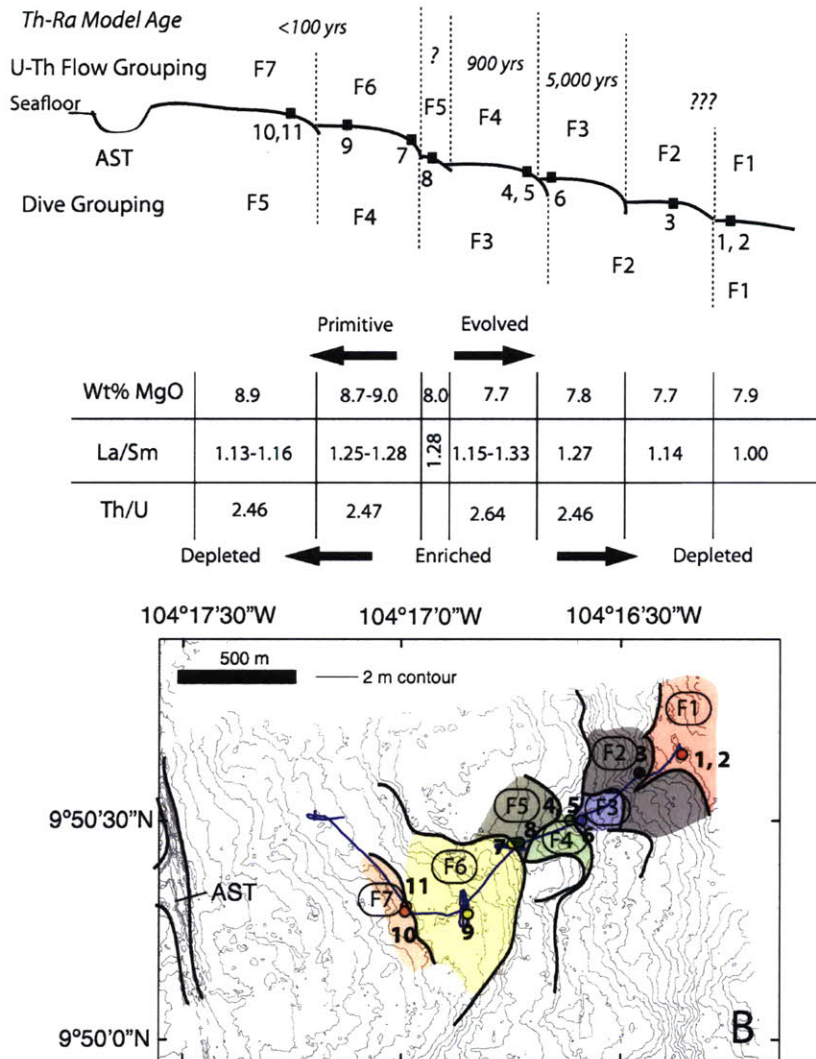
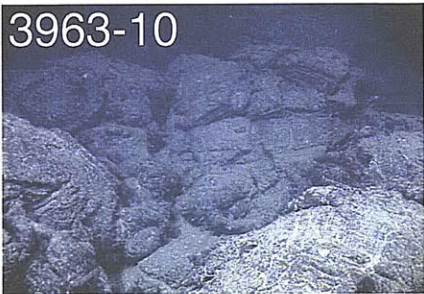
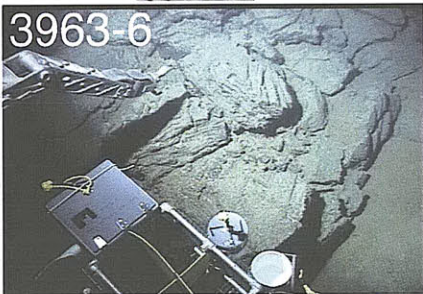
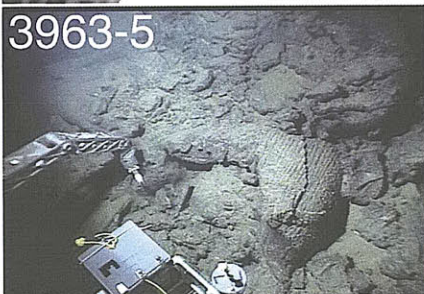
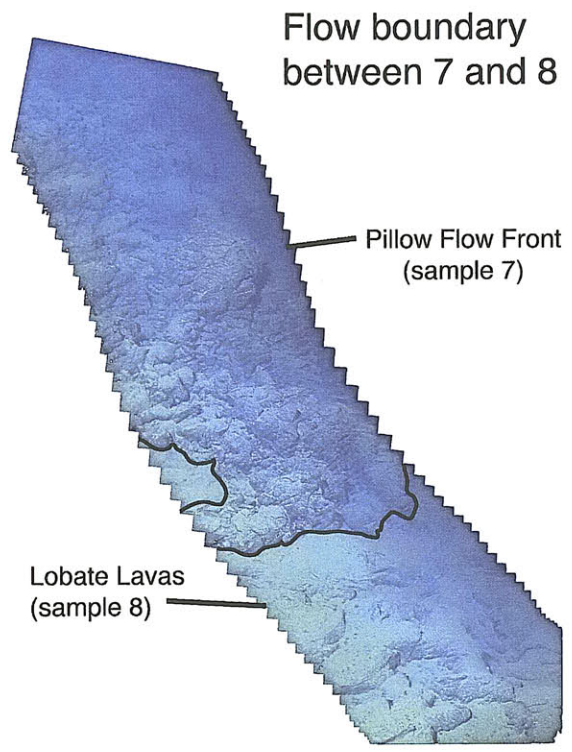
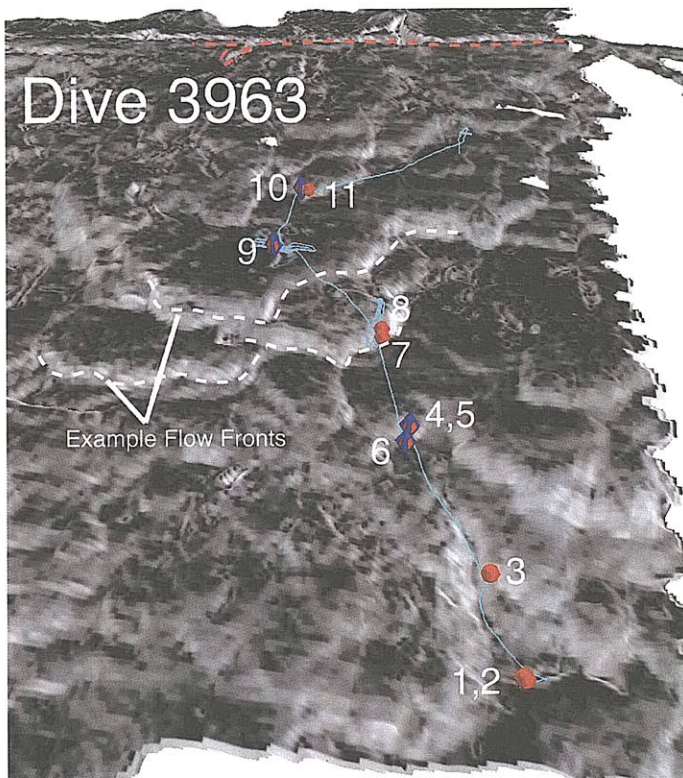


Figure 10. Schematic cross-sectional profiles and interpretations of flow units sampled during (A) *Alvin* dive 3974 and (B) *Alvin* dive 3963 summarizing model ages, geochemistry and compositional trends for flows, and flow divisions determined by geochemistry vs. *in situ* seafloor dive observations. F1=flow 1. In interpretative maps, colors delimit individual lava flows for matching samples. Note that similar colors for dive 3974 and 3963 flow units are not intended to imply matching flows on the west and east flanks. Because U and Th concentrations were determined by isotope dilution for only a subsample of *Alvin* dive 3963 samples, additional subdivisions of flow units shown in Figure 10B were made using the U and Th concentrations reported in Table 3. Because propagated uncertainties for Th/U measured by ICP-MS without isotope dilution are large (>10%), we only show Th/U as measured by isotope dilution.



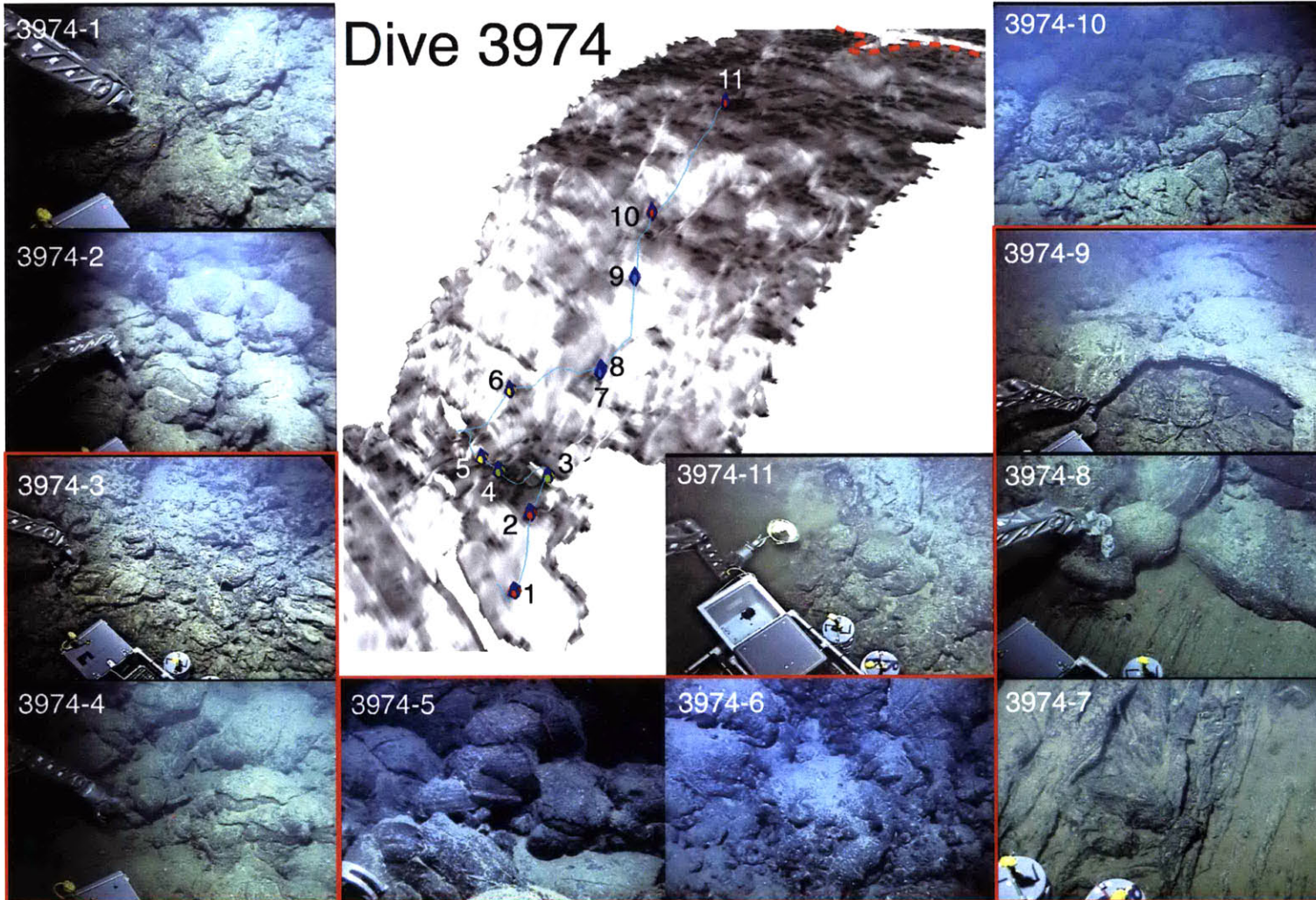


Figure 11. Perspective ABE bathymetric maps of dives 3963 and 3974 illustrate flow fronts along the dive tracks (cyan lines; example flow fronts are marked as dashed white lines in the map of dive 3963). Images are vertically exaggerated to better show the 5-15 m high flow fronts. Light shades indicate steep slopes such as pillow flow fronts; dark areas show relatively flat areas of lobate and sheet flows. For reference, a dashed red line is used to mark the boundary of the AST. Numbered, colored circles mark sample locations; samples age dated using ^{230}Th - ^{226}Ra model ages are further denoted by dark blue diamonds. *Alvin* dive 3974 samples are subdivided by color into flow units based on cluster analysis results of U-series data (see Figures 10, A1; red circles=Flows 1, 2, 6, and 7; green circles=Flow 3; yellow circles=Flow 4; blue circles=Flow 5). A photomosaic of a characteristic flow boundary observed during dive 3963 between samples 3963-7 and 3963-8, constructed using the Patchmap software by Y. Ryzanov [see Schouten et al., 2004], is shown to the right of the dive 3963 map. Note the sharp contact between pillow and lobate flow morphologies. Photos of selected lavas are also shown. Dive 3974 lavas determined from geochemistry to originate from the same flow are group by red boxes (e.g. 3974-3 & 3974-4). In general, pillow flow fronts do indeed represent the termini of flow lobes (e.g., photo of 3974-5 shows young pillow lava overlying the more sedimented lava flow in the foreground from which 3974-4 was collected). However, in some cases, pillow lavas overlying other flow morphologies belong to the same flow unit (e.g., pillow lava 3974-8 overlies sheet lava 3974-7). See text for details. The field of view for photos of 3963-5, 6, 10, and 3974-2, 3, 4, 5, 6, 8, 9, 10, and 11 is estimated at ~2-3 m (note that the lasers are 10 cm apart). The field of view for the photos for 3974-1 and 3974-7 is estimated at ~1.5 m. In general, lavas appear relatively young in dive photos, subtle differences in sedimentation correspond with age differences. In particular, the oldest lava dated in this study (~5 ka), sample 3963-6, is substantially more sedimented (most apparent in the lower right foreground) than sample 3963-5 (~1 ka), which was collected from the overlying pillow front. Samples 3963-9 (not shown) and 3963-10, which have the largest ($^{226}\text{Ra}/^{230}\text{Th}$) measured in this study and are thus interpreted as being extremely young, appear much less sedimented, less altered, and younger in photographs.

Appendix A. Dive Summaries

Dive 3963: Eleven samples were obtained during a west to east traverse of the eastern flank of the ridge crest (Fig. 1, 2, Table 1) [Schouten et al., 2004]. Dive 3963 began ~2.2 km to the east of the AST in a flat location of older-appearing ropey sheet flows (samples 3963-1 and 3963-2). These flows transitioned to lobate flows mixed with flat and ropey sheet flows covered with a similarly thin veneer of sediment. A change in morphology to pillow lavas was accompanied by a change in slope, presumed to be a pillow flow front (sample 3963-3). This morphological sequence was repeated up to a second flow front, from which pillow lava samples 3963-4 and 3963-5 were collected. Sample 3963-6 is a sheet flow from the lobate/sheet terrain at the base of this second pillow flow front. The top of the flow front was covered by younger-looking lobate flows with lighter sediment cover. The morphological sequence was repeated again to the west, and sample 3963-7 was collected from a third flow front. The third pillow flow front was surveyed using sonar Imagenix (Fig. 1, 2). Sample 3963-8 was obtained from the lobate flows at the base of the flow front. Beyond the flow front, a lava channel was located (identified earlier from ABE bathymetry) in a flat area of lobate and sheet flows. Sample 3963-9 was collected from the wall of the channel, and the area was surveyed with Imagenix. The channel was followed towards the ridge axis, and terminated in lobate and sheet terrain. A few hundred meters beyond the channel termination, samples 3963-10 and 3963-11 were obtained from a fourth pillow flow front.

Dive 3974: Eleven more samples were acquired on the western flank during dive 3974 (Fig. 1, 2, Table 1) [Schouten et al., 2004]. The dive traversed west-to-east along and across a series of four flow fronts identified from ABE bathymetry and by their pillow morphology during dive observations, starting ~1.9 km west of the AST and following the fronts back up the western ridge flank towards the AST. As in dive 3963, each flow front was composed of steep (10°-45°), pillow lavas located between flat (0°-4°) areas of mixed sheet and lobate flows [Schouten et al., 2004]. Of the 11 samples collected, five pillow lavas were sampled directly from the flow fronts, and three sheet flows and three lobate flows were sampled from flat areas adjacent to the flow fronts.

In both dives, flat sheet flows sometimes appeared to form channels in the hackly sheet and lobate flows [Schouten et al., 2004]. In at least one case, the flat and hackly sheet flows appeared to flow down a flow front (flat sheets appeared superposed on the adjacent pillow lavas). Dive notes speculate that the pillow lavas may have been a late eruptive phase that extruded from the hackly flow unit [Schouten et al., 2004]. In both dives, sediment cover along the dive track was relatively constant, with slightly more sedimentation farther away from the axis.

Appendix B. Cluster Analysis

We used the JMP® statistical software package to conduct a hierarchical cluster analysis on dive 3974 samples using Ward's criterion, in which the distance between two clusters

is the analysis of variance (ANOVA) sum of squares between the two clusters summed over all of the variables, and clusters are grouped at each generation by merging two clusters such that the within-cluster sum of squares is minimized. We constructed separate dendrograms based exclusively on standardized (1) major element concentration data (Table 2), (2) trace element concentration data (including U and Th ID concentrations) (Tables 3 and 5), and (3) U, Th, and Ra isotope dilution concentration data, Th/U, ($^{238}\text{U}/^{232}\text{Th}$), ($^{230}\text{Th}/^{232}\text{Th}$), ($^{230}\text{Th}/^{238}\text{U}$), and ($^{226}\text{Ra}/^{230}\text{Th}$) (Table 5; Figure A1; n.b. including only U, Th, and Ra concentration data and ($^{230}\text{Th}/^{232}\text{Th}$) does not change the structure of the dendrogram, and results in only minor differences in distances). Though these dendrograms differ in their details, there are several consistent clusterings. With respect to all data sets, samples 3974-3 and 3974-4 are the samples that are most similar and thus are always clustered together. Although 3974-5 and 3974-6 are not consistently the next most similar samples, they are also always clustered together. In addition, samples 3974-7 and 3974-8 belong to the same cluster when considering major elements, but 3974-7 and 3974-9 are clustered together when considering trace element and U-series data. Both major and trace element dendrograms group 3974-8 with the cluster containing 3974-3 and 3974-4, whereas the U-series dendrogram groups 3974-8 with 3974-7 and 3974-9. We note that regardless of which data set we consider (major element, trace element, or U-series), sample 3974-7 is always more similar to 3974-8 and 3974-9 than to 3974-5 and 3974-6.

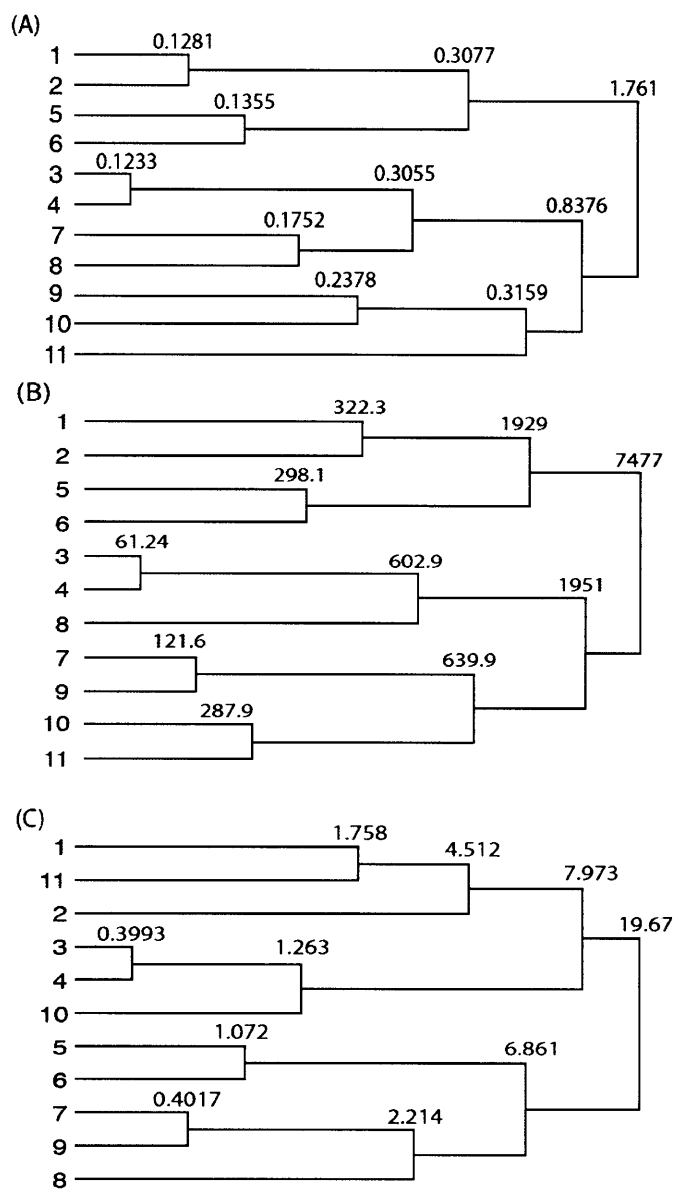


Figure A1. Dendrograms of *Alvin* dive 3974 samples constructed by hierarchical cluster analysis using Ward's criterion for clustering and distance as a measure of similarity. Distances are marked at each linkage; note the dendrograms are not to scale. Data used for each cluster analysis were standardized and include (A) major elements, (B) trace elements (including U and Th concentration data by ID), and (C) U, Th, and Ra concentrations (by ID) and isotopic disequilibria.

CHAPTER 4: ^{238}U - ^{230}Th - ^{226}Ra CONSTRAINTS ON THE VOLCANIC AND MAGMATIC EVOLUTION OF AN OVERLAPPING SPREADING CENTER AT 9°03'N EAST PACIFIC RISE

ABSTRACT

Recent geophysical studies of the overlapping spreading center (OSC) at 9°03'N along the East Pacific Rise (EPR) have imaged significant melt bodies throughout the crust and reveal a complex and asymmetric crustal melt distribution compared to adjacent ridge segments. This complicated geometry is thought to have significant implications for the storage and evolution of melt in the crust, and indeed, a wide range of melt compositions have been sampled at the 9°03'N OSC, including highly differentiated lavas such as FeTi basalts and dacites. Thus, the 9°03'N OSC is an ideal location to explore the relationships between melt composition, melt lens geometry, and crustal accretion.

Here we present major and trace element compositions, and $^{87}\text{Sr}/^{86}\text{Sr}$, $^{143}\text{Nd}/^{144}\text{Nd}$, and U-series isotope compositions for a suite of 22 representative lavas, collected during a cruise in 2007 with the *Jason II* ROV, that come from along and across the east limb of the OSC and span a wide range of compositions. When compared with crystallization models and experiments, the major element compositions of ferrobasalts and dacites are well explained by derivation by fractional crystallization of a primitive basaltic magma similar to that needed to explain compositional trends at 9°50'N EPR. Coherent mixing trends among major element, trace element, and U-series isotopic compositions indicate that mixing of ferrobasaltic and dacitic end members produces intermediate basaltic andesite and andesite compositions. Constant $^{87}\text{Sr}/^{86}\text{Sr}$ ($\sim 0.70250 \pm 50$ ppm, 2σ) and near equilibrium ($^{234}\text{U}/^{238}\text{U}$) and ($^{226}\text{Ra}/^{230}\text{Th}$) isotopic compositions in dacites argue against their formation by assimilation of partial melts of hydrothermally altered crust, a process previously proposed to explain the origin of high-silica MOR lavas.

Significant ^{226}Ra excesses measured in ferrobasalt, FeTi basalts, and basaltic andesites indicate recent ($\ll 8$ kyrs) volcanic activity has occurred along most of the east limb axial graben (9°03'-9°10') and out to 4 km off-axis in the region north of the overlap basin. Axial basalts have the highest ($^{226}\text{Ra}/^{230}\text{Th}$) (2.10- 2.41) and appear extremely young, whereas basalts collected off-axis have consistently lower ($^{226}\text{Ra}/^{230}\text{Th}$) (1.84- 1.96) and appear much older, suggesting that the axial graben is the primary locus for recent volcanic activity. In addition, young-appearing axial dacites have much lower, near equilibrium ($^{226}\text{Ra}/^{230}\text{Th}$) values, but ($^{230}\text{Th}/^{232}\text{Th}$) values that appear unchanged relative to that observed in zero-age basalts, suggesting residence times of ~ 8 kyrs.

4.1. INTRODUCTION

Mid-ocean ridge (MOR) segmentation is a ubiquitous feature of the global ridge system, and understanding the origin and evolution of the discontinuities that separate ridge segments is fundamental to understanding the tectonic and magmatic interactions among the different components of the oceanic lithosphere and the underlying asthenosphere. Ridge discontinuities exist on many scales, ranging from 1st order transform faults that offset ridge axes by 100s of kms, to 4th order discontinuities such as small (<0.5 km), non-overlapping, lateral offsets or kinks or bends in the strike of the ridge axis (Batiza and Margolis, 1986; Langmuir et al., 1986; Macdonald et al., 1988; 1998; White et al., 2001; 2002; 2006). Ridge discontinuities also appear to separate regions of geochemically distinct melt supply, as observed by significant changes in petrology, lava geochemistry, and volcanic and hydrothermal activity across discontinuities (e.g., Haymon et al., 1991; Langmuir et al., 1986; Smith et al., 2001; Thompson et al., 1985). However, although magmatic discontinuities have been inferred from correlations among bathymetry (particularly variations in the axial geometry observed in cross-sectional profiles), tectonic structure (e.g., presence or absence of an axial graben), and magmatic structure (e.g., the presence or absence of an axial magma chamber (AMC)) (e.g., Detrick et al., 1987; Kent et al., 2000; Macdonald et al., 1988), direct evidence of intrinsic relationships between magmatic and tectonic segmentation has typically been obfuscated by a lack of geophysical constraints on crustal melt distribution in places where geochemical data are also available.

In contrast to many large MOR discontinuities, the large overlapping spreading center (OSC) at 9°03'N East Pacific Rise (EPR), a 2nd order discontinuity with an ~8 km offset and ~27 km of overlap, has been the subject of extensive tectonic and geophysical study (Bazin et al. 2001; 2003; Carbotte and Macdonald, 1992; Combier et al., 2008; Dunn et al., 2001; Sempere and Macdonald, 1984; 1986a,b; Toomey et al., 2007; Tong et al., 2002; 2003; Singh et al., 2006; White et al., 2009), including the first detailed 3-D multi-channel seismic reflection survey of a MOR (Kent et al., 2000). However, only limited geochemical and petrologic work has been done to date and these studies (Langmuir et al., 1986; Natland and Melson, 1980; Natland et al., 1986a, b) indicate that this tectonic discontinuity delimits a significant magmatic discontinuity. For example, highly evolved ferrobasalt, FeTi basalts, and high silica lavas are present along the eastern limb of the OSC, but the western limb appears to erupt more primitive mid-ocean ridge basalts (MORB) as well as enriched MORB (E-MORB) with higher Ba/TiO₂ and Sr concentrations (Langmuir et al., 1986).

A recent research cruise (AT15-17) to the OSC at 9°03'N EPR in March-April of 2007 sought to improve our knowledge of this area by combining a DSL-120A side-scan sonar survey with mapping and sampling by ROV *Jason II* and Towcam photo surveys. Two hundred eighty-two rock samples were collected, including evolved ferrobasalts (>11 wt% FeO), FeTi basalts (FeO/MgO>1.75), basaltic andesites, andesites, and dacites (Wanless et al., 2007). Because of the comprehensive spatial coverage provided by this new sample suite on a geophysically and tectonically well-characterized ridge discontinuity, this sample suite presents an ideal opportunity to determine the distribution

of neo-volcanic activity and to understand the linkages between geochemistry and subsurface melt distribution at a significant tectonic discontinuity.

We measured major and trace element, Sr, Nd, and ^{238}U - ^{230}Th - ^{226}Ra isotopic compositions on a representative suite of 22 lavas that encompass a wide compositional range and spatial distribution with respect to the seismically imaged melt lens (Figure 1). The primary goal of this study is to use U-series nuclides to determine eruption ages of lavas. Lava ages are critical for interpreting petrological and geochemical data and for understanding how tectonic and magmatic processes contribute to the distribution of lava and organization of extrusive layer construction at MORs. In addition, U-series nuclides have the potential to provide constraints on magma transport rates and magma chamber residence times, and these constraints are important for understanding magmatic evolution at MORs.

4.2. GEOLOGIC SETTING AND SAMPLE DESCRIPTIONS

The East Pacific Rise from 8°-10°N is a fast-spreading ridge segment with a half-spreading rate of 5.5 cm/yr. It is bounded to the north at 10°10'N by the Clipperton Fracture Zone and to the south at ~8°20'N by the Siqueiros Fracture Zone. The overlapping spreading center (OSC) centered at 9°03'N consists of two north-south trending spreading ridges that overlap by ~27 km and are offset east to west by ~8 km (Figure 1). The OSC has been migrating southward for the last 1.8 My at an average rate

of ~ 42 mm/yr and the propagating eastern limb is thought to be truncating the receding western limb (Carbotte and Macdonald, 1992). An extensive geophysical study at the OSC documented evidence for a continuous supply of melt in the uppermost mantle across the OSC, with the lowest velocity anomaly centered beneath the east limb ridge axis (Dunn et al., 2001; Toomey et al., 2007), a melt accumulation in the overlying lowermost crust (Singh et al., 2006), and a mid-crustal mush zone at the northern end of the overlap basin at $\sim 9^{\circ}08'N$ (Bazin et al., 2003; Combier et al., 2008; Crawford and Webb, 2002).

Kent et al. (2000) conducted a 3-D multi-channel seismic reflection study at the OSC, and this study revealed details of the melt network geometry. A robust, ~ 4 km wide mid- to upper-crustal melt network offset to the west of the eastern limb ridge axis is located just north of the overlap basin (Kent et al., 1993; 2000). Melt reflectors deepen to the west, suggesting melt is being fed from an off-axis source (potentially from beneath the northern part of the overlap basin) to the deep, off-axis part of this melt lens, which is consistent with the melt-rich nature of this melt lens as interpreted by Singh et al. (2006). The melt lens narrows to <1500 m wide to the south at $\sim 9^{\circ}06'N$, and becomes centered beneath the morphological ridge axis. At this point, the melt lens exhibits a sudden decrease in depth before plunging ~ 500 m over 6 km towards the eastern ridge tip in a series of small, ~ 200 m en echelon steps. Beyond $\sim 9^{\circ}02'N$, the melt lens extends south and east of the southwest trending morphological ridge axis (nearly perpendicular to the spreading direction), finally narrowing to ~ 250 m wide at its most southern extent before disappearing.

One of the primary objectives of the 2007 cruise AT15-17 was to sample along and across the wide melt lens (Figure 1). The ridge axis is dominated by the presence of an axial graben, as typically exhibited by intermediate spreading ridges (N.B. here the fast, full spreading rate of 11 cm/yr is partitioned between the two limbs). Within the ~750 m wide axial graben are two troughs, separated by a central, discontinuous volcanic ridge (Combier et al., 2008). Side-scan sonar images (White et al., 2009) and seismically determined bathymetry (Combier et al., 2008) reveal a large, axis-parallel pillow ridge and a flat-topped seamount at the westernmost extent of the wide melt lens (Kent et al., 2000) that are speculated to originate from vertical diking and off-axis volcanism (Figure 1; Combier et al., 2008; White et al., 2009).

Major element analyses of glasses from ROV *Jason II* samples reveal a wide range of compositions, including basalts, ferrobasalts, basaltic andesites, andesites, and dacites; roughly 33% of lavas sampled have >52% SiO₂ (Wanless et al., 2007; in review). Lavas appear to be distributed systematically, such that the most evolved compositions were sampled from the axial graben and overlie the eastern edge of the melt lens. The volcanic ridge in the axial graben is composed primarily of andesitic and dacitic lavas, and the lavas in the troughs surrounding the ridge are predominantly basaltic sheet and lobate flows. The immediate flanks of the axial graben are dacitic and andesitic in composition. Off-axis lavas are almost entirely ferrobasaltic in composition.

We have selected 22 samples that include a wide range of compositions from along and across the axial graben (up to the western extent of the wide melt lens) for U-Th-²²⁶Ra isotopic analysis and ²³⁸U-²³⁰Th and ²³⁰Th-²²⁶Ra model age dating. These samples provide excellent coverage over the east limb and the off-axis region to the west

of the east limb. Because of the coverage this sample suite provides, the relationship between their geochemistry and the imaged distribution of the underlying melt sill may provide important insights into the distribution, residence time, and eruptive frequency of different magma types. These samples and their locations are illustrated in Figure 1, and sample descriptions and locations are reported in Table 1.

A total of eight off-axis samples were selected for U-series analysis: four basalts from the off-axis pillow ridge (265-13, 265-18, 265-19, 265-20); one basalt from the off-axis flat-topped volcano (265-06); one basalt (265-12) from immediately adjacent to the off-axis pillow ridge; and, two basalts from mid-way across the wide melt lens (265-32, 265-33; from herein referred to as ‘flank’ basalts). The remaining 14 samples are axial samples: a ferrobasalt and a FeTi basalt from the axial graben at 9°03’N (266-18, 267-09); two basalts from the axial graben at 9°08’ (265-74, 265-76); six basaltic andesites from 9°05’-9°10’N within the axial graben (264-13, 264-17, 264-20, 265-49, 265-106, 265-108); an andesite (265-64) and a dacite (265-66) from within the axial graben at ~9°08.5’N; and, two dacites (265-83, 265-85) from the immediate flank on the west side of the axial graben at ~9°07.7’N.

Since it is critical that samples be young (less than a few kyrs old) to confidently link them to the seismically imaged melt sill and because we are primarily interested in the distribution of the most recent volcanic activity, most of these samples were selected based on the extremely fresh appearance of glass in hand sample and dive photos (e.g. minimal sediment cover, preserved pillow decorations and buds, vitreous luster; Figure 2). Six of the off-axis samples, 265-06, 265-12, 265-13, 265-18, 265-19, and 265-20, all

had significant Mn crusts in hand sample and substantial sediment cover in dive photos (Figure 2).

4.3. U-SERIES DATING AND MOR CRUSTAL CONSTRUCTION

K-Ar and Ar-Ar dating of non-marine sediments and volcanic rocks and correlation of non-marine and marine magnetic isochrons have traditionally been used to estimate the age of crust throughout the ocean basins (e.g. Cox et al., 1964; Muller et al., 2008), but direct age determinations of young submarine lavas (<375 ka) using these techniques are problematic and lack the resolution to discern the fine-scale age differences of neo-volcanic crust near MOR axes (Duncan and Hogan, 1992). At present, the most promising techniques for dating young MOR lavas are U-series and magnetic paleointensity techniques; these techniques have produced concordant ages on individual samples (cf., Bergmanis et al., 2007; Bowles et al., 2006; Sims et al., 2003; Waters et al., in review; in prep). Although both techniques have contributed greatly to our understanding of crustal construction, U-series dating of young MORB has arguably been explored more extensively than magnetic paleointensity techniques.

U-series dating methods are particularly appealing because they provide constraints on both petrogenetic processes and eruption ages. The half-lives of U-series nuclides, in particular ^{226}Ra (1.6 kyrs) and ^{230}Th (75 kyrs), make them ideally suited for studying recent geological processes, especially magmatism and volcanism. U-series nuclides may fractionate due to partial melting and/or crystallization, creating

disequilibria, but radioactive decay during melt transport, crustal residence, and post-eruption aging will return them towards a steady-state condition called “secular equilibrium,” in which the activities of nuclides are equal and the activity ratios (e.g., $(^{226}\text{Ra}/^{230}\text{Th})$, $(^{230}\text{Th}/^{238}\text{U})$) are unity. In addition, the magnitude of disequilibria produced by partial melting is affected by the initial abundance of the U-series nuclides in the melting rock.

Thus, the extent of U-series disequilibria measured in any lava reflects the integrated signal of a number of processes that modify an initial mantle rock composition—including partial melting, melt transport, crustal residence, and seafloor alteration—and the time scales over which these processes occur, namely subsurface residence in the mantle and crust and post-eruption aging. In some instances, the relationships among U-series disequilibria and other geochemical metrics affected by source composition, partial melting, crystallization, and crustal residence (e.g., long-lived radiogenic isotope compositions, incompatible element ratios, and major and trace element abundances) can be used to help disentangle this convoluted geochemical signal and determine eruption ages. Indeed, studies of MORB using U-series nuclides have demonstrated their ability to place constraints on melting and melt transport rates in the mantle (e.g., Jull et al., 2002; Lundstrom et al., 1995; 1998; 1999; 2000; McKenzie et al., 1985; Rubin et al., 2005; Sims et al., 1995; 1999; 2002), crustal residence times (e.g., Cooper et al., 2003; Rubin et al., 2005; Sims et al., 2002), and eruption ages (e.g., Bergmanis et al., 2007; Goldstein et al., 1992; 1993; 1994; Rubin et al., 1990; 1994; Sims et al., 2003; Standish and Sims, 2010; Sturm et al., 2000; Volpe and Goldstein, 1993).

Because secular equilibrium is reached again in roughly five half-lives following the fractionation of nuclides, or ~8 kyrs and ~375 kyrs for ^{226}Ra and ^{230}Th , respectively, the presence of disequilibrium in a lava, for example $(^{226}\text{Ra}/^{230}\text{Th}) \neq 1$, or $(^{230}\text{Th}/^{238}\text{U}) \neq 1$, immediately limits a lava's eruption age to <8 ka or <375 ka. In addition, if the initial extent of disequilibria in a basalt sample upon eruption can be established, the difference between that initial activity and the current measured activity can be used to explicitly determine the lava eruption age. U-series model ages for off-axis MORB have been calculated by estimating the initial activities from data for the youngest axial basalts and comparing these with the activities measured in a sample of unknown age (Goldstein et al., 1993; 1994; Sims et al., 2003). For example, when calculating model ages of samples from 9°-10°N EPR, initial activity ratios can be estimated based upon measurements from lava collected exclusively within the AST and known to have erupted in 1991-92 (Sims et al., 2002; 2003).

It is important to note that these U-series ages are “model” ages in that they assume a constant source (spatially and temporally) and are the sum of magma chamber residence time and eruption age. When determining U-series model ages, several criteria must be met to assure that the initial extent of disequilibria in the lava of known age and the sample of interest is the same:

- (1) Primary magmatic processes initially created U-series disequilibria and the lavas being dated have not undergone significant secondary alteration. These lavas have remained a closed system with respect to Th/U after eruption.

- (2) After melt generation and transport, the magma has not resided for significant periods of time in a magma chamber relative to the half-lives of ^{230}Th (~75 kyrs) and ^{226}Ra (~1.6 kyrs).
- (3) The source of the axial and off-axis lavas is constant, both spatially and temporally, with respect to Th/U.
- (4) Both the axial lavas and the off-axis lavas were derived by similar degrees of melting and that the depths of melting and melt transport rates were also similar (e.g., McKenzie, 1985; Rubin et al., 2005; Spiegelman and Elliot, 1993; Williams and Gill, 1989).

These criteria have been met by off-axis samples from dating studies at 9°50'N EPR (Sims et al., 2003; Waters et al., in prep.). Having satisfied all of the above listed criteria, both Sims et al. (2003) and Waters et al. (in prep) were able to calculate model ages using best fit trend lines on plots of ($^{238}\text{U}/^{232}\text{Th}$) vs. ($^{230}\text{Th}/^{232}\text{Th}$) and ($^{230}\text{Th}/^{238}\text{U}$) vs. ($^{226}\text{Ra}/^{230}\text{Th}$) to represent initial ($^{230}\text{Th}/^{232}\text{Th}$) and ($^{226}\text{Ra}/^{230}\text{Th}$) disequilibria in young (<200 yrs) lavas collected from within the AST from 9°17'-9°54'N EPR and from the 2005-2006 flow (Sims et al., 2002; 2003; Waters et al., in prep.). Aging from these trend lines follows a vertical trajectory, and the difference in ($^{230}\text{Th}/^{232}\text{Th}$) and ($^{226}\text{Ra}/^{230}\text{Th}$) from the initial value estimated by the trend line can be used to calculate the lava eruption age, again assuming that the initial disequilibria in the sample of known age and the sample of interest are equal.

Because a number of physical volcanic processes contribute to the complicated distribution of lava flows about the ridge axis, eruption ages are essential for

understanding the spatial and temporal extent of these processes. In particular, variations in eruption volumes, frequency, and distribution can have profound effects on upper crustal construction. In addition, eruption ages provide a necessary context for correctly interpreting observed geochemical compositions of lavas in terms of variations in mantle geochemistry, partial melting processes, and subsurface melt distribution.

For example, when compared with high-resolution bathymetric and side-scan sonar imagery and magnetic profiles (Cochran et al., 1999; Escartin et al., 2007; Fornari et al., 1998; Schouten et al., 1999; Sims et al., 2003; Soule et al., 2009), the young U-series ages of many off-axis lavas from 9°17'-9°54'N EPR indicate that volcanic construction occurs over a wide zone extending up to several kilometers outside of the AST (Goldstein et al., 1994; Sims et al., 2003; Waters et al., in prep.; in review). Similarly, U-series observations of ^{238}U - ^{230}Th and ^{230}Th - ^{226}Ra disequilibria have shown that recent volcanism occurs over a surprisingly wide spatial extent at the intermediate-spreading Juan de Fuca and Gorda ridge segments (Goldstein et al., 1992; 1993; Cooper et al., 2003), the slow-spreading Mid-Atlantic Ridge at the Kane Fracture Zone (Sturm et al., 2000), and the ultra-slow spreading Southwest Indian Ridge (Standish and Sims, 2010).

4.4. ANALYTICAL METHODS

Major elements were analyzed on polished glass chips at the USGS Microbeam Laboratory in Denver, Co. using a JEOL 8900 Electron Microprobe. Analysis of seven

to ten separate points (including spots on separate chips of the same sample) were averaged for each sample and then normalized and corrected for instrument drift based on the established values for in-house standards JdF-D2 (Reynolds et al., 1995) and ALV2392-9 (see Smith et al., 2001). Analytical uncertainties are reported in Table 2.

Samples were analyzed for trace elements at the University of Florida using an Element II Inductively Coupled Plasma Mass Spectrometer (ICP-MS). The analyses were performed in medium resolution with Re and Rh used as internal standards. Concentrations were calculated by external calibration using a combination of USGS rock standards. Repeated chemical analyses of in-house MORB standard ALV2392-9 during each run were used to evaluate and correct for instrument drift as well as evaluate the accuracy and precision of the measurements. Analytical uncertainties are given in Table 3. Details of both major element analyses by electron probe and trace element analyses by ICP-MS can be found in Wanless et al. (in review).

Sr isotopic analyses were conducted either at WHOI using a Thermo Finnigan Neptune multi-collector inductively coupled mass spectrometer (MC-ICP-MS) or at Boston University using the Thermo Finnigan Triton thermal ionization mass spectrometer (TIMS). All Nd isotopic measurements were conducted at WHOI on the Neptune. Measurements of Sr and Nd isotopic compositions at WHOI have internal precision of 5-10 ppm. After adjusting to 0.710240 (NBS SRM 987) and 0.511847 (La Jolla Nd Standard), for Sr and Nd, respectively, external precision is estimated at 15-30 ppm. ϵ_{Nd} values were calculated using $(^{143}Nd/^{144}Nd)_{CHUR(O)} = 0.512638$. Replicate analyses by MC-ICP-MS Neptune on the same sample splits for Sr isotopic

measurements are well within analytical uncertainties of the measurements by TIMS Tritium (see Table 4).

^{238}U and ^{232}Th concentrations were measured at WHOI by isotope dilution ICP-MS using the ThermoFinnigan Element 2 and $^{234}\text{U}/^{238}\text{U}$, $^{230}\text{Th}/^{232}\text{Th}$ and ^{226}Ra concentrations (by isotope dilution) were measured using the WHOI ThermoFinnigan Neptune MC-ICP-MS. Analytical details are reported in Table 5. For more information on the ^{238}U - ^{230}Th - ^{226}Ra chemical and analytical procedures at WHOI, extensive details are presented in Appendix A1 of Sims et al. (2008a). More details of Th and U measurement methods and standards are summarized in Ball et al. (2008) and Sims et al. (2008b) and in the caption to Table 5.

4.5. RESULTS

Major and trace element data are compiled in Tables 2 and 3 for convenience; these data will be published as a subset of a larger data set elsewhere (Wanless et al., in prep). We report additional measurements of Sr and Nd isotope compositions in Table 4, as well as U, Th, and ^{226}Ra concentrations by isotope dilution, and ($^{238}\text{U}/^{232}\text{Th}$), ($^{230}\text{Th}/^{238}\text{U}$), ($^{230}\text{Th}/^{232}\text{Th}$), ($^{226}\text{Ra}/^{230}\text{Th}$), and ($^{234}\text{U}/^{238}\text{U}$) in Table 5.

4.5.1. Major Elements

Samples from the east limb of the OSC encompass a wide range of major element compositions, including ferrobasalt ($\text{SiO}_2 < 52$ wt%, $\text{FeO} > 11$ wt%, but $\text{FeO}/\text{MgO} < 1.74$),

FeTi basalt ($\text{FeO}/\text{MgO} > 1.74$, total $\text{FeO} > 12$ wt%, $\text{TiO}_2 > 2$ wt%, and $\text{SiO}_2 < 52$ wt%), basaltic andesite ($52\% < \text{SiO}_2 < 57$ wt%), andesite (57 wt% $< \text{SiO}_2 < 62$ wt%), and dacite ($> 62\%$ SiO_2). The entire suite of $9^\circ 03' \text{N}$ EPR lavas appears to be related by mixing, although the east limb OSC basalts generally appear to represent a continuum of compositions with lavas from $9^\circ 17' \text{N}$ - $9^\circ 54' \text{N}$ EPR (Figure 3). As a group, basaltic lavas from the eastern limb at $9^\circ 03' \text{N}$ EPR are quite homogeneous, but have higher wt% SiO_2 , Na_2O , K_2O , FeO , TiO_2 , and P_2O_5 , and lower wt% MgO (and molar $\text{Mg}\#$), CaO , and Al_2O_3 compared to axial lavas collected from $9^\circ 17' \text{N}$ - $9^\circ 54' \text{N}$ EPR and on the ridge flanks at $9^\circ 50' \text{N}$ EPR (Figure 3; Sims et al., 2002; 2003; Waters et al., in prep). Basalts from $9^\circ 03' \text{N}$ EPR have a lower, narrower range of $\text{Mg}\#$ than $9^\circ 17'$ - $9^\circ 54' \text{N}$ EPR basalts, due to both consistently higher abundances of FeO (11.22-12.08 wt% vs. 8.82-11.74 wt%, median 10.06 wt%) and lower abundances of MgO (6.60-7.21 wt% vs. 6.78-8.94 wt%, median 7.95 wt%). Indeed, there appear to be no primitive basalts (e.g., $\text{MgO} > \sim 8$ wt%) on the eastern limb of the $9^\circ 03' \text{N}$ OSC (Wanless et al., 2007).

When examined more closely, there appears to be a relationship between the spatial distribution of east limb basaltic lavas and their geochemistry. On average, basaltic lavas located farthest from the ridge axis (i.e., those lavas belonging to the pillow ridge and flat-topped volcano) have higher $\text{Mg}\#$, wt% MgO , CaO , and Al_2O_3 ; lower wt% SiO_2 , FeO , TiO_2 , and P_2O_5 ; slightly lower wt% K_2O (and $\text{K}_2\text{O}/\text{TiO}_2 \times 100$; herein referred to as K/Ti) and higher wt% Na_2O ; yet, similar total alkalis and $\text{CaO}/\text{Al}_2\text{O}_3$ in comparison to axial and flank basalts (Figure 3; Table 2). Similarly, axial and flank basalts can be grouped based on similar wt% TiO_2 , Al_2O_3 , and MgO , although flank basalts are transitional between pillow ridge and axial basalts with intermediate $\text{Mg}\#$, wt% CaO ,

FeO, and P₂O₅. Lastly, pillow ridge basalt 265-12 is distinct from all other pillow ridge basalts with notably low wt% CaO and MgO (and Mg#) and high wt% K₂O and appears more akin to axial and flank basalts. However, we note that this sample was collected away from the pillow ridge and is also significantly more enriched in incompatible trace elements as exhibited by much higher K₂O and K₂O/TiO₂ compared to all other east limb basaltic lavas (see section 5.2, Table 3, and Figures 4, 5).

4.5.2. Trace Elements

Basalts from the eastern limb of the OSC at 9°03'N EPR are remarkably homogeneous with respect to both their trace element abundances (Figure 4A, B) and ratios (Figure 5). Sample 265-12 has higher abundances of Th and U, but we do not have other trace element abundances for comparison. Axial basalts have slightly higher abundances in the most incompatible elements and slightly lower abundances of compatible elements (Figure 4B). Flank basalts are intermediate in composition to axial and pillow ridge basalts. East limb basalts have very similar trace element abundance patterns to 9°17'N-9°54'N basalts, but they are generally more enriched than 9°17'N-9°54'N EPR basalts in incompatible trace elements, with the least incompatible elements (i.e. heavy rare earth element (HREE)) showing the most relative enrichment, and the most incompatible elements (Ba, Th, U, Nb) being most similar.

Basaltic andesites, andesites, and dacites have higher incompatible element concentrations and lower compatible element concentrations than basalts (Figure 4A). In addition, basaltic andesite, andesite, and dacite trace element patterns are largely similar, but andesite and dacite compositions appear transposed to higher incompatible element

abundances and lower compatible element abundances than basaltic andesites. These evolved lavas have trace element patterns that are similar to the basalts, but have pronounced Th and U anomalies relative to Ba and Nb, more prominent Sr and Ti depletions, and very large depletions of the most compatible elements (V, Sc, Cu, Cr, and Ni). As with major element systematics, these trace element systematics indicate mixing between evolved and primitive lavas (Figure 5).

4.5.3. $^{87}\text{Sr}/^{86}\text{Sr}$ and $^{143}\text{Nd}/^{144}\text{Nd}$ isotope compositions

We report Sr isotope compositions for 17 lavas and Nd isotope compositions for 18 lavas in Table 4 and Figure 6. These analyses include axial basalts, flank basalts, basaltic andesites, and andesites and dacites. We have no Sr or Nd isotope data for off-axis pillow ridge basalts, although we do report Nd isotope measurements for 265-06, the sample from the flat-topped volcano. All east limb lavas have very homogeneous Sr and Nd isotope compositions that overlap with those of lavas from 9°17'N-9°54'N EPR. There are no systematic differences between axial and flank basalts, nor among basalts, basaltic andesites, andesites, and dacites. This isotopic homogeneity indicates constancy in the time-integrated parent/daughter ratios Rb/Sr and Sm/Nd of the mantle source for east limb lavas in this study, and it implies that the east limb lavas reported in this study originally melted from a common mantle source that is similar to the mantle source for lavas from 9°17'-9°54'N.

4.5.4. ^{238}U - ^{230}Th - ^{226}Ra

^{238}U - ^{230}Th - ^{226}Ra , ($^{230}\text{Th}/^{232}\text{Th}$), and ($^{234}\text{U}/^{238}\text{U}$) isotopic compositions and U, Th and Ra abundances, as measured by isotope dilution (ID), are reported in Table 5.

4.5.4.1. ($^{234}\text{U}/^{238}\text{U}$)

For submarine basalts, ($^{234}\text{U}/^{238}\text{U}$) is a sensitive indicator of alteration, because seawater is significantly enriched in ^{234}U relative to ^{238}U (for seawater, ($^{234}\text{U}/^{238}\text{U}$) = 1.14 \pm 0.03; Thurber, 1962; Ku et al., 1977; Henderson et al., 1993; Robinson et al., 2005). Nearly all samples measured have ($^{234}\text{U}/^{238}\text{U}$) in equilibrium within analytical uncertainties (\pm 0.5%) indicating that these samples have not suffered secondary alteration due to seawater-rock interaction following eruption. Only four samples have ($^{234}\text{U}/^{238}\text{U}$) more than \pm 0.5% out of secular equilibrium: 265-06 (1.006), 265-13 (1.006), 265-74 (1.008), and 265-76 (0.993). However, samples 265-06, 265-74, and 276-76 show no other indications that the ^{238}U concentrations have been perturbed.

In contrast, samples 265-12, 265-13, 265-19, and 265-33 have ($^{234}\text{U}/^{238}\text{U}$) \sim 1.004-1.006 and also have exceptionally high ($^{230}\text{Th}/^{232}\text{Th}$) values compared to other young MORB from 9°-10°N EPR (1.45-1.58 vs. 1.30-1.44; Sims et al., 2002; Waters et al., in prep.). Using the anomalous ($^{230}\text{Th}/^{232}\text{Th}$) values to calculate ($^{230}\text{Th}/^{238}\text{U}$) and ($^{226}\text{Ra}/^{230}\text{Th}$) also results in unreasonably high ($^{230}\text{Th}/^{238}\text{U}$) at a given ($^{226}\text{Ra}/^{230}\text{Th}$), and the ($^{226}\text{Ra}/^{230}\text{Th}$) values are significantly different from those of samples collected in close proximity that have nearly identical U, Th, and ^{226}Ra concentrations. Given the old appearance of these samples in hand specimen and the significant Mn crust (e.g. up to \sim 8 mm on 265-12; Figure 2B, C, F, G), we suspect that the procedure used for cleaning these

glasses (described in Table 5) was insufficient for removing all surface glass contaminants. In particular, Mn crusts are known to have extremely high ($^{230}\text{Th}/^{232}\text{Th}$) (>100) at Th/U relatively similar to MORB (Chabaux et al., 1997). Thus, we consider the U-series abundances and disequilibria for these samples to be affected by post-eruptive secondary contamination and we exclude them from further discussion.

4.5.4.2. ($^{230}\text{Th}/^{232}\text{Th}$)-($^{238}\text{U}/^{232}\text{Th}$) and ($^{230}\text{Th}/^{238}\text{U}$)

The variation in ($^{238}\text{U}/^{232}\text{Th}$) with ($^{230}\text{Th}/^{232}\text{Th}$) for east limb OSC samples is shown in Figure 7. All samples plot to the left of the equiline and have significant ^{230}Th excesses (i.e. ($^{230}\text{Th}/^{238}\text{U}$) >1), indicating recent fractionation in the presence of garnet (<375 ka) (e.g. Beattie, 1993; La Tourette et al., 1994; Salters et al., 1999; Salters and Longhi, 2002; Elkins et al., 2008). Furthermore, all east limb samples overlap with data for axial and off-axis N-MORB samples from $9^{\circ}17'$ - $9^{\circ}54'$ N EPR with respect to ($^{230}\text{Th}/^{232}\text{Th}$) and ($^{238}\text{U}/^{232}\text{Th}$) (Figure 7; Sims et al., 2002; 2003; Waters et al., in review; in prep.). ($^{238}\text{U}/^{232}\text{Th}$) generally decreases and ($^{230}\text{Th}/^{238}\text{U}$) increases with increasing wt% SiO_2 (i.e., from basalt to dacite) and decreasing Mg# at nearly constant ($^{230}\text{Th}/^{232}\text{Th}$): pillow ridge basalts have the highest ($^{238}\text{U}/^{232}\text{Th}$) and smallest ^{230}Th excesses (though all basalts have surprisingly similar ^{230}Th excesses of ~ 1.10 - 1.13), and dacites have the smallest ($^{238}\text{U}/^{232}\text{Th}$) (~ 1.17 - 1.18) and largest ($^{230}\text{Th}/^{238}\text{U}$) (~ 1.16 - 1.18 ; Figures 7B, 8). Pillow ridge basalts have higher ($^{238}\text{U}/^{232}\text{Th}$) (~ 1.27) relative to both flank and axial basalts, which have similar ($^{238}\text{U}/^{232}\text{Th}$) (1.22 - 1.25). Both flank and pillow ridge basalts have slightly higher ($^{230}\text{Th}/^{232}\text{Th}$) (~ 1.41) than axial samples (~ 1.35 - 1.38 ; including basalts, basaltic andesites, and dacites).

Dacites have significantly higher ^{230}Th excesses than basalts and basaltic andesites (Figures 7 and 8). Although, the basalts analyzed in this study all have ^{230}Th excesses that are small compared to $9^\circ\text{-}10^\circ\text{N}$ EPR N-MORB (~ 1.10 as compared to up to $\sim 1.11\text{-}1.19$, though very similar to 2005-2006 eruption samples, Figure 8; Sims et al., 2002; 2003; Waters et al., in prep), basaltic andesites and dacites have larger ^{230}Th excesses (1.10-1.16 and 1.16-1.18, respectively) that are much more akin to more enriched N-MORB at $9^\circ\text{-}10^\circ\text{N}$ EPR. Furthermore, plots of either U or Th vs. $(^{230}\text{Th}/^{238}\text{U})$ and $(^{238}\text{U}/^{232}\text{Th})$ look nearly identical and show enrichments of U and Th that strongly resemble mixing trends. Also, a plot of Mg# vs. $(^{230}\text{Th}/^{238}\text{U})$ shows a strong mixing relationship among ferrobasalts, basaltic andesites, andesites, and dacites (Figure 9A).

4.5.4.3. $(^{226}\text{Ra}/^{230}\text{Th})$

Figure 8 illustrates variations of $(^{226}\text{Ra}/^{230}\text{Th})$ with $(^{230}\text{Th}/^{238}\text{U})$ for all east limb samples. All samples have ^{226}Ra excesses (i.e., $(^{226}\text{Ra}/^{230}\text{Th}) > 1$) with the exception of two dacites. These dacites (265-83, 265-85) are the most evolved dacite samples and appear relatively young in dive photographs despite being collected just to the west of the axial summit graben at $9^\circ 08' \text{N}$ and having equilibrium $(^{226}\text{Ra}/^{230}\text{Th})$ values of $\sim 0.99\text{-}1.04$. Pillow ridge basalts, which appear quite sediment covered in dive photos (Figure 2C, G), have $(^{226}\text{Ra}/^{230}\text{Th})$ of 1.81-1.87. The flank basalt (265-32; Figure 2B) has similar, but slightly higher $(^{226}\text{Ra}/^{230}\text{Th}) \sim 1.96$. Axial basalts appear fresh in dive photos (Figure 2D) and have higher $(^{226}\text{Ra}/^{230}\text{Th})$ of 2.10-2.43, which approaches the zero-age $(^{226}\text{Ra}/^{230}\text{Th})$ values of samples with similar $(^{230}\text{Th}/^{238}\text{U})$ collected from the 1991-1992 and 2005-2006 eruptions at $9^\circ 50' \text{N}$ EPR (2.66-2.89, and 2.41-2.56, respectively; Sims et al., 2002;

Waters et al., in prep). However, ($^{226}\text{Ra}/^{230}\text{Th}$) in east limb basalts appears to be higher at a given Mg# than what would be expected based on the negative correlation observed among zero-age samples from 9°17'N-9°54'N EPR (Figure 9B).

Basaltic andesites from the axis appear as fresh as axial basalts (Figure 2E) but have lower ($^{226}\text{Ra}/^{230}\text{Th}$) ~1.21-1.77. The two axial dacites also appear exceptionally fresh in dive photos yet have very low ($^{226}\text{Ra}/^{230}\text{Th}$) ~1.35-1.36 (Figure 2A; n.b.: sample 265-66 is nominally an andesite but is nearly identical in composition to adjacent axial dacite sample 265-64). Samples with ^{226}Ra excesses ($(^{226}\text{Ra}/^{230}\text{Th}) > 1$) indicate that ^{226}Ra must have been fractionated from ^{230}Th within the past ~8 kyrs (five 1600 yr half-lives of ^{226}Ra), and these extant ^{226}Ra excesses also indicate maximum lava eruption ages of ~8 kyrs. Samples with ^{226}Ra excesses are relatively young compared to the half-life of ^{230}Th (~75 kyrs); thus, the ($^{230}\text{Th}/^{232}\text{Th}$) and ($^{230}\text{Th}/^{238}\text{U}$) for these samples can be considered unchanged by decay since the time of eruption.

4.6. DISCUSSION

4.6.1. Eruption Ages

All samples have ($^{230}\text{Th}/^{238}\text{U}$) > 1, indicating that these samples erupted less than ~375 ka, or five-half lives of ^{230}Th . With the exception of dacite samples 265-83 and 265-85, all samples also have ($^{226}\text{Ra}/^{230}\text{Th}$) > 1, limiting possible eruption ages to <8 kyrs. In addition, ($^{226}\text{Ra}/^{230}\text{Th}$) values measured in axial basalts are similar to zero-age lavas from near 9°50'N, suggesting they are quite young, and this is supported by their young

appearance in dive photos (Figure 2D). Although this is not unexpected for samples collected within the axial graben—crustal ages determined from spreading rates suggest possible lava ages of up to ~13 kyrs within the axial graben (assuming a half-spreading rate of 2.75 cm/yr, or 5.5 cm/yr for the ridge segment from 9°-10°N EPR divided between the east and west limbs)—this is a surprising result for both the off-axis flank and pillow ridge lavas, which were emplaced on crust with nominal spreading ‘ages’ of ~75-150 ka. In contrast, ($^{226}\text{Ra}/^{230}\text{Th}$) values measured in basaltic andesites, andesites, and dacites collected within the axial graben are much lower and suggest ($^{226}\text{Ra}/^{230}\text{Th}$) may be significantly diminished by crustal residence times and mixing.

In addition to determining eruption age limits by the presence or absence of ^{238}U - ^{230}Th - ^{226}Ra disequilibria, when certain criteria are met (outlined in section 4.3), U-series disequilibria can be used to calculate explicit model eruption ages. Samples potentially altered by post-eruptive alteration processes have already been eliminated from consideration (see section 4.5.4.1). In addition, the $^{87}\text{Sr}/^{88}\text{Sr}$ and $^{143}\text{Nd}/^{144}\text{Nd}$ isotopic compositions of the east limb OSC lavas indicate that their parent magmas were generated in a mantle source that is indistinguishable from the source of N-MORB magmas at 9°17'N-9°54'N EPR. This implies that melt compositions, and thus initial ($^{230}\text{Th}/^{238}\text{U}$) and ($^{226}\text{Ra}/^{230}\text{Th}$) disequilibria in east limb magmas are not influenced by mantle source heterogeneity with respect to the parent-daughter ratios of these U-series nuclides. Lastly, although the zero-age trend line defined by axial lavas from 9°17'N-9°54'N EPR inherently accounts for variation in the degrees and depths of melting since it covers a wide range of initial ($^{226}\text{Ra}/^{230}\text{Th}$) and ($^{230}\text{Th}/^{238}\text{U}$), the nearly constant

($^{230}\text{Th}/^{238}\text{U}$) of east limb OSC basalts overlaps with that of 9°17'-9°54'N EPR basalts and implies similar degrees and depths of melting for their parental magmas.

Although three of the four criteria for determining model ages are met, it is unclear if crustal residence times of east limb OSC basalts are similar to those of basalts from 9°17'N-9°54'N EPR. Despite this uncertainty, we assume that residence times are similar and follow the model age dating method of Sims et al. (2003) and Waters et al. (in prep.) to calculate trend line model ages for basalts (Table 6). We caution that these model ages may include a component of the crustal residence time. The implications of extended crustal residence times are discussed below in section 4.6.1. We do not report model ages for basaltic andesites, andesites, and dacites, since these lavas most likely have significantly longer residence times, and thus their model ages will not be equivalent to eruption ages.

^{230}Th - ^{226}Ra trend line model ages indicate that as a group, axial basalt samples are the youngest samples, ranging from ~500-1600 yrs old (Table 6). Flank basalt samples are slightly older at ~1300 yrs old. Pillow-ridge basalts are even older, ~2100 yrs old. Sample 265-06, collected from the flat-topped volcano adjacent to the pillow-ridge, is slightly older than the oldest pillow ridge basalts, ~2400 yrs old. The model age relationships among these samples are grossly consistent with photo and hand sample observations (Figure 2). However, the amount of sedimentation covering several of the pillow ridge samples, including samples 265-06, 265-18, and 265-20 (Figures 2C and 2F), is quite substantial and greater than what might be expected from an eruption age of ~2 kyrs. Qualitative sedimentation metrics (e.g., Macdonald et al., 1988; Haymon et al., 1991) suggest ages of 5-20 kyrs when sediment has accumulated enough to connect

between pillows, as is the case for these samples. However, sedimentation rates along the EPR vary widely, ranging from 0.3-2.6 cm/yr (Dekov and Kupstov, 1992; Lonsdale and Spiess, 1980; Marchig et al., 1986; McMurtry et al., 1981) as do age estimates based on sediment cover (Ballard et al, 1981; Haymon et al., 1991; Macdonald et al., 1988), and such estimates may be different than actual eruption ages by more than an order of magnitude (Haymon et al., 1991; Sturm et al., 2000).

4.6.2. The Effect of Residence Times on Model Ages

In calculating the model ages described above, we assumed residence times equal to those of axial basalt from the 9°17'N-9°54'N region. However, given the evolved nature of ferrobasalts at the east limb of the 9°03'N OSC, it is possible that their residence times are longer than the residence times of the N-MORB that comprise the zero-age trend line, and that the corresponding time needed for crystallization to occur may be reflected in the ($^{226}\text{Ra}/^{230}\text{Th}$). However, assuming the initial ($^{226}\text{Ra}/^{230}\text{Th}$) of magma injected into the crust beneath the east limb of the 9°03'N OSC is equivalent to that at 9°17'-9°54'N, then longer residence times would result in lower initial ($^{226}\text{Ra}/^{230}\text{Th}$) upon eruption than the zero-age N-MORB trend line ($^{226}\text{Ra}/^{230}\text{Th}$) assumes, and the calculated model ages in Table 6 would be erroneously older than the true eruption age.

If the true eruption ages are older than our model ages, as we speculate based on sediment cover, the initial ($^{226}\text{Ra}/^{230}\text{Th}$) of off-axis 9°03'N OSC lavas must have been higher than the initial ($^{226}\text{Ra}/^{230}\text{Th}$) of 9°17'N-9°54'N lavas upon eruption. This is possible by either shorter residence times or greater primary ($^{226}\text{Ra}/^{230}\text{Th}$) disequilibria upon injection into the crust. Significantly greater primary disequilibria seems unlikely

because major element constraints suggest that both ferrobasalts and the more primitive basaltic lavas from 9°17'N-9°54'N derive from similar parental magmas (see section 4.6.2. below), and because ($^{230}\text{Th}/^{232}\text{Th}$) and ($^{230}\text{Th}/^{238}\text{U}$) are similar between primitive basalts and ferrobasalts. In contrast, shorter residence times may be possible if primitive basaltic magma injected into the relatively cool crust of the OSC quickly crystallizes to ferrobasalt compositions and is then transported by vertical diking to the seafloor (Combier et al., 2008). This is consistent with the offset to lower Mg# at a given ($^{226}\text{Ra}/^{230}\text{Th}$) for axial lavas as compared to zero-age lavas from 9°17'N-9°54'N (Figure 9B), though from the current data set, there is no way of knowing whether axial and off-axis lavas had similar initial ($^{226}\text{Ra}/^{230}\text{Th}$). Indeed, axial lavas may have longer residence times than off-axis lavas due to lateral transport from the western edge of the melt lens to beneath the ridge axis.

If we assume that the east limb axial basalts with the highest ($^{226}\text{Ra}/^{230}\text{Th}$) (265-76, 266-18) are of zero-age, then the trend line model ages reported in Table 6 are actually estimates of residence time for these lavas, and may suggest that transport from the western edge of the melt lens to the axis and subsequent residence is on the order of ~500-1000 yrs. However, without knowledge of true eruption ages and the initial ($^{226}\text{Ra}/^{230}\text{Th}$) disequilibria upon eruption, basaltic magma residence times are unconstrained. In turn, the complexity of the magmatic system underlying the 9°03'N OSC and the effect of residence times on ($^{226}\text{Ra}/^{230}\text{Th}$) disequilibria in basaltic magmas add additional, and currently irreconcilable, uncertainty to eruption model ages.

4.6.3. Petrologic Relationships Among Primitive Basalts (9°17'N-9°54'N) and Ferrobasalts

In general, trends of major element abundances vs. molar Mg# ($\text{Mg}/(\text{Mg}+\text{Fe}) \times 100$) of basalts can be approximated by fractional crystallization from a primitive basaltic magma (e.g., sample 2752-6 from 9°50'N EPR (Sims et al., 2002), Mg#~64, using the model from Weaver and Langmuir (1990); Figure 3). Most high Mg# MORB initially crystallize olivine, followed by crystallization of olivine and plagioclase, and then crystallization of olivine, plagioclase, and clinopyroxene (Figure 3; e.g., Grove et al., 1992; Presnall et al., 1978; Yang et al., 1996). Interestingly, basalts from 9°03'N EPR appear to extend the liquid line of descent (LLD) of N-MORB from 9°17'N-9°54'N EPR, implying very similar parent magmas. This observation is consistent with experimental results indicating that extensive crystallization of plagioclase and olivine followed by plagioclase, olivine, clinopyroxene, and ilmenite from a primitive MORB can produce FeTi basalt (Dixon and Rutherford, 1979; Juster et al., 1989; Walker et al., 1979), and with least-squares calculations of major element compositions of 85°W Galapagos Spreading Center lavas (Perfit and Fornari, 1983). LLDs calculated assuming a single parent magma for N-MORB from 9°17'N-9°54'N EPR reproduce general major element trends for 9°17'N-9°54'N EPR lavas quite well with crystallization of olivine and plagioclase, and continued crystallization of olivine and plagioclase as well as clinopyroxene is consistent with the major element compositions of east limb 9°03'N OSC ferrobasalts (Weaver and Langmuir, 1990).

The onset of clinopyroxene crystallization in east limb ferrobasalts is consistent with crystallization at lower temperatures. For example, using the model of Weaver and

Langmuir (1990) the onset of olivine crystallization in sample 2752-6 at a constant 0.5 kbar (roughly equivalent to the ~1.5 km depth axial magma chamber beneath 9°50'N EPR) occurs at 1216°C, plagioclase crystallization occurs at 1201°C, and clinopyroxene (augite) crystallization occurs at 1144°C. The model of Weaver and Langmuir (1990) does not account for fractional crystallization of either low-Ca pyroxene such as pigeonite or Fe-Ti rich oxides like titanomagnetite or ilmenite, and hence much of the LLD at low Mg# is inaccurate, particularly with respect to FeO and TiO₂ enrichment (Figures 3B, 3D).

4.6.4. Previous Models for the Genesis of MOR High-Silica Lavas

There are two main models that have been proposed to explain the formation of high silica lavas in fast-spreading mid-ocean ridge settings. The first model posits an origin through extensive fractional crystallization during crustal residence and late stage differentiation of Fe-Ti oxides (e.g., Juster et al., 1989; Shi, 1993; Thy and Lofgren, 1994; Toplis and Carroll, 1995). The second model suggests that high silica lavas are formed by partial melting of hydrated altered wall rock, in particular, anatexis in the roof zone of the AMC (e.g., Casey et al., 1981; Gillis and Coogan, 2002; Gregory and Taylor, 1979; Michael and Schilling, 1989; Wanless et al., in review).

4.6.5. Apparent Discrepancies with Assimilation of Partial Melts of Hydrothermally Altered Wall Rock

Assimilation of partial melts of hydrothermally altered AMC roof material is a plausible explanation for many of the geochemical features observed in east limb 9°03'N

OSC dacites. However, the dacitic end member appears to be quite well defined, whereas hydrothermal alteration should variably alter wall rock, and different degrees of partial melting of such compositionally and mineralogically diverse rock should result in a broader range of high silica end member compositions. In addition, there are several other features of our data set that are in apparent contradiction to a model requiring assimilation of partial melts of altered ocean crust to generate MOR dacites.

In particular, recent (<~1 Ma) assimilation of hydrothermally altered gabbroic or dike material should increase both ($^{234}\text{U}/^{238}\text{U}$) and $^{87}\text{Sr}/^{86}\text{Sr}$ in more evolved lavas over that of basalts (Figure 10). $^{87}\text{Sr}/^{86}\text{Sr}$ and ($^{234}\text{U}/^{238}\text{U}$) in seawater are ~0.709 and 1.14, respectively, and concentrations are high enough (~7.45 ppm and ~3.1 ppb) in EPR seawater (Ku et al., 1976; Ravizza et al., 2001) to substantially affect rock compositions for low degrees of water-rock interaction (Figure 10). Altered oceanic crust is typically a sink for fluid mobile elements such as Rb, Cs, K, U, and Pb, and almost always shows increased $^{87}\text{Sr}/^{86}\text{Sr}$ (Bach et al. 2003; Hauff et al., 2003). It has been argued that the precipitation of Sr-rich minerals in cooler recharge zones depletes seawater type hydrothermal fluids of Sr (Berndt et al., 1988; Michael and Schilling, 1989), but studies of hydrothermal fluids sampled from vents at 9°46'N-9°54'N EPR have $^{87}\text{Sr}/^{86}\text{Sr}$ ~0.70381-0.70790, suggesting that even vent fluids in the upflow zone may retain a significant seawater component (Ravizza et al., 2001), and that hydrothermal fluids with seawater influenced $^{87}\text{Sr}/^{86}\text{Sr}$ isotopic composition should have a significant impact on the $^{87}\text{Sr}/^{86}\text{Sr}$ composition of altered wallrock.

Indeed, we find hydrothermal fluid-rock interaction of a fresh rock sample with average $^{87}\text{Sr}/^{86}\text{Sr}$ = 0.70249 and [Sr]=120 ppm with a hydrothermal fluid with

conservative $^{87}\text{Sr}/^{86}\text{Sr}$ of 0.70381 and $[\text{Sr}] \sim 13.1$ ppm (Ravizza et al., 2001) requires a fluid:rock ratio of only 1 to change the $^{87}\text{Sr}/^{86}\text{Sr}$ to >0.7026 . Given the minimum $^{87}\text{Sr}/^{86}\text{Sr}$ and typical $[\text{Sr}]$ used for hydrothermal fluid, this represents a conservative estimate. Using the same fluid ($[\text{U}]=0.3$ ppb) and assuming seawater ($^{234}\text{U}/^{238}\text{U}$)=1.14, a fluid:rock ratio of 25 is required to change the rock to $(^{234}\text{U}/^{238}\text{U})\sim 1.01$. Using seawater as an end member fluid gives much lower fluid:rock ratios of 0.5 and 2 for $^{87}\text{Sr}/^{86}\text{Sr}$ and $(^{234}\text{U}/^{238}\text{U})$, respectively. Thus, $^{87}\text{Sr}/^{86}\text{Sr}$ appears to be a more sensitive indicator of seawater contamination than $(^{234}\text{U}/^{238}\text{U})$. However, all lavas, including basalts, basaltic andesites, andesites, and dacites, have $(^{234}\text{U}/^{238}\text{U})\sim 1$ and $^{87}\text{Sr}/^{86}\text{Sr}$ within ~ 50 ppm of typical axial MORB (~ 0.70248) from $9^{\circ}17'\text{N}$ - $9^{\circ}54'\text{N}$ EPR and show no clear evidence of a hydrothermally altered wall rock melt component, particularly one altered enough to have amphibole as a stable mineral. We also see no signs of increasing $^{87}\text{Sr}/^{86}\text{Sr}$ or $(^{234}\text{U}/^{238}\text{U})$ with increasing wt% SiO_2 or decreasing Mg#, which would be expected if end member dacitic melts derived from melting of altered wall rock and intermediate magmas originated from mixing of unaltered basalt and dacite magmas.

A second observation that leads us to believe that assimilation of altered wall rock is not a plausible mechanism is that magmatic and hydrothermal fluids are typically enriched in U over relatively immobile Th, and alteration of basaltic rock generally results in U enrichment (Bach et al., 2003; Hauff et al., 2003; Jochum and Verma, 1996; Macdougall et al., 1979; Nakamura et al., 2007; Ridley et al., 1994; Valsami-Jones and Ragnarsdottir, 1997; Verma, 1992). Given our current understanding of equilibrium partitioning of U-series nuclides between a variety of minerals (including amphibole, clinopyroxene, olivine, orthopyroxene, plagioclase, ilmenite, magnetite, and apatite) and

silicate melt (e.g., Berlo et al., 2004; Blundy and Wood, 2003; Fabbri et al., 2009; Klemme et al., 2006; Miller et al., 2007; Prowatke and Klemme, 2006), we expect that subsequent partial melting and assimilation of wall rock should produce ^{238}U excesses over ^{232}Th (Figure 11, Table 7), and additional U in the source composition would only serve to accentuate this effect and produce higher ($^{238}\text{U}/^{232}\text{Th}$) and lower ($^{230}\text{Th}/^{238}\text{U}$). However, dacites have systematically lower ($^{238}\text{U}/^{232}\text{Th}$) and higher ($^{230}\text{Th}/^{238}\text{U}$) than basalts (Figure 7).

Finally, we also observe equilibrium ($^{226}\text{Ra}/^{230}\text{Th}$) in visibly young dacitic lavas. If partial melting of wall rock were a continuous process that produced dacitic magmas in an isolated magma chamber, one would expect that some volume of recently formed dacitic magma would be erupted on the seafloor. However, partial melting of altered wall rock (likely consisting of some proportion of plagioclase, which would fractionate Ra from Th) would almost certainly decrease ($^{226}\text{Ra}/^{230}\text{Th}$) disequilibria (Figure 11, Table 7), yet we see very small to absent ^{226}Ra excesses in young appearing dacite lavas, indicating that the process that formed dacites originally produced ($^{226}\text{Ra}/^{230}\text{Th}$)>1 and that event is long past (i.e., >8 kyrs).

4.6.6. Crystallization Origin for the Petrogenesis of Dacites

The observations of near equilibrium ($^{234}\text{U}/^{238}\text{U}$) and depleted EPR mantle-like $^{87}\text{Sr}/^{86}\text{Sr}$ compositions in high silica lavas suggests assimilation of partial melts of hydrothermally altered oceanic crust is not a fundamental process contributing to the formation of dacitic magmas. We propose that extensive fractional crystallization is a

simpler explanation for the formation of dacites, and one that we find more consistent with major element, trace element, $^{87}\text{Sr}/^{86}\text{Sr}$, ($^{234}\text{U}/^{238}\text{U}$), and ^{238}U - ^{230}Th - ^{226}Ra systematics.

Arguments against a crystallization origin for dacites have been made based on model LLDs calculated using the MELTS program (Ghiorso and Sack, 1995; Wanless et al., in review). In particular, dacites have too high wt% Al_2O_3 and K_2O , and too low wt% CaO , FeO , and P_2O_5 at a given Mg# (Figure 3; Ghiorso and Sack, 1995; Wanless et al., in review). However, unlike the LLDs calculated from MELTS, the experimental data of Juster et al. (1989) appear to reproduce the end member dacites quite well (Figure 3). Juster et al. (1989) conducted 1 atm isobaric experiments over a range of temperatures and oxygen fugacities on a synthetic analogue of a Galapagos Spreading Center FeTi basalt (POO.82N2) from the 85°W region (Byerly et al., 1976). In particular, the most silica rich experimental compositions have wt% CaO , K_2O , Al_2O_3 , and FeO that closely resemble the most silica rich east limb magmas (Figures 3B-E). The low wt% P_2O_5 compared to MELTS can be explained by apatite saturation (see Figure 12 of Juster et al., 1989).

Thus, extensive fractional crystallization (~85%) appears to provide a plausible mechanism for the origin of end member major element dacite compositions. Intermediate basaltic andesite and andesite compositions most likely result from these dacite magmas mixing with ferrobaltic magmas. This mixing relationship is apparent in plots of major elements, trace elements, and U-series isotopes (Figures 3, 5, 7, 8, 9). Mixing trends among geochemical parameters like wt% MgO vs. ($^{238}\text{U}/^{232}\text{Th}$) indicate that a dacitic magma component was formed independently from magmas of intermediate compositions, which are likely mixes of basalt and dacite magmas. The mixing trend

observed on a plot of ($^{230}\text{Th}/^{238}\text{U}$) vs. ($^{226}\text{Ra}/^{230}\text{Th}$) indicates that intermediate magma compositions were formed by mixing of the dacitic magmas with young basaltic magma with large ^{226}Ra excesses (Figure 8).

A simple modal fractional crystallization calculation (85% crystallization), using the “non-amphibole bearing gabbro” mineral modes with “andesite” partition coefficients from Wanless et al. (in review) and an average $9^{\circ}17'-9^{\circ}54'\text{N}$ EPR N-MORB (Sims et al., 2002) for an initial composition, appears to reproduce the trace element abundance pattern reasonably well (Figure 12). In particular, plagioclase fractionation alone does an excellent job reproducing the negative Sr and Eu anomalies. The biggest differences are that modeled Th and U abundances are lower, and the Nb abundance is higher, than dacite compositions. We suspect the discrepancy with U, Th, and Nb concentrations in the fractional crystallization model reflects uncertainties in partitioning behavior between low-Ca pyroxene, Fe-Ti oxides and relatively dry silica-rich melt. In addition, fractionation of accessory phases like apatite may control U-Th partitioning. However, recent partitioning experiments show a wide range of $D_{\text{Th}}/D_{\text{U}}$ between apatite and silicate melt, with both $D_{\text{Th}}/D_{\text{U}}$ greater than and less than one (Prowatke and Klemme, 2006).

A second line of evidence used to argue against a differentiation origin for high silica MOR lavas is the over-enrichment of Cl gas (Michael and Schilling, 1989). Chlorine concentrations are too high to be derived from differentiation alone, even assuming complete incompatibility, and thus the over-enrichment of Cl has been argued to come from assimilation of hydrothermally altered crust with a significant seawater component (Michael and Schilling, 1989). Although this argument is perhaps more difficult to explain, we support the notion that Cl over-enrichment may result from

accumulation of Cl in overlying high silica lavas by exsolution of a Cl rich vapor phase during crystallization of dense, underplating ferrobasalt and FeTi basalt. Michael and Schilling (1989) could not rule out such a mechanism on the basis of geochemical evidence, but they decided against this mechanism largely because of the difficulties in conceiving of a physically plausible model in which exsolved Cl-rich fluids could be transferred to a highly differentiated magma.

However, the magma supply at the 9°03'N OSC appears to be quite robust and if the roof of the melt lens is a permeability boundary (Kent et al., 2000), the source of the Cl could be the extensive crystal mush zone where magma is evolving to ferrobasalt and FeTi basalt compositions, and transport of this Cl rich vapor phase may parallel transport of magma from the off-axis melt source towards the shallow melt lens beneath the ridge axis, where the high silica lavas are forming. We note that the excess degassing and accumulation of volatile contents in subaerially erupted silicic lavas has commonly been attributed to degassing of deeper, underlying magma bodies (e.g., Kayzar et al., 2009; Kazahaya et al., 1994; Stevenson and Blake, 1998; Wallace, 2001).

Finally, a last observation used to against crystallization as the origin for high silica MOR lavas is that there appears to be a gap in the crystallization sequence from FeTi basalt to dacite. However, this is consistent with arguments made by Grove and Donnelly-Nolan (1986) that experimentally determined plagioclase+augite+low Ca pyroxene+magnetite cotectics have nearly flat liquidus slopes such that there is a large change in composition for a small change in temperature. For example, the crystallization on FeTi basalt of Juster et al. (1989) show a change from 51.9 wt% SiO₂ to 67.3 wt% SiO₂ over a 35°C decrease in temperature (1075°C to 1040°C). A result of the rapid

change in composition is that there is a lesser probability of sampling magmas of intermediate composition. In addition, based on the concept that magma chambers are density filters (Sinton and Detrick, 1992; Stolper and Walker, 1980), we suggest that with differentiation beyond FeTi basalt liquid compositions, magmas may also become too dense to erupt, as they are significantly enriched in Fe and Ti. If magmas evolve beyond this stage, then they are likely to continue crystallizing until their density is again low enough to be erupted. Thus, the only erupted intermediate lavas are those that are low Ti, low Fe, mixed magmas, and not those that follow the LLD.

4.6.7. ^{238}U - ^{230}Th - ^{226}Ra Systematics among Basaltic Andesites and Dacites

The relatively constant ($^{230}\text{Th}/^{232}\text{Th}$) for all samples indicates that evolution from basalt to dacite occurs on a time scale that is much shorter than the half-life of ^{230}Th (~75 kyrs). Given that dacites appear young in field observations and dive photos, and given their location within or directly adjacent to the axial graben, we suggest that they are indeed very young, and that the measured ($^{226}\text{Ra}/^{230}\text{Th}$) in dacites is very close to the initial ($^{226}\text{Ra}/^{230}\text{Th}$) present upon eruption. Thus, because the most evolved dacites (265-83 and 265-85) have equilibrium ($^{226}\text{Ra}/^{230}\text{Th}$), and because they appear to be end member compositions, it is likely that they have not experienced significant melt recharge. This is also consistent with the idea that dacites are formed in isolated melt pockets or even cupolas near the roof of a magma chamber (Wallace, 2001). A similar eruption age for these samples is supported by the similar locations and visual appearance of these samples and by the apparent relationships between sedimentation and ^{230}Th - ^{226}Ra model ages of basalts (see section 4.6.1 above).

Samples 265-83 and 265-85 appear to represent a fairly accurate end member composition for mixing with a young axial ferrobasalt magma to produce basaltic andesites (Figure 8, 9), and its residence time was probably on the order of ~ 8 kyrs, just enough time to bring its ($^{226}\text{Ra}/^{230}\text{Th}$) to equilibrium, but not long enough to significantly change ($^{230}\text{Th}/^{238}\text{U}$). If we assume, based on their young appearance in dive photos, that both the youngest axial ferrobasalts and these dacites have ($^{226}\text{Ra}/^{230}\text{Th}$) that is unchanged from the time of eruption, we can also infer that zero-age intermediate lavas generated by mixing of these lavas (as suggested by major and trace element systematics) should also lie along a mixing line between zero-age axial ferrobasalts and dacites. We suggest that we can use this zero-age ($^{230}\text{Th}/^{238}\text{U}$)-($^{226}\text{Ra}/^{230}\text{Th}$) mixing trend line to calculate model ages for intermediate lavas that do not lie near this trend line (i.e., outside of analytical uncertainties).

A zero-age trend line for mixed lavas (Figure 8) was calculated using a double-error, non-linear least squares fit to a line (Sohn and Menke, 2002), giving the equation ($^{226}\text{Ra}/^{230}\text{Th}$)= $-21.01425 \times (^{230}\text{Th}/^{238}\text{U}) + 25.74449$, with a high $r=0.935$ and low MSWD=2.654. Basaltic andesite samples 264-13, 264-17, 264-20, 265-64, 265-66, young axial basalts 265-74, 265-76, 266-18, and end member dacite 265-85 were all included in the calculation. Note that the flank basalts that lie along this mixing trend, which are clearly older in dive photos (Figure 2), have higher initial ($^{226}\text{Ra}/^{230}\text{Th}$) at a given ($^{230}\text{Th}/^{238}\text{U}$), and are not part of this mixing trend. We use the zero-age trend line of Sims et al. (2002) and Waters et al. (in prep.) for calculating basalt model ages (see section 6.1.).

Of the three evolved lava samples analyzed in this study that do not already lie along this trend line, only sample 265-49 is interpreted to potentially result from direct mixing of a dacite and ferrobasalt. However, the calculated model age of ~3600 yrs for this sample is extremely unrealistic considering its location and its young appearance in dive photos (Figure 2). Two other basaltic andesites (265-106, 265-108) have lower ($^{230}\text{Th}/^{238}\text{U}$), similar to basalts, and they appear to be either products of fractional crystallization or mixes of different end member compositions (see Figures 3, 5). Thus, residence times may have had a different effect on the ($^{226}\text{Ra}/^{230}\text{Th}$) values of these lavas, and we cannot use the ferrobasalt-dacite trend line to calculate model ages. If we do assume that these lavas were derived from a zero-age basalt parent from $9^{\circ}17'\text{N}$ - $9^{\circ}54'\text{N}$ EPR (with trend line initial ($^{226}\text{Ra}/^{230}\text{Th}$)) via fractional crystallization and no mixing, then the model ages for samples 265-106 and 265-108 are 2800 and 4200 yrs, respectively (Table 6), with the caveat that we cannot decouple residence time from eruption age and that these model ages are therefore the sum of the residence time and eruption age.

4.6.8. Implications for Volcanic Accretion at the $9^{\circ}03'\text{N}$ OSC

The spatial distribution of lava ages indicates that the most recent volcanism is indeed occurring within the axial summit graben, but that substantial amounts of off-axis volcanic accretion are occurring. If we take our model ages at face value, the off-axis pillow ridge overlying the western edge of the seismically imaged melt lens appears to be composed of lavas ~2 ka. The contiguous flat-topped volcano to the south is slightly older (~2400 yrs). On this basis, we speculate that off-axis volcanism began at this

seamount ~2400 yrs ago, tapping the melt supply directly beneath it. As the melt supply developed, extensional stresses focused at this asperity, and volcanism began propagating northward and formed the off-axis pillow ridge within a few hundred years.

The relatively young age (~1300 yrs) of lava collected from mid-way across the ridge flank between the axial graben and off-axis pillow ridge suggest more recent volcanic activity in this area. Off-axis eruption of these flank lavas is consistent with their transitional geochemical compositions and spatial locations with respect to the underlying melt network. Lavas from the pillow ridge to the west are generally more primitive, whereas lavas from the axial graben to the east are more evolved. Sampling a continuum of geochemical compositions from pillow ridge to axial graben is consistent with a scenario where melts supplied from beneath the western edge of the melt lens are transported laterally towards the ridge axis over time (e.g., Kent et al., 2000).

There is also seismic evidence that the melt lens is currently shallower (~1.8 km depth) underneath the western ridge flank (Kent et al., 2000; see Figure 5b of Combier et al., 2008) than beneath the pillow ridge. Ridge segment scale observations have linked AMC depth with magma supply (e.g., Macdonald et al., 1988), and there may be a direct connection between volcanic activity and melt lens depth even at a local scale. Along these same lines, we note that the shallowest portion of the melt lens is located beneath the ridge axis, which is clearly the most active part of the OSC. There are also locations beneath the axial graben where the melt lens is notably shallower than surrounding regions, such as at 9°06'N, and the overlying lavas also appear younger than lavas directly to the north (Nunnery et al., 2009).

Axial basalts are extremely fresh appearing and have model ages 500-1600 yrs, although they may be younger than this, particularly given their evolved nature and possibly longer residence times. There is no systematic difference in the ages of axial basalts collected from $\sim 9^{\circ}08'N$ versus those collected from $9^{\circ}03'N$, suggesting neovolcanism occurs along much of the axis. However, our sample coverage is not great enough to discern any differences in eruptive frequency between the northern part of the axial graben overlying the wide melt lens or the southern propagating tip that deviates from the trace of the melt lens.

The young appearances and ages of a wide range of lava compositions (basalt to dacite) erupted within the axial graben suggest a highly heterogeneous melt lens and mush zone that is effective at keeping melts of distinct composition from mixing. Off-axis volcanism is primarily limited to basaltic volcanism, suggesting that whatever processes contribute to the formation of high-silica lavas occur primarily under the ridge axis. Whereas the pillow ridge basalts represent the most primitive melts found at the east limb of the $9^{\circ}03'N$ OSC and are the most crystal rich lavas, axial basalts are more evolved but are generally aphyric (Zaino, 2009). Because pillow ridge lavas were likely sourced from the western, deepest extent of the wide melt lens and were transported via vertical dikes directly to the seafloor, these lavas probably spent little time in a developed AMC. Their evolved compositions likely result from rapid crystallization in a cold, mid-crustal, crystal mush zone. In contrast, axial basalts that reside in a melt-rich AMC probably reflect efficient melt-crystal segregation (Sinton and Detrick, 1992). Thus, pillow ridge basalts are crystal rich as compared to the generally aphyric basalts that pass through the shallow AMC and erupt within the ridge axis from 9° - $10^{\circ}N$ EPR.

The two basaltic andesites that do not appear to follow the mixing trend between axial ferrobasalts and dacites were sampled from south of the wide melt lens at $\sim 9^{\circ}06'N$, in contrast to the majority of basaltic andesites sampled north of $\sim 9^{\circ}09'N$. This suggests a direct relationship between the nature of the basaltic magma supply and how intermediate lavas are generated. There were an abundance of FeTi basalts collected off-axis from $9^{\circ}05'N$ - $9^{\circ}06'N$, and these lavas are coincident with observed melt runnels that are sourced from beneath the overlap basin and appear to feed the axis-centered part of the melt lens (Kent et al., 2000; see Figure 7 of White et al., 2009). Thus, whereas basaltic andesites from north of $9^{\circ}06'N$ may be formed by mixing of axial dacite magma with axial basalt magma, basaltic andesites from south of $9^{\circ}06'N$ may be formed by mixing of axial dacite magma with FeTi basalt magma from these melt runnels. Alternatively, samples 265-106 and 265-108 may be crystallization products of these FeTi basalt magmas.

4.7. CONCLUSIONS

Major element, trace element, $^{87}\text{Sr}/^{86}\text{Sr}$ and $^{143}\text{Nd}/^{144}\text{Nd}$ isotope compositions, and U-series disequilibria place strong constraints on the petrogenesis and eruption times of basalt, basaltic andesite, andesite, and dacite lavas from along and across the east limb of the of OSC at $9^{\circ}03'N$ EPR. Basaltic lavas range from slightly evolved ferrobasalts to FeTi basalts and likely differentiate from a parent magma similar to that inferred from the more primitive magmas erupted within the AST at $9^{\circ}17'N$ - $9^{\circ}54'N$ EPR. $^{87}\text{Sr}/^{86}\text{Sr}$ and

$^{143}\text{Nd}/^{144}\text{Nd}$ isotopic compositions are indistinguishable from $9^{\circ}17' - 9^{\circ}54' \text{N}$ EPR lavas and imply partial melting of a similar mantle source composition. Comparison of east limb basalt major element data with experiments by Juster et al. (1989) suggests a crystallization origin for dacitic magmas, and mixing of dacites with ferrobasalt and FeTi basalts to produce basaltic andesites, andesites, and dacites of intermediate composition. Trace element data and U-series disequilibria further support this observation of mixing, and equilibrium ($^{226}\text{Ra}/^{230}\text{Th}$) values in dacites imply crystallization times of ~ 8 kyrs. Models for an origin of dacitic magma by partial melting of hydrothermally altered magma chamber wall rock are inconsistent with $^{87}\text{Sr}/^{86}\text{Sr}$ and ($^{234}\text{U}/^{238}\text{U}$) isotope compositions and ^{238}U - ^{230}Th - ^{226}Ra systematics in east limb dacite magmas.

^{230}Th - ^{226}Ra disequilibria indicate that young volcanic activity (< 8 kyrs) appears to be distributed widely throughout the region. Because of the complex magmatic system at the $9^{\circ}03' \text{N}$ OSC and the highly evolved nature of east limb OSC lavas, U-series model eruption ages for basalt are likely affected by uncertainties in crustal residence times. However, when taken at face value, ^{230}Th - ^{226}Ra model ages suggest that lavas from the flat-topped seamount and pillow ridge at the western edge of the seismically imaged melt lens (Kent et al., 2000) are surprisingly young (2.1-2.4 kyrs) given their location with respect to the ridge axis. Lava collected from north of the overlap basin near $9^{\circ}09' \text{N}$ and mid-way between the axial graben and pillow ridge also appears relatively young (~ 1.3 kyrs). However, the axial graben appears to be the primary location for the most recent volcanic activity and sources the youngest, and most evolved ferrobasalts, as well as basaltic andesites, andesites, and dacites.

Acknowledgments.

This study was funded by NSF grants OCE-0527053 to K.W.W. Sims and OCE-0623838 to K.W.W. Sims and S.A. Soule. This manuscript benefited from thoughtful discussions with Ken Sims, Maurice Tivey, Glenn Gaetani, Mike Perfit, Dorsey Wanless, and Emily Klein. I am thankful to Huai-Jen Yang for running the Weaver and Langmuir model. Sr isotope analyses conducted by TIMS at Boston University were made possible with patient help from Jeremy Inglis and Ethan Baxter. Jurek Blusztajn is thanked for assistance in the laboratory and on the Neptune at WHOI, particularly with regards to Sr and Nd isotopic analyses. Scott White is thanked for providing bathymetric and side-scan sonar maps. Finally, I am grateful to the scientific staff and the crew of the *Atlantis* on “MEDUSA” cruise AT15-17, whose seagoing efforts have made this work possible.

References

- Bach, W., B.P. Peucker-Ehrenbrink, S.R. Hart, and J.S. Blusztajn (2003) Geochemistry of hydrothermally altered oceanic crust: DSDP/ODP Hole 504B-Implications for seawater-crust exchange budgets and Sr- and Pb-isotopic evolution of the mantle, *Geochem., Geophys., Geosyst.*, 4(3), doi:10.1029/2002GC000419.
- Ball, L., K. Sims, S. Weyer, and J. Schweiters (2008), Measurement of $^{234}\text{U}/^{238}\text{U}$ and $^{230}\text{Th}/^{232}\text{Th}$ in volcanic rocks using the Neptune PIMMS, *J. Anal. At. Spectrom.*, 23, 173-180, doi: 10.1039/b703193a.
- Ballard, R.D., J. Francheteau, T. Juteau, C. Rangin, W. Normark (1981), East Pacific Rise at 21°N: the volcanic, tectonic, and hydrothermal processes of the central axis, *Earth Planet. Sci. Lett.*, 55, 1-10.
- Batiza, R. and S.H. Margolis (1986) A model for the origin of small non-overlapping offsets (SNOOS) of the East Pacific Rise, *Nature*, 320, 439-441.
- Batiza, R. and Y. Niu (1992) Petrology and magma chamber processes at the East Pacific Rise-9°30'N, *J. Geophys. Res.*, 97, 6779-6797.
- Bazin, S., A. Harding, G. Kent, J. Orcutt, C. Tong, J. Pye, S. Singh, P. Barton, M. Sinha, R. White, R. Hobbs, H.V. Avendonk (2001) Three-dimensional shallow crustal emplacement at the 9°03'N overlapping spreading center on the East Pacific Rise: correlations between magnetization and tomographic images, *J. Geophys. Res.* 106, 16,101-16,117.

- Bazin, S., A.J. Harding, G.M. Kent, J.A. Orcutt, S.C. Singh, C.H. Tong, J.W. Pye, P.J. Barton, M.C. Sinha, R.S. White, R.W. Hobbs, and H.J.A. Van Avendonk (2003) A three-dimensional study of a crustal low velocity region beneath the 9°03'N overlapping spreading center, *Geophys. Res. Lett.* 30.
- Beattie P. (1993). Uranium-thorium disequilibria and partitioning on melting of garnet peridotite. *Earth and Planetary Science Letters* 363, 63-65.
- Bergmanis, E.C., J. Sinton, and K.H. Rubin (2007) Recent eruptive history and magma reservoir dynamics on the southern East Pacific Rise at 17°30'S, *Geochem., Geophys., Geosyst.*, 8(12), doi: 10.1029/2007GC001742.
- Berlo, K., S. Turner, J. Blundy, C. Hawkesworth (2004), The extent of U-series disequilibria produced during partial melting of the lower crust with implications for the formation of the Mount St. Helens dacites, *Contrib. Mineral. Petrol.*, 148, 122-130.
- Berndt, M.E., W.E. Seyfried, and J.W. Beck (1988) Hydrothermal alteration processes at mid-ocean ridges: Experimental and theoretical constraints from Ca and Sr exchange reactions and Sr isotopic ratios, *J. Geophys. Res.*, 93, 4573-4583.
- Blundy, J., and B. Wood (2003), Mineral-melt partitioning of uranium, thorium and their daughters, in *Rev. Mineral. Geochem.*, 52, 59-123.
- Bowles, J., J.G. Gee, D.V. Kent, M.R. Perfit, S.A. Soule, and D.J. Fornari (2006), Paleointensity applications to timing and extent of eruptive activity, 9°-10°N East Pacific Rise, *Geochem., Geophys., Geosyst.*, 7(6), doi:10.1029/2005GC001141.
- Byerly, G.R., W.G. Melson, and P.R. Vogt (1976) Rhyodacites, andesites, ferro-basalts, and ocean tholeiites from the Galapagos Spreading Center, *Earth and Planetary Science Letters*, 30, 215-221.
- Carbotte, S.M. and K.C. Macdonald (1992), East Pacific Rise 8°-10°30'N: Evolution of ridge segments and discontinuities from SeaMARC II and three-dimensional magnetic studies, *J. Geophys. Res.*, 97, 6959-6982.
- Casey, J.F., J.F. Dewey, P.J. Fox, J.A. Karson, and E. Rosencrantz (1981) Heterogeneous nature of ocean crust and upper mantle: a perspective from the Bay of Islands ophiolite complex, in *The Sea: The Oceanic Lithosphere*, 7, Chap. 8, 305-338.
- Chabaux, F., R.K. O'Nions, A.S. Cohen, and J.R. Hein (1997) ^{238}U - ^{234}U - ^{230}Th disequilibrium in homogeneous oceanic Fe-Mn crusts: Palaeoceanographic record or diagenetic alteration? *Geochim. Cosmochim. Acta*, 61(17), 3619-3632.
- Cochran, J.R., D.J. Fornari, B.J. Coakley, R. Herr, and M.A. Tivey (1999), Continuous near-bottom gravity measurements made with a BGM-3 gravimeter in DSV Alvin on the East Pacific Rise crest near 9°30'N and 9°50'N, *J. Geophys. Res.*, 104, 10,841-10,861.
- Comber, V., S.C. Singh, M. Cannat, J. Escartin (2008) Mechanical decoupling an thermal structure at the East Pacific Rise axis 9°N: Constraints from axial magma chamber geometry and seafloor structures, *Earth Planet. Sci. Lett.*, 272, 19-28.
- Cooper, K.M., S.J. Goldstein, K.W.W. Sims, and M.T. Murrell (2003), Uranium-series chronology of Gorda Ridge volcanism: new evidence from the 1996 eruption, *Earth Planet. Sci. Lett.*, 206, 459-475.
- Cox, A., R.R. Doell, G.B. Dalrymple (1964) Reversals of the Earth's Magnetic Field, *Science*, 144(3626), 1537-1543.

- Cormier, M.-H., W.B.F. Ryan, A.K. Shah, W. Jin, A.M. Bradley, and D.R. Yoerger (2003), Waxing and waning volcanism along the East Pacific Rise on a millennium time scale, *Geology*, *31*(7), 633-636.
- Crawford W. C. and E.S. Webb (2002). Variations in the distribution of magma in the lower crust and at the Moho beneath the East Pacific Rise at 9°-10°N. *Earth Planet. Sci. Lett.* *203*, 117-130.
- Dekov, V.M., and V.M. Kuptsov (1992) Late Quaternary rates of accumulation of metal-bearing sediments on the East Pacific Rise, *Oceanology*, *32*, 94-101.
- Dixon, S., and M.J. Rutherford (1979) Plagiogranites as late-stage immiscible liquids in ophiolite and mid-ocean ridge suites: An experimental study, *Earth Planet. Sci. Lett.*, *45*, 45-60.
- Duncan, R.A. and L.G. Hogan (1994), Radiometric dating of young MORB using the ⁴⁰Ar-³⁹Ar incremental heating method, *Geophys. Res. Lett.* *21*, 1927-1930.
- Dunn, R., D. Toomey, S. Solomon (2001) Three-dimensional seismic structure and physical properties of the crust and shallow mantle beneath the East Pacific Rise, *J. Geophys. Res.*, *105*, 23,537-23,555.
- Detrick, R.S., P. Buhl, E.E. Vera, J.C. Mutter, J.A. Orcutt, J.A. Madsen, and T.M. Brocher (1987), Multi-channel seismic imaging of a crustal magma chamber along the East Pacific Rise, *Nature (London)* *326*(6108), 35-41.
- Elkins L. J., Gaetani, G.A., & Sims, K.W.W. (2008) Partitioning of U and Th during garnet pyroxenite partial melting: Constraints on the source of alkaline ocean island basalts. *Earth Planet. Sci. Lett.* *265*, 270-286.
- Escartin, J., S.A. Soule, D.J. Fornari, M.A. Tivey, and H. Schouten (2007), Interplay between faults and lava flows in construction of the upper oceanic crust: The East Pacific Rise crest 9°25'-9°58'N, *Geochem., Geophys., Geosyst.*, *8*(6), doi: 10.1029/2006GC001399.
- Fabrizio, A., M.W. Schmidt, D. Gunther, and J. Eikenberg (2009), Experimental determination of Ra mineral/melt partitioning for feldspars and ²²⁶Ra-disequilibrium crystallization ages of plagioclase and alkali-feldspar, *Earth Planet. Sci. Lett.* *280*, 137-148.
- Fornari, D.L., R. Haymon, M. Perfit, T.K.P. Gregg, and M.H. Edwards (1998), Axial summit trough of the East Pacific Rise, 9-10°N: Geological characteristics and evolution of the axial zone on fast spreading mid-ocean ridges, *J. Geophys. Res.*, *103*, 9827-9855.
- Ghiorso, M.S., and R.O. Sack (1995) Chemical Mass Transfer in Magmatic Processes. IV. A Revised and Internally Consistent Thermodynamic Model for the Interpolation and Extrapolation of Liquid-Solid Equilibria in Magmatic Systems at Elevated Temperatures and Pressures. *Contrib. Mineral. Petrol.*, *119*, 197-212.
- Gillis, K.M., and L.A. Coogan (2002) Anatectic migmatites from the roof of an ocean ridge magma chamber, *J. Petrol.*, *43*, 2075-2095.
- Goldstein, S.J., M.T. Murrell, D.R. Janecky, J.R. Delaney, and D. Clague (1992), Geochronology and petrogenesis of MORB from the Juan de Fuca and Gorda Ridges by ²³⁸U-²³⁰Th disequilibrium, *Earth Planet. Sci. Lett.*, *109*, 255-272.
- Goldstein, S.J., M.T. Murrell, and R.W. Williams (1993), ²³¹Pa and ²³⁰Th chronology of Mid-Ocean Ridge Basalts. *Earth Planet. Sci. Lett.*, *115*, 151-160.

- Goldstein, S.J., M.R. Perfit, R. Batiza, D.J. Fornari, and M.T. Murrell (1994), Off-axis volcanism at the East Pacific Rise detected by uranium-series dating of basalts, *Nature*, 367, 157-159.
- Gregory, R.T., and H.P. Taylor (1979) Oxygen isotope and field studies applied to the origin of oceanic plagiogranites (abstr.) *Intl. Ophiolite Symp.*, 117-118, Geol. Surv. Dept. of Cyprus, Nicosia.
- Grove, T.L., and J.M. Donnelly-Nolan (1986) The evolution of young silicic lavas at Medicine Lake Volcano, California: Implications for the origin of compositional gaps in calc-alkaline series lavas, *Contrib. Mineral. Petrol.*, 92, 281-302.
- Grove, T.L., R.J. Kinzler, and W.B. Bryan (1992) Fractionation of mid-ocean ridge basalt (MORB) *Am. Geophys. Union Geophys. Monogr.*, 71, 281-310.
- Haase, K.M., N.A. Stroncik, R. Hékinian, and P. Stoffers (2005) Nb-depleted andesites from the Pacific-Antarctic Rise as analogs for early continental crust, *Geology*, 33(12), 921-924, doi: 10.1130/G21899.1.
- Hauff, F., K. Hoernle, and A. Schmidt (2003) Sr-Nd-Pb composition of Mesozoic Pacific crust (Site 1149 and 801, ODP Leg 185): Implications for alteration of ocean crust and the input into the Izu-Bonin-Mariana subduction system, *Geochem., Geophys., Geosyst.*, 4(8), doi:10.1029/2002GC000421.
- Haymon, R.M., D. Fornari, M.H. Edwards, S. Carbotte, D. Wright, K.C. Macdonald (1991) Hydrothermal vent distribution along the East Pacific Rise crest (9°09' - 54'N) and its relationship to magmatic and tectonic processes on fast-spreading ridges, *Earth Planet. Sci. Lett.* 104, 513-535.
- Henderson, G.M., A.S. Cohen, and R.K. Onions (1993), U-234/U-238 Ratios and Th-230 Ages for Hateruma Atoll Corals - Implications for Coral Diagenesis and Seawater U-234/U-238 Ratios, *Earth Planet. Sci. Lett.*, 115, 65-73.
- Hofmann, A.W. (1988), Chemical differentiation of the Earth: the relationship between mantle, continental crust, and oceanic crust, *Earth. Planet. Sci. Lett.*, 90, 297-314.
- Hooff, E.E.E., H. Schouten, and R.S. Detrick (1996), Constraining crustal emplacement processes from the variation in seismic layer 2A thickness at the East Pacific Rise, *Earth Planet. Sci. Lett.*, 142, 289-309.
- Iwamori, H. (1994) ^{238}U - ^{230}Th - ^{226}Ra and ^{235}U - ^{231}Pa disequilibria produced by mantle melting with porous and channel flows, *Earth Planet. Sci. Lett.* 125, 1016.
- Jochum, K.P., and S.P. Verma (1996), Extreme enrichment of Sb, Tl and other trace elements in altered MORB, *Chem. Geol.* 130, 289-299.
- Jull, M., Kelemen, P.B. & Sims, K. (2002), Consequences of diffuse and channelled porous melt migration on uranium series disequilibria. *Geochim. Cosmochim. Acta* 66(23), 4133-4148.
- Juster, T.C., T.L. Grove, and M.R. Perfit (1989), Experimental constraints in the generation of FeTi basalt, andesites, and rhyodacites at the Galapagos spreading center, 85°W and 95°W, *J. Geophys. Res.*, 94, 9251-9274.
- Kayzar, T.M., K.M. Cooper, M.K. Reagan, and A.J.R. Kent (2009), Gas transport model for the magmatic system at Mount Pinatubo, Philippines: Insights from $(^{210}\text{Pb})/(^{226}\text{Ra})$, *J. Volcanol. Geotherm. Res.*, 181, 124-140.
- Kazahaya, K., H. Shinohara, and G. Saito (1994), Excessive degassing of Izu-Oshima volcano: magma convection in a conduit, *Bull. Volcanol.*, 56, 207-216.

- Kent, G.M., A.J. Harding, and J.A. Orcutt (1993), Distribution of magma beneath the East Pacific Rise near the 9°03'N overlapping spreading center from forward modeling of common depth point data, *J. Geophys. Res.*, 98, 13,971-13,995.
- Kent, G.M., S. Singh, A. Harding, M. Sinha, J. Orcutt, P. Barton, S. Bazin, R. Hobbs, C. Tong, J. Pye (2000) Evidence from three-dimensional seismic reflectivity images for enhanced melt supply beneath mid-ocean ridge discontinuities, *Nature* 406, 614-618.
- Klemme, S., D. Gunther, K. Hametner, S. Prowatke, T. Zack (2006), The partitioning of trace elements between ilmenite, ulvospinel, armalcolite and silicate melts with implications for the early differentiation of the moon, *Chem. Geol.*, 234, 251-263.
- Ku, T.-L., K.G. Knauss, and G.G. Mathieu (1977) Uranium in open ocean: Concentration and isotopic composition, *Deep Sea Res.*, 1005-1017.
- La Tourette, T. Z., Kennedy, A.K. & Wasserburg, G.J. (1993) Thorium-uranium fractionation by garnet: Evidence for a deep source and rapid rise of oceanic basalts. *Science* 261, 739-742.
- Langmuir, C. H., Bender, J.F. & Batiza, R. (1986) Petrological and tectonic segmentation of the East Pacific Rise, 5°30'-14°30'N. *Nature* 322, 422-429.
- Le Bas, M.J., R.W. Le Maitre, A. Streckeisen, and B. Zanettin (1986), A chemical classification of volcanic rocks based on the total alkali-silica diagram, *J. Petrol.*, 27(3), 745-750.
- Lonsdale, P. and F.N. Spiess (1980), Deep-tow observations in the East Pacific Rise, 8°45'N, and some interpretations, in: B.R. Rosendahl, R. Hekinian, et al., Initial Reports of the Deep Sea Drilling Project, 54, pp. 43-62, U.S. Government Printing Office, Washington, D.C.
- Lundstrom, C.C. (2000) Models of U-series disequilibria generation in MORB: the effects of two scales of melt porosity. *Phys. Earth Planet. Int.* 121, 189-204.
- Lundstrom, C.C., J. Gill, Q. Williams, and M.R. Perfit, (1995) Mantle melting and basalt extraction by equilibrium porous flow. *Science*, 270(5244), 1958-1961.
- Lundstrom, C.C., Q. Williams, and J.B. Gill (1998) Investigating solid mantle upwelling rates beneath mid-ocean ridges using U-series disequilibria, 1: a global approach. *Earth Planet. Sci. Lett.*, 157, 151-165.
- Lundstrom, C.C., D.E. Sampson, M.R. Perfit, J. Gill, and Q. Williams (1999) Insights into mid-ocean ridge basalt petrogenesis: U-series disequilibria from the Siqueiros Transform, Lamont Seamounts, and East Pacific Rise. *J. Geophys. Res.* 104(B6), 13,035-13,048.
- Macdonald, K.C. (1998) Linkages between faulting, volcanism, hydrothermal activity, and segmentation on fast-spreading centers, in *Magmatism at mid-ocean ridges*, edited by W.R. Buck, P.T. Delaney, J.A. Karson, and Y. Lagabriele, pp. 27-58. AGU, Washington, D.C.
- Macdonald K. C., Sempere, J.-C. & Fox, P.J. (1984) East Pacific Rise from Siquieros to Orozco fracture zones: Along-strike continuity of axial neovolcanic zone and structure and evolution of overlapping spreading centers. *J. Geophys. Res.*, 89, 6049-6069.
- Macdonald, K.C., R.M. Haymon, S.P. Miller, J.-C. Sempere, P.J. Fox (1988) Deep-tow and Sea Beam studies of dueling propagating ridges on the East Pacific Rise near 20°40'S, *J. Geophys. Res.* 93, 2875-2898.

- Macdougall, J.D., R.C. Finkel, J. Carlson, and S. Krishnaswami (1979), Isotopic evidence for uranium exchange during low-temperature alteration of oceanic basalt, *Earth. Planet. Sci. Lett.*, 42, 27-34.
- Marchig, V., J. Erzinger, and P.M. Heinze (1986) Sediment in the black smoker area of the East Pacific Rise (18.5°S), *Earth. Planet. Sci. Lett.* 79, 93-106.
- McKenzie, D. (1985), ²³⁰Th-²³⁸U disequilibrium and the melting processes beneath ridge axes, *Earth Planet. Sci. Lett.*, 72, 149-157.
- McMurtry, G.M., J.J. Veeh, and C. Moser (1981), Sediment accumulation rate and patterns on the northwest Nazca plate, in: Nazca Plate: Crustal Formation and Andean Convergence, L.D. Kulm, J. Dymond, E.J. Dasch, D.M. Hussong, eds., *Mem. Geol. Sci. Am.* 154, 211-250.
- Michael, P.J. and J.-G. Schilling (1989) Chlorine in mid-ocean ridge magmas: Evidence for assimilation of seawater-influenced components, *Geochim. Cosmochim. Acta*, 53, 3131-3143.
- Miller, S.A., D.S. Burnett, P.D. Asimow, D.L. Phinney, and I.D. Hutcheon (2007), Experimental study of radium partitioning between anorthite and melt at 1 atm, *Am. Mineral.*, 92, 1535-1538.
- Muller, D., M. Sdrolias, C. Gaina, W.R. Roest (2008) Age, spreading rates, and spreading asymmetry of the world's ocean crust, *Geochem., Geophys., Geosyst.*, 9(4), doi:10.1029/2007GC001743.
- Nakamura, K., Y. Kato, K. Tamaki, and T. Ishii (2007), Geochemistry of hydrothermally altered basaltic rocks from the Southwest Indian Ridge near the Rodriguez Triple Junction, *Mar. Geol.*, 239, 125-141.
- Natland, J.H., and W.G. Melson (1980) Compositions of basaltic glasses from the East Pacific Rise and Siqueiros fracture zone, near 9°N, in: *Initial Reports of the Deep Sea Drilling Project*, 54, 705-724.
- Natland, J.H. and J.D. MacDougall (1986a) Parental abyssal tholeiites and alkali basalt at the East Pacific Rise near 9°N and the Siqueiros fracture zone, *Eos. Trans. Am. Geophys. Union*, 67, 410-411.
- Natland, J., C. Langmuir, J. Bender, R. Batiza, and C. Hopson (1986b) Petrologic systematics in the vicinity of the 9°N nontransform offset, East Pacific Rise, *Eos. Trans. Am. Geophys. Union*, 67, 1254.
- Nunnery, J.A. (2009) Relationships between Seafloor Geologic Features and Underlying Melt Bodies at the 9°03'N Overlapping Spreading Center, East Pacific Rise, M.S. Thesis, Duke University.
- Perfit, M., and D.J. Fornari (1983) Geochemical studies of abyssal lavas recovered by DSRV *Alvin* from Eastern Galapagos Rift, Inca Transform, and Ecuador Rift 2. Phase chemistry and crystallization history, *J. Geophys. Res.*, 88(2) B12, 10,530-10,550.
- Perfit, M., D. Fornari, M. Smith, J. Bender, C. Langmuir, and R. Haymon (1994), Small-scale spatial and temporal variations in MORB geochemistry and implications for ridge crest magmatic processes, *Geology*, 22, 375-379.
- Presnall, D.C., S.A. Dixon, T.H. O'Donnell, N.L. Brenner, R.L. Schrock, D.W. Dycus (1978) Liquidus phase relations on the join Diopside-Forsterite-Anorthite from 1 atm to 20 kbar: their bearing on the generation and crystallization of basaltic magma, *Contrib. Mineral. Petrol.*, 66, 203-220.

- Prowatke, S., and S. Klemme (2006), Trace element partitioning between apatite and silicate melts, *Geochim. Cosmochim. Acta*, 70, 4513-4527.
- Ravizza, G., J. Blusztajn, K.L. Von Damm, A.M. Bray, W. Bach, and S.R. Hart (2001) Sr isotope variations in vent fluids from 9°46'-9°54'N East Pacific Rise: Evidence of a non-zero Mg fluid component, *Geochim. Cosmochim. Acta*, 65(5), 729-739.
- Reynolds, J.R. (1995), Segment-scale systematic of mid-ocean ridge magmatism and geochemistry, Ph.D. thesis, 483 pp., Columbia Univ., Palisades, N.Y.
- Richter, S. and S.A. Goldberg (2003), Improved techniques for high accuracy isotope ratio measurements of nuclear materials using thermal ionization mass spectrometry. *Int. J. Mass Spectrom.* 229, 181-197.
- Ridley, W.I., M.R. Perfit, I.R. Jonasson, and M.F. Smith (1994), Hydrothermal alteration in oceanic ridge volcanics: A detailed study at the Galapagos Fossil Hydrothermal Field, *Geochim. Cosmochim. Acta*, 58(11), 2477-2494.
- Robinson, L.F., N.S. Belshaw, and G.M. Henderson (2004), U and Th concentrations and isotope ratios in modern carbonates and waters from the Bahamas. *Geochim. et Cosmochim. Acta*, 68(8), 1777-1789.
- Rubin, K.H., and J.D. MacDougall, Dating of neovolcanic MORB using ($^{226}\text{Ra}/^{230}\text{Th}$) disequilibrium (1990), *Earth Planet. Sci. Lett.*, 101, 313-321.
- Rubin, K.H., J.D. MacDougall, and M.R. Perfit (1994), ^{210}Po - ^{210}Pb dating of recent volcanic eruptions on the sea floor, *Nature*, 368, 841-844.
- Rubin, K.H., I. van der Zander, M.C. Smith, and E.C. Bergmanis (2005), Minimum speed limit for ocean ridge magmatism from ^{210}Pb - ^{226}Ra - ^{230}Th disequilibria, *Nature*, 437, 534-538.
- Salters, V. J. M. & Longhi, J.E. (1999) Trace element partitioning during the initial stages of melting beneath ocean ridges. *Earth Planet. Sci. Lett.*, 166, 15-30.
- Salters, V. J. M., Longhi, J.E. & Bizimis, M. (2002) Near mantle solidus trace element partitioning at pressures up to 3.4 GPa. *Geochemistry, Geophysics, Geosystems* 3(7), (2001GC000148).
- Schouten, H., M.A. Tivey, D.J. Fornari, and J.R. Cochran (1999), Central anomaly magnetization high: constraints on the volcanic construction and architecture of seismic layer 2A at a fast-spreading Mid-Ocean Ridge, the EPR at 9°30'-50'N, *Earth Planet. Sci. Lett.*, 169, 37-50.
- Sempéré, J.-C. and K.C. Macdonald (1986a) Deep-tow studies of the overlapping spreading centers at 9°03'N on the East Pacific Rise, *Tectonics* 5(6), 881-900.
- Sempéré, J.-C. and K.C. Macdonald (1986b) Overlapping spreading centers: implications from crack growth simulation by the displacement discontinuity method. *Tectonics* 5(1), 151-163.
- Sempéré, J.-C., K.C. Macdonald, and S.P. Miller (1984) Overlapping spreading centers: 3-D inversion of the magnetic field at 9°N on the East Pacific Rise, *Geophys. J.R. Astron. Soc.* 79, 799-811.
- Shi, P. (1993) Low-pressure phase relationships in the system Na_2O - CaO - FeO - MgO - Al_2O_3 - SiO_2 at 1100°C, with implications for the differentiation of basaltic magmas, *J. Petrol.* 34, 743-762.
- Sims, K. W. W., D.J. DePaolo, M.T. Murrell, W.S. Baldrige, S.J. Goldstein, and D. Clague (1995) Mechanisms of magma generation beneath Hawaii and mid-ocean

- ridges: Uranium/Thorium and Samarium/Neodymium isotopic evidence. *Science* 267(5197), 508-512.
- Sims, K.W.W., Jull, M. & Kelemen, P. (1999). U-series disequilibria and melt transport in the mantle beneath mid-ocean ridges. Presented at American Geophysical Union Meeting, San Francisco CA. Abstract in E.O.S. (Trans. Amer. Geophys. Union), V22D.
- Sims, K.W.W., S.J. Goldstein, J. Blichert-Toft, M.R. Perfit, P. Kelemen, D.J. Fornari, P. Michael, M.T. Murrell, S.R. Hart, D.J. DePaolo, G. Layne, and M. Jull (2002), Chemical and isotopic constraints on the generation and transport of melt beneath the East Pacific Rise, *Geochim. Cosmochim. Acta*, 66, 3481-3504.
- Sims, K.W.W., J. Blichert-Toft, D.J. Fornari, M.R. Perfit, S.J. Goldstein, P. Johnson, D.J. DePaolo, S.R. Hart, M.T. Murrell, P.J. Michael, G.D. Layne, and L. Ball (2003), Aberrant youth: Chemical and isotopic constraints on the origin of off-axis lavas from the East Pacific Rise, 9°-10°N, *Geochem., Geophys., Geosyst.*, 4(10), Paper number 2002GC000443.
- Sims, K.W.W., S.R. Hart, M.K. Reagan, J. Blusztajn, H. Staudigel, R.A. Sohn, G.D., Layne, L.A. Ball, and J. Andrews (2008a), ^{238}U - ^{230}Th - ^{226}Ra - ^{210}Pb - ^{210}Po , ^{232}Th - ^{226}Ra , and ^{235}U - ^{231}Pa constraints on the ages and petrogenesis of Vailulu'u and Malumalu Lavas, Samoa, *Geochem., Geophys., Geosyst.*, 9(4), Q04003, doi:10.1029/2007GC001651.
- Sims, K.W.W., J.B. Gill, A. Dosseto, D.L. Hoffmann, C.C. Lundstrom, R.W. Williams, L. Ball, D. Tollstrup, S. Turner, J. Prytulak, J.J.G. Glessner, J.J. Standish, and T. Elliott (2008b), An Inter-Laboratory Assessment of the Thorium Isotopic Composition of Synthetic and Rock Reference Materials, *Geostandards and Geoanalytical Research*, 32, 65-91.
- Singh, S., A. Harding, G. Kent, M. Sinha, V. Combier, S. Bazin, C. Tong, J. Pye, P. Barton, R. Hobbs, R. White, J. Orcutt (2006) Seismic reflection images of the moho underlying melt sills at the East Pacific Rise, *Nature* 442, 287-290.
- Smith, M.C., M.R. Perfit, D.J. Fornari, W.I. Ridley, M.H. Edwards, G.J. Jurras, and K.L. Von Damm (2001), Magmatic processes and segmentation at a fast spreading mid-ocean ridge; detailed investigation of an axial discontinuity on the East Pacific Rise crest at 9°37'N, *Geochem., Geophys., Geosyst.*, 2 (Paper 2000GC000134).
- Sohn, R.A. and W. Menke (2002), Application of maximum likelihood and bootstrap methods to nonlinear curve-fit problems in geochemistry, *Geochem., Geophys., Geosyst.*, 3(7), doi:10.1029/2001GC000253.
- Soule, S.A., D.J. Fornari, M.R. Perfit, M.A. Tivey, W.I. Ridley, and H. Schouten (2005), Channelized lava flows at the East Pacific Rise crest 9°-10°N: the importance of off-axis lava transport in developing the architecture of young oceanic crust, *Geochem., Geophys., Geosyst.*, 6(8), doi: 10.1029/2005GC000912.
- Soule, S. A., J. Escartín, and D. J. Fornari (2009), A record of eruption and intrusion at a fast spreading ridge axis: Axial summit trough of the East Pacific Rise at 9–10°N, *Geochem. Geophys. Geosyst.*, 10, Q10T07, doi:10.1029/2008GC002354.
- Spiegelman, M., and T. Elliot (1993), Consequences of melt transport for uranium series disequilibrium in young lavas, *Earth Planet. Sci. Lett.*, 118, 1-20.

- Standish, J.J., and K.W.W. Sims (in press) Dispersed mid-ocean ridge volcanism: Implications from U-series age dating for crustal accretion along the ultraslow spreading Southwest Indian Ridge.
- Stevenson, D.S., and S. Blake (1998) Modelling the dynamics and thermodynamics of volcanic degassing, *Bull. Volcanol.*, 60, 307-317.
- Stolper, E., and D. Walker (1980), Melt density and the average composition of basalt, *Contrib. Mineral. Petrol.*, 74, 7-12.
- Sturm, M.E., S.J. Goldstein, E.M. Klein, J.A. Karson, M.T. Murrell (2000), Uranium-series age constraints on lavas from the axial valley of the Mid-Atlantic Ridge, MARK area, *Earth Planet. Sci. Lett.*, 181, 61-70.
- Thompson, G., B. Bryan, R. Ballard, K. Hamuro, and W.G. Melson (1985) Axial processes along a segment of the East Pacific Rise, 10-12°N, *Nature*, 318, 429-433.
- Thurber, D. (1962) Anomalous $^{234}\text{U}/^{238}\text{U}$ in nature, *J. Geophys. Res.*, 67, 4518.
- Thy, P., and G.E. Lofgren (1994) Experimental constraints on the low-pressure evolution of transitional and mildly alkalic basalts: the effect of Fe-Ti oxide minerals and the origin of basaltic andesites, *Contrib. Mineral. Petrol.* 116, 340-351.
- Toomey, D.R., D. Joussetin, R.A. Dunn, W. Wilcock, R.S. Detrick (2007) Skew of mantle upwelling beneath the East Pacific Rise governs segmentation, *Nature* 446, doi:10.1038/nature05679.
- Tong, C.H., J. Pye, P. Barton, R. White, M. Sinha, S. Singh, R. Hobbs, S. Bazin, A. Harding, G. Kent, J. Orcutt (2002) Asymmetric melt sills and upper crustal construction beneath overlapping spreading ridge segments: Implications for the development of melt sills along ridge crests, *Geology* 30, 83-86.
- Tong, C.H., P. Barton, R.S. White, M.C. Sinha, S.C. Singh, J.W. Pye, R.W. Hobbs (2003) Influence of enhanced melt supply on upper crustal structure at a mid-ocean ridge discontinuity: a three-dimensional seismic tomographic study of 9°N East Pacific Rise, *J. Geophys. Res.* 108, doi:10.1029/2002JB002163.
- Toplis, M.J., and M.R. Carroll (1995) An experimental study of the influence of oxygen fugacity on Fe-Ti oxide stability, phase relations, and mineral-melt equilibria in ferro-basaltic systems, *J. Petrol.*, 36, 1137-1170.
- Valsami-Jones, E., K.V. Ragnarsdottir (1997) Controls on uranium and thorium behaviour in ocean-floor hydrothermal systems: examples from the Pindos ophiolite, Greece, *Chem. Geol.*, 135, 263-274.
- Verma, S.P. (1992) Seawater alteration effects on REE, K Rb, Cs, Sr, U, Th, Pb and Sr-Nd-Pb isotope systematics of Mid-Ocean Ridge Basalt, *Geochem. J.*, 26, 159-177.
- Volpe A. M. & Goldstein, S.J. (1993) ^{226}Ra - ^{230}Th disequilibrium in axial and off-axis mid-ocean ridge basalts. *Geochim. Cosmochim. Acta* 57, 1233-1242.
- Walker, D., T. Shibata, and S.E. DeLong (1979) Abyssal tholeiites from the Oceanographer fracture zone, II, Phase equilibria and mixing, *Contrib. Mineral. Petrol.*, 70, 111-125.
- Wallace, P.J. (2001) Volcanic SO₂ emissions and the abundance and distribution of exsolved gas in magma bodies, *J. Volcanol. Geotherm. Res.*, 108, 85-106.
- Wanless, V.D., M.R. Perfit, W.I. Ridley, E. Klein, and A. Zaino (2007) From basalt to

- dacite: examining magmatic evolution at the 9°03'N overlapping spreading center, East Pacific Rise, *Eos. Trans. Am. Geophys. Union*, 88, Fall Meet Suppl Abstract T33B-1347.
- Weaver, J.S., and C.H. Langmuir (1990) Calculation of phase equilibrium in mineral-melt systems, *Computers Geosci.*, 16, 1-19.
- White, S.M. (2001) The Linkage of Volcanic and Tectonic Segmentation on Fast Spreading Mid-Ocean Ridges: Constraints on the Spatial and Temporal Extent of Volcanic Systems from the Distribution of Volcanic Edifices and Lava Flow Morphology at the East Pacific Rise. Ph.D. Thesis, Univ. California Santa Barbara, pp. 174.
- White, S.M., R.M. Haymon, D.J. Fornari, M.R. Perfit, and K.C. Macdonald (2002) Correlation between volcanic and tectonic segmentation of fast-spreading ridges: Evidence from volcanic structures and lava flow morphology on the East Pacific Rise at 9°-10°N, *J. Geophys. Res.*, 107(B8), 2173, doi: 10.1029/2001JB000571.
- White, S.M., R.M. Haymon, and S. Carbotte (2006) A new view of ridge segmentation and near-axis volcanism at the East Pacific Rise, 8°-12°N, from EM300 multibeam bathymetry, *Geochem., Geophys., Geosyst.*, 7(12), doi:10.1029/2006GC001407.
- White, S.M., J.L. Mason, K.C. Macdonald, M.R. Perfit, V.D. Wanless, E.M. Klein (2009) Significance of widespread low effusion rate eruptions over the past two million years for delivery of magma to the overlapping spreading centers at 9°N East Pacific Rise, *Earth Planet. Sci. Lett.* 280, 175-184.
- Williams, R.W., and J.B. Gill (1989), Effects of partial melting on the uranium decay series, *Geochim. et Cosmochim. Acta*, 53, 1607-1619.
- Yang, H.-J., R.J. Kinzler, T.L. Grove (1996) Experiments and models of anhydrous, basaltic olivine-plagioclase-augite saturated melts from 0.001 to 10 kbar, *Contrib. Mineral. Petrol.*, 124, 1-18.
- Zaino, A.J. (2009) Petrology and mineral chemistry of the 9°03'N overlapping spreading center, East Pacific Rise, M.S. Thesis, Duke University.

Table 1. Sample descriptions and locations of 9°03'N EPR Overlapping Spreading Center East Limb Lavas.

Field # (Time Stamp)	Lab #	Latitude (°N, Dec. Min.)'	Longitude (°W, Dec. Min.)'	Depth (m)	Flow Morph. ^b	Dive Photo Description ^c
Axial Basalts^a						
040907-1859	265-74	9°08.417'	104°12.441'	2597	L	Lustrous, vitreous pillow bud from mound of fresh looking, glassy lobate lava with very slight dusting of sediment
040907-2033	265-76	9°08.305'	104°12.381'	2583	P	Elongate tubular, lustrous glassy pillow bud collected from a fresh appearing, virtually un-sedimented bulbous pillow lava
041207-1150	266-18	9°02.808'	104°12.697'	2620	P	Piece of small toothpaste pillow lava construction in very slightly sedimented field of decorated lobate lavas (no sediment pockets); not as young appearing as 265-74 or 265-76
041507-1124	267-09	9°02.844'	104°12.527'	2601	P	Pillow bud from young appearing, very slightly sedimented large pillows (no sedimented pockets), not as visible vitreous luster as in 265-74, 265-76, but similar to 266-18
Flank Basalts^a						
040807-0624	265-31	9°09.008'	104°13.491'	2409	P	Pillow bud from field of small, sediment dusted pillows; sediment pockets are present
040807-0643	265-32	9°09.007'	104°13.410'	2703	P	Pillow bud from field of small, sediment dusted pillows; sediment pockets are present; appears similar to sampling location of 265-31, may be same flow field
040807-0652	265-33	9°09.013'	104°13.363'	2700	H	Piece of lightly sedimented hackly sheet flow; sediment collected in pockets
Pillow Ridge Basalts^a						
040707-0646	265-06	9°06.890'	104°14.338'	2680	L	Exterior crust of very old appearing, almost completely sedimented lobate flow collected from flat-topped volcano contiguous to volcanic pillow ridge at the western edge of the large melt lens
040707-0909	265-12	9°07.233'	104°13.841'	2757	P	Bud from heavily sedimented pillow lava just off of the volcanic pillow ridge; sediment cover is similar to 265-06

Table 1 (cont'd).

Field # (Time Stamp)	Lab #	Latitude (°N, Dec. Min.)'	Longitude (°W, Dec. Min.)'	Depth (m)	Flow Morph.^b	Dive Photo Description^c
040707-0953	265-13	9°07.415'	104°13.868'	2742	L	Bud from sedimented lobate flow with lots of small pillows and buds; sediment in pockets and light sediment cover; similarly, but perhaps slightly more sedimented than 265-31, 32, 33, but less sedimented than 265-06, 265-12
040707-1443	265-18	9°08.171'	104°14.073'	2701	P	Pillow bud from larger pillow construction in field of moderately sedimented flattened pillows/lobate flows; substantial sediment in pockets and observable Mn crust, less sedimented than 265-06, 265-12, but more sedimented than 265-13
040707-1628	265-19	9°08.406'	104°14.096'	2724	P	Pillow bud from area of small, knobby pillows; sedimentation is similar to that of 265-31, 32, 33
040707-1718	265-20	9°08.521'	104°14.121'	2700	P	Pillow bud from area of moderately sedimented large pillows with observable Mn crust, sedimentation similar to that of 265-18
Axial Basaltic Andesites^a						
040607-0829	264-13	9°09.838'	104°12.646'	2577	P	Sample with ropy glass surface taken from exterior crust of hollow pillow in field of unsedimented pillow and lobate lavas; lava appears dark, lustrous, and young
040607-1009	264-17	9°09.505'	104°12.484'	2567	P	Bud taken from unsedimented and young appearing lustrous, glassy, toothpaste pillow lava
040607-1135	264-20	9°09.364'	104°12.447'	2551	P	Bud taken from exceptionally fresh appearing, lustrous, vitreous elongate pillow tubes
040807-1228	265-49	9°09.304'	104°12.507'	2573	P	Elongate pillow toe from dark, lustrous pillow lava with very slight sediment dusting
041007-1735	265-106	9°05.851'	104°12.082'	2583	P	Fresh glass bud collected from large pillow lava with patchy iridescence; appears older than 264-20 and 265-49

Table 1 (cont'd).

041007-1803	265-108	9°05.854'	104°12.073'	2585	L	Sample collected from toe of tubular, lustrous lobate/pillow lava with extensive, orange FeS staining at base of flow and slight sediment dusting on top; flow appears to overlie an older, more heavily sedimented pillow flow
Axial Andesites/Dacites^s						
040607-0848	264-14	9°09.687'	104°12.582'	2583	R	Jumbled, ropey sheet flow with light sediment cover but no visible sediment pockets; oxidized with 0.1mm manganese crust, 1mm thick layer of dull surface glass, entirely glass sample
040907-0022	265-66	9°08.601'	104°12.418'	2578	P	Flat slab from exterior of very large, brownish tubular pillow with elephant skin texture; appears as a folded sheet in hand sample; very little apparent sediment cover
040807-2317	265-64	9°08.716'	104°12.431'	2586	P	Flat plate from exterior of pillow lava, similar to 265-66
Near-Axial Flank Dacites^a						
040907-2314	265-83	9°07.699'	104°12.503'	2589	P	Pillow crust from very long, large, tubular pillow with striated elephant-skin surface texture; slightly more sedimented than 265-64 and 66
041007-0006	265-85	9°07.695'	104°12.617'	2603	R	Hackly crust collected from sheet flow; similar sediment to 265-83—some sediment accumulation in pockets

^aVolcanic rock classification determined based on total alkali-silica diagram (Le Bas et al., 1986).

^bFlow morphology is indicated by L=lobate, P=pillow, R=ropey sheet; H=hackly sheet.

^cDive photo descriptions are compiled from the AT15-17 Cruise Report (Klein et al., 2007) and from photos from the Jason Virtual Van (<http://4dgeo.who.edu/webdata/virtualvan/html/VV-at15-17/index.html>)

Table 2. Major element abundances of 9°03'N EPR Overlapping Spreading Center East Limb Lavas.

Sample	SiO ₂	TiO ₂	Al ₂ O ₃	FeO*	MnO	MgO	CaO	Na ₂ O	K ₂ O	P ₂ O ₅	Total	K/Ti ^a	Mg# ^b	FeO/ MgO ^c	CaO/ Al ₂ O ₃
265-74	51.01	1.99	13.93	11.92	0.22	6.81	11.05	2.90	0.14	0.20	100.19	7.24	50.45	1.75	0.79
265-76	51.08	1.89	13.98	11.61	0.22	6.98	11.25	2.84	0.14	0.19	100.19	7.18	51.74	1.66	0.80
266-18	50.82	2.01	13.70	12.08	0.22	6.91	10.88	3.14	0.16	0.22	100.14	7.94	50.47	1.75	0.79
267-09	50.76	1.95	13.90	11.99	0.22	6.90	10.82	2.95	0.14	0.24	99.87	7.14	50.63	1.74	0.78
265-31	51.62	2.01	13.89	11.72	0.23	6.85	11.07	3.05	0.15	0.20	100.79	7.70	51.03	1.71	0.80
265-32	51.36	1.96	13.89	11.53	0.22	6.90	11.11	3.00	0.15	0.18	100.29	7.52	51.62	1.67	0.80
265-33	51.23	1.97	13.93	11.48	0.22	6.83	11.16	3.02	0.15	0.18	100.17	7.73	51.45	1.68	0.80
265-06	51.09	1.85	13.89	11.44	0.21	7.00	11.32	3.00	0.13	0.17	100.11	7.01	52.19	1.63	0.81
265-12	51.41	1.92	13.75	11.45	0.22	6.60	10.69	3.11	0.19	0.20	99.54	10.00	50.67	1.74	0.78
265-13	50.83	1.85	14.01	11.22	0.22	7.21	11.28	2.93	0.12	0.18	99.83	6.64	53.38	1.56	0.81
265-18	50.93	1.83	14.09	11.33	0.21	7.18	11.19	3.01	0.13	0.18	100.08	6.98	53.03	1.58	0.79
265-19	50.73	1.84	14.12	11.25	0.21	7.20	11.19	2.96	0.13	0.18	99.81	6.84	53.28	1.56	0.79
265-20	50.56	1.88	13.87	11.30	0.22	7.15	11.28	2.98	0.13	0.18	99.56	6.92	53.01	1.58	0.81
264-13	53.41	1.68	14.44	10.43	0.20	5.76	9.53	3.42	0.33	0.20	99.40	19.57	49.60	1.81	0.66
264-17	52.61	1.77	14.12	10.95	0.20	6.23	10.07	3.27	0.25	0.20	99.66	14.30	50.34	1.76	0.71
264-20	54.59	1.71	13.95	10.68	0.21	5.10	8.84	3.60	0.39	0.21	99.28	22.73	45.96	2.10	0.63
265-49	52.88	1.80	14.07	11.22	0.21	5.86	10.04	3.25	0.27	0.20	99.81	14.94	48.22	1.91	0.71
265-106	53.33	1.94	13.26	12.35	0.24	5.11	8.71	3.67	0.32	0.39	99.31	16.54	42.43	2.42	0.66
265-108	53.77	1.95	13.28	12.60	0.23	5.08	8.80	3.63	0.32	0.38	100.04	16.60	41.81	2.48	0.66
264-14	61.75	1.30	13.46	8.71	0.17	2.47	5.54	3.94	0.83	0.22	98.39	63.91	33.59	3.52	0.41
265-66	62.81	1.43	13.13	9.05	0.18	1.99	4.98	3.86	0.89	0.24	98.55	62.23	28.13	4.55	0.38
265-64	64.04	1.28	13.12	8.27	0.16	1.60	4.45	3.46	0.97	0.20	97.55	75.51	25.69	5.16	0.34
265-83	67.46	0.76	13.27	6.68	0.13	0.67	2.98	3.88	1.37	0.16	97.37	180.2	15.18	9.96	0.22
265-85	65.01	1.06	13.13	7.99	0.16	1.18	3.78	3.67	1.22	0.20	97.41	115.5	20.82	6.78	0.29

The 2 σ errors calculated from variation in the analyses of ALV2392-9 during these analytical runs are as follows: SiO₂ (0.29 wt.% or 0.57 relative %), TiO₂ (0.07 wt.% or 5.4%), Al₂O₃ (0.17 wt.% or 1.1%), FeO (0.17 wt.% or 1.8%), MnO (0.05 wt.% or 26.8%), MgO (0.11 wt.% or 1.3%), CaO (0.14 wt.% or 1.2%), Na₂O (0.09 wt.% or 3.6%), K₂O (0.02 wt.% or 18.8%), and P₂O₅ (0.04 wt.% or 29.8%).

^a K/Ti is defined as K₂O/TiO₂ x 100; ^b Molar Mg# = Mg/(Mg+Fe) x 100; ^c Basalts with FeO/MgO>1.75 are classified as FeTi basalts.

Table 3. Trace element abundances of 9°03'N EPR Overlapping Spreading Center East Limb Lavas.

Sample	265-74	265-76	266-18	267-09	265-31	265-32	265-33	265-18	264-13	264-17
Li	8.4	8.2	8.7	8.2	7.9	7.8	8.2	7.5	15.4	10.9
Sc	40.7	41.8	41.4	42.5	41.8	42.6	42.3	42.9	34.5	38.0
V	339	339	354	354	342	351	341	338	265	297
Cr	71.4	82.1	71.6	87.2	112	114	124	166	86.5	117
Co	40.0	41.1	41.8	41.0	41.1	42.1	42.8	41.8	33.2	37.2
Ni	45.7	49.7	45.0	46.1	53.9	57.7	62.0	52.7	40.4	50.2
Cu	57.2	60.8	62.2	60.3	59.2	64.5	58.3	63.6	46.4	54.9
Zn	90.7	90.9	97.2	95.8	93.6	95.6	93.8	94.7	96.9	94.9
Ga	16.3	16.3	17.0	18.6	18.2	16.7	16.5	18.1	18.6	17.3
Cs	0.02	0.01	0.02	0.02	0.02	0.02	0.02	0.01	0.04	0.03
Rb	1.32	1.20	1.41	1.50	1.25	1.27	1.26	1.00	3.76	2.34
Ba	10.8	10.0	11.3	11.1	8.7	9.3	10.9	6.9	23.4	15.9
Th	0.21	0.20	0.23	0.23	0.20	0.21	0.21	0.16	0.65	0.40
U	0.09	0.08	0.10	0.09	0.08	0.08	0.09	0.07	0.26	0.16
Nb	3.48	3.27	3.89	3.65	3.21	3.32	3.35	2.76	6.41	4.81
Ta	0.23	0.22	0.26	0.25	0.22	0.22	0.22	0.19	0.43	0.32
La	4.47	4.20	5.01	4.79	4.71	4.46	4.56	4.27	9.75	6.95
Ce	13.8	13.1	15.5	15.0	14.6	14.0	14.2	13.4	29.0	21.0
Pb	0.61	0.57	0.63	0.59	0.42	0.64	0.68	0.38	1.36	0.92
Pr	2.35	2.24	2.62	2.56	2.40	2.38	2.43	2.21	4.57	3.39
Nd	12.5	12.0	14.0	13.5	12.7	12.7	12.9	11.9	22.5	17.3
Sr	120	121	121	113	118	118	118	126	112	115
Sm	4.37	4.17	4.88	4.69	4.44	4.47	4.51	4.15	7.36	5.77
Hf	3.47	3.33	3.88	3.58	3.52	3.51	3.62	3.23	7.72	5.32
Zr	128	121	144	140	131	130	131	122	288	201
Eu	1.51	1.48	1.66	1.58	1.48	1.52	1.55	1.40	2.02	1.73
Gd	5.69	5.54	6.33	6.10	5.83	5.81	5.92	5.46	9.05	7.23
Tb	1.08	1.04	1.19	1.14	1.09	1.10	1.11	1.02	1.72	1.38
Dy	7.06	6.86	7.83	7.36	7.24	7.25	7.30	6.74	11.5	9.09
Ho	1.51	1.46	1.68	1.56	1.54	1.55	1.56	1.44	2.49	1.95
Y	44.0	42.9	48.6	43.6	44.4	45.6	45.9	41.9	75.4	58.8
Er	4.32	4.21	4.82	4.47	4.45	4.52	4.50	4.15	7.33	5.73
Tm	0.66	0.65	0.74	0.68	0.68	0.69	0.69	0.63	1.16	0.90
Yb	4.28	4.16	4.75	4.35	4.45	4.39	4.41	4.16	7.50	5.77
Lu	0.65	0.63	0.73	0.66	0.68	0.67	0.68	0.64	1.15	0.88

Table 3 (cont'd).

Sample	264-20	265-49	265-106	265-108	264-14	265-66	265-64	265-83	265-85
Li	15.8	11.9	15.6	15.7	26.4	36.9	33.6	32.4	31.4
Sc	32.4	36.9	33.9	33.5	23.6	26.2	19.9	11.0	14.5
V	250	287	240	235	160	184	140	32	73
Cr	73.2	107	40.6	38.7	40.7	15.3	12.3	3.4	4.6
Co	32.3	35.9	32.4	32.1	21.2	23.1	17.3	8.3	12.3
Ni	42.3	46.6	29.8	30.5	21.7	14.7	9.8	4.7	6.6
Cu	52.4	51.6	42.9	45.0	29.4	24.4	19.1	14.0	18.8
Zn	98.7	93.3	113	114	114	143	124	103	108
Ga	18.5	17.2	19.7	19.3	26.2	42.1	35.4	29.2	28.1
Cs	0.05	0.03	0.04	0.04	0.10	0.12	0.12	0.17	0.15
Rb	3.70	2.45	3.18	3.19	7.79	11.6	10.5	15.5	13.8
Ba	23.6	16.6	22.7	23.0	43.5	62.6	57.1	76.4	68.1
Th	0.64	0.41	0.59	0.59	1.28	2.00	1.82	2.80	2.43
U	0.25	0.17	0.24	0.25	0.51	0.71	0.65	1.05	0.92
Nb	6.46	4.91	8.18	8.31	11.4	16.8	14.8	15.6	15.3
Ta	0.44	0.33	0.53	0.54	0.80	1.23	1.10	1.08	1.05
La	9.79	7.04	10.9	11.2	19.4	28.9	26.3	30.7	29.1
Ce	29.1	21.3	33.9	34.6	57.0	84.2	76.5	87.2	82.5
Pb	1.40	0.99	1.20	1.28	2.67	6.24	5.05	3.80	3.59
Pr	4.61	3.43	5.54	5.66	8.47	12.5	11.4	12.3	11.8
Nd	22.6	17.5	28.3	28.9	39.1	58.3	52.8	54.0	52.1
Sr	107	113	116	116	97.5	114	89.7	76.2	80.6
Sm	7.36	5.84	9.46	9.66	12.4	17.1	15.4	16.5	16.0
Hf	7.70	5.46	8.77	8.94	14.8	23.1	20.9	24.8	23.0
Zr	283	205	339	341	542	945	842	922	872
Eu	2.01	1.75	2.60	2.67	2.75	3.78	3.35	3.05	3.01
Gd	9.14	7.36	11.6	12.1	14.8	20.4	18.1	18.9	18.5
Tb	1.76	1.40	2.19	2.27	2.86	3.83	3.43	3.64	3.55
Dy	11.7	9.30	14.4	15.0	19.3	25.3	22.8	24.5	23.8
Ho	2.52	2.00	3.10	3.18	4.14	5.42	4.88	5.27	5.12
Y	75.0	59.7	93.8	95.0	124	164	148	159	154
Er	7.44	5.87	8.99	9.23	12.4	16.4	14.7	16.2	15.5
Tm	1.17	0.91	1.40	1.43	1.98	2.58	2.33	2.62	2.49
Yb	7.62	5.84	9.06	9.25	13.1	16.8	15.2	17.5	16.7
Lu	1.16	0.90	1.40	1.42	2.04	2.55	2.31	2.72	2.58

Samples were analyzed for trace elements at the University of Florida using an Element II Inductively Coupled Plasma Mass Spectrometer (ICP-MS). The analyses were performed in medium resolution with Re and Rh used as internal standards. Concentrations were calculated by external calibration using a combination of USGS rock standards. Repeated chemical analyses of in-house MORB standard ALV2392-9 during each run were used to evaluate and correct for instrument drift as well as evaluate accuracy and precision of the measurements. Precision (2σ) was found to be better than $\pm 5\%$ for the REE, Ba, Hf, Nb, Rb, Sr, Th, Y, Zr, and better than $\pm 9\%$ for Pb, Ta, and U.

Table 4. $^{87}\text{Sr}/^{86}\text{Sr}$ and $^{143}\text{Nd}/^{144}\text{Nd}$ isotopic compositions of 9°03'N EPR Overlapping Spreading Center East Limb Lavas.

Sample	$^{87}\text{Sr}/^{86}\text{Sr}^{\text{a}}$	b	c	d	e	$^{143}\text{Nd}/^{144}\text{Nd}^{\text{a}}$	b	ϵ_{Nd}	$^{143}\text{Nd}/^{144}\text{Nd}^{\text{c}}$	ϵ_{Nd}
<i>Axial Basalts</i>										
265-74	0.702498					<u>0.513162</u>		10.22		
265-76	<u>0.702528</u>					0.513140		9.79		
266-18	<u>0.702491</u>					<u>0.513168</u>		10.34		
267-09	<u>0.702451</u>					<u>0.513186</u>		10.69		
<i>Flank Basalts</i>										
265-31	0.702473					0.513152		10.03		
265-32	<u>0.702483</u>	0.702582	0.702482	0.702474		<u>0.513151</u>	0.513156	10.01		
265-33	0.702480					0.513156		10.11		
<i>Pillow Ridge Basalts</i>										
265-06						0.513156		10.10		
265-18					0.70249				0.513190	10.8
<i>Axial Basaltic Andesites</i>										
264-13	0.702512					0.513164		10.26		
264-17	0.702468					0.513151		10.01		
264-20	<u>0.702499</u>				0.70244	<u>0.513144</u>		9.87	0.513179	10.6
265-49	0.702498	<u>0.702689</u>	0.702487	0.702475	0.70244	<u>0.513150</u>	0.513157	9.98	0.513196	10.9
265-106	<u>0.702520</u>	<u>0.702564</u>				<u>0.513166</u>	<u>0.513157</u>	10.30		
265-108	<u>0.702682</u>			0.702519		<u>0.513150</u>	0.513156	9.99		
<i>Andesites/Dacites</i>										
264-14	0.702519				0.70243	0.513160		10.19	0.513153	10.0
265-66	0.702493									
265-64	0.702534				0.70258	0.513158		10.14	0.513185	10.7
265-83	0.702524				0.70253	0.513159		10.16	0.513147	9.9
265-85					0.70248	0.513165		10.27	0.513148	9.9

^a Analyzed by Thermo Finnigan Neptune multiple-collector, inductively-coupled-plasma mass spectrometer (MC-ICP-MS) at Woods Hole Oceanographic Institution (WHOI).

^b Replicate analyses by WHOI Neptune.

^c Replicate analyses by WHOI Neptune of solution analyzed by the Thermo Finnigan Triton multiple-collector thermal ionization mass spectrometer (MC-TIMS) at Boston University (see note below).

^d Analyzed by Thermo Finnigan Triton MC-TIMS at Boston University.

^e Analyses reported by Wanless et al., submitted to Journal of Petrology, 2009; Sr and Nd isotopic compositions were analyzed by Nu Plasma MC-ICP-MS at the University of Florida.

^f Underlined values indicate that the leaching procedure used was the same weak leaching procedure as that used for U-series measurements (see Table 5 for details). All other samples were leached for 1 hour in 2.5N HCl at 100°C.

Table 5. ($^{230}\text{Th}/^{232}\text{Th}$), ($^{230}\text{Th}/^{238}\text{U}$), ($^{226}\text{Ra}/^{230}\text{Th}$), ($^{234}\text{U}/^{238}\text{U}$), and U, Th, and ^{226}Ra concentrations of 9°03'N EPR Overlapping Spreading Center East Limb Lavas^a.

Sample	Th (ppm) ^b	U (ppm) ^b	($^{238}\text{U}/^{232}\text{Th}$) ^c	Th/U	($^{230}\text{Th}/^{232}\text{Th}$) ^d	($^{230}\text{Th}/^{238}\text{U}$) ^e	[^{226}Ra] fg/g ^c	($^{226}\text{Ra}/^{230}\text{Th}$) ^e	($^{234}\text{U}/^{238}\text{U}$) ^f
265-74	0.161	0.066	1.241	2.445	1.378	1.111	56.15	2.27	1.008
265-76	0.185	0.075	1.233	2.460	1.370	1.111	67.81	2.41	0.993
	0.183	0.072	1.202	2.525		1.140	67.80	2.45	
<i>average</i>	<i>0.184</i>	<i>0.074</i>	<i>1.218</i>	<i>2.493</i>	<i>1.370</i>	<i>1.126</i>	<i>67.81</i>	<i>2.43</i>	<i>0.993</i>
266-18	0.177	0.072	1.238	2.451	1.366	1.104	64.10	2.39	1.000
267-09	0.158	0.065	1.244	2.438	1.366	1.098	50.68	2.10	1.003
265-32	0.149	0.061	1.248	2.431	1.405	1.126	45.36	1.96	1.001
265-33	0.191	0.078	1.234	2.458	1.528	1.238	58.36	1.80	1.005
					1.515	1.228		1.81	
265-06	0.156	0.065	1.272	2.385	1.410	1.108	43.35	1.81	1.006
					1.387	1.091	44.25	1.84	
265-12	0.283	0.111	1.196	2.537	1.453	1.215	41.42	0.91	1.005
					1.429	1.195		0.92	
265-13	0.149	0.062	1.273	2.383	1.584	1.244	46.88	1.79	1.006
					1.567	1.231		1.81	
265-18	0.154	0.065	1.275	2.379	1.416	1.111	45.02	1.85	1.004
					1.404	1.101		1.87	
265-19	0.153	0.064	1.275	2.379	1.509	1.183	46.39	1.81	1.004
					1.499	1.176		1.82	
265-20	0.154	0.065	1.275	2.378	1.410	1.106	44.46	1.84	1.004
					1.409	1.105		1.84	
264-13	0.603	0.238	1.196	2.537	1.381	1.155	137.59	1.49	1.002
264-17	0.369	0.148	1.215	2.497	1.381	1.136	100.41	1.77	1.004
264-20	0.588	0.230	1.187	2.555	1.382	1.164	115.93	1.25	0.999
	0.584	0.229	1.190	2.549		1.161	115.92	1.29	
<i>average</i>	<i>0.586</i>	<i>0.230</i>	<i>1.189</i>	<i>2.552</i>	<i>1.382</i>	<i>1.163</i>	<i>115.92</i>	<i>1.28</i>	<i>0.999</i>
265-49	0.390	0.156	1.216	2.494	1.374	1.130	72.01	1.21	1.001
265-106	0.558	0.230	1.252	2.423	1.378	1.101	140.88	1.65	1.004
265-108	0.569	0.235	1.253	2.421	1.384	1.104	116.97	1.34	0.996

Table 5 (cont'd).

Sample	Th (ppm) ^b	U (ppm) ^b	(²³⁸ U/ ²³² Th) ^c	Th/U	(²³⁰ Th/ ²³² Th) ^d	(²³⁰ Th/ ²³⁸ U) ^g	[²²⁶ Ra] fg/g ^e	(²²⁶ Ra/ ²³⁰ Th) ^g	(²³⁴ U/ ²³⁸ U) ^f
265-66	1.468	0.573	1.184	2.562	1.373	1.159	312.24	1.39	1.003
265-64	1.559	0.608	1.183	2.565	1.378	1.166	329.70	1.37	1.004
265-83	1.965	0.756	1.167	2.599	1.349	1.156	307.08	1.04	1.004
265-85	2.334	0.900	1.170	2.594	1.374	1.175	352.85	0.99	1.003
TML/3	30.384	10.819	1.078	2.814	1.082	1.002	3,669	1.01	1.002
	30.625	10.775	1.067	2.842	1.083	1.002	3,675	1.01	
					1.078	0.998			
					1.081	1.000	3,709	1.02	
					1.073	0.993	3,698	1.02	
					1.074	0.994			
AThO/3	7.522	2.264	0.913	3.322	1.017	1.114	861.4	1.01	1.001
					1.028	1.124	834.6	0.98	

^a Duplicate measurements represent spiking and purification of U and Th for separate samples of the same glass dissolution. In the laboratory, the samples were hand-picked under a microscope, then ultrasonically leached in sequential treatments of 0.1N HCl plus 2% H₂O₂ (15 min), DI water (twice, each time for 15 min), 0.1N oxalic acid plus 2% H₂O₂, and DI water (twice, each time for 15 min). Samples were then hand-picked by microscope for a second time to assure clean glass devoid of visible alteration. Sample splits (~1-3 g) were then dissolved, aliquoted, spiked and then U, Th, and Ra were separated using chemical techniques outlined in Sims et al. (2008a, b).

^b[U] and [Th] were measured using a ID-ICP-MS using the Thermo Finnigan Element. Measurement reproducibility (2σ) for [U] and [Th] are estimated at <2.1% and <2.5%, respectively.

^c() denotes activity $\lambda_{238} = 1.551 \times 10^{-10} \text{ yr}^{-1}$; $\lambda_{232} = 4.948 \times 10^{-11} \text{ yr}^{-1}$; (²³⁸U/²³²Th) errors (2σ) range from 1.9%-2.9% and do not include uncertainties in λ_{238} (0.07%) or λ_{232} (0.5%).

^dTh isotopic compositions measured by Thermo Finnigan Neptune MC-ICP-MS at WHOI (Ball et al., 2008; Sims et al., 2008b); activity ratios calculated using $\lambda_{230} = 9.195 \times 10^{-6} \text{ yr}^{-1}$ and $\lambda_{232} = 4.948 \times 10^{-11} \text{ yr}^{-1}$; errors (2σ) range from 0.7% - 1.6% and do not include uncertainties in λ_{230} (0.4%) or λ_{232} (0.5%).

^e(²²⁶Ra) measured by isotope dilution using the Thermo Finnigan Neptune MC-ICP-MS at WHOI after Sims et al. (2008a); $\lambda_{226} = 4.331 \times 10^{-4} \text{ yr}^{-1}$; measurement errors (2σ) range from 2.9% -4.9% and do not include uncertainties in λ_{226} (0.4%) or λ_{230} . For all samples accuracy is limited by uncertainties (2σ; 1.5%) on the NBS ²²⁶Ra standard used to calibrate the ²²⁸Ra spike.

^f(²³⁴U/²³⁸U) measured by Thermo Finnigan Neptune MC-ICP-MS at WHOI; $\lambda_{234} = 2.823 \times 10^{-6} \text{ yr}^{-1}$, errors (2σ) < 0.6%; for these samples (²³⁴U/²³⁸U) = 1 within error, using an equilibrium (²³⁴U/²³⁸U) of 54.48 ppm for U010 (Richter and Goldberg, 2003). NBS 960 was first bracketed by standard U010 to cross-calibrate U010. U010 was then used as a bracketing standard for all sample measurements to determine mass bias.

^g Numbers in parentheses are based on estimates of (²³⁰Th/²³²Th) for samples with anomalously high (²³⁰Th/²³²Th). See text for details.

Table 6. 9°03'N Overlapping Spreading Center East Limb Basalt ^{230}Th - ^{226}Ra model ages^a.

Sample	Minimum Model Age (yrs)	Maximum Model Age (yrs)	Basalt Trend Line Age (yrs)
Axial Basalts			
265-74	0	1744	1029 ± 148
265-76 (avg.)	0	1267	461 ± 134
266-18	0	1638	959 ± 151
267-09	695	2255	1604 ± 170
Flank Basalts			
265-32	92	2157	1348 ± 184
Pillow Ridge Basalts			
265-06	1516	2987	2366 ± 247
265-18	1164	2765	2101 ± 235
265-20	1123	2783	2099 ± 158

^aTrend line model ages were calculated using the zero-age trend including samples from the 1991-92 and 2005-06 eruptions ~9°50'N EPR as reported in Sims et al. (2002) and Waters et al. (in prep.) assuming vertical decay from an initial zero-age trend line ($^{226}\text{Ra}/^{230}\text{Th}$) at the sample ($^{230}\text{Th}/^{238}\text{U}$). Errors incorporate only analytical uncertainties in the ($^{226}\text{Ra}/^{230}\text{Th}$) of the sample. Th-Ra minimum and maximum model ages were determined by calculating the mean offset from the zero-age trend line for the critical value of the Student's T-distribution at the 95% confidence level. We assume that trend lines representing maximum and minimum initial ($^{226}\text{Ra}/^{230}\text{Th}$) for this zero-age population (at the 95% confidence interval) can be represented by lines offset from the best-fit zero-age trend line by this critical value. Negative minimum ages are reported as zero years.

Table 7. U, Th, and Ra mineral/melt partition coefficients used for equilibrium melting calculations. Partition coefficients were compiled from Berlo et al. (2004), Blundy and Wood (2003), Klemme et al. (2006), and Miller et al. (2007). Most phases have $D_{Th/U} > 1$ and $D_{Ra/Th} \ll 1$, which will increase U/Th and Ra/Th in the melt during melting or crystallization.

Element	Olivine	Opx	Cpx	Plagioclase	Ilmenite	Amphibole
Ra	1E-7	1E-7	9E-7	0.040	1E-07	0.028
Th	0.00001	0.0015	0.045	0.0003	0.0027	0.022
U	0.00006	0.0007	0.008	0.00006	0.01	0.007
D_{Th}/D_U	0.2	2.1	5.6	5.0	0.3	3.1
D_{Ra}/D_{Th}	0.01	0.00007	0.00002	130	0.00004	1.3

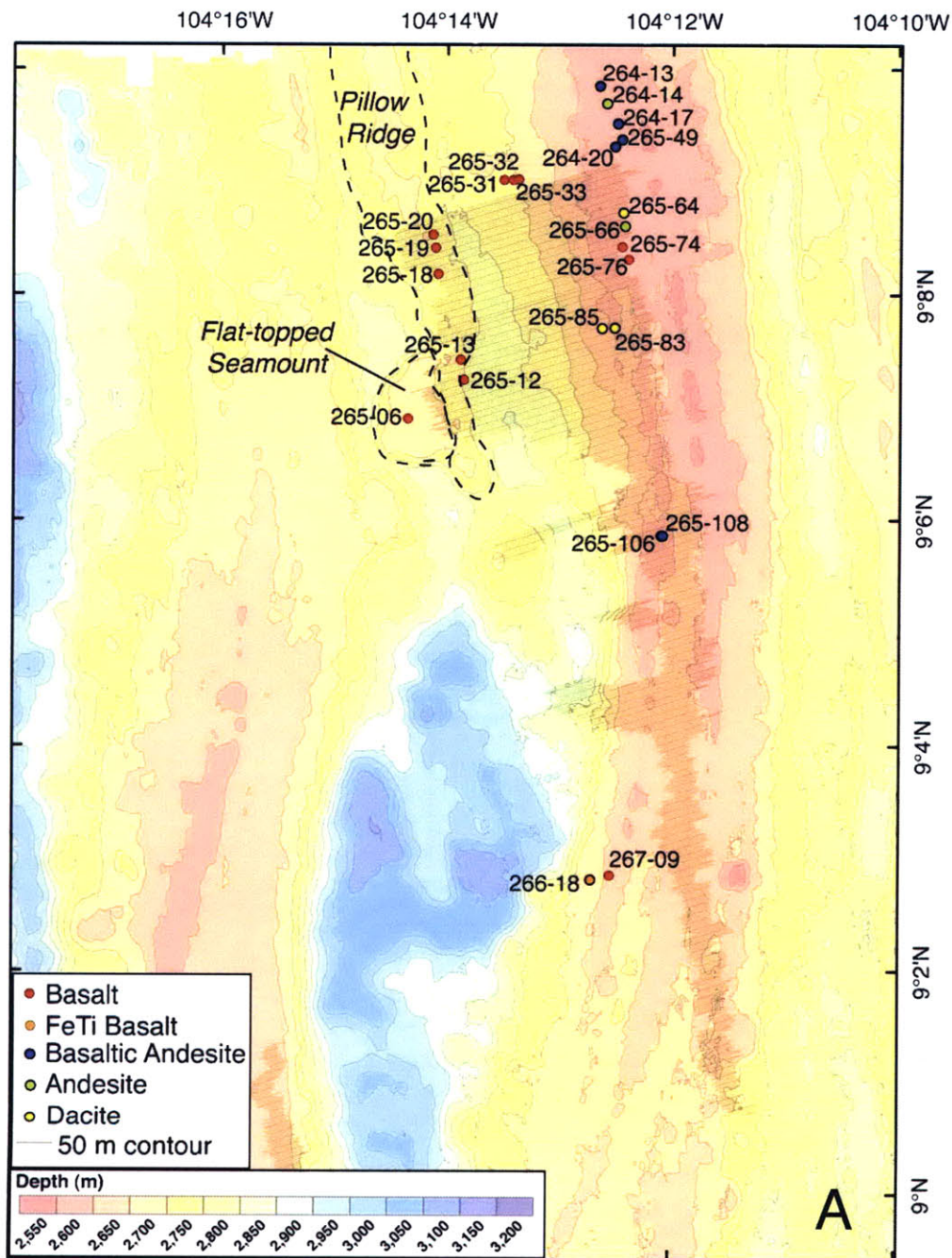


Figure 1. (A) EM300 bathymetric map (White et al., 2006) of study area showing locations and types of samples analyzed in this study. The off-axis volcanic pillow ridge that overlies the western extent of the axial magma chamber (AMC; shown as gray overlay; Kent et al., 2000) is encircled by a dashed line, as is the flat topped volcano from the center of which sample 265-06 was collected. (B) DSL-120A side-scan sonar map of study area (White et al., 2009). Basaltic samples are shown as red circles, FeTi basalts by orange circles, basaltic andesites by blue circles, andesites by green circles, and dacites by yellow circles.

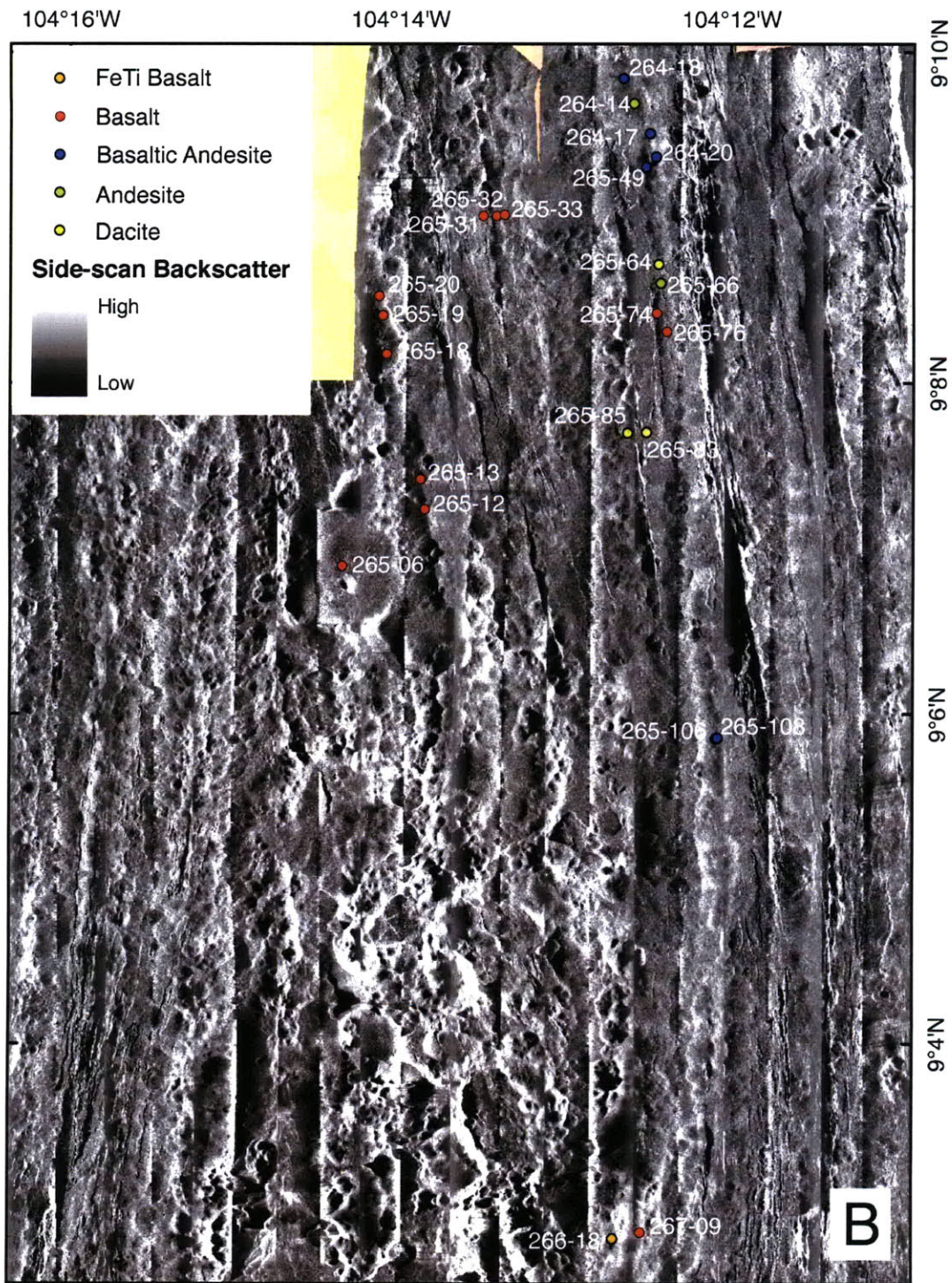
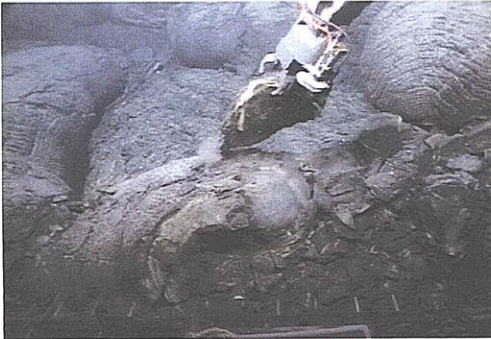


Figure 1 (cont'd).

A) 265-64: Axial Dacite



B) 265-33: Flank Basalt



C) 265-06: Flat-topped Volcano Basalt



D) 265-74: Axial Basalt



E) 265-49: Axial Basaltic Andesite



F) 265-12: Off-axis Basalt from Away from Pillow Ridge

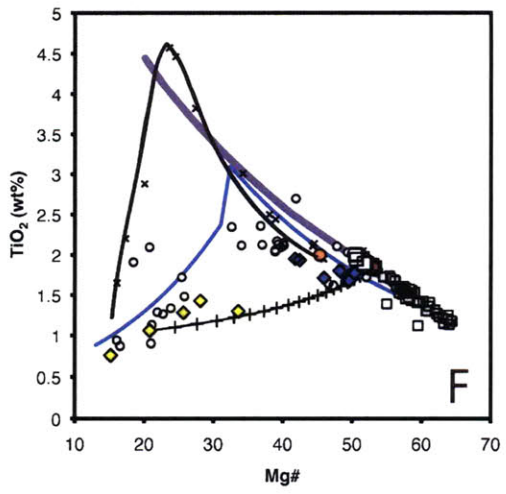
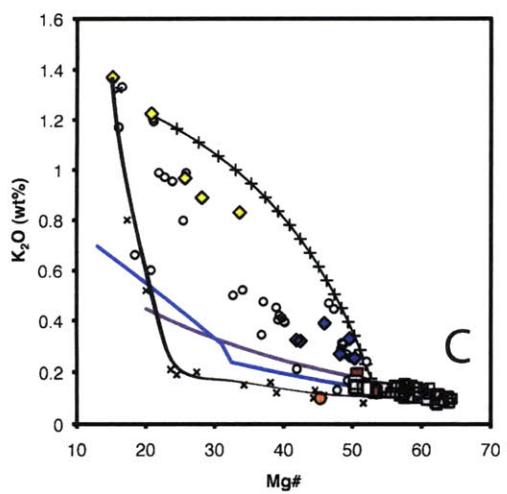
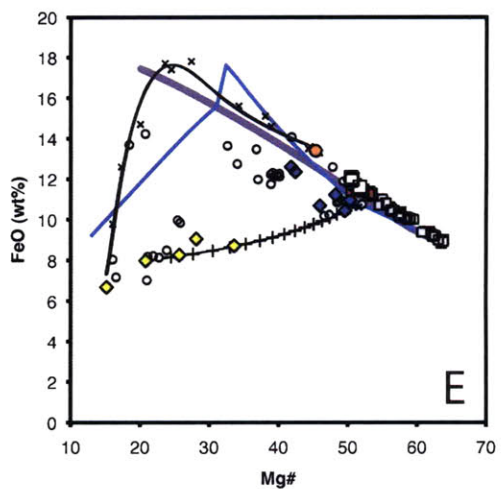
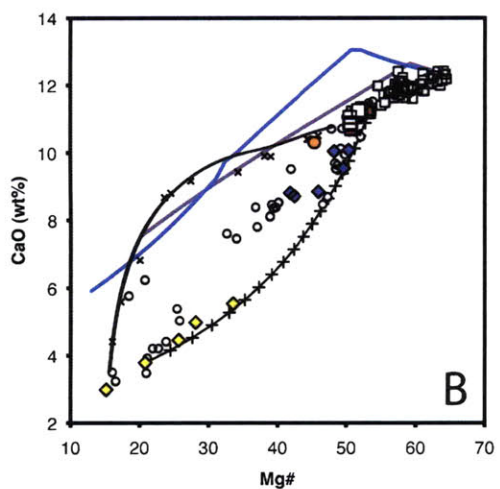
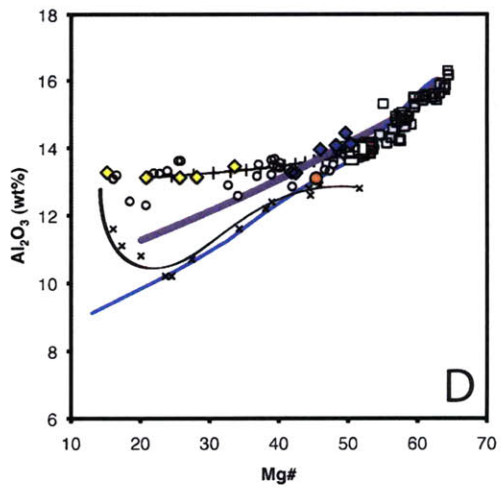
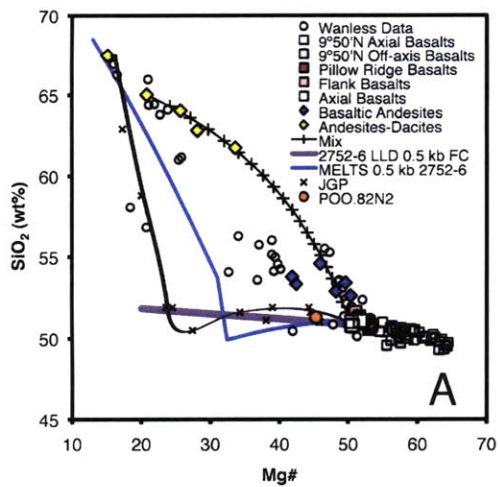


G) 265-13: Off-axis Pillow Ridge Basalt



Figure 2. Jason II Virtual Van dive photos for select rock samples (<http://4dgeo.who.edu/webdata/virtualvan/html/VV-at15-17/index.html>). Samples span a range of compositions and locations about the eastern limb of the OSC at 9°03'N EPR. In general, off-axis basalts (B, C F, G) appear much older than samples collected from within the axial summit graben.

Figure 3. Molar Mg# ($\text{Mg}/(\text{Fe}+\text{Mg}) \times 100$) vs. wt% (A) SiO_2 , (B) CaO , (C) K_2O , (D) Al_2O_3 , (E) FeO , and (F) TiO_2 , showing east limb axial basalts (light red squares), flank basalts (medium red squares), pillow ridge basalts (dark red squares), basaltic andesites (blue diamonds), and andesites-dacites (yellow diamonds) collected at the OSC at $9^\circ 03' \text{N}$ EPR. Additional east limb lava major element data from Wanless et al. (in prep.) are plotted for comparison (light blue circles). Also plotted are basalts collected from within the axial summit trough from $9^\circ 17' \text{N}$ - $9^\circ 54' \text{N}$ EPR (white squares; Sims et al., 2002; Waters et al., in prep), and basalts collected from up to 5 km off-axis on the ridge flanks at $9^\circ 50' \text{N}$ EPR (gray squares; Sims et al., 2003; Waters et al., in prep). Ferrobasalts from $9^\circ 03' \text{N}$ EPR appear to be related to basalts from $9^\circ 17' \text{N}$ - $9^\circ 54' \text{N}$ EPR by fractional crystallization of a similar parent magma; liquid lines of descent (LLD) calculated with the model of Weaver and Langmuir (1990) at 0.5 kbar using the parental melt composition of primitive basalt 2752-6 (Sims et al., 2002) are shown by purple curves. Because this model does not account for oxide crystallization such that there is no decrease in FeO or TiO_2 , we have plotted dry LLDs (blue lines) determined by MELTS at 0.5 kbar using 2752-6 as the parent melt, as well as the experiments of Juster et al. (1989) (JGP) using the 85°W Galapagos Spreading Center FeTi basalt POO.82N2 as a starting composition (orange circle). Black lines are drawn in to highlight the trends of these experimental data. Dacites from $9^\circ 03' \text{N}$ EPR appear to represent end member compositions of extensive crystallization (as shown by the experiments of Juster et al. (1989), but not seen by either Weaver and Langmuir or MELTS models), and mixing between axial ferrobasalt (266-18) and dacite (265-85) compositions appears to explain much of the range of basalt, basaltic andesite, and andesite-dacite compositions (black curve; plusses mark 5% increments of mixing). Note that two basaltic andesites do not appear to be related to other lavas by mixing, but can instead be explained by larger extents of crystallization, perhaps at different $f\text{O}_2$. Similar mixing relationships exist among trace elements and U-series isotopic data (see Figures 4, 5, 9). Basaltic lavas from $9^\circ 03' \text{N}$ EPR have lower Mg# than basalts from $9^\circ 17'$ - $9^\circ 54' \text{N}$ EPR, as they are more Fe-rich and Mg-poor. When considered in light of their spatial distribution, some notable systematics emerge among basaltic lavas: flank basalts from mid-way across the wide melt lens appear compositionally transitional to lavas collected within the axial graben and pillow ridge basalts. In addition, with the exception of sample 265-12, which was sampled just off of the large pillow mound, lavas sampled from the pillow mound and nearby flat-topped volcano are very similar to each other. We note that 265-12 is generally more enriched than all other pillow ridge basalts with regard to incompatible trace elements. See text for details.



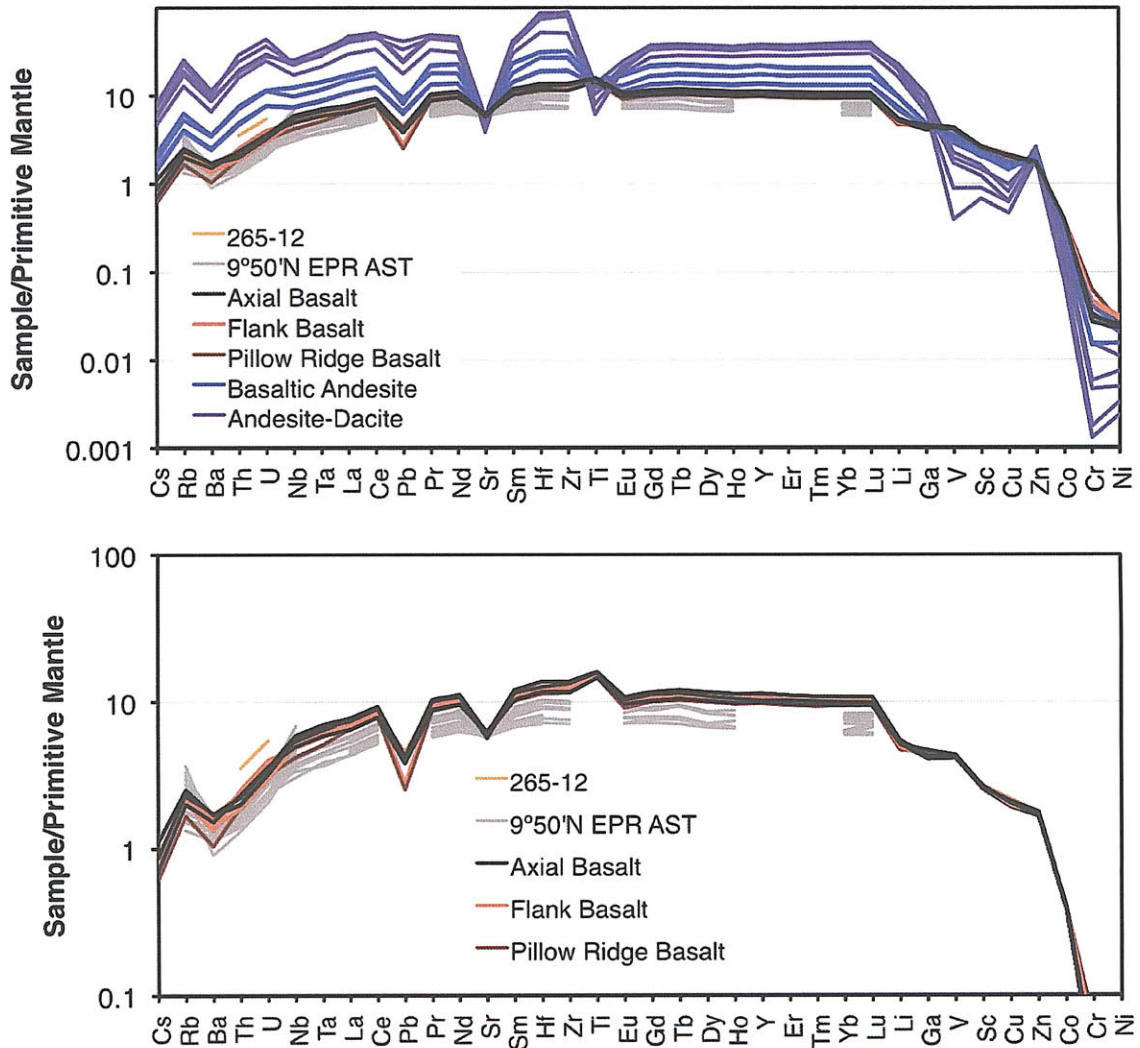


Figure 4. (A) Spidergram of primitive mantle (McDonough and Sun, 1995) normalized trace element abundances for all samples in this study in order of increasing compatibility from left to right (after Hofmann, 1988). Compatible elements (Li, Ga, V, Sc, Cu, Zn, Co, Cr, and Ni) were arranged so as to eliminate any anomalies. (B) Spidergram of primitive mantle normalized trace element abundances for all basalts in this study. Shown for comparison are data from basalts collected from within the axial summit trough from 9°17'N-9°54'N EPR (Sims et al., 2002).

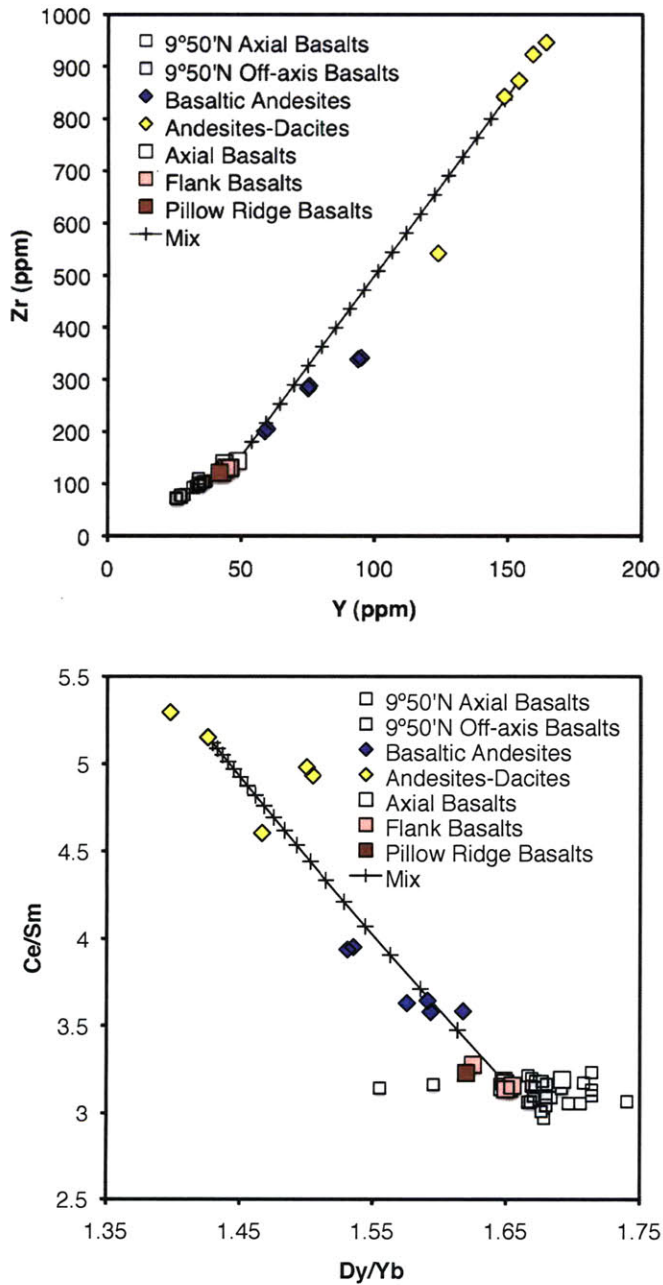


Figure 5. Plots of Y vs. Zr and Dy/Yb vs. Ce/Sm for east limb 9°03'N OSC samples as compared to axial (white squares) and off-axis (gray squares) basalts from ~9°50'N EPR (Sims et al., 2002; 2003; Waters et al., in prep.). Axial basalts are plotted as light red squares, flank basalts as medium red squares, pillow ridge basalts as dark red squares, basaltic andesites as blue diamonds, and andesites-dacites as yellow diamonds. Black lines indicate mixing trajectories between axial basalt 266-18 and dacite 265-85, with plusses to indicate 5% mixing increments.

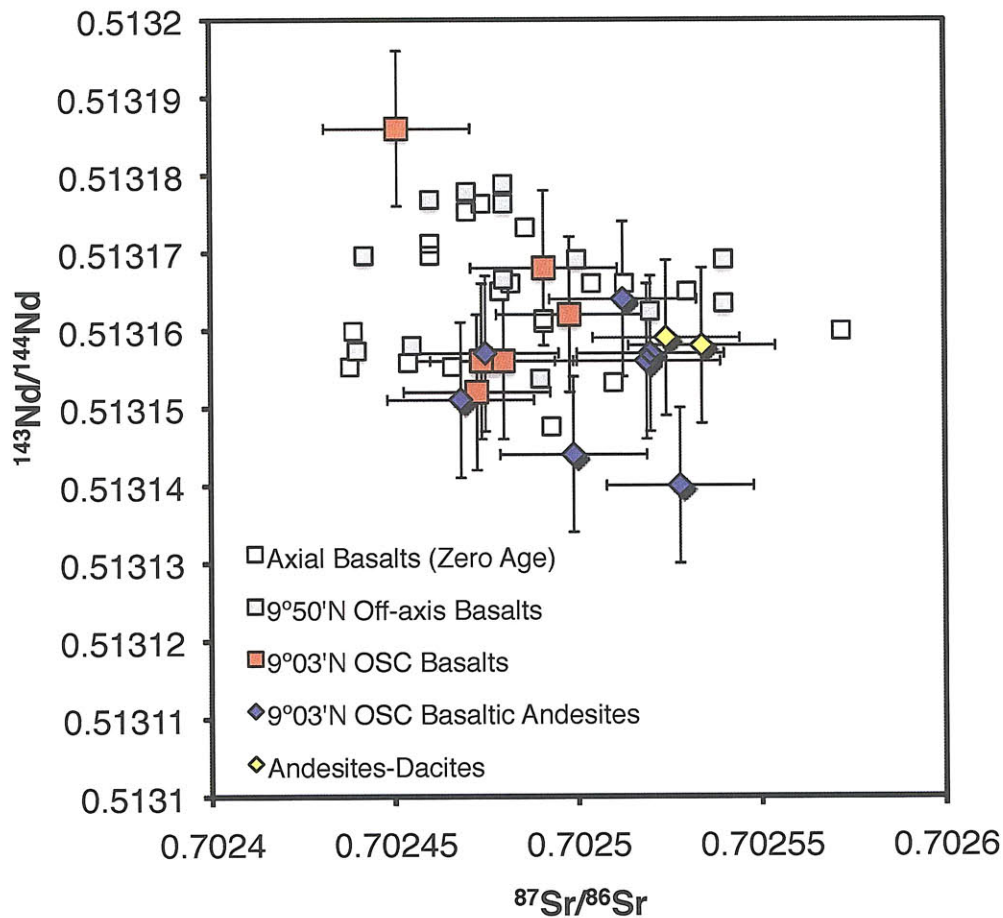
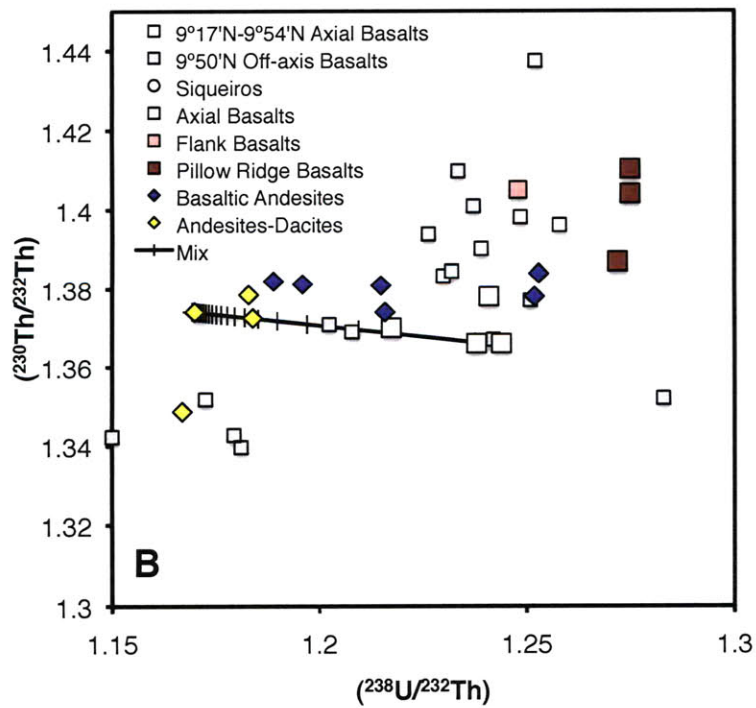
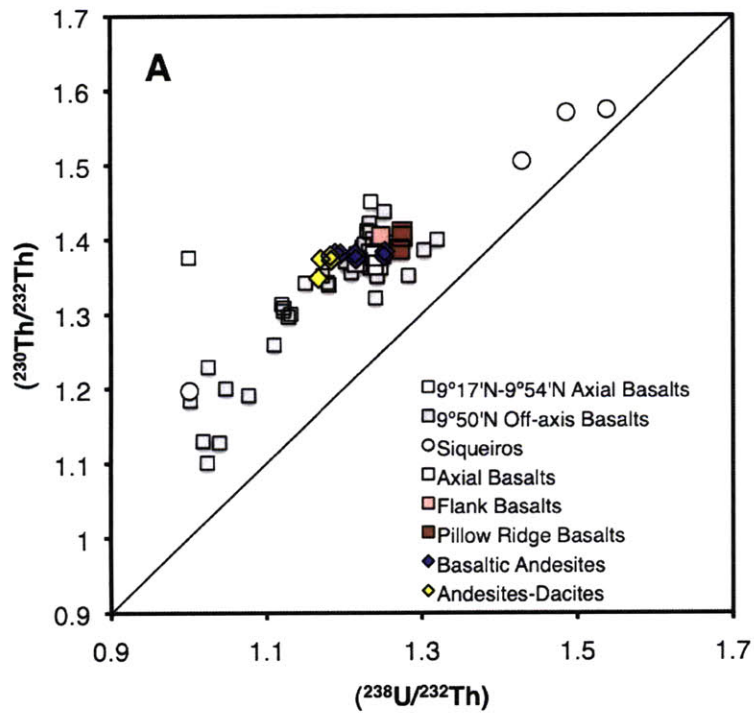


Figure 6. Plot of $^{87}\text{Sr}/^{86}\text{Sr}$ vs. $^{143}\text{Nd}/^{144}\text{Nd}$, showing basalts as red squares, basaltic andesites as blue diamonds, and andesite-dacites as yellow diamonds. Shown for comparison are axial (white squares) and off-axis (gray squares) basalts from $9^{\circ}17'\text{N}$ to $9^{\circ}54'\text{N}$ EPR (Sims et al., 2002; 2003).

Figure 7 (facing page). (A) Equiline diagram showing variation of $(^{238}\text{U}/^{232}\text{Th})$ with $(^{230}\text{Th}/^{232}\text{Th})$ for east limb lavas. Lavas overlap with data for N-MORB from $9^{\circ}17'$ - $9^{\circ}54'\text{N}$ EPR. (B) Expanded view of (A) which shows that $9^{\circ}03'\text{N}$ east limb lavas define a nearly horizontal array (note: the four basaltic samples that may have been contaminated with ^{230}Th -enriched Mn oxide crusts or otherwise altered have not been plotted; see Table 5 for data). Axial basalts from $9^{\circ}17'$ - $9^{\circ}54'\text{N}$ EPR including samples from the 1991-1992 and 2005-2006 eruption sequences are plotted as white squares (Sims et al., 2002), off-axis samples from $9^{\circ}30'$ - $9^{\circ}54'\text{N}$ are plotted as gray squares (Sims et al., 2003; Waters et al., in review; in prep), and samples from the Siqueiros Fracture Zone are plotted as white circles (Lundstrom et al., 1999). A mixing trajectory between axial basalt sample 266-18 and dacite sample 265-85 is shown as a black line with pluses indicating 5% increments of mixing.



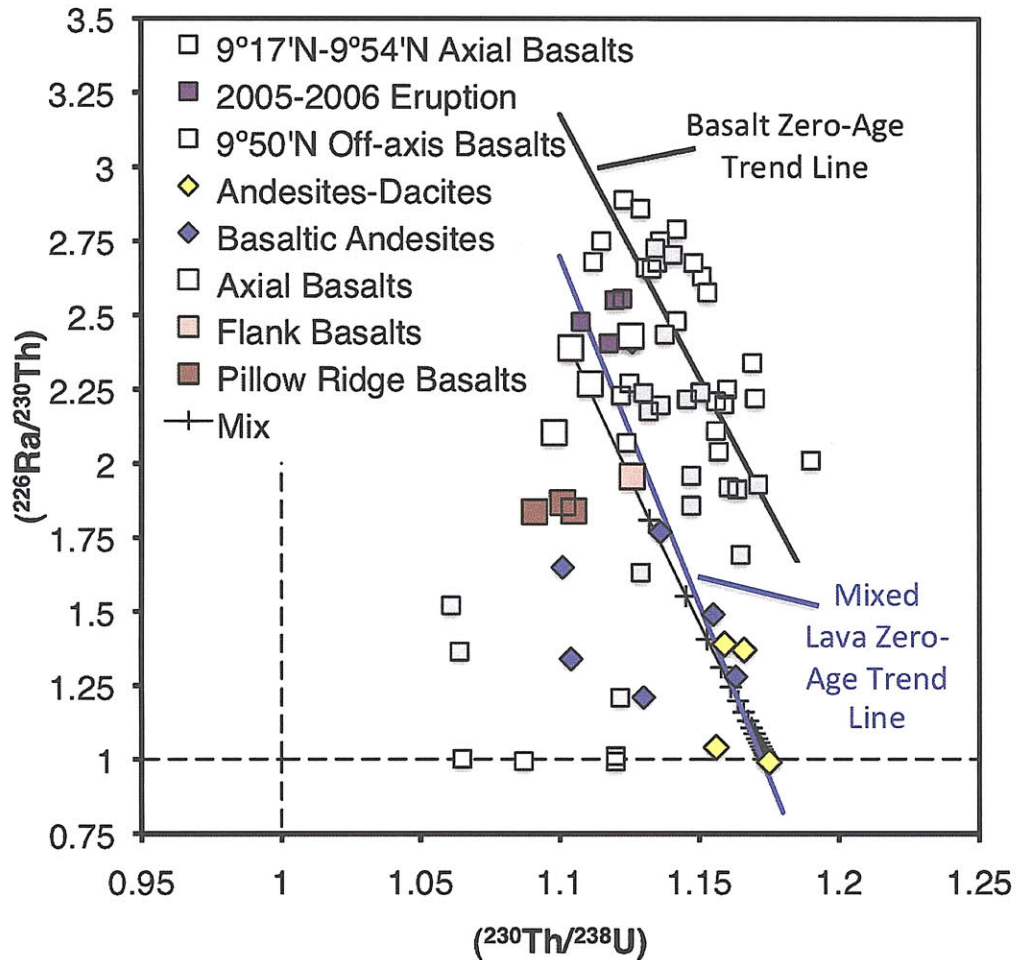


Figure 8. ($^{226}\text{Ra}/^{230}\text{Th}$) vs. ($^{230}\text{Th}/^{238}\text{U}$) for East Limb samples as compared to axial and off-axis samples collected further north from $9^{\circ}17' - 9^{\circ}54' \text{N}$ EPR and samples collected from the Siqueiros Fracture Zone. Symbols and data sources are the same as in Figure 7. Note that samples from the 2005-2006 eruption sequence at $\sim 9^{\circ}50' \text{N}$ EPR have been marked as purple squares (data from Waters et al., in prep.). Equilines are denoted by dashed lines at $(^{226}\text{Ra}/^{230}\text{Th}) = (^{230}\text{Th}/^{238}\text{U}) = 1$. The solid black line shows the zero-age trend line including 2005-06 (Waters et al., in prep) and 1991-92 samples (Sims et al., 2002; 2003), and the solid blue line shows the zero-age trend line of mixed lavas from this study. The thin black line with pluses shows mixing in 5% increments between dacite sample 265-85 and the young axial basalt, sample 266-18.

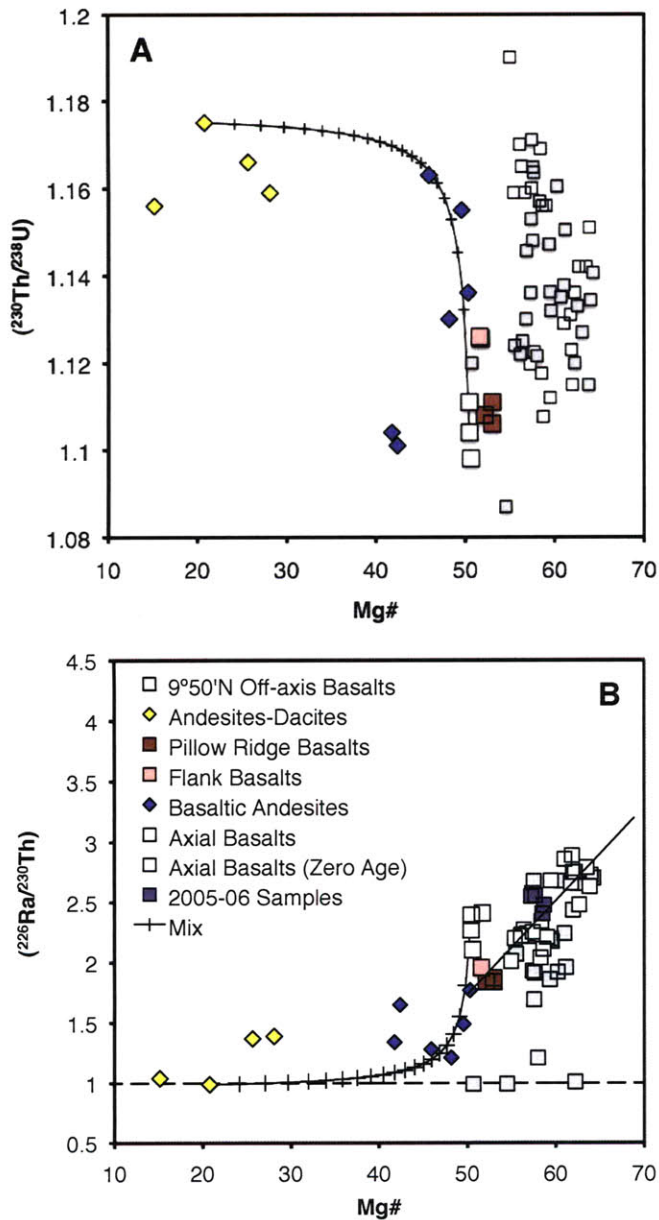


Figure 9. Plot of molar Mg# ($\text{Mg}'/(\text{Mg}' + \text{Fe}')$) vs. (A) $(^{230}\text{Th}/^{238}\text{U})$ and (B) $(^{226}\text{Ra}/^{230}\text{Th})$. Symbols are as in Figures 7 and 8. A mixing curve between dacite 265-85 and young axial basalt 266-18 is shown as a black line with 5% mixing increments shown as pluses. Note that axial basalts from 9°03'N plot at lower Mg# for a given ^{226}Ra excess as compared to what is expected from the zero-age correlation observed at 9°17'N-9°54'N EPR. It is coincidental that flank and pillow ridge basalts intersect the zero-age correlation—they are clearly older in dive photos and have diminished ^{226}Ra excesses (see Figures 2 and 8).

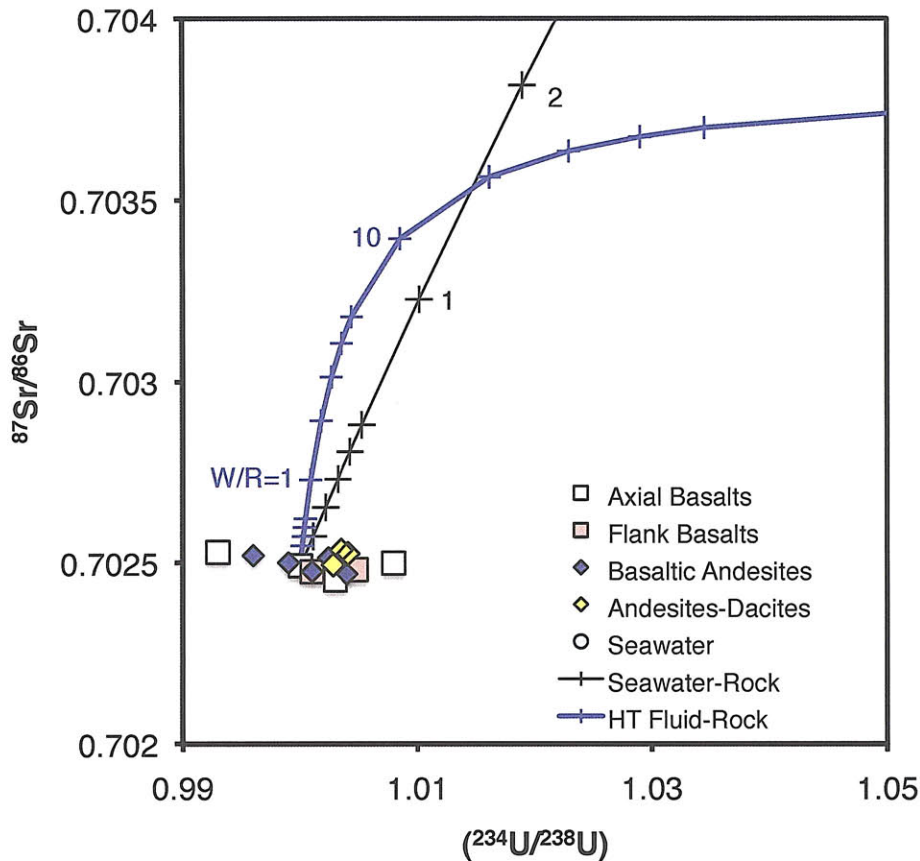


Figure 10. Plot of $(^{234}\text{U}/^{238}\text{U})$ vs. $^{87}\text{Sr}/^{86}\text{Sr}$, showing the effect of seawater-rock and hydrothermal fluid interaction (black line) in comparison to east limb lava compositions. Pluses along seawater-rock and hydrothermal fluid curves mark water:rock ratios (W/R). Interaction of even small amounts of seawater with wall rock (e.g., W/R ~ 0.5) is sufficient to change the $^{87}\text{Sr}/^{86}\text{Sr}$ composition of the lavas from 0.70248 to 0.70265, which is more similar to 9° - 10°N EPR E-MORB compositions (Waters et al., in review) than typical N-MORB (e.g., Sims et al., 2002; 2003). A similar calculation shows hydrothermal fluid-rock interaction is less sensitive, but should still result in significant changes in $^{87}\text{Sr}/^{86}\text{Sr}$ at low W/R (< 2). Although $(^{234}\text{U}/^{238}\text{U})$ is less sensitive to water/rock interaction than $^{87}\text{Sr}/^{86}\text{Sr}$, even a W/R as low as ~ 2 is sufficient to change the $(^{234}\text{U}/^{238}\text{U})$ from $\sim 1 \pm 0.05\%$ to > 1.01 . We assume $[\text{Sr}]_{\text{seawater}} = 7.45$ ppm and $^{87}\text{Sr}/^{86}\text{Sr}_{\text{seawater}} = 0.70916$, and $[\text{U}]_{\text{seawater}} = 3.1$ ppb and $(^{234}\text{U}/^{238}\text{U})_{\text{seawater}} = 1.14$ for East Pacific Rise seawater (Ku et al., 1976, Ravizza et al., 2001). $[\text{Sr}]_{\text{rock}}$, $[\text{U}]_{\text{rock}}$, $^{87}\text{Sr}/^{86}\text{Sr}_{\text{rock}}$, and $(^{234}\text{U}/^{238}\text{U})_{\text{rock}}$ are assumed to be 120 ppm, 0.70248, 80 ppb, and 1.00, respectively. For hydrothermal fluids, we use values of $^{87}\text{Sr}/^{86}\text{Sr} = 0.70381$, $[\text{Sr}] = 13$ ppm, $(^{234}\text{U}/^{238}\text{U}) = 1.14$, and $[\text{U}] = 0.3$ ppb (Ravizza et al., 2001). Neither basaltic lava nor high silica lava shows any sign of incorporation of hydrothermally altered material.

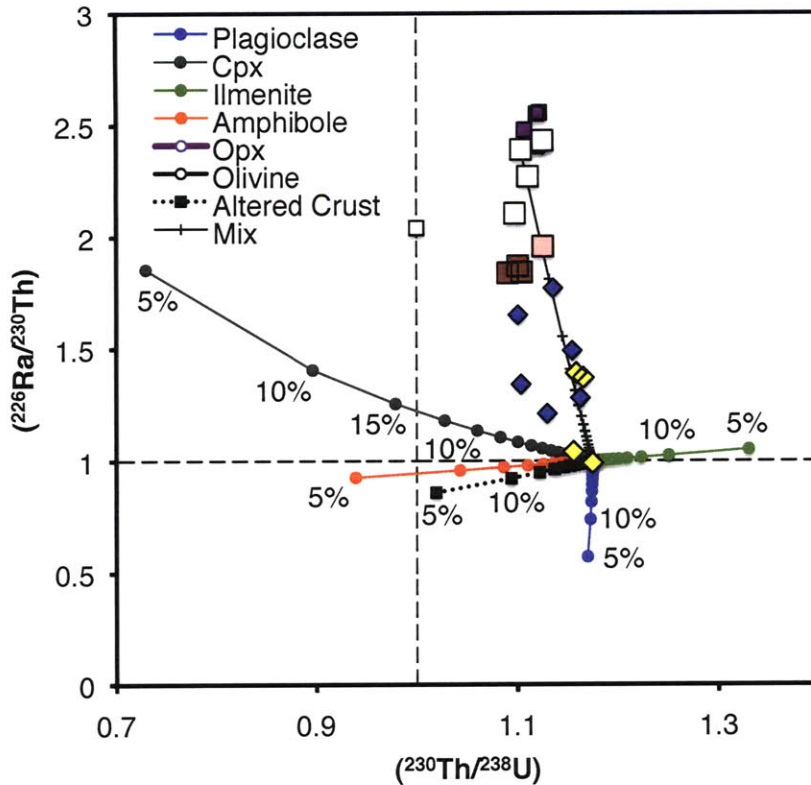


Figure 11. Plot of $(^{230}\text{Th}/^{238}\text{U})$ vs. $(^{226}\text{Ra}/^{230}\text{Th})$ illustrating the effect of modal equilibrium partial melting of different mineral phases (plagioclase=blue, clinopyroxene (Cpx)=black, ilmenite=green, amphibole=red, orthopyroxene (Opx)=purple) expected in gabbro or dikes. Also shown as is the mixing line between ferrobasalt 266-18 and dacite 265-85 (solid black line; see Figure 8). Although ilmenite can produce ^{230}Th excesses, it occurs in minor amounts and cannot control the direction of fractionation of Th from U in a bulk rock. Plagioclase fractionates Ra from Th with little change in Th/U. Clinopyroxene and amphibole result in lower $(^{230}\text{Th}/^{238}\text{U})$ with small changes in $(^{226}\text{Ra}/^{230}\text{Th})$. Melting of orthopyroxene (and olivine) have little effect on Ra/Th or U/Th. Thus, partial melting of a hydrothermally altered wall rock (dotted black line) with 5% amphibole, 20% clinopyroxene, 49% plagioclase and 1% ilmenite (Haase et al., 2005; Wanless et al., in review) will result in a net decrease in $(^{226}\text{Ra}/^{230}\text{Th})$ and $(^{230}\text{Th}/^{238}\text{U})$, which is inconsistent with measured U-series systematics. Symbols along melting trajectories indicate 5% increments. Data symbols are the same as in Figure 8. The horizontal and vertical dashed lines show equilibrium $(^{226}\text{Ra}/^{230}\text{Th})$ and $(^{230}\text{Th}/^{238}\text{U})$, respectively. Mineral/melt partition coefficients are given in Table 7. The source composition was assumed to have $[^{226}\text{Ra}]=33.3$ fg/g, $[\text{Th}]=0.226$ ppm, $[\text{U}]=0.084$ ppm, $(^{230}\text{Th}/^{232}\text{Th})=1.325$, $(^{230}\text{Th}/^{238}\text{U})=1.175$, and $(^{226}\text{Ra}/^{230}\text{Th})=1.00$, a composition similar to an enriched N-MORB from $9^{\circ}50'\text{N}$ EPR decayed to equilibrium $(^{226}\text{Ra}/^{230}\text{Th})$ over 8 kyrs (cf., Waters et al., in prep.).

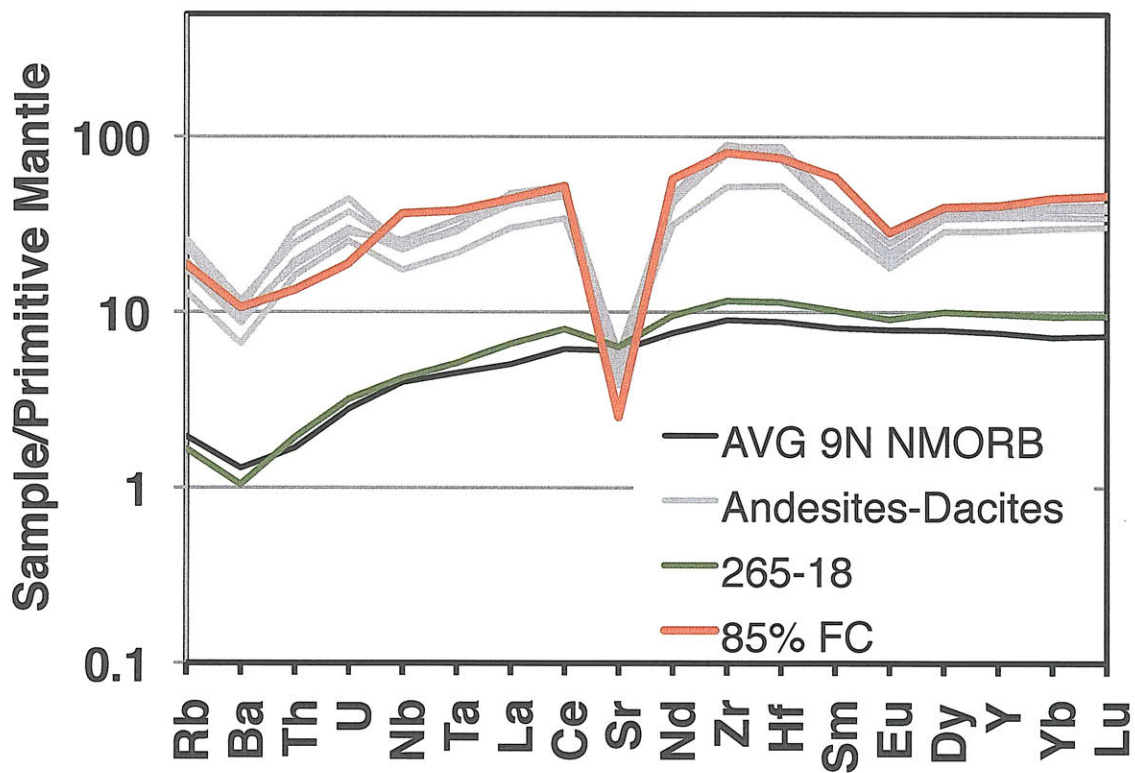


Figure 12. Primitive mantle-normalized trace element spidergram, showing average 9°17'-9°54'N EPR N-MORB (solid black line), a typical 9°03'N OSC east limb ferrobasalt (solid green line), and andesites and dacites from this study (gray lines). Also shown is an 85% fractionally crystallized average 9°17'-9°54'N EPR MORB. Mineral modes and partition coefficients for the fractional crystallization model were taken from Wanless et al. (in review), assuming a “non-amphibole bearing gabbro” composition (19% olivine: 30% clinopyroxene: 50% plagioclase: 1% ilmenite) and “andesite partition coefficients.”